FINAL REPORT ON

EXPLOITATION OF MICRODOPPLER AND MULTIPLE SCATTERING PHENOMENA FOR RADAR TARGET RECOGNITION

Office of Naval Research
Research Grant N00014-03-1-0021

For the period October 1, 2002 through May 31, 2006

Submitted by

Professor Hao Ling

Department of Electrical and Computer Engineering
The University of Texas at Austin
Austin, TX 78712-1084

August 24, 2006

REPORT DOCUMENTATION PAGE

Form Approved
OMB No. 0704-0188

1. AGENCY USE ONLY *(Leave blank)*	2. REPORT DATE	3. REPORT TYPE AND DATES COVERED
	Aug. 24, 2006	Final Report 1 Oct. 02 - 31 May. 06

4. TITLE AND SUBTITLE

Final Report on Exploitation of MicroDoppler and Multiple Scattering Phenomena for Radar Target Recognition

5. FUNDING NUMBERS

Research Grant
ONR
N00014-03-1-0021

6. AUTHOR(S)

Hao Ling

7. PERFORMING ORGANIZATION NAMES(S) AND ADDRESS(ES)

The University of Texas at Austin
Department of Electrical and Computer Engineering
Austin, TX 78712-1084

8. PERFORMING ORGANIZATION REPORT NUMBER

No. 3

9. SPONSORING / MONITORING AGENCY NAMES(S) AND ADDRESS(ES)

Office of Naval Research
Ballston Centre Tower One
800 North Quincy Street
Arlington, VA 22217-5660

Program Officer
G. D. McNeal
ONR 313

10. SPONSORING / MONITORING AGENCY REPORT NUMBER

11. SUPPLEMENTARY NOTES

a. DISTRIBUTION / AVAILABILITY STATEMENT

Approval for Public Release
Distribution Unlimited

12. DISTRIBUTION CODE

13. ABSTRACT ***(Maximum 200 words)***

This report summarizes the scientific progress on the reserach grant "Exploitation of MicroDoppler and Multiple Scattering Phenomena for Radar Target Recognition" during the period 1 October 2002 - 31 May 2006. Research on the microDoppler and multiple scattering phenomena through radar measurement, electromagnetic simulation and signal processing is presented.

14. SUBJECT TERMS

MicroDoppler, Mulitple Scattering, Radar Target Recognition

15. NUMBER OF PAGES

150

16. PRICE CODE

17. SECURITY CLASSIFICATION OF REPORT	18. SECURITY CLASSIFICATION OF THIS PAGE	19. SECURITY CLASSIFICATION OF ABSTRACT	20. LIMITATION OF ABSTRACT
Unclassified	Unclassified	Unclassified	

FINAL REPORT ON

EXPLOITATION OF MICRODOPPLER AND MULTIPLE SCATTERING PHENOMENA FOR RADAR TARGET RECOGNITION

Office of Naval Research
Research Grant N00014-03-1-0021

For the period October 1, 2002 through May 31, 2006

Submitted by

Professor Hao Ling

Department of Electrical and Computer Engineering
The University of Texas at Austin
Austin, TX 78712-1084

August 24, 2006

EXPLOITATION OF MICRODOPPLER AND MULTIPLE SCATTERING PHENOMENA FOR RADAR TARGET RECOGNITION

Project Starting Date:	October 1, 2002
Reporting Period:	October 1, 2002 – May 31, 2006
Principal Investigator:	Professor Hao Ling (512) 471-1710 ling@ece.utexas.edu
Graduate Students:	J. Philson, Y. Zhou, M. G. Anderson, A. Lin, P. Tabrizi, S. Sundar Ram
Undergraduate Student:	J. Soric
Visiting Researcher:	C. Ozdemir

A. SCIENTIFIC OBJECTIVES: Conventional radar signal processing is based on two simplified assumptions about target scattering: (i) that the target is a rigid body; (ii) that the target can be modeled as a collection of independent point scatterers without any multiple scattering effects. However, real radar data can deviate significantly from these two simplified assumptions. First, real-world targets are often observed by radar sensors under dynamic conditions where non-rigid body motions can exist. These non-rigid body motions give rise to "microDoppler" phenomena, which have been observed in a number of SAR and ISAR sensors. Examples of microDoppler phenomena include returns from moving components on the target such as scanning antennas or rotating wheels, as well as those from flexing and vibration of the target frame. Second, strong multiple scattering physics are often encountered in inlets and cavity structures on the target. For instance, the most prominent feature on an air target is often the range-delayed return from the jet inlet duct. Significant modeling work has been carried out by the computational electromagnetics community to characterize the complex scattering from inlet structures, yet little effort has been placed on utilizing the results to develop better imaging algorithms to map the inlet interior. The objectives of this research program are: (i) to gain in-depth understanding of these higher-order phenomena through simulation and

measurement, (ii) to develop physics-based models and the associated signal processing strategies to extract the resulting radar features, and (iii) to exploit and utilize these additional features to enhance the performance of automatic target recognition (ATR) algorithms.

B. SUMMARY OF RESULTS AND SIGNIFICANT ACCOMPLISHMENTS: During this program, we have carried out simulation and experimental research to understand and exploit microDoppler and multiple scattering phenomena. Our research accomplishments in microDoppler phenomena include:

1.1 MicroDoppler radar development, data collection and processing.

1.2 Doppler and direction-of-arrival (DDOA) radar development for human tracking.

1.3 Frontal imaging of humans by exploiting microDoppler.

Our research accomplishments in multiple scattering phenomena include:

2.1 Fast ray tracing simulation for characterizing multiple scattering phenomena.

2.2 Shape reconstruction of targets with strong multiple scattering.

2.3 Imaging buried targets in ground penetrating radar.

The detailed descriptions of our accomplishments are discussed below.

1.1. MicroDoppler Radar Data Collection and Processing. During the first year of this program, we developed a wideband radar testbed that is fully tunable between 4 to 10 GHz (see Fig. 1). The purpose of this hardware effort is to provide data collection capability that allows us to study the microDoppler phenomenology in greater detail. The radar is a homodyne system with full I/Q detection. Data acquisition is accomplished using a National Instruments DAQ card and the results can be displayed on a laptop computer. Careful calibration of the radar was carried out using an audio subwoofer covered by aluminum tape (Fig. 2). We carried out extensive data collection on various types of targets having mechanical movements such as vibration and rotation. Figs. 3 and 4 show the resulting spectrograms of a car and a fan. We also investigated the microDoppler phenomenon from human movements in significant detail. The problem of human gait was previously investigated in [1-3]. We collected a data base over a wide variety of parameter spaces, include various types of movements (walking, running,

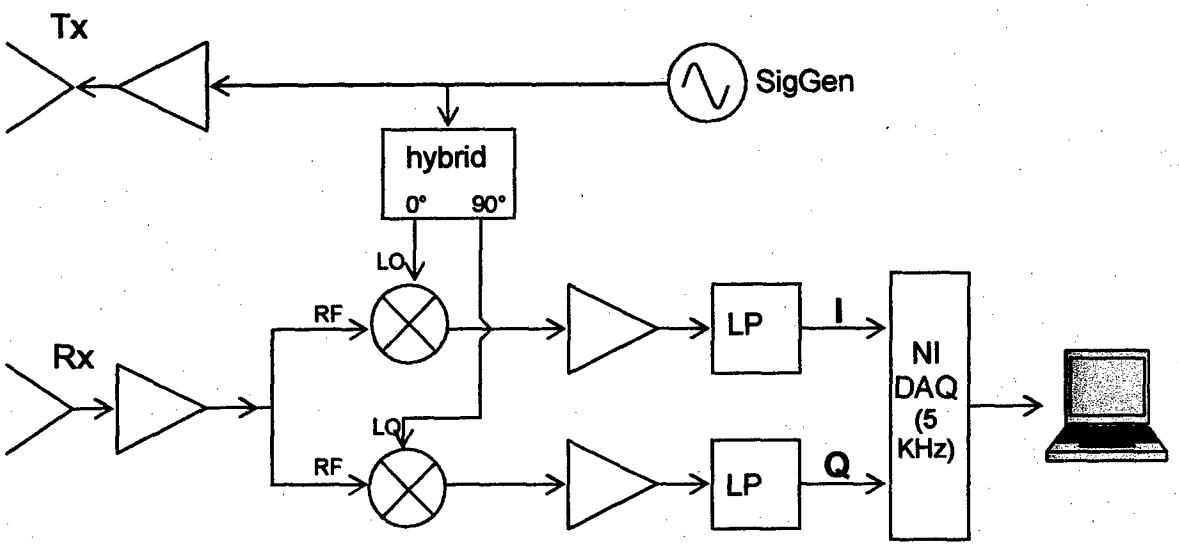

Fig. 1. A low-cost Doppler radar system built at UT-Austin. The radar is tunable from 4 to 10 GHz.

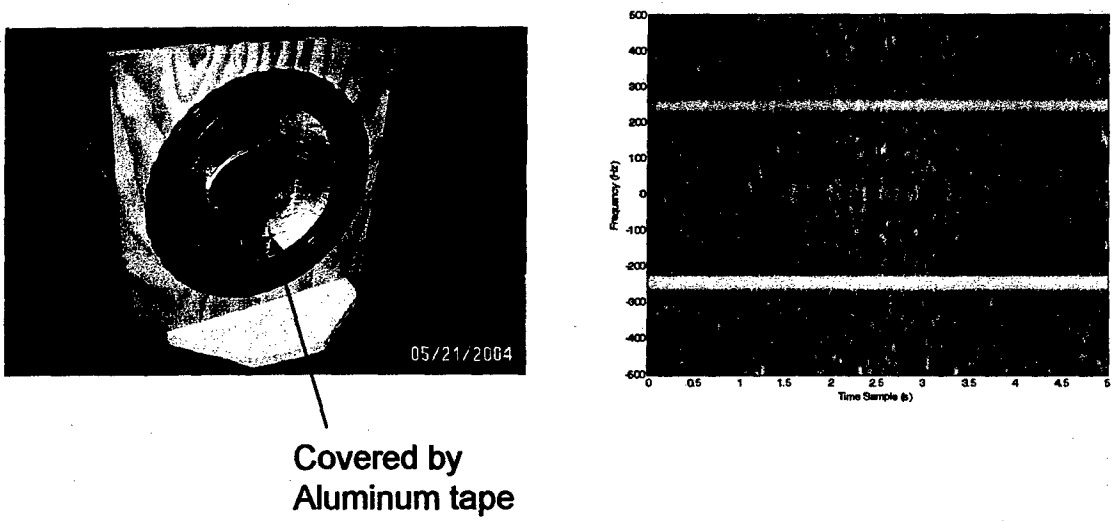

Fig. 2. The calibration data an audio subwoofer covered by aluminum tape and driven by a single-tone audio amplifier. The figure on the right is the spectrogram (Doppler frequency vs. dwell time) of the collected radar return.

Fig. 3. Measured microDoppler return versus dwell time from a parked car at 5.5 GHz, HH-pol (UT-Austin).

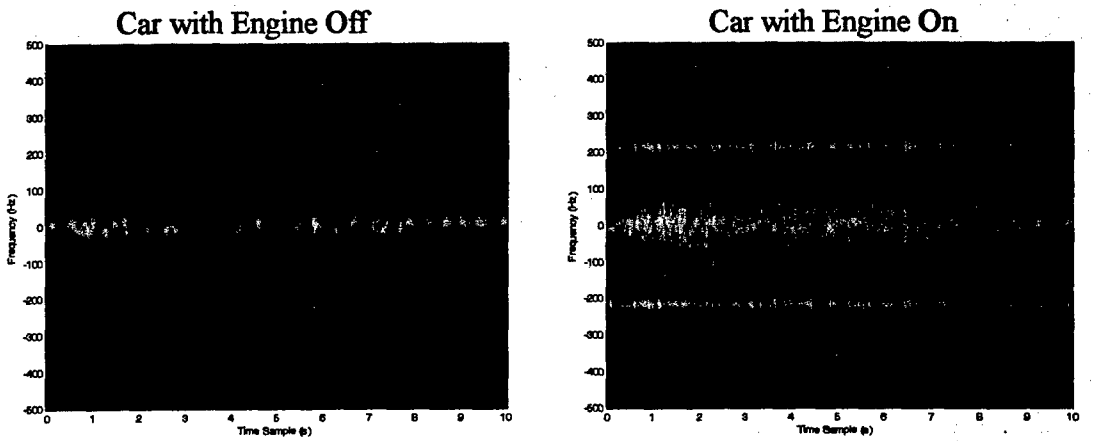

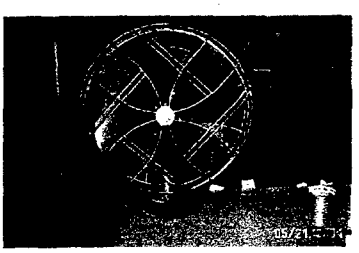

Fig. 4. Measured microDoppler return versus dwell time from a table fan at 6 GHz, VV-pol (UT-Austin).

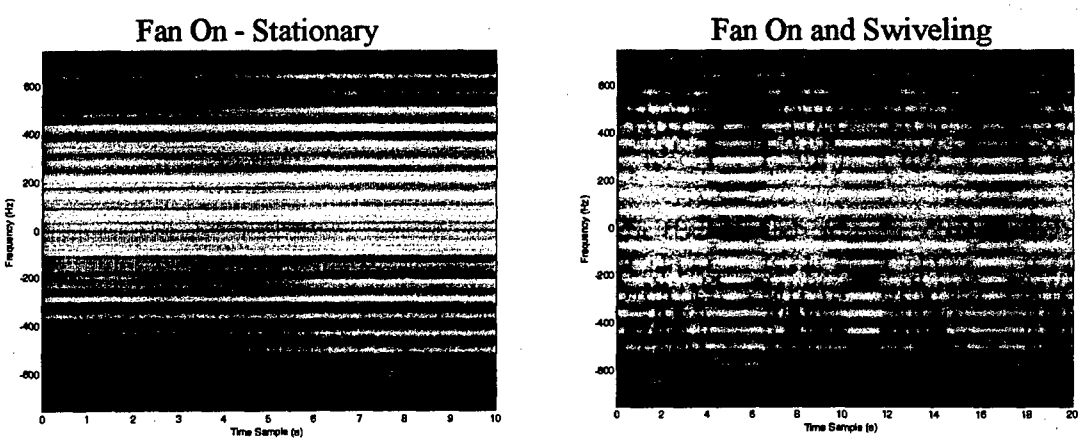

crawling, and involuntary motions such as respiration), different environments (indoor, through different types of walls), over a wide range of frequencies, and for different human subjects. Fig. 5 shows some of the representative results. We then analyzed the data by using joint time-frequency processing, and explored useful features for identification. Fig. 6 shows our effort to estimate the stride size of a human subject from the walking data. It is estimated based on the extracted stride period and the walking speed, which are both obtainable from the radar data. The resulting stride size is then plotted versus the walking speed in Fig. 7 for 6 different human subjects. It is observed that the curves all show a monotonic increase as the walking speed of the individual is increased. However, there appears to be a kink in each curve, representing a change in the walking pattern. As the person speeds up more, his or her stride size can not grow indefinitely, but rather saturates beyond a certain speed. This saturation point appears to be different for different individuals. This study shows that it may be possible to classify and identify humans from their microDoppler features.

1.2. Doppler and Direction-of-Arrival (DDOA) Radar Development for Human Tracking We designed and constructed a second-generation radar by combining the Doppler discrimination offered by human movements with the DOA information that can be collected using an antenna array to provide the necessary information for human movement tracking. Note that conventional DOA detection requires the use of multiple receiver elements, where the number of elements must be greater than the number of targets. This leads to high cost as well as a physically bulky system below 5 GHz. Here we take advantage of the Doppler information from multiple moving humans to achieve Doppler-DOA (DDOA) tracking with only a ***two***-element array. The approach is to use the short-time Fourier processing to separate the target via their contrasting Doppler returns. Then by extracting the phase difference between the received signals at the two elements, we can determine the DOA of each mover individually. More explicitly, if we assume the time signals received at the two antenna elements to be $f_1(t)$ and $f_2(t)$, then after the Doppler processing the signals become $F_1(f_D)$ and $F_2(f_D)$, respectively. If the targets of interest generate different Doppler frequencies f_{Di} due the difference in their velocities

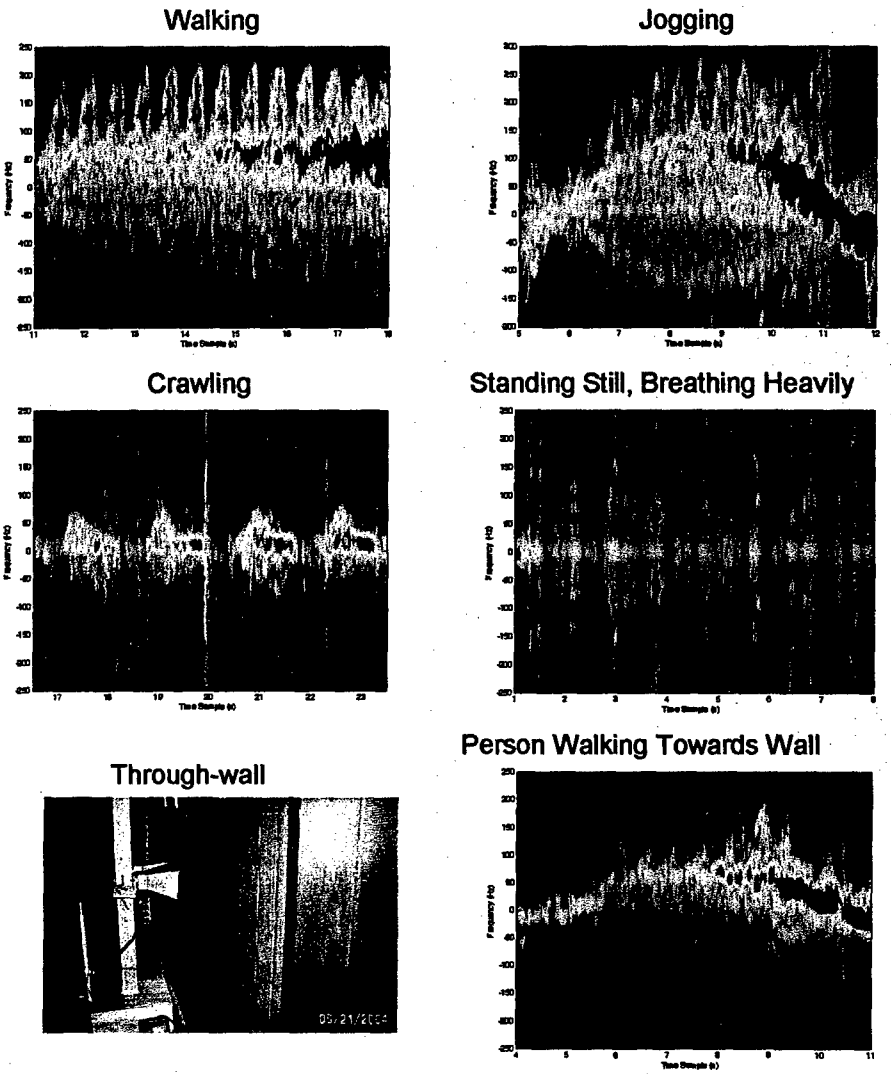

Fig. 5. The collected spectrograms from a person indoors under various movements at 6 GHz.

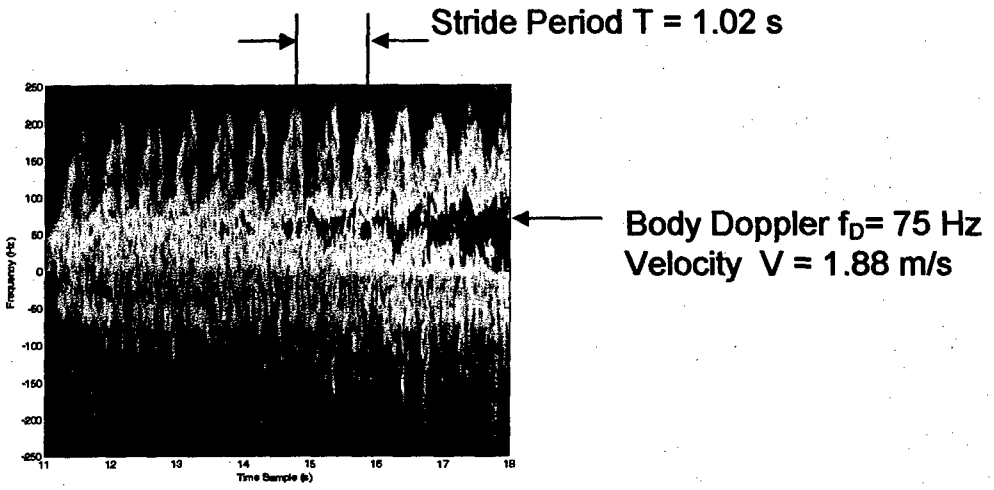

Stride Size = V * T = 1.88 m/s * 1.02 s = 1.92 m

Actual distance per stride as measured = 1.89 m ± 0.04 m

Fig. 6. Estimating the stride size of a human subject from the radar spectrogram.

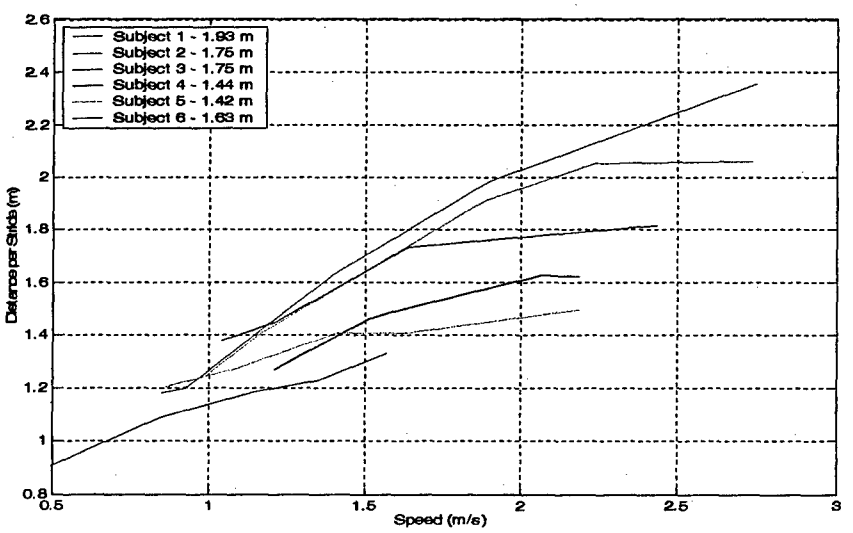

Fig. 7. Stride size versus walking speed for 6 different human subjects.

with respect to the radar transceiver, then the DOA of target i with respect to the array boresight is given by:

$$\theta_i = \sin^{-1}\left[\frac{\angle F_1(f_{Di}) - \angle F_2(f_{Di})]}{(2\pi d/\lambda_c)}\right]$$

where d is the spacing between the elements and λ_c is the RF wavelength.

To implement this concept, we designed and built a two-element receiver to extract the DDOA information simultaneously (Fig. 8). The system is designed using two integrated receiver boards from Analog Devices. It has very low cost (under $100 for each board) and small form factor, since the boards came from mass-market products for the wireless networking market. The system operates at 2.4 GHz. Two microstrip patch antennas are used as the front-end and a National Instruments DAQ system is used for data acquisition. Some results collected from this radar are shown in Figs. 9 and 10. Fig 9 shows the Doppler vs. DOA plot of an acoustic subwoofer driven at 40 Hz and placed at 40 degrees with respect to the radar boresight. It shows the correct bearing angle and Doppler information at +-40Hz (the two-sided Doppler response is due to the FM modulation created by the subwoofer vibration). Fig. 10 shows the snapshot data from a person walking away from the radar. As we can see from the data, the human target includes various limb microDopplers and is not as localized as the subwoofer response. Nevertheless, reliable DDOA information can be acquired. Further, a continuous real-time tracking of the person in an indoor environment can be achieved. Fig. 11 shows how the same concept is applicable to multiple targets, as three speakers with different Doppler returns are used as test targets. The Doppler separation among the target allows the DOA of the speakers to be obtained using the two-element array. Fig. 12 shows the result of multiple human tracking using the radar. The factor that limits the performance of this radar for multiple human tracking is the overlapping microDoppler returns from the human targets. Extensive testing was also conducted for different through-wall scenarios. The range of the radar is about 15m through a 15" exterior brick wall up using a transmit power of 100mW. The same concept can be extended to the elevation dimension using an additional third element.

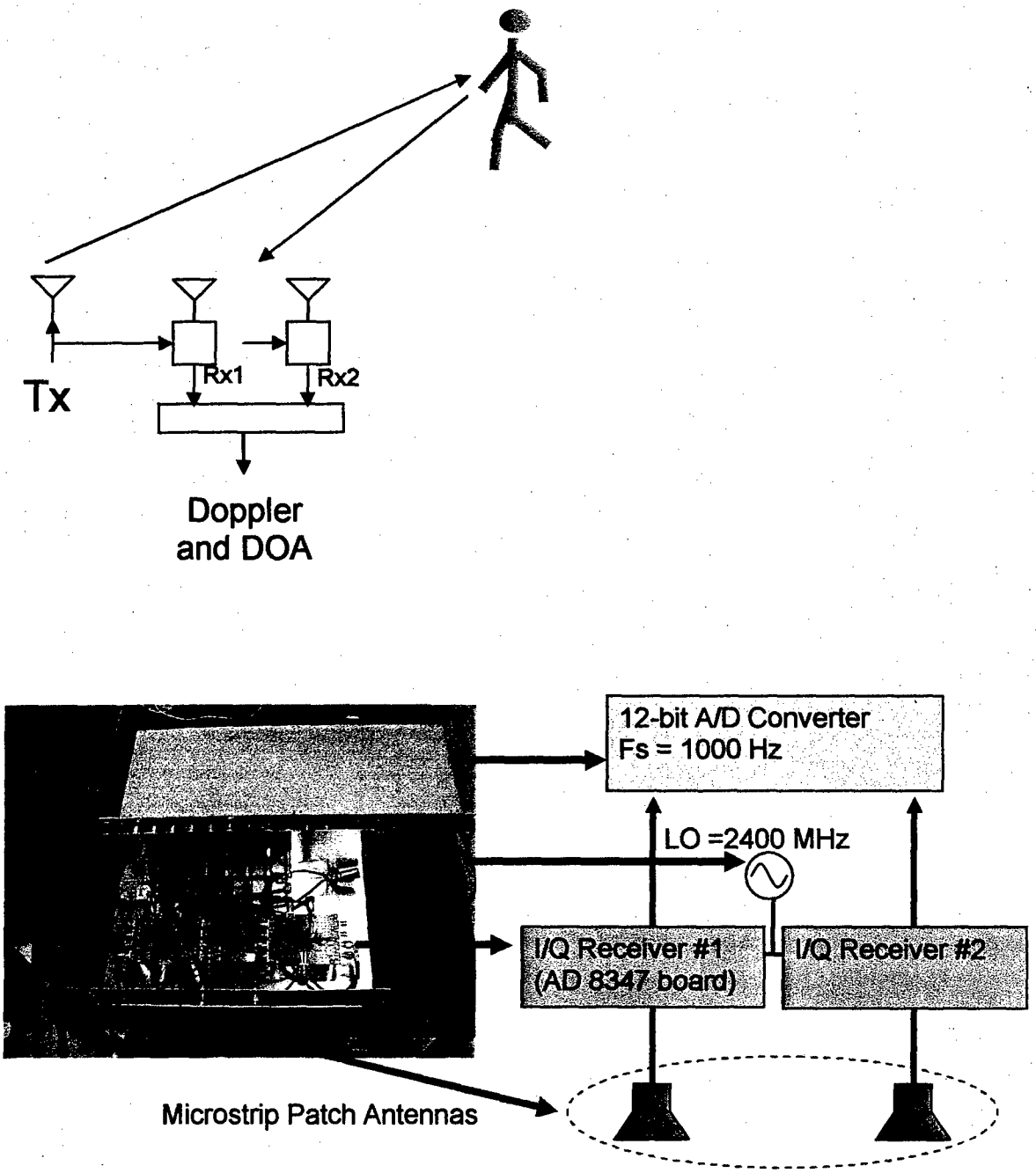

Fig. 8. A two-element radar sensor for measuring both Doppler and direction of arrival (DDOA). The sensor uses two Analog Devices integrated receiver boards, which cost less than $100 each. Initial data collection was carried out at 2.4 GHz.

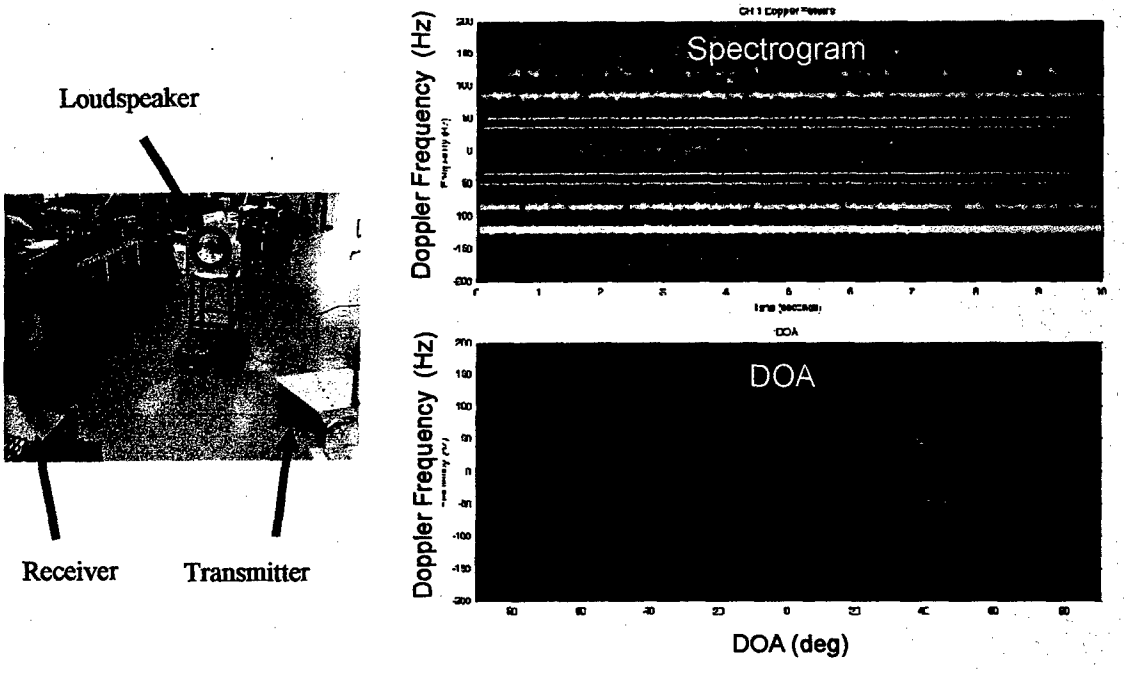

Fig. 9. Doppler and DOA of mechanical vibrations (subwoofer).

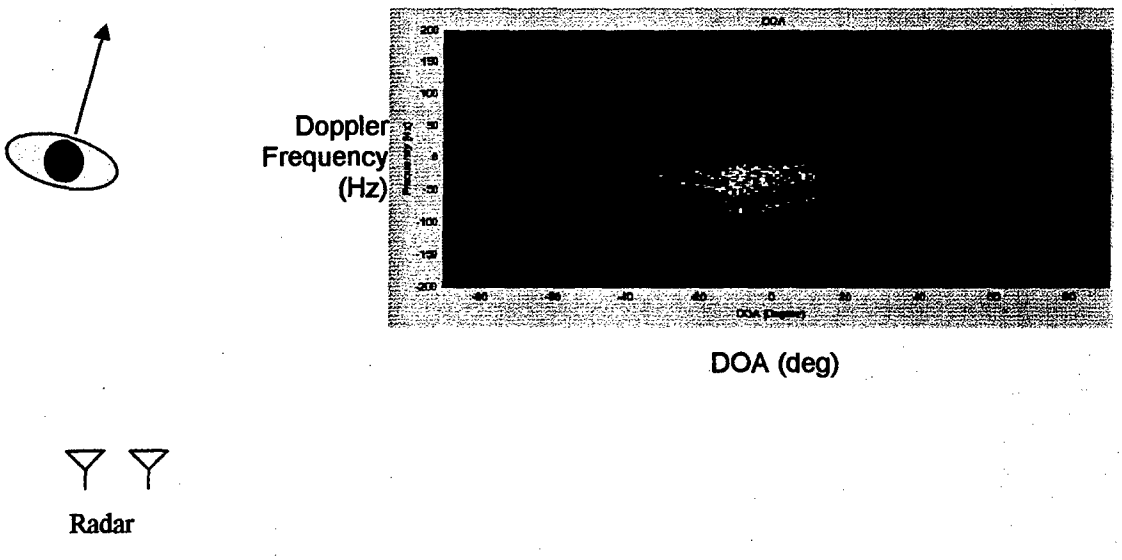

Fig. 10. Doppler and DOA of a moving person.

(a)

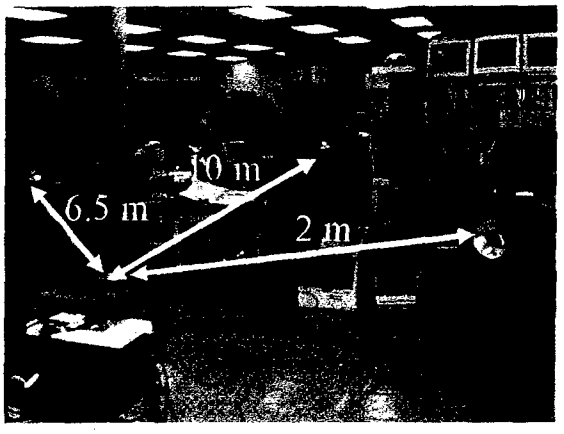

(b)

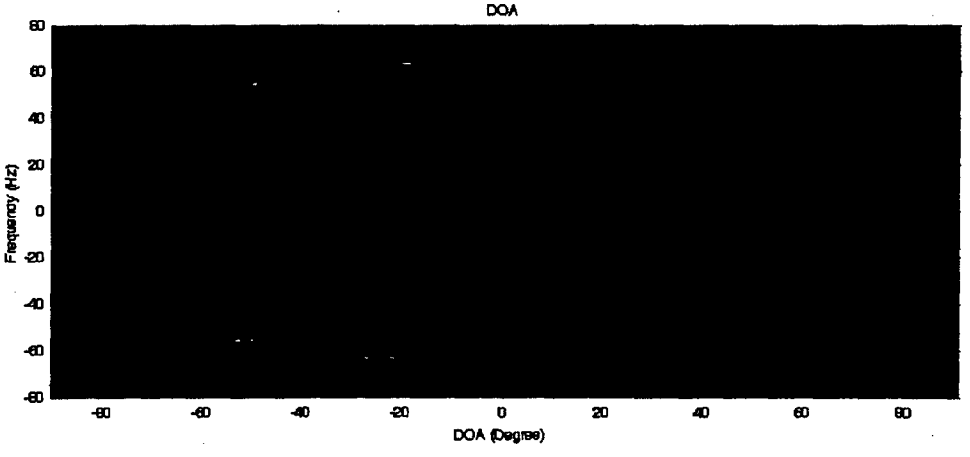

Fig. 11. Three loudspeakers measurement: (a) Setup and (b) Measured Doppler and DOA.

(a)

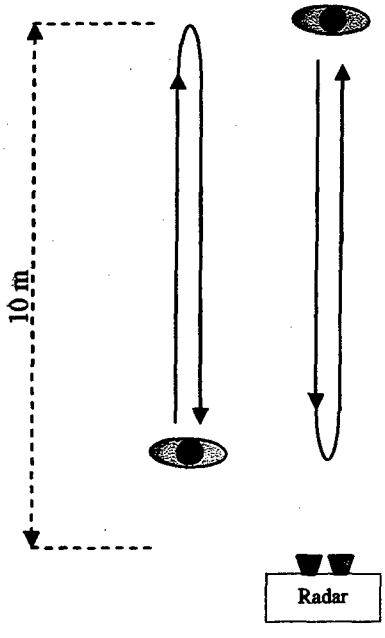

(b)

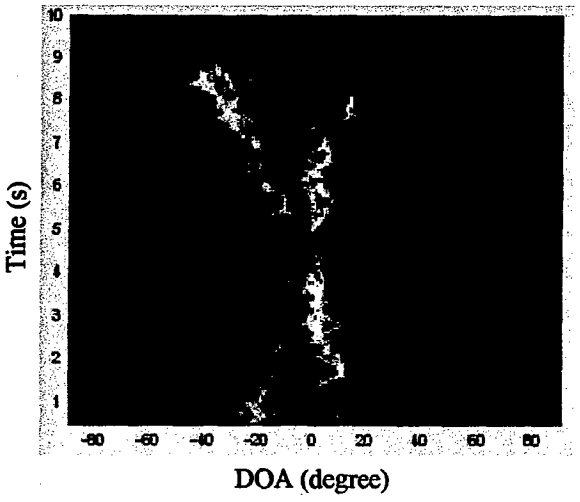

Fig. 12. Measurement of two humans walking in opposite direction: (a) Setup and (b) DOA vs. time

1.3. Frontal Imaging of Humans by Exploiting MicroDoppler. In our research on human tracking, the microDoppler phenomenon increases the Doppler overlap between targets. This is a nuisance from the tracking point of view. However, it may be possible to exploit this phenomenon in a different context. In this research, we investigated a two-dimensional frontal imager by using only a three-element receiving array and a transmitter. The concept entails resolving the microDoppler frequencies of the returned signals from a moving human, and then measuring the phase difference at each Doppler frequency component to determine the direction-of-arrival of the various body parts. If each body part gives rise to a different Doppler frequency, then the resulting bearing map should correspond closely to a two-dimensional frontal view of the human.

Fig. 13 shows the conceptual operation and the radar system block diagram. Different moving body parts of a human give rise to microDoppler shifts with respect to the radar. Therefore, by first Doppler processing the data, we can extract the DOA information of the different Doppler frequency bins by measuring the phase difference among the receiver elements. The azimuth DOA of the received signals can be obtained from the measured phase difference between the two array outputs, $\Delta\phi = \phi_2 - \phi_1$, using the expression: $\theta_{AZ} = \sin^{-1}(\lambda_c \Delta\phi / 2\pi d)$ where d is the spacing between the two antennas. An additional receiving antenna (Rx3) is placed directly above Rx2. Since Rx2 and Rx3 are placed vertically apart, they form a new array pair to acquire the DOA in the elevation plane, θ_{EL}. By correlating the azimuth and elevation bearing information at each Doppler bin f_{Di}, a data matrix $[A(f_{Di}), \theta_{AZ}(f_{Di}), \theta_{EL}(f_{Di})]$ can be constructed, where $A(f_{Di})$ is the radar return strength at the Doppler bin f_{Di} Provided that each body part gives rise to a different Doppler frequency, the resulting $[A, \theta_{AZ}, \theta_{EL}]$ corresponds to an approximate two-dimensional frontal image of the human.

The radar testbed described in Section 1.2 was extended for this purpose by incorporating one additional vertical receiver element. During the measurement period the subject remained at 2 m distance from the radar boresight while moving each body part sequentially. After correlating the azimuth and elevation DOA measurements based on their Doppler information, a two-dimensional or frontal view of the human is constructed and shown in Fig. 14(a). The measured frontal view shows the position of each limb, making an outline of the subject. The dynamic range of the image is 40 dB.

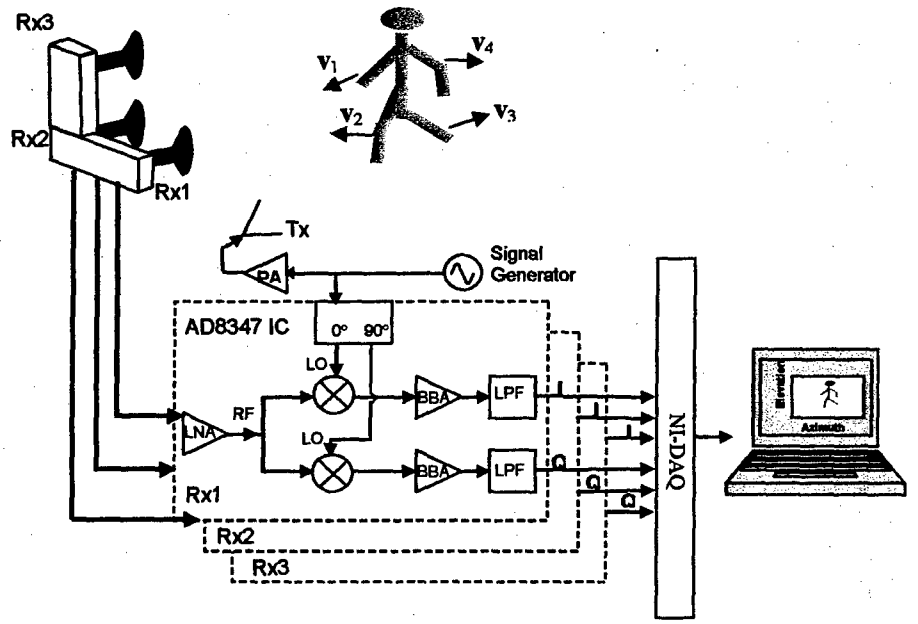

Fig. 13. Radar system block diagram and conceptual operation. The moving body parts (arms, legs) of a human produce different Doppler returns and are imaged by the radar.

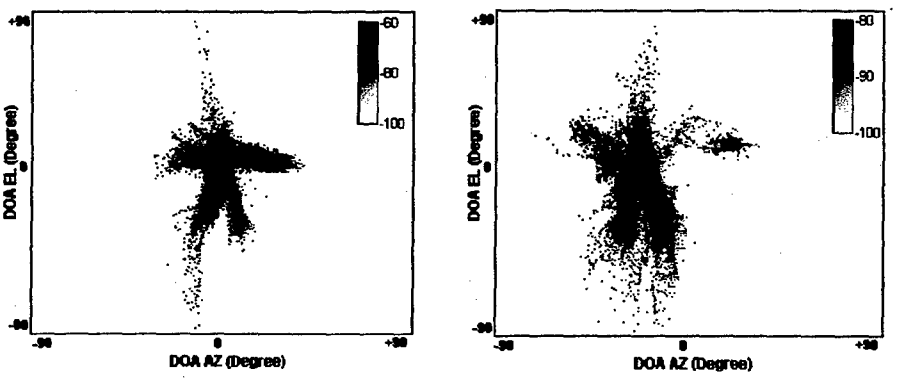

Fig. 14. (a) Measured frontal view of a human in free space.
(b) Measured frontal view of a human through an indoor wall.

The measurement was then repeated in-situ with a 5" thick gypsum/wooden wall in an interior room. The subject stood at approximately 1 m behind the wall while the radar measured the return versus time. Fig. 14(b) shows the measured through-wall view of the human. In comparison with the free-space image shown in Fig. 14(a), the through-wall image appears larger since the subject stands closer to the radar. The image also appears to be less focused due to the significant attenuation from the wall. However, the outline of the human is still visible. It is worthwhile pointing out that while the proposed radar concept has very low-complexity, it is based on the assumption that different body parts give rise to different Doppler frequencies. When this condition is not met in practice, the resulting bearing information is not accurate. Therefore, the present radar concept can be termed an "imaging of opportunity" that captures glimpses of the human subject. This is similar to other types of target-motion induced sensing schemes such as the inverse synthetic aperture radar.

2.1. Fast Ray Tracing Simulation for Characterizing Multiple Scattering Phenomena. In order to accurately simulate multiple scattering phenomena in complex targets, we researched an efficient simulation algorithm based on the shooting and bouncing ray (SBR) technique [4]. The key time bottleneck in the SBR technique is the ray tracing process. Therefore, we explored ways to speed up the ray tracing time. The Binary Space Partition (BSP) tree algorithm [5] is the most standard ray tracer in use. The BSP-tree based ray tracer is considered the fastest among all of the spatial subdivision approaches. Recently, the multiplaten z-buffer ray-tracing algorithm was proposed by Hu et al [6, 7] as an alternative to the traditional BSP tree algorithm. In the multiplaten z-buffer (MPZ) approach, a multi-layered z-buffer is first generated from the scan conversion process (Fig. 15(a)). Instead of just storing the z-coordinates of the visible pixels as in the traditional z-buffer process, multiple z-buffers are created to store the z-coordinates of all of the facets within each pixel during the scan conversion. During the ray trace, a ray is tracked by moving along the ray direction pixel-by-pixel. Within every pixel, the z-depth of the ray is compared to all of the z-buffer values for that pixel to check for possible intersections (Fig. 15(b)). Once an intersection is found, the hit point and the reflection direction can be calculated, and the tracing process is then iterated until the ray

departs from the bounding box. We found that, contrary to the BSP algorithm, the complexity of the MPZ is independent of the number of facets comprising the target. However, the computation time is dependent on the number of pixels traversed by a ray.

To further speed up the performance of MPZ algorithm, we developed a multi-aspect MPZ (MAMPZ) approach. The approach is motivated by the fact that the number of pixels a ray traverses between bounces can be reduced dramatically by decreasing the angle between the ray direction and the z-buffer direction. In the algorithm, multiple multi-layered z-buffers are first generated from the scan conversion process along many aspect angles. The maximum number of multi-layered z-buffers is limited only by the available memory resource. The more aspect angles that be stored, the less pixels a ray traverses in one bounce, and the better the time performance. During the ray trace, the multi-layered z-buffer structure that has the closest aspect to the ray direction is selected to carry out the ray tracing. A ray is then tracked by moving along the ray direction inside this MPZ structure pixel-by-pixel to check for possible intersections. Once an intersection is found, the hit point and the reflection direction are calculated. Based on the new ray direction, a new MPZ is chosen, and the tracing process is iterated until the ray departs from the bounding box. As can be seen in Fig. 16 for a test Y-cavity structure, the

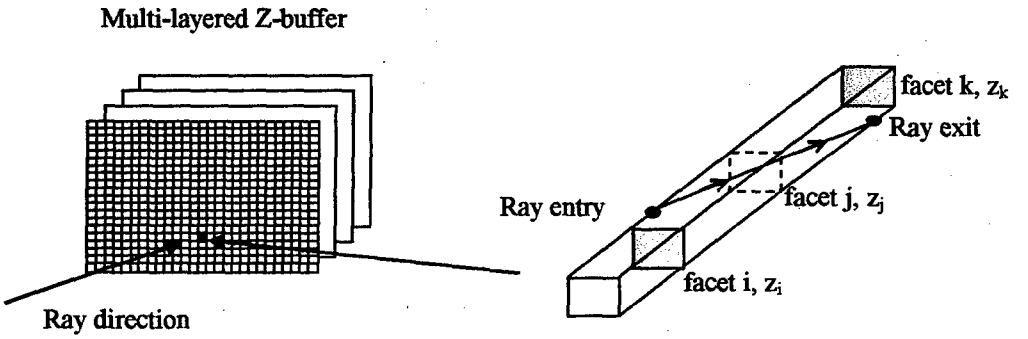

Fig. 15. (a) Multi-layered z-buffer. (b) Ray tracing using the multilayered z-buffer.

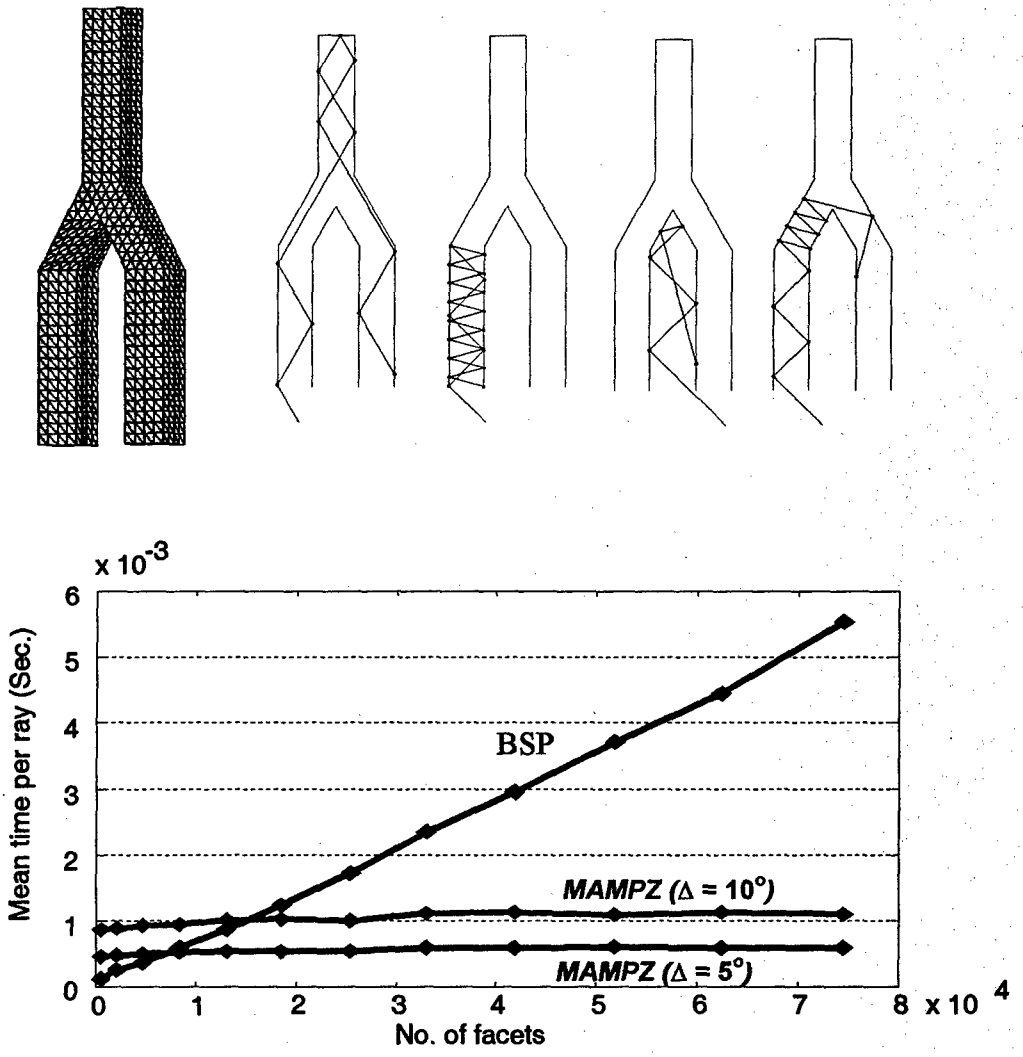

Fig. 16. (a) Geometry of a test Y-cavity with two end ends and typical rays in the cavity. (b) The computation time of the MAMPZ algorithm versus the BSP tree algorithm as a function of the number of target facets.

complexity of the MPZ is independent of the number of facets comprising the target, in contrast to the BSP tree algorithm. Furthermore, the performance of the MAMPZ can be improved by using more MPZ over a denser set of angles (the angular spacing is denoted as Δ in the figure). Therefore, by trading off computer memory and the overhead scan-conversion time, the speed of the ray tracing can be significantly improved. We also extended the MPZ algorithm to the ray tracing of IGES parametric surfaces, i.e., curved surfaces. Traditionally, algorithms for IGES surfaces are much slower than that for the planar facets. The MPZ IGES parametric surface ray tracer is potentially attractive since the numerical search for the intersection can be seeded with a very good initial guess.

2.2. Shape Reconstruction of Targets with Strong Multiple Scattering. Radar imaging is a fast and robust way to image the geometrical shape of a target. However, it is well known that artifacts can occur in radar imagery due to multiple scattering mechanisms on the target. One solution to this problem is to rigorously solve the electromagnetic inverse scattering problem. For instance, we can cast the inversion algorithm into an optimization problem. By using a computational electromagnetics solver (such as ray tracing), we can try to minimize the difference between the measured scattered field data and the predicted scattered field to determine the shape of the target. Recently, some researchers have explored the use of genetic algorithms (GA) together with computational electromagnetic solvers to attack the inverse scattering problem [8-10]. This is a very time-consuming process. In this research effort, we developed a technique combining the hybrid GA (HGA) with the "tabu list" concept to increase the efficiency of the inversion. The HGA combines the simple GA with a local search algorithm to improve the speed of the simple GA. In addition, the tabu list concept [11, 12] is adopted to exclude those regions in the parameter space that have already been explored by the local search. In this manner, there will be no revisiting of the explored regions and the GA population can be spread out to explore new regions, thus improving the search efficiency. The illustration of the tabu region around a local minimum is shown in Fig. 17. In subsequent GA reproductions, all of the new members are checked against the stored tabu list to ensure that none is in the tabu regions of the sample space.

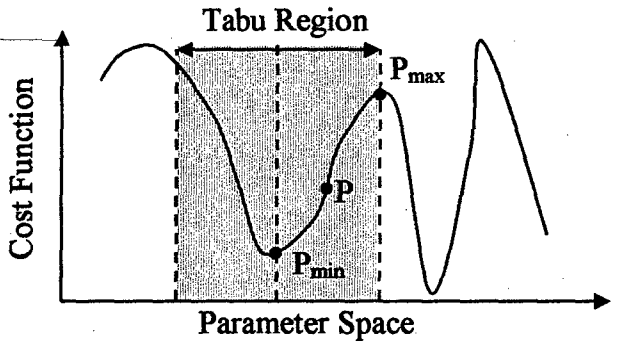

Fig. 17. Establishment of the "tabu region"

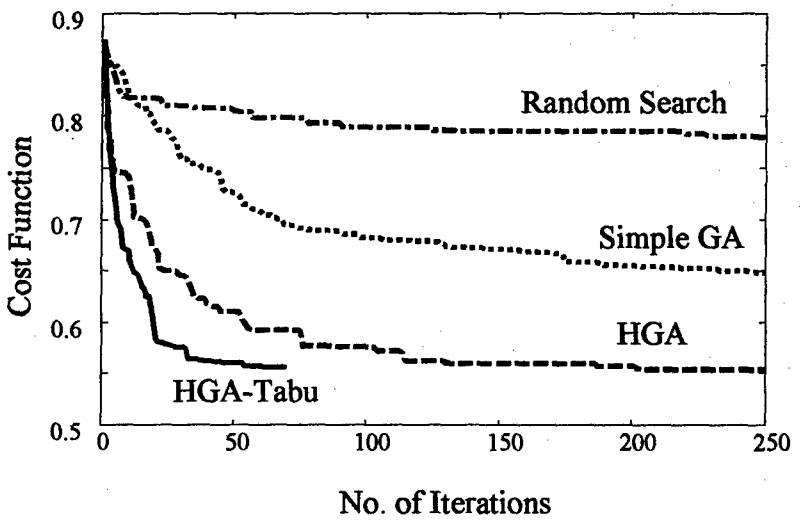

Fig. 18. Convergence comparison for inversion of Ips011 for random search, simple GA, HGA and HGA-Tabu

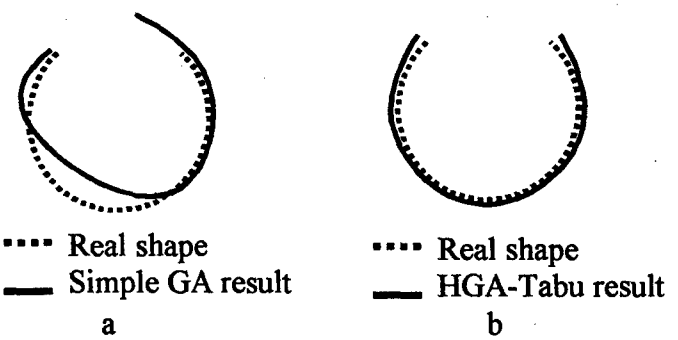

Fig. 19. Ips011 inversion results from measured data

a Typical inversion result by simple GA

b Typical inversion result by HGA-Tabu

We applied the HGA-Tabu algorithm to reconstruct the shape of a metallic, partially open, circular cylindrical cavity with a diameter of 10.8cm (Ips011 in the Ipswich data set) [13]. This target contains a high degree of multiple scattering. The measurement was taken at a single frequency of 10GHz in a bistatic configuration. There were a total of 36 transmitter positions around the object and 18 receiver locations for each transmitter position. In the inversion, we started from a set of randomly created shapes that were described by N ordered points in a two-dimensional space. The profile of the object was then obtained using spline interpolation. Next, the numerical solution to the electric field integral equation was used as the forward electromagnetic solver to generate the computed scattered field from each assumed shape. The HGA-Tabu algorithm was then applied as the optimizer to minimize the cost function. Fig. 18 shows the convergence comparison between random search, simple GA, HGA and HGA-Tabu, when the inversion algorithms were applied to the measured data. All the results were averaged over 10 independent runs with different initial populations. As expected, the simple GA showed improvement over the random search. The HGA further improved the convergence rate of the simple GA. The best results were consistently obtained by the HGA-Tabu. To achieve an RMS of 0.55, the HGA required an average of 220 generations while the HGA-Tabu algorithm required only an average of 75 generations. Fig. 19a shows the typical shape from the simple GA after 250 generations plotted against the real profile of the cavity. The result indicates that more iterations are needed for convergence. Fig. 19b shows the typical reconstructed shape from the HGA-Tabu after 75 generations. As we can see, the inverted shape is very close to the real profile. Inversion results from the HGA-Tabu showed faster convergence and higher success rate than those of the simple GA and hybrid GA. The computation overhead per generation for the new algorithm was small. The algorithm could be combined with the fast ray tracing solver described in 2.1 to handle large 3D targets.

2.3. Imaging Buried Targets in Ground Penetrating Radar. Under funding from the NATO-B2 research scholarship programme, Prof. Caner Ozdemir of Mersin University in Turkey spent 4 months in the summer of 2003 at the University of Texas at Austin as a visiting scientist. During his visit, he conducted research in the three-dimensional

imaging of buried targets using ground penetration radar. In particular, a three-dimensional algorithm to image buried objects in a homogeneous background medium was researched and developed. This technique is based on the approximate Fourier transform relationship between the frequency-spatial variables and the distance-angle information of the buried scatterer. The algorithm is computationally fast since it forms 3D images by using a fast Fourier transform (FFT) followed by a simple transformation from the distance-angle domain to the image domain. Therefore, by measuring the wideband bistatic scattering over a spatial grid above ground (as shown in Fig. 20) and applying the imaging algorithm, a 3D image of the buried target can be reconstructed.

A measurement setup was built to examine the performance of the algorithm. Objects with various electrical properties buried in dry sand were used in the experiments. A rectangular copper plate whose dimensions are 46cm in the x-direction and 30cm in the z-direction was buried at 46cm below the sand surface. Multi-frequency data from 5 to 6 GHz were collected on a 10x10 uniform receiving grid using a vector network analyzer. After applying the proposed algorithm, we generated a 3D GPR image of the region below the surface. Fig. 21 (a) shows the 2D projected GPR images onto the principal Z-Y, X-Y and X-Z planes. Overlaid on the images are the projected outlines of the plate. We observe two main hot spots in the image. The stronger one corresponds to the scattering from the middle of the plate where a specular point exists. The weaker one corresponds to the diffraction mechanism from the front edge of the plate. Both image features agree well with the geometrical locations of the plate. In addition, resolutions in the cross range directions (i.e., in the x- and z-directions) are nearly the same as the resolution in the range (y) direction. This is in contrast to most GPR imagery, in which the cross-range resolution is usually quite poor compared to the resolution in the depth direction [14-16].

Simulation was also carried out using a physical optics calculation. After obtaining the simulation data of the experimental setup, we applied the same imaging algorithm to form the simulated GPR image. Fig. 21 (b) demonstrates the 2D projected GPR images from the simulation data. By comparing the measured GPR images to the simulated ones, we see good agreement between the two. Since the physical theory of diffraction contribution was absent in the simulation, we notice that the edge diffraction contribution in the simulation is weaker than that from the measured image. Finally, data were also

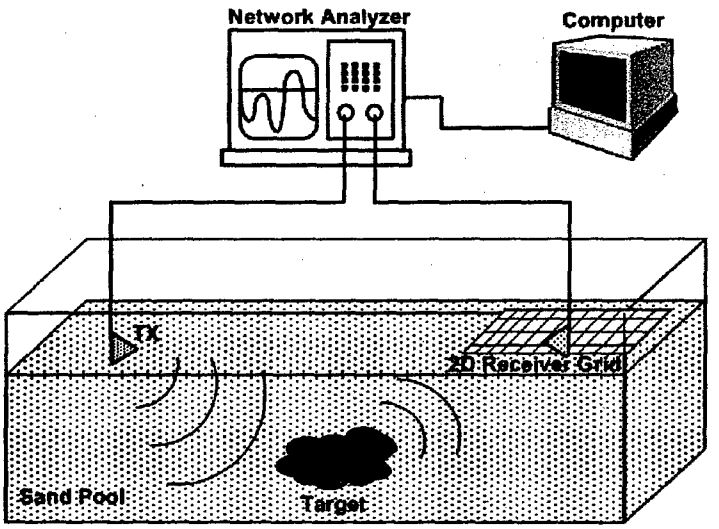

Fig. 20. Experiment setup.

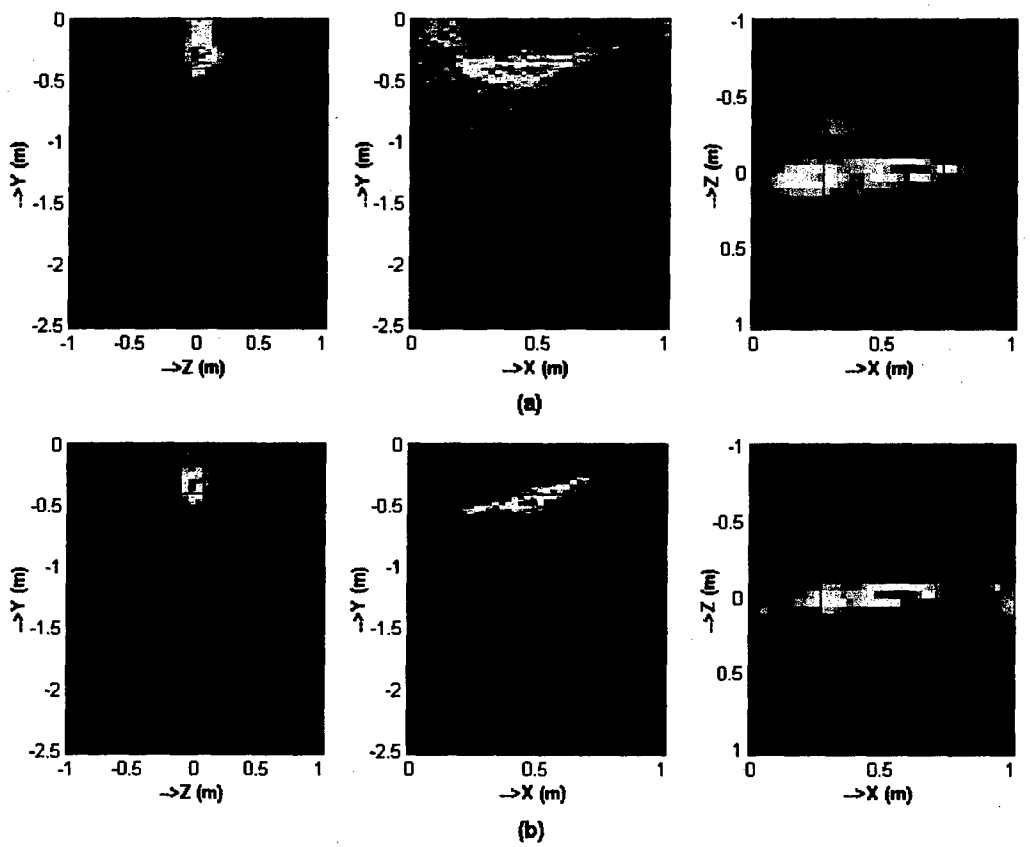

Fig. 21. 2D projected views of the 3D GPR images from (a) measurement data, (b) simulation data.

collected and images formed using other non-metallic objects. High-resolution images could be formed consistently using the algorithm. This can be attributed to the fact that the present coherent imaging algorithm uses many spatial points to provide sufficient signal-to-noise ratio. Therefore, even when the dielectric constant of the target was close to that of background medium and the return was significantly weaker than high-contrast targets, the target could still be observed in the resulting image, albeit at a lower SNR.

C. FOLLOW-UP STATEMENT:

During this program, we have carried out in-depth research in microDoppler and multiple scattering phenomena. We have designed a number of radar sensors, collected a large database of measured data, carried out extensive data analysis and feature interpretation, developed simulation tools and gained a basic understanding of these phenomena. Furthermore, we have carried out signature exploitation efforts to utilize these phenomena in identification, imaging and target shape reconstruction. The potential impacts of this basic research program on naval radar surveillance capabilities are twofold. First, through simulation, measurement and signal processing, this research resulted in an in-depth understanding of the radar features due to target micro-dynamics and multiple scattering physics. Second, our research led to novel exploitation of target features that can significantly improve the non-cooperative target recognition (NCTR) capabilities for existing and future naval radar sensors.

D. REFERENCES:

1. J. L. Geisheimer, E. F. Greneker and W. S. Marshall, "High-resolution Doppler model of the human gait," *SPIE Proc., Radar Sensor Technology and Data Visualization*, vol. 4744, pp. 8-18, July 2002.

2. J. L. Geisheimer, WS. S. Marshall and E. Greneker, "A continuous-wave (CW) radar for gait analysis," *Proc. IEEE Asilomar Conf. Signal Syst. Comp.*, pp. 4-7, Nov. 2001.

3. V. C. Chen, "Analysis of radar micro-Doppler with time-frequency transform," *Proc. of the 10th IEEE Workshop on Statistical Signal and Array Processing*, pp. 463-466, Pocono Manor, PA, Aug. 2000.

4. H. Ling, R. Chou and S. W. Lee, "Shooting and bouncing rays: calculating the RCS of an arbitrarily shaped cavity," *IEEE Trans. Antennas Propagat.*, vol. AP-37, pp. 194-205, Feb. 1989.

5. K. Sung and P. Shirley, "Ray tracing with the BSP tree," *Graphics GEMS IV*, edited by Kirk, D., Academic Press, 1992, pp. 271-274.

6. J. L. Hu, Y. Ma, S. M. Lin and W. B. Wang, "Multiplaten Z-buffer algorithm and its application to multiple scattering," *Electron. Lett.*, vol. 33, pp. 825-826, 1997.

7. J. L. Hu, C. H. Chan and S. M. Lin, "Computation of RCS of jet engine with complex terminations based on multiplaten Z-buffer algorithm," *Microwave Optical Tech. Lett.*, vol. 23, pp. 281-284, Dec. 1999.

8. C.C Chiu and P. T. Liu, Image reconstruction of a perfectly conducting cylinder by the genetic algorithm, *IEE Proc. - Microwave, Antennas Propag.*, Vol. 143, No. 3, pp. 249-253, 1996.

9. T. Takenaka, Z. Q. Meng, T. Tanaka and W. C. Chew, Local shape function combined with genetic algorithm applied to inverse scattering for strips, *Microwave Optical Tech. Lett.*, Vol. 16, No. 6, pp. 337-341, 1997.

10. M. Pastorino, A. Massa and S. Caorsi, A microwave inverse scattering technique for image reconstruction based on a genetic algorithm, *IEEE Trans. Instrum. Meas.*, Vol. 49, pp. 573 –578, June 2000.

11. Glover, F., "Tabu search-part I," *ORSA Journal on Computing*, Vol. 1, pp. 190-206, 1989.

12. Glover, F. and Laguna, M., *Tabu Search: Mordern Heuristic Techniques for Combinatorial Problems*, Blackwell Scientific Publication, Oxford, 1993.

13. R. V. McGahan and R. E. Kleinman, Second annual special session on image reconstruction using real data, *IEEE Antennas Propagat. Mag.*, Vol. 39, No. 2, pp. 7-9, Apr. 1997.

14. A. Sullivan, R. Damarla, N. Geng, Y. Dong and L. Carin, "Ultra wide-band synthetic aperture radar for detection of unexploded ordnance: modeling and measurements," *IEEE Trans. Antennas Propagat.*, vol. 48, pp. 1306–1315, Sept. 2000.

15. S. Vitebskiy, L. Carin, M. Ressler and F. Le, "Ultrawide-band, short-pulse ground-penetrating radar: simulation and measurement," *IEEE Trans. Geosci. Remote Sensing*, vol. 35, pp. 762-772, May 1997.

16. L. Capineri, P. Grande, J.A.G. Temple, "Advanced image-processing technique for real-time interpretation of ground-penetrating radar images," *Int. J. Imaging Systems Tech.*, vol. 1, no. 9, pp. 51-59, 1998.

E. PUBLICATIONS:

I. LIST OF JOURNAL ARTICLES (ONR supported in whole or in part)

1. H. Deng and H. Ling, "Application of adaptive local cosine transform to detection and estimation of ultra-wideband signals through dispersive propagation channels," *Microwave Optical Tech. Lett.*, vol. 35, pp. 150-153, October 2002.

2. J. Li, H. Ling and V. C. Chen, "An algorithm to detect the presence of 3D target motion from ISAR data," *Multidimensional Systems and Signal Processing*, special issue on Radar Signal Processing and Its Applications, vol. 14, pp. 223-240, January-July 2003.

3. J. Li and H. Ling, "Use of genetic algorithms in ISAR imaging of targets with higher order motions," *IEEE Trans. Aerospace Electronic Syst.*, vol. AES-39, pp. 343-351, January 2003.

4. Y. Zhou, J. Li and H. Ling, "Shape inversion of metallic cavities using a hybrid genetic algorithm combined with a tabu list," *Elect. Lett.*, vol. 39, pp. 280-281, February 2003.

5. J. Li, Y. Zhou and H. Ling, "Sparse parameterization of electromagnetic scattering data using a genetic algorithm with adaptive feeding," *Elect. Lett.*, vol. 39, pp. 1104-1105, July 2003.

6. J. Li and H. Ling, "ISAR feature extraction from non-rigid body targets using adaptive chirplet signal representation," *IEE Proc. – Radar, Sonar and Navigation*, special issue on time-frequency analysis for synthetic aperture radar and feature extraction, vol. 150, pp. 284-291, August 2003.

7. C. Ozdemir, S. Lim and H. Ling, "A synthetic aperture algorithm for ground-penetrating radar imaging," *Microwave Optical Tech. Lett.*, vol. 42, pp. 412-414, September 2004.

8. Y. Zhou and H. Ling, "On the multiplaten z-buffer algorithm for ray tracing in high-frequency electromagnetic scattering computations," *Microwave Optical Tech. Lett.*, vol. 43, pp. 298-301, November 2004.

9. C. Ozdemir and H. Ling, "An experimental investigation of buried-object imaging in a homogeneous medium using synthetic aperture radar concepts," *Microwave Optical Tech. Lett.*, vol. 48, pp. 1209-1214, June 2006.

10. A. Lin and H. Ling, "Frontal imaging of human using a three-element Doppler and direction-of-arrival (DDOA) radar," *Elect. Lett.*, vol. 42, pp. 660-661, May 2006.

11. A. Lin and H. Ling, "A Doppler and direction-of-arrival (DDOA) radar for multiple-mover sensing based on a two-element array," accepted for publication in *IEEE Trans. Aerospace Electronic Syst.*, June 2006.

12. A. Lin and H. Ling, "Three-dimensional tracking of humans using a very low-complexity radar," accepted for publication in *Elect. Lett.*, August 2006.

II. LIST OF CONFERENCE PROCEEDINGS (ONR supported in whole or in part)

1. Y. Zhou and H. Ling, "Evaluation of the multiplaten z-buffer algorithm for electromagnetic ray tracing in high-frequency electromagnetic scattering computations," URSI National Radio Science Meeting, p. 471, Columbus, OH, June 2003.

2. H. Ling and Y. Wang, "A revisit of random arrays and some recent applications," URSI National Radio Science Meeting, p. 160, Columbus, OH, June 2003.

3. C. Ozdemir, S. Lim and H. Ling, "An algorithm for ground penetration imaging using synthetic aperture radar concept," URSI International Union of Radio Science General Assembly, pp. 1098-1100, Pisa, Italy, May 2004.

4. Y. Zhou and H. Ling, "A multi-aspect z-buffer algorithm for ray tracing in high-frequency electromagnetic scattering computations," URSI National Radio Science Meeting, p. 130, Monterey, CA, June 2004.

5. R. Bhalla and H. Ling, "IFSAR modeling of terrains and targets using a ray-based electromagnetic technique," IASTED International Conference on Antennas, Radar and Wave Propagation, paper 425-082, 5 pp., Banff, Canada, July 2004.

6. R. Bhalla and H. Ling, "Multi-baseline IFSAR study using a SBR based simulator," SPIE Defense and Security Symposium, Algorithms for Synthetic Aperture Radar Imagery XII, vol. 5805, pp. 102-111, Orlando, FL, April 2005.

7. R. Bhalla, J. Li and H. Ling, "3D SAR image formation from sparse aperture data using 3D target grids," SPIE Defense and Security Symposium, Algorithms for Synthetic Aperture Radar Imagery XII, vol. 5805, pp. 44-53, Orlando, FL, April 2005.

8. A. Lin and H. Ling, "Human tracking using a two-element antenna array," SPIE Defense and Security Symposium, Radar Sensor Technology IX, vol. 5788, pp. 57-64, Orlando, FL, April 2005.

9. A. Lin and H. Ling, "Through-wall measurements of a Doppler and direction-of-arrival (DDOA) radar for tracking indoor movers," International IEEE AP-S Symposium, paper no. S099p03a, 4 pp., Washington, DC, July 2005.

10. A. Lin and H. Ling, "Two-dimensional human tracking using a three-element Doppler and direction-of-arrival (DOA) radar," 2006 IEEE Radar Conference, paper no. 7152, Verona, NY, April 2006.

11. A. Lin and H. Ling, "Location tracking of indoor movers using a two-frequency Doppler and direction-of-arrival (DDOA) radar," International IEEE AP-S Symposium, Albuquerque, NM, July 2006.

III. LIST OF RELATED PRESENTATIONS

1. H. Ling, "Recent research on Xpatch at the University of Texas," AFOSR High Frequency Workshop, Dayton, Ohio, August 28, 2003.

2. C. S. Liang and H. Ling, "generalized analyses of electromagnetic scattering from periodic surfaces," 2004 Electromagnetics Code Consortium Annual Meeting, Boeing Company, Renton, Washington, May 20, 2004.

3. H. Ling, "MicroDoppler exploitation: data collection and analysis," Naval International Cooperative Opportunities in Science and Technology (NICOP) program on Time-Frequency ISAR and NCTI, London, England, June 7, 2004.

4. H. Ling, "Wideband interpolation for in-situ large antenna aperture and array simulations," Boeing Phantom Works, St. Louis, Missouri, July 8, 2004.

5. H. Ling, "Low-cost radar sensors for personnel detection and tracking in urban areas," DARPA Force Multiplier Program Kickoff, Austin, TX, May 17, 2005.

6. H. Ling, "Low-cost radar sensors for personnel detection and tracking in urban areas," Office of Naval Research, Washington, DC, July 8, 2005.

7. H. Ling, "Multiple scattering and microDoppler effects in radar imaging and target recognition," IMA Workshop on Imaging from Wave Propagation, Institute for Mathematics and its Applications, University of Minnesota, Minneapolis, Minnesota, October 20, 2005.

8. H. Ling, "Low-complexity radar sensors for locating and tracking humans inside buildings," DARPA VisiBuilding program workshop, November 14, 2005.

9. H. Ling, "Advanced in scattering center research," Air Force Research Lab, Wright-Patterson Air Force Base, Ohio, December 13, 2005.

10. H. Ling, "Low-cost radar sensors for personnel detection and tracking in urban areas," DARPA Force Multiplier Program Review, Austin, TX, December 16, 2005.

11. H. Ling, "Low-complexity radar sensors for personnel detection and tracking in urban areas," DARPA Force Multiplier Program Briefing, Washington, DC, January 10, 2006.

12. A. Lin, "A low-complexity radar for human tracking," Naval Research Laboratory, Washington, DC, April 17, 2006.

V. LIST OF THESES AND DISSERTATIONS

M.S. Theses

J. Philson, "Genetic algorithm approach to radar waveform synthesis," December 2003.

M. G. Anderson, "Multiple frequency continuous wave radar design for microDoppler extraction," May 2005.

P. Tabrizi, "An adaptive leakage signal canceller for a CW radar," May 2006.

S. Sundar Ram, "Investigation of and improvements to a continuous wave radar system for human detection through walls," May 2006.

Ph.D. Dissertations

Y. Zhou, "High frequency electromagnetic scattering prediction and scattering feature extraction," May 2005.

A. Lin, "A low-complexity radar for human tracking," May 2006.

VI. CONTRACTS AND GRANTS

H. Ling, "Exploitation of microDoppler and multiple scattering phenomena for radar target recognition," Office of Naval Research, October 1, 2002 - May 31, 2006.

R. L. Rogers and H. Ling, "Extended line-of-sight communications for unattended ground sensors," DARPA, October 1, 2002 - December 31, 2005.

H. Ling, "Dynamic signature exploitation," Air Force Research Lab (via SAIC), June 1, 2003 - May 31, 2004.

H. Ling and D. Tanner, "A passive radar sensor exploiting existing wireless infrastructures," Texas Advanced Technology Program, January 1, 2004 – August 31, 2006.

H. Ling, "Wideband wireless channel sounder for multiple antenna channel measurements and estimations," Research Grant, Univ. of Texas, December 4, 2003 – August 31, 2004.

H. Ling, "Silicon Graphics Octane 2 Workstation," equipment donation, Lockheed Martin Aeronautics Company, Fort Worth, TX, May 2004.

H. Ling, "In-situ large antenna aperture and array simulations," Air Force Research Lab (via Boeing), June 1, 2004 – May 24, 2007.

H. Ling, "Multi-sensor phenomenology and representations," Air Force Research Lab (via SAIC), July 8, 2004 – March 31, 2007.

J. Li, E. Banatoski, H. D. Foltz, H. Ling and J. S. Son, "Acquisition of ultra-wideband measurement and modeling facilities for multidisciplinary research," Major Research Instrumentation Award, National Science Foundation, August 15, 2004 – Aug. 14, 2007.

H. Ling, "Low-cost radar sensors for personnel detection and tracking in urban areas," DARPA (via Office of Naval Research), May 1, 2005 – December 31, 2006.

H. Ling and D. P. Neikirk, "Low-cost radar sensors for locating and tracking individuals within buildings," National Institute of Justice (via Air Force Research Lab), January 16, 2006 – January 15, 2008.

R. L. Rogers and H. Ling, "Compact OTH communications feasibility study," DARPA, January 9, 2006 - January 8, 2007.

F. INTERACTIONS/COLLABORATIONS WITH NAVY SCIENTISTS:

The PI collaborated with Dr. Victor Chen of Naval Research Laboratory and Mr. William Miceli of the Office of Naval Research in jointly editing a special issue of the *IEE Proceedings on Radar, Sonar and Navigation*. The issue focused on time-frequency analysis for synthetic aperture radar and feature extraction and appeared in August 2003. Seventeen papers on joint time-frequency analysis for radar imaging and feature extraction were included.

Our participation in the Virtual Electromagnetic Design program funded by the High-Performance Computing Office since 2004 is another forum where we come into close

contact with a number of Navy scientists, including Dr. Mark Kragalott of Naval Research Laboratory and Dr. John Asvestas of NAVAIR, Patuxent River, MD.

Finally, our graduate student Mr. Adrian Lin presented a talk at Naval Research Laboratory in April 2006 on his dissertation research on human tracking.

G. NEW DISCOVERIES, INVENTIONS, OR PATENT DISCLOSURES:

None.

H. HONORS AND AWARDS:

Mr. Hosung Choo, a graduate research assistant in our laboratory, received first place at the student paper competition at the 2003 URSI National Radio Science Meeting held in Columbus, Ohio in June 2003.

Mr. Adrian Lin, a graduate research assistant, was a finalist at the student paper competition at the 2006 IEEE Radar Conference held in Verona, NY.

APPENDIX

Selected Publications Supported by

ONR Research Grant N00014-03-1-0021

the proposed codec averagely saves 8% bit rate compared to JM3.9 with the best settings. Complexity comparison between JM3.9 with five reference frames and the proposed algorithm is also analysed. The sprite buffer can be restricted within the constant size (e.g. 2.25 times the frame size). Therefore the memory cost in the proposed sprite coding is less than that in JM3.9. For computing complexity analysis, we only consider the computing time of motion estimation. In JM3.9, the local motion estimation (LME) is performed five times (i.e. once for each reference frame). In the proposed codec, LME is performed only once. The total time of motion estimation in the proposed codec is for one LME and one GME. By utilising the fast GME algorithm, the total time for LME plus GME is less than five times LME in JM3.9. Similar to the traditional dynamic sprite coding techniques, the proposed codec has the disadvantage that sprite warping has to been performed in the decoder. However, considering the significant improvement of coding efficiency, the extra computing complexity for sprite warping is acceptable.

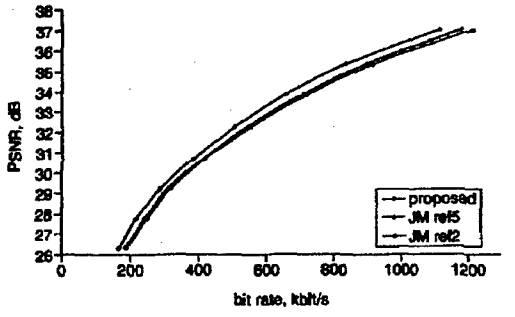

Fig. 3 *PSNR bit rate curves achieved from testing on Stefan sequence*

Conclusions: We have presented a highly efficient algorithm for dynamic sprite coding. The high coding efficiency is achieved due to two reasons. First, the new techniques developed in JVT codec are utilised; secondly, the fractional resolution sprite prediction is incorporated into the proposed algorithm.

12 November 2002
Electronics Letters Online No: 20030199
DOI: 10.1049/el:20030199

Yan Lu (*Department of Computer Science, Harbin Institute of Technology, Harbin, 150001, People's Republic of China*)

E-mail: ylu@jdl.ac.cn

Wen Gao (*Institute of Computing Technology, Chinese Academy of Sciences, Beijing 100080, People's Republic of China*)

Feng Wu (*Microsoft Research Asia, Beijing 100080, People's Republic of China*)

References

1 SMOLIC, A., SIKORA, T., and OHM, J-R.: 'Long-term global motion estimation and its application for sprite coding, content description, and segmentation', *IEEE Trans. Circuits Syst. Video Technol.*, 1999, **9**, pp. 1227–1242

2 Joint Video Team of ISO/IEC MPEG and ITU-T VCEG: 'Joint committee draft (CD)', Fairfax, USA, May 2002

Shape inversion of metallic cavities using hybrid genetic algorithm combined with tabu list

Yong Zhou, Junfei Li and Hao Ling

An approach combining the hybrid genetic algorithm (GA) with the tabu list concept is proposed to increase the search efficiency of the hybrid GA. The algorithm is applied to reconstruct the shape of a metallic cavity based on the Ipswich measurement data. Inversion results show good agreement with the actual shape and significant improvement in convergence rate over both simple GA and hybrid GA.

Introduction: Electromagnetic inverse scattering entails the reconstruction of the shape or material of an object from its scattered field data. The inverse problem can be cast into an optimisation problem whereby the difference between the measured fields and the computed fields from a forward electromagnetic solver is minimised. Genetic algorithms (GAs) have been tried as the global optimiser in these problems [1–3]. While GA is well suited in searching for the global optimum, it suffers from slow convergence. Since the evolutionary process for the standard GA to reach a cost minimum is in general very slow in comparison to a local search algorithm, a natural improvement to speed up the simple GA is to hybridise the simple GA with a local search. This type of algorithm is usually called the hybrid GA (HGA) and has been explored by researchers in different disciplines [4, 5]. While showing improvements in performance, the hybridisation of the two approaches also causes some inefficiency. As the parent selection scheme of GA gives priority to the best members, it usually leads to a population that is highly clustered around the local minima. This clustering is necessary for the simple GA to evolve closer to the exact minimum. For HGA, however, since the local minima have been completely explored by the local search, such clustering will lead to the re-exploration of these regions, which is quite wasteful.

Tabu search (TS) is another global search strategy that has been developed for combinatorial problems [6, 7]. It is a local search algorithm with memory. The most important feature of TS is that it utilises a tabu list to prevent the revisiting of local minima. In this Letter, we propose a technique combining HGA with the tabu list concept to increase the efficiency of the HGA. The tabu list is adopted to exclude those regions in the parameter space that have already been explored by the local search. In this manner, there will be no revisiting of the explored regions and the GA population can be spread out to explore new regions, thus improving the search efficiency. We apply this algorithm to the electromagnetic inverse problem of shape reconstruction of metallic cavity structures containing strong multiple scattering effects. Results based on the Ipswich measurement data set are presented.

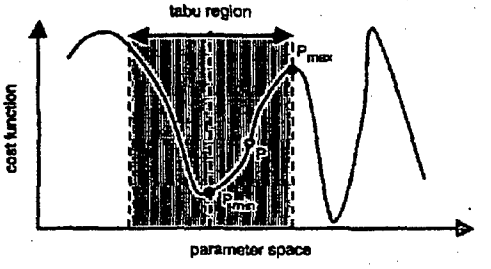

Fig. 1 *Establishment of 'tabu region'*

HGA-tabu approach: In our HGA-tabu implementation, the initial generation is produced randomly. The new population is then produced through the selection, crossover and mutation operators. After these standard GA processes, the best member P is selected as the initial guess to carry out a local search. We adopt the gradient search reported in [8] as the local search algorithm. The resulting local minimum in the parameter space is denoted as $\bar{P}_{min}$ (see Fig. 1). $\bar{P}_{min}$ is then placed into the new GA population. In addition, a gradient search is also carried out to obtain the local maximum $\bar{P}_{max}$ from the same initial guess in order to estimate the extent of the local minimum. Once both local searches are completed, we define the region that is centred at the minimum and limited by the radius $|\bar{P}_{max} - \bar{P}_{min}|$ as the 'tabu region', and record it into a tabu list. Symmetry around the local minimum is assumed in this construct. In subsequent GA reproductions, all of the new members are checked against this tabu list to ensure that none is in the tabu regions of the sample space. Thus the population is forced to spread out to the unexplored regions, resulting in higher HGA search efficiency. Further, a new tabu region is appended to the tabu list every time a new local minimum is explored by local search.

In implementing the inverse problem to reconstruct the shape of a cavity from its scattered field data, we start from a set of randomly created shapes that are described by N ordered points in a two-

dimensional space. The profile of the object is then obtained using spline interpolation. Next, the method of moments (MoM) solution to the electric field integral equation is used as the forward electromagnetic solver to generate the computed scattered field E^{cal} from each assumed shape. A cost function is defined as the root-mean-squared (rms) difference between E^{cal} and the measured scattered-field E^{meas}. The HGA-tabu algorithm is then applied as the optimiser to minimise the cost function. Binary-encoded GA is used in our implementation.

Results: We have applied the HGA-tabu algorithm to reconstruct the shape of a metallic, partially open, circular cylindrical cavity with a diameter of 10.8 cm (Ips011 in the Ipswich data set) [9]. The measurement was taken at a single frequency of 10 GHz in a bistatic configuration. There were a total of 36 transmitter positions around the object and 18 receiver locations for each transmitter position. The electric field was parallel to the axis of the cylinder.

The number of the population for GA was set to 200, the geometry was described by $N=5$ points, and the crossover and mutation rates were set to 0.8 and 0.4, respectively. The search area was chosen to be 16.2×16.2 cm. We first tested the inversion algorithms using MoM-simulated field data as the input. The results showed that the HGA-tabu was able to converge to the correct shape after an average of 75 generations and the final shape was in excellent agreement with the actual shape. In comparison to the HGA, the HGA-tabu also showed an improvement of about 100 generations for convergence.

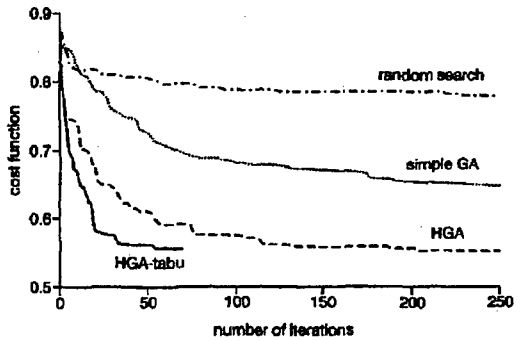

Fig. 2 *Convergence comparison for inversion of Ips011 for random search, simple GA, HGA and HGA-tabu*

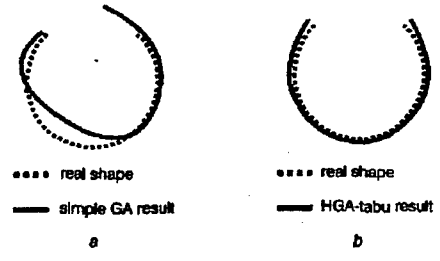

Fig. 3 *Ips011 inversion results from measured data*
a Typical inversion result by simple GA
b Typical inversion result by HGA-tabu

Next, we applied the inversion algorithms to the actual measured data for Ips011. Fig. 2 shows the convergence comparison between random search, simple GA, HGA and HGA-tabu. All the results were averaged over 10 independent runs with different initial populations. As expected, the simple GA showed improvement over the random search. The HGA further improved the convergence rate of the simple GA. The best results were consistently obtained by the HGA-tabu. To achieve an rms of 0.55, the HGA required an average of 220 generations while the HGA-tabu algorithm required only an average of 75 generations. (We note here that, due to the difference between the numerical modelling and the measurement, the rms error between the MoM-computed fields from the *exact* shape and the measured field data is 0.73.) Fig. 3*a* shows the typical shape from the simple GA after 250 generations plotted against the real profile of the cavity. The result indicates that more iterations are needed for convergence. Fig. 3*b* shows the typical reconstructed shape from the HGA-tabu after 75 generations. As we can see, the inverted shape is very close to the real profile. The overhead of implementing the gradient search in each generation is about 10% of the total computation cost. The time for the tabu list check is negligible, as there is no cost function evaluation.

Conclusion: An approach combining the hybrid genetic algorithm with the tabu list concept has been proposed in this Letter. The tabu list was set up to increase the search efficiency by forbidding revisits of local minima already explored by the local search. The algorithm has been applied to reconstruct the shape of a metallic cavity based on the measured Ipswich data. Inversion results from the HGA-tabu showed faster convergence and higher success rate than those of the simple GA and hybrid GA. The computation overhead per generation for the new algorithm was small. The algorithm could potentially be useful in other optimisation problems.

Acknowledgment: This work is supported by the Office of Naval Research under Contract No. N00014-03-1-0021.

6 November 2002
Electronics Letters Online No: 20030207
DOI: 10.1049/el:20030207

Yong Zhou and Hao Ling (*Department of Electrical and Computer Engineering, The University of Texas at Austin, Austin, TX 78712-1084, USA*)

Junfei Li (*Department of Electrical Engineering, The University of Texas-Pan American, Edinburg, TX 78539, USA*)

References

1 CHIU, C.C., and LIU, P.T.: 'Image reconstruction of a perfectly conducting cylinder by the genetic algorithm', *IEE Proc., Microw. Antennas Propag.*, 1996, **143**, (3), pp. 249–253
2 PASTORINO, M., MASSA, A., and CAORSI, S.: 'A microwave inverse scattering technique for image reconstruction based on a genetic algorithm', *IEEE Trans. Instrum. Meas.*, 2000, **49**, pp. 573–578
3 ZHOU, Y., and LING, H.: 'Electromagnetic inversion of Ipswich objects with the use of the genetic algorithm', *Microw. Opt. Tech. Lett.*, 2002, **33**, pp. 457–459
4 YEN, J., LIAO, J.C., LEE, B., and RANDOLPH, D.: 'A hybrid approach to modeling metabolic systems using genetic algorithm and simplex method', *IEEE Trans. Syst. Man Cyber.*, 1998, **28**, pp. 173–283
5 PARK, C., and JEONG, B.: 'Reconstruction of a high contrast and large object by using the hybrid algorithm combining a Levenberg-Marquardt algorithm and a genetic algorithm', *IEEE Trans. Magn.*, 1999, **35**, pp. 1582–1585
6 GLOVER, F.: 'Tabu search—part I', *ORSA J. Comput.*, 1989, **1**, pp. 190–206
7 GLOVER, F., and LAGUNA, M.: 'Tabu search: modern heuristic techniques for combinatorial problems' (Blackwell Scientific Publication, Oxford, UK, 1993)
8 OTTO, G.P., and CHEW, W.C.: 'Microwave inverse scattering-local shape function imaging for improved resolution of strong scatters', *IEEE Trans. Microw. Theory Tech.*, 1994, **42**, pp. 137–141
9 MCGAHAN, R.V., and KLEINMAN, R.E.: 'Second annual special session on image reconstruction using real data', *IEEE Antennas Propag. Mag.*, 1997, **39**, pp. 7–9

Publicly verifiable authenticated encryption

Changshe Ma and Kefei Chen

A new authenticated encryption scheme with public verifiability is presented. The new scheme requires less computational costs and communication overhead than the conventional signature-then-encryption approaches. Furthermore the message is not divulged during the public verification.

Introduction: Secure and authenticated message deliver/storage is one of the major aims of computer and communication security research. Horster, Michels and Petersen (HMP for short) [1] proposed an efficient authenticated encryption scheme with lower expansion

4 KAGAWA, K., *et al.*: 'Pixel design of pulsed CMOS image sensor for retinal prosthesis with digital photosensitivity control', *Electron. Lett.*, 2003, **39**, p. 419
5 SHEN, C., *et al.*: 'Improved SOI image sensor design based on backside illumination on silicon-on-sapphire (SOS) substrate'. IEEE Int. SOI Conf., Williamsburg, VA, USA, 2002, pp. 73–74
6 STETT, A., *et al.*: 'Electrical multisite stimulation of the isolated chicken retina', *Visi Res.*, 2000, **40**, pp. 1785–1795

Sparse parameterisation of electromagnetic scattering data using genetic algorithm with adaptive feeding

J. Li, Y. Zhou and H. Ling

A method is presented to parameterise scattering data from complex targets. Based on a global model with both scattering centres and resonances, a genetic algorithm with adaptive feeding is proposed for a sparse representation. The algorithm is tested with measurement data and shows better performance than non-global parameterisation methods.

Introduction: Obtaining a sparse, physical representation of electromagnetic scattering data from a complex target is a problem of fundamental importance in radar signature analysis [1–9]. The scattering centre model is the standard way to represent scattering from large targets and has been used with success by the radar signature community for over two decades. Many techniques including super-resolution [1, 2], CLEAN [3], genetic algorithms (GA) [4–6] and evolutionary programming-based CLEAN [7] have been reported for determining model parameters based on the scattering centre model.

For targets containing convex, interior structures such as cavities, a model combining scattering centres and resonances has been shown to be a more efficient and physically meaningful representation of both exterior and interior scattering features [8, 9]. However, finding the model parameters in such cases is more challenging, since the scattering centre and resonance bases have complementary behaviours in time and frequency. In [8], a CLEAN-based algorithm was used to extract one scattering centre and/or resonance at a time iteratively. In [9], Prony's method was first used to extract all the scattering centres and then all the resonances. One drawback of these methods is that the parameterisation results are not very sparse since the scattering centres and resonances are not extracted simultaneously.

To improve the sparsity, we present in this Letter a global algorithm to parameterise complex scattering data using the combined scattering centre and resonance model. The method is based on a GA with adaptive feeding. The latter is devised to compensate for the disparity in strength between scattering centres and resonances and improve the performance of the GA.

GA with adaptive feeding: The scattering model is assumed to comprise responses from both scattering centres and resonances as [9]:

$$E(f) = \sum_{m=1}^{M} a_m f^{\alpha_m} e^{-j2\pi t_m f} + \sum_{n=1}^{N} b_n \frac{1}{j2\pi(f - f_n) + \beta_n} e^{-j2\pi f \tau_n} \quad (1)$$

where M and N are the number of scattering centres and resonances, respectively, and f the frequency. For each scattering centre, t_m is the time delay, α_m the frequency dependency coefficient and a_m the complex amplitude. For each resonance of complex amplitude b_n, f_n is the resonant frequency, τ_n the turn-on time and β_n the Q-factor. The parameterisation process can be formulated as a minimisation problem:

$$\{\alpha_m, t_m, f_n, \beta_n, \tau_n\} = \arg\min \|E(f) - E^m(f)\|_2 \quad (2)$$

where E^m denotes the measurement data to be parameterised. The amplitudes a_m and b_n are not included in the bracket as they can be derived from other unknowns using minimum least squares fitting.

GA has been used in many engineering applications as a global optimisation scheme. However, here we find that the standard simple GA (SGA) has difficulty in converging to the desired global optimum. Since the energy in a resonant term is typically much lower than that in a scatterer centre, the resonant terms are easily missed in the SGA process. To overcome this, a parameterisation based on a community GA with adaptive feeding is devised. Fig. 1 illustrates the approach in extracting M scattering centres and N resonances. Each solid box represents a community [10] using a different parameterisation order number. For example, the highest order uses M scattering centres and N resonances while the lowest order uses one scattering centre and no resonance. The parameterisation consists of an iteration process as follows. First, for each community, standard GA operations including selection, crossover and mutation are used to reproduce members in the next generation for better solutions. Secondly, at the end of each generation, the residual signal of each community is calculated as the error between the best solution in the community and the original data $E^m(f)$ and is parameterised with GA. The order number for residual parameterisation is specified in the dashed box. It is the difference between the order number of the current community and the next higher community. Thirdly, the parameters from the best solution of a lower order community and its residue are combined to form a candidate solution in the next higher order community. A zero-mean Gaussian perturbation is added during this step to create a community-level mutation. By adaptively feeding the solutions from the lower order communities forward to the higher order communities, the convergence of the highest order community is significantly accelerated without sacrificing the optimality of the final solution.

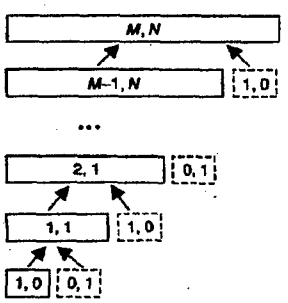

Fig. 1 *GA with adaptive feeding*
Best solution from lower order community (solid box) and residue (dashed box) combined and fed into next higher-order community. Convergence of highest order community with M scattering centres and N resonances accelerated

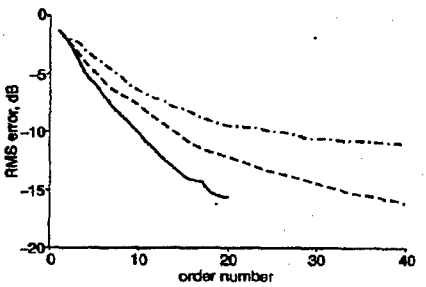

Fig. 2 *Comparison of three parameterisation results of VFY 218 measurement data*
– · – · – CLEAN with scattering centres only
– – – – – CLEAN with scattering centres and resonances
——— GA with adaptive feeding

VFY 218 measurement data results: The algorithm was first tested using numerical simulation data from a well-understood target, a plate with a partially open cavity [9]. The proposed method successfully extracted the four dominant scattering centres and three resonances with a 5% RMS error. By comparison, the RMS error from the CLEAN method is 10% after 20 terms, while the SGA always missed the weakest resonance. We next applied it to the VFY 218 measurement data [11]. The scattering data came from a 1:30 scale model aircraft using horizontal polarisation in the 8 to 16 GHz frequency band. The look angle was at 19.6° from nose-on so that the inlet contribution was prominent in the return. Fig. 2 shows RMS error against total model order number $(M+N)$ for three different methods. The GA results were averaged over six runs. The CLEAN curve

with scattering-centre-only model decreases very little after 30 terms, indicating this model is very inefficient in modelling the resonance part of the data after the scattering centres are extracted. The CLEAN curve with both scattering centre and resonance model is better. However, the rate of convergence still slows down considerably after the first 18 terms. The GA curve shows the best sparsity. It requires only 20 terms to achieve the same accuracy as the CLEAN approach with 40 terms. The model orders used in the GA are $M=14$ and $N=6$. However, we found that the results were not very sensitive to the model order selection.

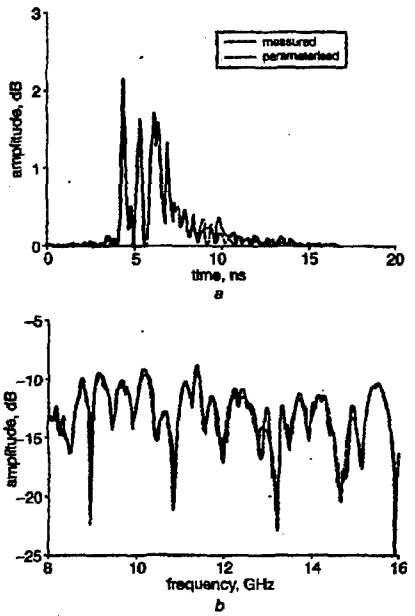

Fig. 3 *Accuracy of parameterisation in time and frequency domains*
a Time domain
b Frequency domain

To further interpret the physical significance of the GA-parameterised data, we correlated the extracted scattering centre positions with the peaks in the target range profile and found that they lined up well. Furthermore, the two strongest resonances extracted are at frequencies of 9.8 and 11.3 GHz. This is consistent with the size of the rectangular engine inlet openings, which have dimensions of 2.5×1.5 cm. (The cutoff frequencies of the TE_{01} and TE_{11} modes are estimated at 10 and 11.7 GHz, respectively.) The other four resonances at 8.6, 9.1, 9.4 and 13.3 GHz are harder to interpret given the complex shape of the actual inlet structure.

Comparisons of the parameterised result with the original measurement data in the time and frequency domains are shown in Fig. 3. We see fairly good agreements between the two. We suspect the small parameterisation error to be due to the model mismatch of (1) to the complex measurement data. Thus, increasing the model order for this data does not reduce the error significantly. We also processed data from 0° to 180° from nose-on in 5° increments, and found the GA with adaptive feeding to consistently outperform CLEAN at all angles.

Conclusions: We have proposed a GA-based method for parameterising scattering data from complex targets. Based on a global model with both scattering centres and resonances, our method uses GA with the adaptive feeding idea to simultaneously extract all the model parameters. The proposed method can achieve sparser results than other non-global based methods. The effectiveness of the proposed method is demonstrated using the VFY 218 measurement data. The resulting sparse model facilitates target feature interpretation and can be used for signature reconstruction in modelling and simulation applications.

Acknowledgment: This work is supported by the Office Of Naval Research under Contract No. N00014-03-1-0021.

9 April 2003
Electronics Letters Online No: 20030723
DOI: 10.1049/el:20030723

J. Li (*Department of Electrical Engineering, University of Texas-Pan American, Edinburg, TX 78539, USA*)

Y. Zhou and H. Ling (*Department of Electrical and Computer Engineering, University of Texas at Austin, Austin, TX 78712, USA*)

References

1 HURST, M.P., and MITTRA, R.: 'Scattering center analysis via Prony's method', *IEEE Trans. Antennas Propag.*, 1987, **35**, (8), pp. 986–988
2 MOGHADDAR, A., OGAWA, Y., and WALTON, E.K.: 'Estimating the time delay and frequency decay parameters of scattering components using a modified MUSIC algorithm', *IEEE Trans. Antennas Propag.*, 1994, **42**, (10), pp. 1412–1418
3 BHALLA, R., and LING, H.: 'Three-dimensional scattering center extraction using the shooting and bouncing ray technique', *IEEE Trans. Antennas Propag.*, 1996, **44**, (11), pp. 1445–1453
4 LI, Q., *et al.*: 'Scattering center analysis of radar targets using fitting scheme and genetic algorithm', *IEEE Trans. Antennas Propag.*, 1996, **44**, (2), pp. 198–207
5 HUGHES, E.J., and LEYLAND, M.: 'Using multiple genetic algorithms to generate radar point-scatterer models', *IEEE Trans. Evol. Comput.*, 2000, **4**, (2), pp. 147–163
6 SU, T., and MITTRA, R.: 'A genetic-algorithm-based extrapolation technique for high frequency scattering analysis'. Proc. 2002 URSI National Radio Science Mtg, San Antonio, TX, USA, 2002, Vol. 3, p. 307
7 CHOI, I.-S., and KIM, H.-T.: 'One dimensional evolutionary programming-based CLEAN', *Electron. Lett.*, 2001, **37**, (6), pp. 400–401
8 TRINTINALIA, L.C., and LING, H.: 'Joint time-frequency ISAR using adaptive processing', *IEEE Trans. Antennas Propag.*, 1997, **45**, (2), pp. 221–227
9 MOORE, J., and LING, H.: 'Super-resolved time-frequency analysis of wideband backscattered data', *IEEE Trans. Antennas Propag.*, 1995, **43**, (6), pp. 623–626
10 WEILE, D.S., and MICHIELSSEN, E.: 'E-plane microwave filters: community genetic algorithm optimization' *in* RAHMAT-SAMII, Y., and MICHIELSSEN, E. (Eds.): 'Electromagnetic optimization by genetic algorithms' (John Wiley & Sons, New York, 1999), pp. 324–343
11 WANG, H.T.G., SANDERS, M.L., and WOO, A.: 'Radar cross section measurement data of VFY 218 configuration'. Naval Air Warfare Center, China Lake, CA, USA, Tech. Rep. NAWCWPNS TM07621, 1994

400 mW uncooled MiniDIL pump modules

S. Mohrdiek, T. Pliska, R. Bättig, N. Matuschek, B. Valk, J. Troger, P. Mauron, B.E. Schmidt, I.D. Jung, C.S. Harder and S. Enochs

A new generation of wavelength stabilised, uncooled 980 nm pump modules in MiniDIL housings is presented, enabling 400 mW ex-fibre power over a temperature range of 10°C to 70°C. At 100°C 200 mW power is still obtained with a robust fibre coupling scheme.

Introduction: As the focus in optical telecommunications systems turns more towards affordability, there is a push to produce EDFAs of lower cost, smaller size and less power consumption. Operation of 980 nm pump modules without a thermo-electric cooler (TEC) has been presented in [1]. The removal of the bulky and power-consuming TEC allowed us to develop pump modules in a smaller, less expensive MiniDIL housing. Though low cost is crucial, performance and reliability comparable to conventional Butterfly-type modules has to be demonstrated, in order to satisfy the yet stringent requirements for metro systems.

In this Letter we present results of 550 mW fibre coupled power at 25°C, 400 mW at 70°C and 200 mW at the extreme temperature of 100°C, with MiniDIL modules incorporating the latest developments in pump laser devices [2, 3] and wavelength stabilisation by fibre Bragg gratings (FBGs) [4]. Little change in fibre coupling efficiency with temperature demonstrates the robustness of the fibre alignment scheme.

Application of adaptive chirplet representation for ISAR feature extraction from targets with rotating parts

J. Li and H. Ling

Abstract: The problem of feature extraction from inverse synthetic aperture radar (ISAR) data collected from targets with rotating parts is addressed. In traditional ISAR imaging, rigid-body motion is usually assumed. When non-rigid-body motions are present, it is not possible to obtain a focused image of both the target and the rotating part. To solve this problem, the radar signal is first parameterised using the adaptive chirplet signal representation. The signal from the body and that from the rotating part are then separated in the parameter space. Point-scatterer simulation results show that better geometrical features of the body and better micro-Doppler features of the rotating part can be extracted after the separation. The algorithm is also demonstrated using the measurement data from an in-flight aircraft and a walking person.

1 Introduction

Recently, there has been increasing interest in studying the so-called micro-Doppler phenomenon [1, 2] for radar target identification applications. Micro-Doppler is used to describe the fine Doppler feature from some moving part on the target that is different from the main body Doppler feature. In most of the conventional work on inverse synthetic aperture radar (ISAR) imaging, the target is assumed to have rigid-body motion [3, 4]. However, non-rigid-body targets can often be found in real-world situations. As a simple case, a target may consist of a main body and a rotating part. For example, an in-flight aircraft with jet engine rotation, a ship with scanning antenna motion and a ground vehicle with spinning tyre motion all involve this type of configuration. Under these conditions, difficulties in understanding the resulting ISAR image arise due to the violation of the rigid-body assumption.

In this paper, we set out to extract better target features from ISAR data when a target has a rotating part beside the main body. The challenge is that the body image is contaminated due to the interference from the rotating part. It is also more difficult to extract the motion information from the rotating part as it is overshadowed by the body returns. Our approach is to first parameterise the radar signal using the adaptive chirplet representation [5, 6]. The chirplet basis is a four-parameter function localised in the joint time–frequency plane. While both Gaussian [7] and chirp-type [8] bases have been reported for joint time–frequency processing of ISAR data, the chirplet basis is selected to represent the radar signal in this paper. Since both amplitude modulation (AM) and frequency modulation (FM) are part of the basis, the chirplet can more efficiently represent the radar signal from a target with a rotating part. With the adaptive chirplet representation, different motion behaviours of the target components are mapped into different parameters of the corresponding bases. Consequently, the returns from the body and the rotating part can be more easily separated. After the separation, better target feature extraction can be realised by processing the two parts individually. This includes both the extraction of the geometrical features from the main body and the micro-Doppler features from the moving part.

In the following section, we present the model and formulation of the problem. After a close examination of the point-scatterer signal model of a target with individual motions, we show that the chirplet basis is well suited for parameterising and separating the rotating part signal from the main body signal. The chirplet-based adaptive signal representation algorithm is tested with point-scatterer simulation data and results are shown from two sets of measurement data. The first data set is from an in-flight aircraft with jet engine rotation motion. The second data set is from a walking person with arm swinging motion.

2 Signal model and formulation

2.1 Point-scatterer model of radar signal from target with rotating part

The point-scatterer model is usually used in radar imaging to model the radar signal scattered by an unknown target. In this model, the radar return signal is expressed as a sum of point-scatterer responses

$$E(f,t)=\sum_{m=1}^{M}\sigma_m \exp\left\{-j\frac{4\pi f}{c}[R_m(t)+x_m\cos\theta_m(t)+y_m\sin\theta_m(t)]\right\} \quad (1)$$

IEE Proceedings online no. 20030729

doi: 10.1049/ip-rsn:20030729

Paper first received 31st January and in revised form 6th June 2003

J. Li is with the Department of Electrical Engineering, The University of Texas-Pan American, Edinburg, TX 78539, USA

H. Ling is with the Department of Electrical and Computer Engineering, The University of Texas at Austin, Austin, TX 78712, USA

where the radar signal E is a two-dimensional function of transmitting radar frequency f and pulse dwell time t. The target consists of M point-scatterers, each with position (x_m, y_m) and complex scattering coefficient σ_m. Suppose the radar is stationary, the target motion is described by the translation motion $R_m(t)$ and the angular motion $\theta_m(t)$ for each scatterer.

A rigid-body target is usually assumed in traditional ISAR imaging, i.e. all the point-scatterers in (1) share the same translation motion $R_m(t)$ and rotational motion $\theta_m(t)$. Here, we shall consider a non-rigid-body target consisting of two parts, a main body and a rotating part. In this case, we can simplify the model in (1) by using different motions for the two parts while still applying the rigid-body assumption for each part. This leads to

$$\begin{aligned} E(f,t) &= E_B(f,t) + E_R(f,t) \\ &= \sum_{m=1}^{M} \sigma_m \exp\left\{-j\frac{4\pi f}{c}[R_B(t) + x_m \cos\theta_B(t) \right. \\ &\quad \left. + y_n \sin\theta_B(t)]\right\} + \sum_{n=1}^{N} \sigma_n \exp\left\{-j\frac{4\pi f}{c}[R_R(t) \right. \\ &\quad \left. + x_n \cos\theta_R(t) + y_n \sin\theta_R(t)]\right\} \end{aligned} \tag{2}$$

with subscripts B and R denoting the body and the rotating part, respectively.

Both the main body and the rotating part move with respect to the radar. The difference is that the rotating part has an additional rotation motion beside all the motions of the main body. For the main body, during the imaging interval we can apply the small-angle approximation usually used in ISAR imaging. That is

$$\begin{cases} \cos\theta_B(t) \approx 1 \\ \sin\theta_B(t) \approx \theta_B(t) \end{cases} \tag{3}$$

We also assume that a standard motion compensation algorithm [4, 9, 10] has been utilised to remove both the translation motion and the nonuniform rotational motion from the body, after which we can write

$$\begin{cases} R_B(t) \leftarrow 0 \\ \theta_B(t) \leftarrow \omega_B t \end{cases} \tag{4}$$

where ω_B is the effective body rotation rate after the motion compensation. The arrow symbol above is used to indicate a new assignment of the variable on the left after the motion compensation operation.

For the rotating part, the motion relative to the main body is rotation only. This implies that the rotating part has the same translation motion as that of the body while the rotation motion will change accordingly, i.e.

$$\begin{cases} R_R(t) \leftarrow 0 \\ \theta_R(t) \leftarrow \theta_R^1(t) \end{cases} \tag{5}$$

However, the small-angle approximation does not hold for the rotating part. Since its rotation rate is usually much larger than that of the main body, a rotating scatterer might undergo many cycles while the main body rotates only a few degrees during the imaging interval. Substituting (3)–(5) into (2), we have

$$\begin{aligned} E(f,t) = &\sum_{m=1}^{M} \sigma_m \exp\left\{-j\frac{4\pi f}{c}[x_m + y_m\omega_B t]\right\} \\ &+ \sum_{n=1}^{N} \sigma_n \exp\left\{-j\frac{4\pi f}{c}[x_n \cos\theta_R^1(t) + y_n \sin\theta_R^1(t)]\right\} \end{aligned} \tag{6}$$

which is the radar signal from a target with a rotating part in the two-dimensional (frequency, dwell time) domain after motion compensation of the main body. Since it is more efficient to process range compressed data, we Fourier transform (6) with respect to f and bring the radar data into the (range, dwell time) domain. The radar signal through a fixed range cell r is given by

$$\begin{aligned} E_r(t) = &\sum_{m=1}^{M} \sigma_m f_{bw} \mathrm{sinc}\left[\frac{2\pi f_{bw}}{c}(r - x_m)\right] \\ &\times \exp\left\{+j\frac{4\pi f_c}{c}(r - x_m - y_m\omega_B t)\right\} \\ &+ \sum_{n=1}^{N} \sigma_n f_{bw} \mathrm{sinc}\left\{\frac{2\pi f_{bw}}{c}[r - x_n \cos\theta_R^1(t) \right. \\ &\left. - y_n \sin\theta_R^1(t)]\right\} \exp\left\{+j\frac{4\pi f_c}{c}[r - x_n \cos\theta_R^1(t) \right. \\ &\left. - y_n \sin\theta_R^1(t)]\right\} \end{aligned} \tag{7}$$

where f_c and f_{bw} are the carrier frequency and the bandwidth of the radar, respectively.

Some observations can be made here about (7). There exist substantial differences between the main body signal and the rotating part signal. Each body-scatterer in the first term has constant amplitude σ_m and constant Doppler frequency $-(2f_c/c)\omega_B y_m$ with respect to t. However, the signal of each rotating scatterer in the second term contains both AM and FM components. This can be seen by the presence of the time-varying function $\theta_R^1(t)$ in both the *sinc* and the exponential terms. Consequently, a second Fourier transform of (7) with respect to t will focus the target body in cross-range, but not the rotating part return. This results in the observed interference from the rotating part in the ISAR image.

2.2 Chirplet basis

The chirplet basis function [5, 6] is well suited for parameterising the AM–FM radar signal in (7). A chirplet is a four-parameter basis of the form

$$\begin{aligned} h_k(t) = &\left(\frac{\pi}{\alpha_k}\right)^{\frac{1}{4}} \exp\{-\alpha_k(t - t_k)^2\} \exp\{-j2\pi f_k(t - t_k) \\ &- j\pi\beta_k(t - t_k)^2\} \end{aligned} \tag{8}$$

where t_k is the time centre of the signal, f_k is the centre frequency, β_k is the frequency modulation rate and α_k defines the time extent of the signal. The joint time–frequency plot of a chirplet function is illustrated in Fig. 1*a*.

Actually, the chirplet basis is one of the many options that can be used to model the radar signal accurately. However, there are some attractive attributes of this basis. First, the basis function is an AM–FM signal and only a sparse set of these bases is needed to approximate the time–frequency structure of the radar signal in (7). Secondly, the chirplet basis is a well understood basis with only four parameters. Only moderate computation time is needed to search for the basis parameters. Thirdly and most importantly, the parameters of the chirplet can be used to separate the two components of the signal. This is because signals from the main body and the rotating part are captured by chirplet bases with different parameters.

To see this more explicitly, let us assume a first-order rotational motion in the time neighbourhood of each chirplet

$$\theta_R^1(t) = \theta_c + \omega_R(t - t_k) \tag{9}$$

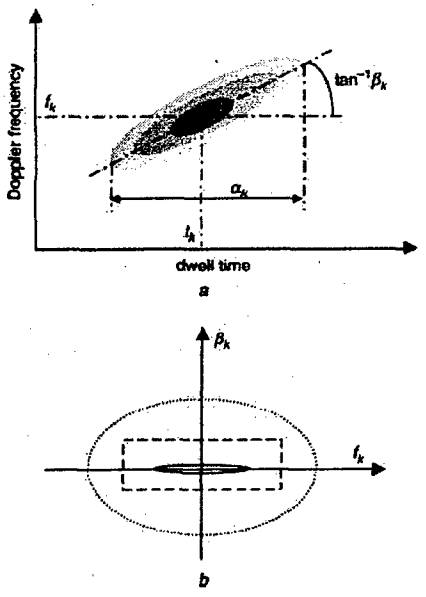

Fig. 1 *Chirplet basis and chirplet parameters*

a Joint time–frequency representation of a chirplet basis
b Distribution of chirplet parameters for the main body (solid) and rotation parts (dotted) and separation thresholds (dashed)

where θ_c is the angle at the time centre. The rotating part is assumed to have a constant rotation rate ω_R during the time interval near t_k although it could have more complex motions during the whole imaging interval.

After substituting (9) into (7), we take the first and second derivatives of the phase term with respect to t and compare them to those from (8) to arrive at expressions for f_k and β_k. The results can be written as

$$f_k = -\frac{2f_c}{c}\omega_R[x_n \sin \omega_R(t-t_k) - y_n \cos \omega_R(t-t_k)]$$
$$= -\frac{2f_c}{c} l_n \omega_R \sin[\omega_R(t-t_k) - \zeta_n] \quad (10a)$$

$$\beta_k = -\frac{2f_c}{c} l_n \omega_R^2 \cos[\omega_R(t-t_k) - \zeta_n] \quad (10b)$$

where (l_n, ζ_n) are the polar representations of (x_n, y_n). It can be seen from (10*a*) and (10*b*) that the parameters f_k and β_k are distributed along an ellipse as follows:

$$\frac{f_k^2}{(l_n\omega_R)^2} + \frac{\beta_k^2}{(l_n\omega_R^2)^2} = \left(\frac{2f_c}{c}\right)^2 \quad (11)$$

where the size and the axial ratio of the ellipse are controlled by ω_R and l_n. Similarly, the equation to associate the chirplet parameters with the main body signal is given by

$$\frac{f_k^2}{(l_m\omega_B)^2} + \frac{\beta_k^2}{(l_m\omega_B^2)^2} = \left(\frac{2f_c}{c}\right)^2 \quad (12)$$

where the scatterer radial length l_m and the rotation rate ω_B are used for the main body.

Even though (11) and (12) have exactly the same form, the main body and the rotating part are separable in the parameter space because of their different motions. Essentially, while the sizes of the two parts are comparable, the rotating part rotates much faster than the main body during the imaging interval, i.e.

$$\omega_R \gg \omega_B \quad (13)$$

Consequently, the chirplet parameters f_k and β_k for the main body and the rotating part are distributed very differently in the parameter space. A rotating part scatterer is represented as a larger and rounder ellipse while a body-scatterer is represented as a smaller and flatter ellipse. Actually, the ellipse for the main body is nearly a line segment on the f_k axis since the first term of (7) is assumed to have zero Doppler rate. The different distributions of the chirplet parameters are illustrated in Fig. 1*b*, where the outer ellipse represents the rotating part signal while the inner one represents the main body signal. A simple criterion to separate the two parts can thus be defined; the body signal has small f_k and β_k while the rotating part signal has either large f_k or β_k.

Another interesting observation we can make from the above discussion is that the main body and the rotating part signals have large overlaps in f_k, while they have little overlap in β_k. Therefore, the Doppler rate is more important than the Doppler frequency in separating the two signal components. This point will be further illustrated by examples later.

To summarise, if we parameterise the radar signal in question into a set of chirplet bases, it is possible to separate the contributions from the target body and the rotating part based on the parameters of the chirplet bases, as we have discussed above.

2.3 Signal separation based on adaptive chirplet signal representation

To decompose the radar signal into a set of chirplet bases, we apply the adaptive signal parameterisation algorithm [11, 12]. We start with the radar signal in a fixed range cell with returns from both the body and the rotating part, which is labelled as $E_r(t)$ in (7). Next, we parameterise $E_r(t)$ by projecting the signal onto chirplet bases of different parameters and find the one with the maximum projection value. Next, a residual signal is generated by subtracting the contribution of the just-found basis from the signal. This process is then iterated to generate a series of chirplet basis functions that, when summed, can approximate the original signal. The steps are summarised below:

Step 1. Set iteration index number k to 1 and the residual signal $R_k(t)$ to $E_r(t)$

Step 2. Find the kth chirplet $h_k(t)$ by maximising the projection from the residual signal $R_k(t)$ onto the basis, i.e.

$$\{t_k, f_k, \alpha_k, \beta_k\} = \arg \max |\langle R_k(t), h_k(t)\rangle| \quad (14)$$

where the inner product is defined as

$$\langle R_k(t), h_k(t)\rangle = \int_{t_0}^{t_1} R_k(t) h_k^*(t) dt \quad (15)$$

The radar data are assumed to exist over the time interval t_0 to t_1. The coefficient of the chirplet is the corresponding projection

$$c_k = \langle R_k(t), h_k(t)\rangle \quad (16)$$

Step 3. Subtract the extracted signal from the residual

$$R_{k+1}(t) \leftarrow R_k(t) - c_k h_k(t) \quad (17)$$

Step 4. Increment k by one and repeat steps 2 and 3 until k reaches a preset number or until the energy of the residual signal is below some threshold set based on the signal-to-noise ratio. Suppose N chirplets are found from this procedure, the radar signal is parameterised as

$$E_r(t)\approx\sum_{k=1}^{N}c_k\left(\frac{\pi}{\alpha_k}\right)^{\frac{1}{4}}\exp\left\{-a_k(t-t_k)^2e^{-j2\pi f_k(t-t_k)}e^{-j\pi\beta_k(t-t_k)^2}\right\} \quad (18)$$

After the parameterisation of the radar signal, the body signal can be separated from the rotating part signal using the criteria discussed previously. We classify those chirplets with small f_k and β_k as the main body components and the chirplets with either large f_k or large β_k as the rotating part components. The final body-only signal and the rotating part signal are assembled from the corresponding chirplet bases according to (18).

Following the separation, we can process the main body signal and the rotating part signal individually for better information extraction. Based on our discussion about (7), for the target body the feature of interest is the geometrical information in the ISAR image. A better body image can be reconstructed after removing the rotating part components. For the rotating part signal, it may be impossible to also construct a focused image of the rotating part if the PRF of the radar is too low. However, it is possible to extract useful information about the motion of the rotating part from the separated data.

3 Point-scatterer simulation results

We first test our algorithm with point-scatterer simulation data. Six point-scatterers are used in the simulation with five points representing the rigid body and one representing the rotating part. The positions and the strengths of the six scatterers are shown in Fig. 2. Scatterer 6 rotates around scatterer 2 at a rate of 6.67 Hz and a rotation radius of 20 cm. We assume the radar has a 10 GHz centre frequency, 800 MHz bandwidth and 1400 Hz PRF. The target body rotates about 4° over 384 pulses during the data collection time.

Simulated radar data are generated using the point-scatterer model in (6). The resulting radar image is shown in Fig. 3. The three point-scatterers in the centre range cell are shadowed by a noisy vertical micro-Doppler band due to the motion of the rotating point-scatterer. Our objective is to reconstruct the five body-scatterers and to estimate the rotation rate of the rotating scatterer from the radar signal.

Different behaviours of the body and the rotating part are better identified in the joint time–frequency

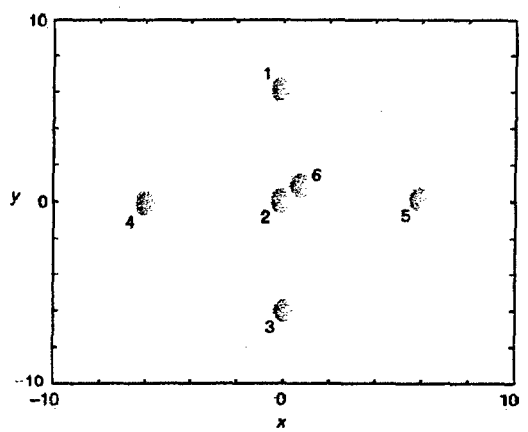

Fig. 2 *Point-scatterer representation of the original target consisting of five rigid points (1–5) and one rotating point (6) with strengths 2, 5, 2, 1, 1, and 3.33, respectively*

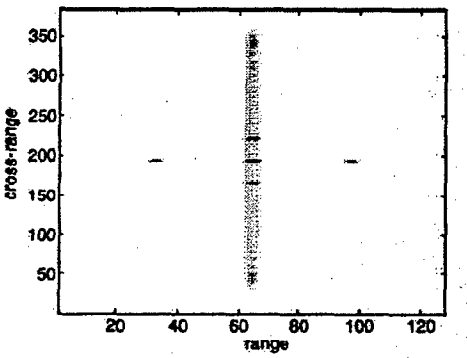

Fig. 3 *Simulated ISAR image of the target with non-rigid-body motion*

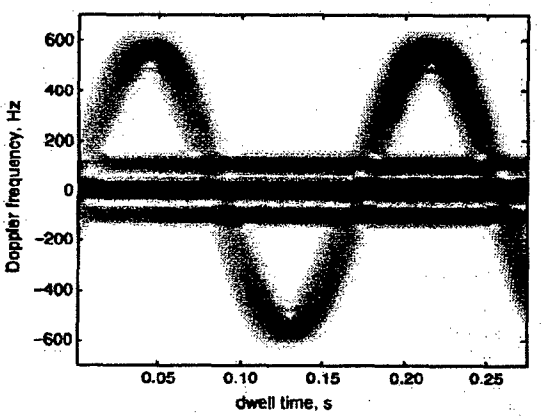

Fig. 4 *Spectrogram of the radar signal through range cell 65*

domain. The spectrogram obtained from the short-time Fourier transform is shown in Fig. 4 using the data in range cell 65, which contains responses from scatterers 1, 2, 3 and 6. In this Figure, we see interesting features about the target. First, there are three horizontal Doppler lines. The one at zero Doppler is due to scatterer 2. The two at ±100 Hz are due to scatterers 1 and 3. Secondly, there is a sinusoidal-like micro-Doppler curve due to the rotating scatterer 6. Amplitude modulation of this signal is also observed.

Following the steps in Section 2.3, we first parameterise the signal using $N = 100$ chirplets. The spectrogram of the resulting parameterised signal is shown in Fig. 5. We see fairly good agreement between the original signal and the parameterised signal. Next, we separate the contributions from the static and dynamic parts of the target based on the Doppler frequency f_k and the Doppler rate β_k of the chirplet bases. A simple threshold of 3200 Hz/s on the Doppler rate and 300 Hz on the Doppler frequency is used to discriminate the static and dynamic part of the target. The spectrograms of the resulting radar signals are shown in Figs. 6*a* and 6*b* for the rigid body and the rotating part, respectively. We see that the body with nearly constant Doppler and the rotating part with fast changing Doppler are separated.

We use the same procedure to parameterise and separate the radar signals from range cells 60 to 70. After removing the rotating part interference, the final ISAR image is shown in Fig. 7. The five scatterers of the static body are now correctly focused. To obtain more

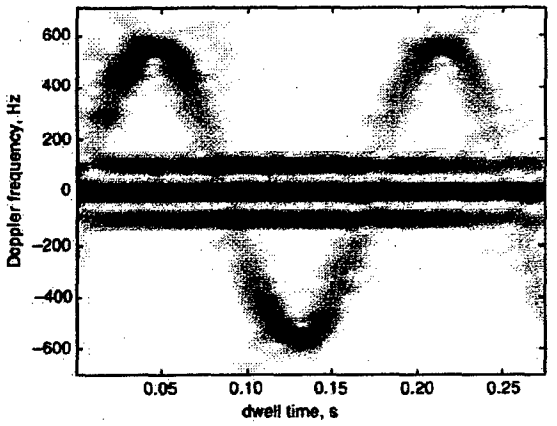

Fig. 5 *Spectrogram of the parameterised radar signal using 100 chirplet bases*

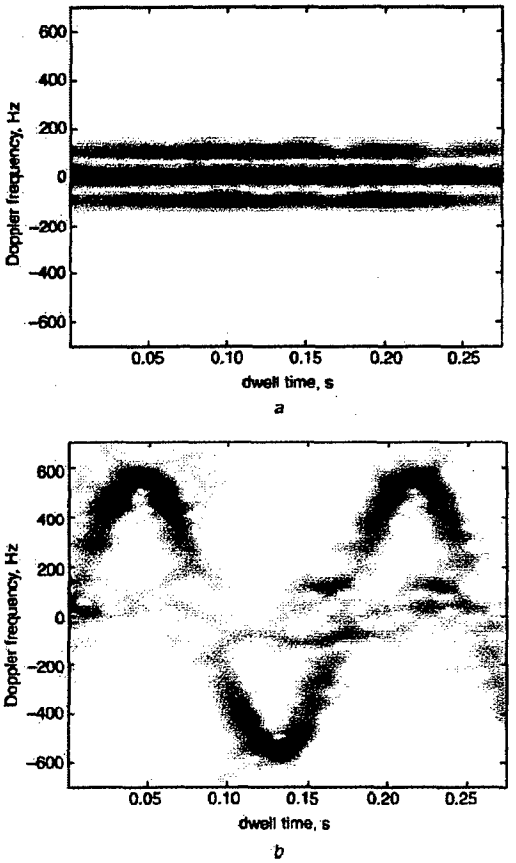

Fig. 6 *Separated body and rotating part signal*

a Spectrogram of the three main body scatterers
b Spectrogram of the rotating part

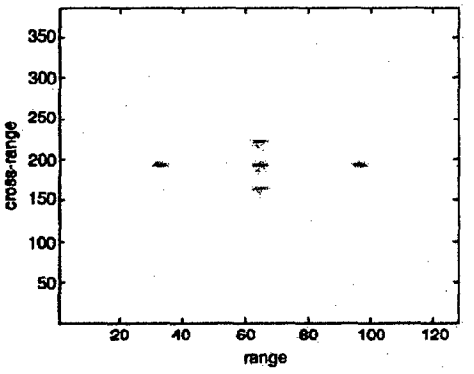

Fig. 7 *Reconstructed ISAR image using the main body signals only*

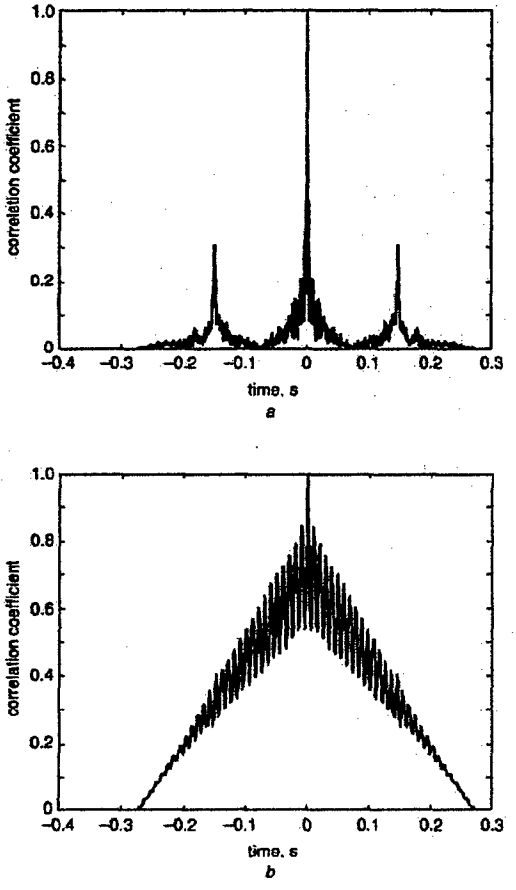

Fig. 8 *Rotation rate estimation using autocorrelation*

a Result from the rotating part signal after separation
b Result from the original signal before separation

information about the rotation motion, an autocorrelation analysis of the separated rotating point signal is shown in Fig. 8*a*. The period of the rotation motion is determined to be 0.15 s from this Figure. This agrees with the true rotation rate of 6.67 Hz. For comparison, the autocorrelation of the raw radar signal before separation is shown in Fig. 8*b*. It is difficult to detect the periodicity from the plot as the rotating scatterer signal is heavily contaminated by the large body return.

4 Measurement data results

The algorithm is next applied to two sets of measurement data. The first data set is the radar data collected from an in-flight aircraft during the frontal view of the target. The second data set is the radar data collected from a walking person. In both cases, the goal is to separate the main body signal from the rotating part return for better target feature extraction.

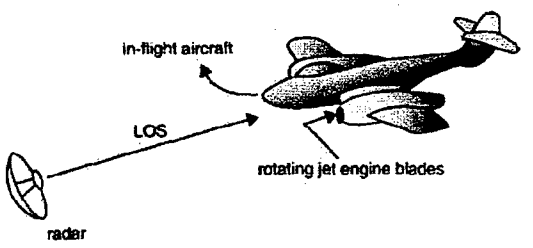

Fig. 9 *ISAR imaging of an aircraft during frontal view*

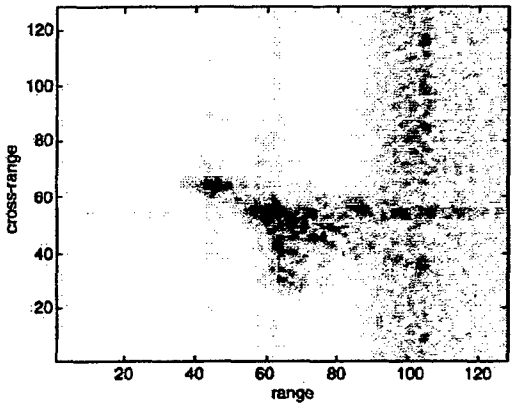

Fig. 10 *ISAR image of the aircraft with JEM lines*

4.1 Jet engine modulation removal from an in-flight aircraft

The geometry of the problem is shown in Fig. 9. The radar collects backscattering data from an in-flight aircraft. The resulting ISAR image obtained using a joint time–frequency based motion compensation algorithm [9] is shown in Fig. 10. We observe a vertical noisy band due to the rotating engine blades, which is the well known jet engine modulation (JEM) phenomenon [13]. The geometry of the aircraft body is obscured due to the presence of the JEM lines.

Simple Doppler gating is typically used to alleviate this problem. The result in Fig. 11*a* is generated by putting zeros in cross-range cells 1–32 and 62–128 in the image area with JEM lines. The high Doppler frequency components in the jet engine return are removed in this manner. However, we see that in areas where the JEM lines overlap with the target image, this technique does not work well, as it cannot distinguish the aircraft body signal from the JEM signal with low Doppler frequency.

Using the chirplet-based adaptive signal representation, we first parameterise the radar signal. Figure 11*b* is the reconstructed ISAR image using a separation criterion based on β_k only, i.e. we remove those chirplet bases with large β_k from the parameterised signal. It is much better than Fig. 11*a* in revealing the aircraft body feature. This confirms our previous observation that the Doppler rate is a better discriminator than the Doppler frequency in separating the two signals. Finally, we use both β_k and f_k to separate the two signals. The aircraft body image reconstructed from chirplet bases with both small β_k and small f_k is shown in Fig. 11*c*. We see an even better representation of the aircraft

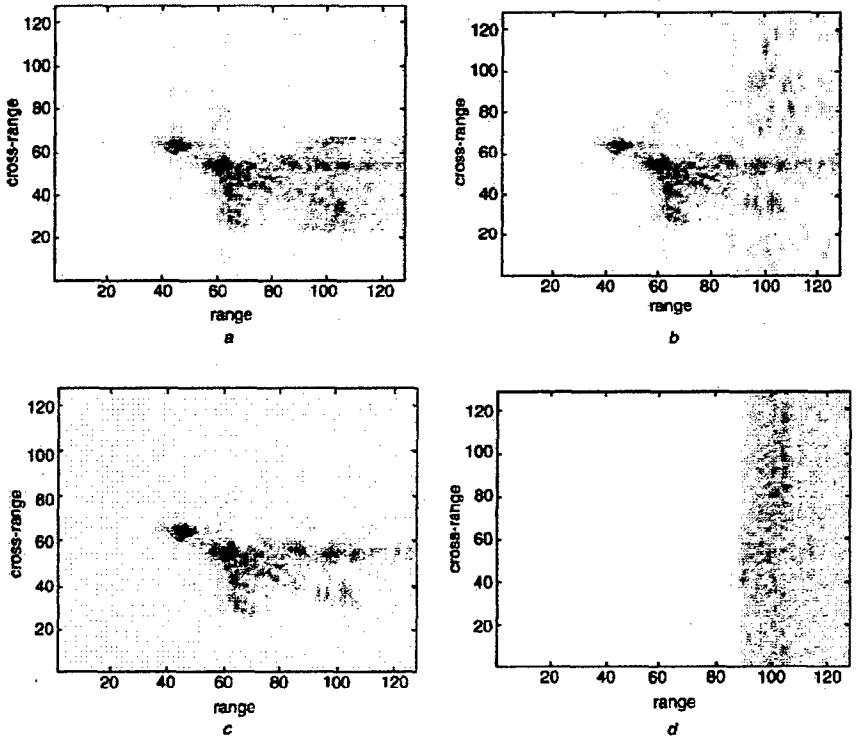

Fig. 11 *Aircraft body and JEM line separation*

a Body ISAR image with Doppler frequency gating only
b Body ISAR image with Doppler rate gating only
c Body ISAR image based on both Doppler frequency and Doppler rate parameters
d Separated JEM signal

body feature in the JEM region. The JEM signal is also displayed in Fig. 11*d*. The signal is aliased because of the low PRF of the radar in comparison with the rotation rate of the engine blades. This example shows that this algorithm works despite the strong Doppler aliasing of the rotating part signal.

4.2 Arm swing rate estimation from a walking person

The second data set is the measured radar data collected from a walking person. The geometry of the problem is shown in Fig. 12. Two types of motions are involved; the translation motion of the person's body and the swinging motion of the arms (or legs). Figure 13 shows the range profiles after coarse range alignment using amplitude correlation. Due to the limited range resolution relative to the target size, it is very hard to discern any useful features about either the body or the arms in this Figure. Figure 14 is the spectrogram of the radar signal through range cell 32. Interesting target features are revealed in this Figure. The horizontal Doppler line is due to the body motion as the person walks at a relatively constant speed during the 1.28 s dwell interval. The sinusoidal-like curve shows the micro-Doppler phenomenon from the swinging arm motion. The Doppler spread is caused by the varying speed of the arm and the changing angle between the instantaneous swinging motion and the radar incident wave. We also observe the periodicity of the arm motion.

To separate the body and the arm returns, the adaptive chirplet representation is applied. After the parameterisation, we again separate the body return from the arm return by classifying those bases with large Doppler frequency f_k or large Doppler rate β_k as contributions from the arms. The spectrograms of the separated body and arm signals are shown in Figs. 15*a* and 15*b*, respectively. The main features of the target are kept after the separation, indicating good accuracy of the parameterisation. We also observe a significant denoising effect from the parameterisation. This is because noise in the measured data does not have the time–frequency characteristics of a chirplet and it is left in the residual signal after the parameterisation. The arm-swing period can be easily estimated from the arm-only data by taking the autocorrelation of the time sequence. The peaks in Fig. 16*a* correspond to the period of the signal, which is found to be 0.44 s. Based on this swing rate and the speed of the person (2.3 m/s) estimated from the same radar data, the stride size of the person is determined to be about 1.0 m. For comparison, we have also generated the autocorrelation of the original data without the joint time–frequency processing (Fig. 16*b*). In this case, the radar return from the arm is overshadowed by the body

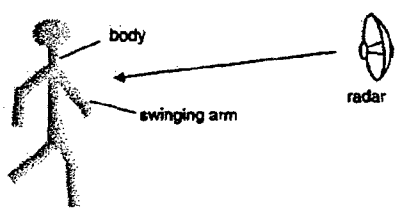

Fig. 12 *ISAR imaging of a walking person*

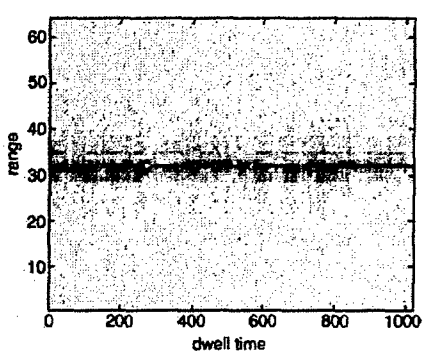

Fig. 13 *Radar data after range compression*

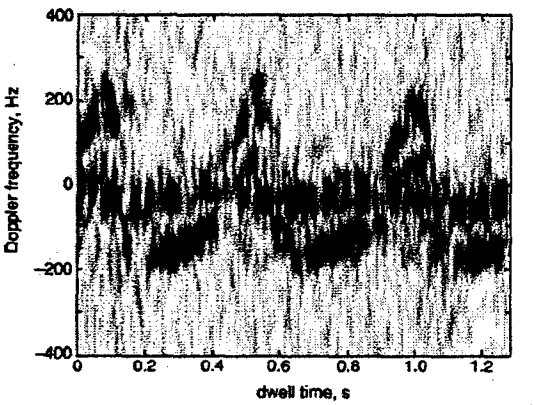

Fig. 14 *Spectrogram of the radar signal containing body and arm components*

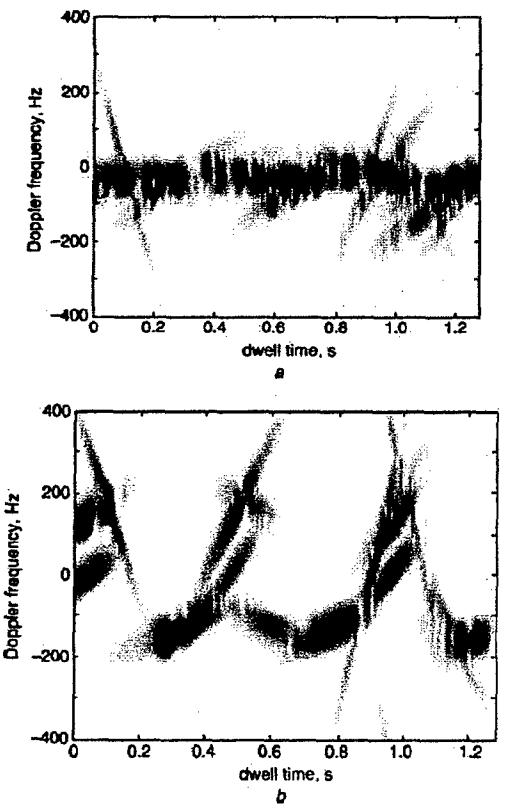

Fig. 15 *Separated signal components*

a Body
b Swinging arm

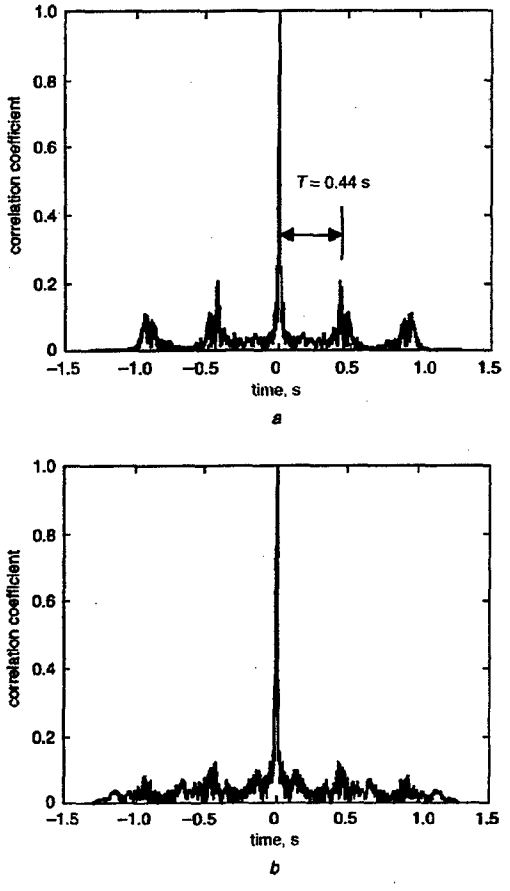

Fig. 16 *Arm-swing rate estimation using autocorrelation*
a After signal separation
b Before signal separation

return and the peaks in the autocorrelation function are significantly less pronounced.

Finally, we note here that only a simple exhaustive search has been implemented to carry out the chirplet decomposition in our examples. In the walking person example, the decomposition of a signal with 1024 data samples into 50 chirplets took 1050 s using MATLAB on a personal computer with a 2.26 GHz Pentium 4 CPU. A fast implementation of the chirplet decomposition has recently been reported in [14] and should speed up the processing significantly.

5 Conclusions

In this paper, a chirplet-based adaptive signal representation algorithm has been applied to extract features from ISAR data of a target with a rigid main body and a rotating part. Because the micro-Doppler feature of the rotating part is very different from the body Doppler, the two interfere with each other if processed together. To overcome this problem, we parameterise and separate the two parts using the adaptive signal representation. In particular, after formulating an AM–FM model for the radar signal, the four-parameter chirplet basis is used to account for the time and frequency localisation of the signal. After the parameterisation, the separation is achieved by a criterion based on the extracted Doppler frequency and Doppler rate parameters. The algorithm has been successfully tested with point-scatterer simulations and applied to two measurement data sets. In the aircraft data, we are able to reconstruct a better aircraft body image after the separation. In the walking person data, we are able to more accurately estimate arm swing rate. The results demonstrate the potential application of this algorithm for target identification using ISAR data from non-rigid-body targets.

6 Acknowledgments

This work is supported by the Office of Naval Research under contract No. N00014-98-1-0615. The authors also thank Dr. V.C. Chen of Naval Research Laboratory for providing the measurement data used in this work. In addition, J. Li gratefully acknowledges summer support from the Computing and Information Technology Center at the University of Texas-Pan American.

7 References

1 Chen, V.C.: 'Analysis of radar micro-Doppler with time-frequency transform'. Proc. 10th IEEE Workshop on Statistical signal and array processing, Pocono Manor, PA, USA, Aug. 2000, pp. 463-466
2 Greneker, E.F., Geisheimer, J.L., and Asbell, D.: 'Extraction of micro-Doppler data from vehicle targets at X-band frequencies', *Proc. SPIE-Int. Soc. Opt. Eng.*, 2001, **4374**, pp. 1–9
3 Ausherman, A., Kozma, A., Waker, J.L., Jones, H.M., and Poggio, E.C.: 'Developments in radar imaging', *IEEE Trans. Aerosp. Electron. Syst.*, 1984, **20**, (4), pp. 363–400
4 Carrara, W.G., Goodman, R.S., and Majewski, R.M.: 'Spotlight synthetic aperture radar - Signal processing and algorithms' (Artech House, Boston, MA, 1995)
5 Qian, S., Chen, D., and Yin, Q.: 'Adaptive chirplet based signal approximation'. Proc. ICASSP, Seattle, WA, USA, May 1998, vol. III, pp. 1871-1874
6 Bultan, A.: 'A four-parameter atomic decomposition of chirplets', *IEEE Trans. Signal Process.*, 1999, **47**, pp. 731–745
7 Trintinalia, L.C., and Ling, H.: 'Joint time-frequency ISAR using adaptive processing', *IEEE Trans. Antennas Propag.*, 1997, **45**, (2), pp. 221–227
8 Wang, Y., Ling, H., and Chen, V.C.: 'Application of adaptive joint time-frequency processing to ISAR image enhancement and Doppler feature extraction for targets with rotating parts', *Proc. SPIE-Int. Soc. Opt. Eng.*, 1998, **3462**, pp. 156–163
9 Wang, Y., Ling, H., and Chen, V.C.: 'ISAR motion compensation via adaptive joint time-frequency techniques', *IEEE Trans. Aerosp. Electron. Syst.*, 1998, **34**, (2), pp. 670–677
10 Rihaczek, A.W., and Hershkowitz, S.J.: 'Radar resolution and complex-image analysis' (Artech House, Boston, MA, 1996)
11 Mallat, S.G., and Zhang, Z.: 'Matching pursuits with time-frequency dictionaries', *IEEE Trans. Signal Process.*, 1993, **41**, (12), pp. 3397–3415
12 Qian, S., and Chen, D.: 'Signal representation using adaptive normalized Gaussian functions', *Signal Process.*, 1994, **36**, (1), pp. 1–11
13 Bell, M., and Grubbs, R.A.: 'JEM modeling measurement for radar target identification', *IEEE Trans. Aerosp. Electron. Syst.*, 1993, **29**, (1), pp. 73–87
14 Yin, Q., Qian, S., and Feng, A.: 'A fast refinement for adaptive Gaussian chirplet decomposition', *IEEE Trans. Signal Process.*, 2002, **50**, (6), pp. 1298–1306

A SYNTHETIC-APERTURE ALGORITHM FOR GROUND-PENETRATING RADAR IMAGING

Caner Ozdemir,[1] Sungkyun Lim,[2] and Hao Ling[2]
[1] Dept. of Electrical-Electronics Engineering
Mersin University
Ciftlikkoy, 33343 Mersin, Turkey
[2] Dept. of Electrical and Computer Engineering
University of Texas at Austin
Austin, TX 78712-1084

Received 2 February 2004

ABSTRACT: *A formulation for ground-penetrating radar (GPR) imaging using the synthetic-aperture concept is introduced. We show that it is possible to form a 3D image by inverse Fourier transforming the multifrequency, multispatial scattered field. The proposed algorithm for GPR imaging is tested with measured and simulated data. The resultant images demonstrate good agreement between the measured and simulated cases.* © 2004 Wiley Periodicals, Inc. Microwave Opt Technol Lett 42: 412–414, 2004; Published online in Wiley InterScience (www.interscience.wiley.com). DOI 10.1002/mop.20320

Key words: *ground penetrating radar (GPR); synthetic aperture radar (SAR); radar imaging*

1. INTRODUCTION

The imaging of buried objects or inhomogeneities underground using ground-penetrating radar (GPR) has been a topic of interest for a wide variety of applications ranging from mine detection to archeology. Many GPR imaging algorithms have been proposed in the literature [1–5]. Although good depth resolution can usually be realized in GPR images using frequency diversity, good resolution in the cross-range dimensions is much harder to achieve. Capineri et al. [3] proposed a method for obtaining good resolution in GPR images out of B-scan data by applying the Hough transformation technique. Morrow and Van Genderen [4] and Van Dongen et al. [5] applied the back-propagation and conjugate-gradient inversion techniques to form two-dimensional (2D) and three-dimensional (3D) images for a borehole radar. However, these techniques have a significant computational burden. Therefore, there is a need for obtaining images with good range and cross-range resolution with a fast algorithm.

We previously developed a synthetic-aperture algorithm for imaging antenna–platform interactions based on multifrequency, multispatial scattered-field data [6–8]. In this paper, we extend our algorithm to generate 3D GPR images of scattered data from buried objects underground. This technique is based on the approximate Fourier transform relationship between the frequency-spatial variables and the distance-angle information of the buried scatterer. The algorithm is quite attractive, since it forms 3D images by using a fast Fourier transform (FFT) followed by a simple transformation from the distance-angle domain to the image domain. It is computationally fast. Furthermore, the cross-range resolution can be made as good as the range resolution by controlling the size of the collection aperture.

2. SAR APPROACH FOR GPR IMAGING

Similar to the antenna synthetic-aperture radar algorithm [6–8], our GPR imaging algorithm is based on collecting the multifrequency scattered electric field over a two-dimensional spatial grid lying on top of the ground, as shown in Figure 1. We assume the target point P is located at an unknown location (x_i, y_i, z_i). We make two approximations that are commonly used in SAR imaging. First, we assume that the frequency bandwidth is small in comparison to the center frequency. We further assume that the aperture dimensions are small in comparison to R_{2i}, the path length from P to the receiver. Under these assumptions, the scattered electric field at the receiver can be approximated as follows:

$$E_S(k, x', z') = A_i \cdot e^{-jk(R_{1i}+R_{2i})} \cdot e^{-jk_c x' \sin\alpha_i} \cdot e^{-jk_c z' \sin\alpha_i \sin\beta_i}, \quad (1)$$

where A_i is the strength of the scattered field, $k = 2\pi\sqrt{\varepsilon_r}/\lambda$ is the wave number in the soil, ε_r is the relative permittivity of the ground, k is proportional to the radar frequency, and k_c corresponds to the wave number at the center frequency. From the above equation, it is obvious that there exist Fourier transform relationships between the variables (k, x', z') and $(R_i = R_{1i} + R_{2i}, U = \sin\alpha, V = \sin\alpha.\sin\beta)$. Therefore, by taking the 3D inverse Fourier transform of the scattered electric field with respect to k, x' and z', it is possible to pinpoint the total travel distance and the angles related to the scatterer location as follows:

$$E_S(R, U, V) = IFT\{A_i \cdot e^{-jkR_i} \cdot e^{-jk_c x' \cdot U_i} \cdot e^{-jk_c z' \cdot V_i}\}$$
$$= A_i \cdot \delta(R - R_i) \cdot \delta(U - U_i) \cdot \delta(V - V_i) \quad (2)$$

After inverse transforming the multifrequency, multispatial scattered electric-field data, the scatterer point P will manifest itself as a peak at (R_i, U_i, V_i) with the corresponding amplitude A_i. In practice, since the spatial aperture size and the frequency bandwidth are not infinite, the actual spot size of the scatterer will be inversely proportional to these variables. Once the GPR image in the (R, U, V) domain is generated, we can then transform it to the spatial (x, y, z) domain by using the trigonometric relationship between the variables (R, α, β) and (x, y, z). The transformation from (R, U, V) to (x, y, z) is unique and correctly maps the scatterer location [8]. However, the resultant point-spread response in the image is slightly distorted, due to the nonlinear nature of this transformation.

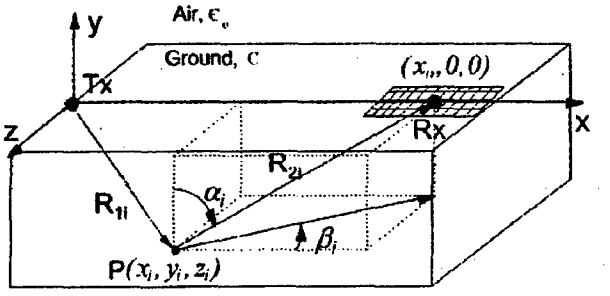

Figure 1 Geometry for GPR imaging

3. MEASUREMENT AND SIMULATION RESULTS

3.1. Experimental Setup

To test our GPR imaging algorithm, we built an experimental setup, as shown in Figure 2. In this setup, a wooden pit was constructed and filled with sand. Our GPR imaging algorithm requires the knowledge of the dielectric constant of the ground medium. The dielectric constant of the sand was measured by comparing the phase delay between a pair of antennas by carrying out the following experiment. First, a transmitter antenna and a receiver antenna are directed to each other in the air at a distance of 1 m and an S_{21} measurement for a frequency sweep from 4 to

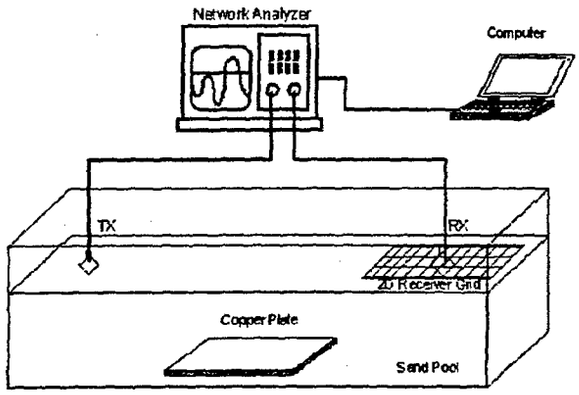

Figure 2 Experimental setup

6 GHz was done. Secondly, the same measurement (this time, inside the sand) was repeated. It is known that the phase delay between these two measurements is proportional to the square root of the permittivity of the sand. Figure 3 shows the unwrapped phase of the transmitted electric field for 201 discrete frequencies from 4 to 6 GHz for both the air and sand measurements. By taking the square of the phase delay between the sand measurement and the air measurement, we plotted the estimated dielectric constant of the sand over the frequencies (see Fig. 4). From this figure, it is deduced that the permittivity of the sand is nearly constant at the average value of 2.26 for the frequencies from 5 to 6 GHz. We used this value as the sand's dielectric constant throughout our analysis.

For our main GPR experiment, a rectangular copper plate of dimensions 46 cm in the x-direction and 30 cm in the z-direction was buried at 46 cm below the sand surface. The plate is located 50 cm away from the transmitter along the x-axis. S_{21} between the transmitter and the receiver was measured using an HP8753C network analyzer. Identical coax-fed rectangular waveguide antennas of dimensions are 3.81 and 1.91 cm were used as the transmitter and the receiver. Both antennas were directed towards the sand so that their main beam lighted the region below the sand surface. The transmitter antenna was assumed to be placed at the origin and the receiving grid was assumed to be centered at 1 m

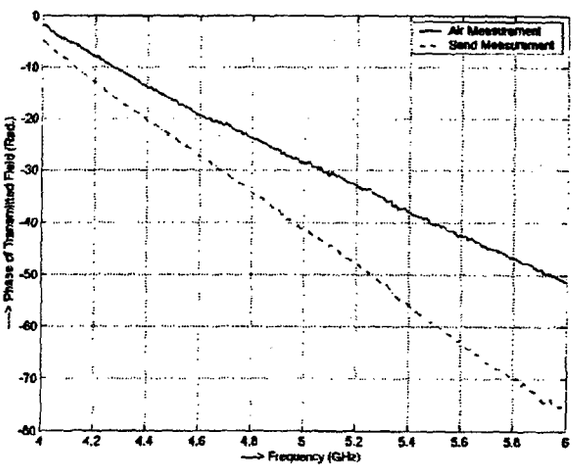

Figure 3 Unwrapped phase of the transmitted electric for both the air sand measurements

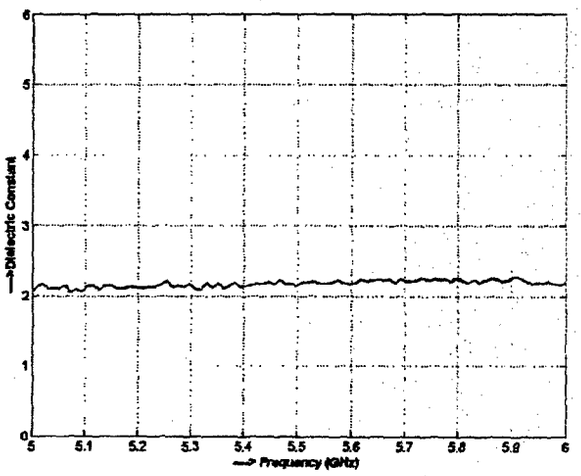

Figure 4 Measured dielectric constant variation of the sand from S_{21} measurements

along the positive x-direction. Both antennas were horizontally polarized such that the electric field was parallel to the metal plate. The scattered field was collected over 100 different spatial points. The size of the 10 × 10 receiving grid was 31.04 cm in the x-direction and 14.83 cm in the z-direction. For all 100 points, the signal frequency varied from 4.9226 to 5.9352 GHz over 25 evenly sampled points.

3.2. *Measurement Results*

The measured data from the experimental setup shown in Figure 2 were collected onto a computer and processed. After applying the proposed algorithm, we generated a 3D GPR image in the (R, U, V) domain. To achieve better resolution of the image, the frequency-spatial data were zero-padded four times in all R, U, and V domains and then our FFT-based imaging algorithm was applied. Therefore, we generated a 3D GPR image whose size was 100 × 40 × 40. For display purposes, the 3D image was projected onto 2D R–U, R–V and U–V planes, as shown in Figure 5(a). Then, to

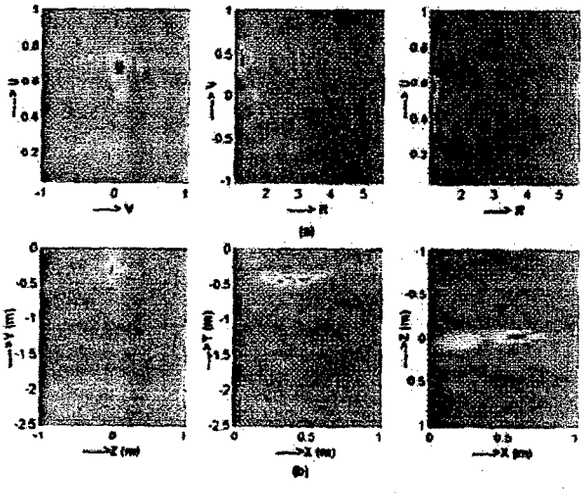

Figure 5 2D projected GPR images for the measurement data in the (a) (R, U, V) and (b) (X, Y, Z) domains. [Color figure can be viewed in the online issue, which is available at www.interscience.wiley.com.]

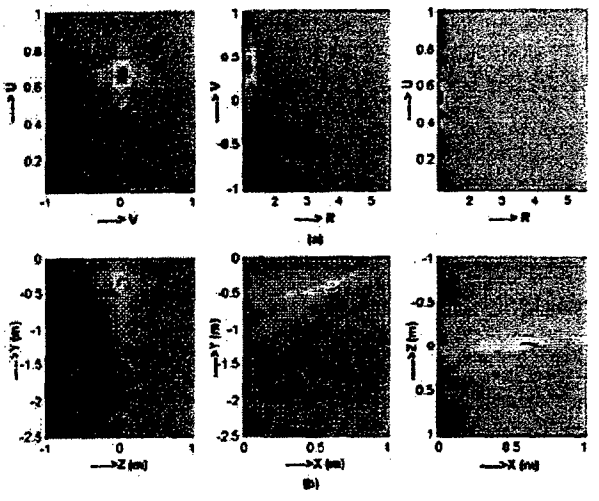

Figure 6 2D projected GPR images for the simulation data in the (a) (R, U, V) and (b) (X, Y, Z) domains. [Color figure can be viewed in the online issue, which is available at www.interscience.wiley.com.]

obtain the 3D GPR image of the region below the surface, we applied the necessary coordinate transformations. Figure 5(b) shows the 2D projected GPR images onto the principal Z–Y, X–Y, and X–Z planes. The projected outlines of the plate are overlaid upon the images. We observe that our algorithm estimates the scattering from beneath the target of the copper plate well. We also note two main hot spots in the image. The stronger one corresponds to the scattering from the middle of the plate, where a specular point exists. The weaker one corresponds to the diffraction mechanism from the front edge of the plate. This mechanism is expected, since the tip of the electric field is parallel to this front edge of the plate. Both image features agree well with the geometrical locations of the plate. In addition, the resolutions in the cross-range directions (that is, in the x- and z-directions) are nearly the same as the resolution in the range (y) direction. Note that the spots in the image do not have a simple point-spread form and they are somewhat defocused. This is due the nonlinear transformation from the (R, α, β) to the (x, y, z), and a method to overcome this effect has been discussed in [7, 8]. Nonetheless, we can still see the separation between the two points on the plate, which are spaced 23 cm apart. Therefore, our technique is able to achieve good resolutions in both the range and cross-range dimensions.

3.3. Simulation Results

To assure the validity of our measured results, a simulation was also carried out using a physical-optics calculation that utilizes the shooting and bouncing ray (SBR) technique [9]. During the simulation, the ray density was selected as five rays per wavelength. After running our simulator and obtaining the simulated data of the experimental setup, we applied the same imaging algorithm to form the simulated GPR image. Figures 6(a) and 6(b) demonstrate the 2D projected GPR images from the simulation data in (R, U, V) and (x, y, z) domains, respectively. By comparing the measured GPR images of Figure 5 to the simulated ones of Figure 6, good agreement between the two was obtained. Since the physical theory of diffraction contribution was absent in our simulation, we note that the edge-diffraction contribution in the simulation is weaker than that from the measured image.

4. CONCLUSION AND DISCUSSION

We have presented a Fourier based imaging algorithm for ground-penetrating radar (GPR), based on the synthetic-aperture radar concept. The algorithm utilizes the phase information of the scattered field. By inverse Fourier transforming the scattered-field data, we have shown that it is possible to form a good-resolution 3D GPR image of the region below the ground surface. To test our imaging algorithm, data were collected from a buried metallic plate by using an experimental setup. Our imaging algorithm successfully formed a 3D GPR image of the plate with a good estimation of the dominant scattering points off the target. The measured image was also compared to that formed from the simulation data that was generated using the physical optics calculation. Good agreement between the measured and simulated images was observed. Both results demonstrate good resolution images. On the other hand, the image distortion issue that worsens the image quality, due to nonlinear transformation from the distance-angle domain to the image domain. The limitation of the present imaging algorithm is that it assumes the soil medium to be homogeneous and the soil property to be known a priori. High-resolution images can be formed consistently by using this algorithm.

ACKNOWLEDGMENTS

This work is supported by the Scientific and Research Council of Turkey (TUBITAK) under NATO-B2 research scholarship programme and in part by the Office of Naval Research under contract no. N00014-03-1-0021. The authors would also like to thank to Dr. Hosung Choo (now with Hongik University, Korea) for his help during the experiments.

REFERENCES

1. D.J. Daniels, Surface-Penetrating Radar, IEE Press, London, 1996.
2. J.E. Mast, H. Lee, and J.P. Murtha, Application of microwave pulse-echo radar imaging to the nondestructive evaluation of buildings, Int J Imaging Syst Tech 4 (1992), 164–169.
3. L. Capineri, P. Grande, and J.A.G. Temple, Advanced image-processing technique for real-time interpretation of ground-penetrating radar images, Int J Imaging Syst Tech 9 (1998), 51–59.
4. I.L. Morrow and P.A. Van Genderen, 2D polarimetric backpropagation algorithm for ground-penetrating radar applications, Microwave Opt Technol Lett 28 (2001), 1–4.
5. K.W.A. Van Dongen, P.M. Van Den Berg, and J.T. Fokkema, A directional borehole radar for three-dimensional imaging, Proc 9th Int Conf GPR I (2002), 25–30.
6. C. Ozdemir, R. Bhalla, L.C. Trintinalia, and H. Ling, ASAR: Antenna synthetic aperture radar imaging, IEEE Trans Antennas Propagat 46 (1998), 1845–1852.
7. C. Ozdemir, R. Bhalla, and H. Ling, A radiation center representation of antenna radiation patterns on a complex platform, IEEE Trans Antennas Propagat 48 (2000), 992–1000.
8. C. Ozdemir and H. Ling, ACSAR: Antenna coupling synthetic aperture radar (ACSAR) imaging algorithm, J Electromagn Waves Applic 13 (1999), 285–306.
9. H. Ling, R. Chou, and S.W. Lee, Shooting and bouncing rays: calculating the RCS of an arbitrary shaped cavity, IEEE Trans Antennas Propagat 37 (1989), 194–205.

ON THE MULTIPLATEN Z-BUFFER ALGORITHM FOR RAY TRACING IN HIGH-FREQUENCY ELECTROMAGNETIC SCATTERING COMPUTATIONS

Yong Zhou and Hao Ling
Department of Electrical and Computer Engineering
The University of Texas at Austin
Austin, TX 78712-1084

Received 19 April 2004

ABSTRACT: *A ray tracer based on the multiplaten Z-buffer (MPZ) algorithm is implemented and its performance is evaluated against the binary space-partition tree algorithm. Our results indicate that the computational complexity of the MPZ is independent of the number of facets, thus making it potentially attractive for targets described by a large number of facets. A multi-aspect MPZ (MAMPZ) is also proposed to further enhance the speed performance of the MPZ algorithm. It is shown that by storing multi-aspect Z-buffers, it is possible to significantly accelerate the ray-tracing time of the MPZ.* © 2004 Wiley Periodicals, Inc. Microwave Opt Technol Lett 43: 298–301, 2004; Published online in Wiley InterScience (www.interscience.wiley.com). DOI 10.1002/mop.20450

Key words: *ray tracing; multiplaten Z-buffer; binary space-partition tree*

1. INTRODUCTION

Ray tracing is a key step in high-frequency electromagnetic scattering computations [1, 2]. Numerical tracing of rays for a complex target model is often a very time-consuming operation. Therefore, a faster ray-tracing algorithm could significantly speed up the scattering prediction from complex targets. In this paper, we evaluate the multiplaten Z-buffer (MPZ) ray-tracing algorithm proposed by Hu et al. [3, 4] as an alternative to the traditional binary space-partition (BSP) tree algorithm [5]. In the standard BSP algorithm, a BSP tree is first built, based on the facet model of the target, by recursively cutting the bounding box of the object along a spatial plane. Ray tracing is then performed by traversing the BSP tree. The BSP-tree-based ray tracer is considered the fastest among all of the spatial-subdivision approaches. For a target consisting of N facets, the computation time of the algorithm scales between the optimal lower bound of $O(\log N)$ to the upper bound of $O(N)$, depending on the actual spatial distribution of target facets.

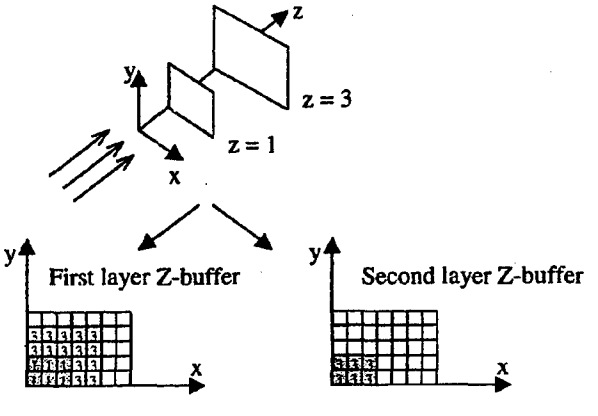

Figure 1 Setup of the multiplaten Z-buffer

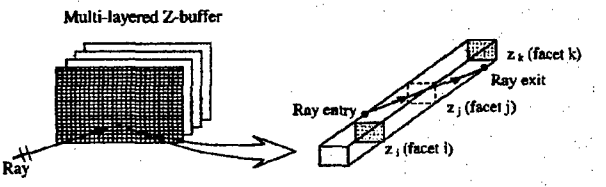

Figure 2 Mechanism of the MPZ ray-tracing algorithm

In the multiplaten Z-buffer approach, a multilayered Z-buffer is first generated using the scan-conversion process. Instead of simply storing the z-coordinates of the visible pixels as in the traditional Z-buffer process, multiple Z-buffers are created to store the z-coordinates of all of the facets within each pixel during the scan conversion. During the ray trace, a ray is tracked by moving pixel by pixel along the ray direction. Within every pixel, the z-depth of the ray is compared to all of the Z-buffer values for that pixel to check for possible intersections. Once an intersection is found, the hit point and the reflection direction can be calculated, and the tracing process is then iterated until the ray departs from the bounding box. Although it was claimed that the MPZ algorithm should be superior to the traditional ray-tracing process, no evaluation about its time performance was reported in [3, 4]. The first objective of this paper is to evaluate the performance of the MPZ against that of the BSP algorithm. Our results indicate that, in contrast to the BSP algorithm, the computational complexity of the MPZ is independent of the number of facets, thus making it potentially attractive for targets described by a large number of facets. Our second objective is to explore ways to further enhance the performance of the MPZ. It is shown that by storing multi-aspect Z-buffers, it is possible to significantly accelerate the performance of the MPZ.

This paper is organized as follows. In section 2, we review the MPZ algorithm and describe its implementation. In section 3, we compare the performance of the MPZ against that of the BSP algorithm. The results for a wide range of targets are tested to determine the computational complexity as a function of the number of facets. Based on the results, in section 4 we further propose a multi-aspect approach to speed up the computation performance of MPZ algorithm. The conclusions of our study are discussed in section 5.

2. MPZ ALGORITHM AND ITS IMPLEMENTATION

Z-buffers were originally developed to remove hidden surfaces in computer graphics displays. Rius et al. first adopted the usage of the Z-buffer in the GRECO code in the early 1990s to carry out physical-optics calculations [6]. To set up the Z-buffer, the target is first rotated so that the z-direction is aligned with the incident direction. A facet-by-facet scan conversion is then processed. Only the z-depth closest to the observer (that is, the visible surface of the target) is stored in the Z-buffer in pixel form. The multilayered Z-buffer is a natural extension of the traditional single-layer Z-buffer. Instead of only storing the z-depths of the visible surfaces, MPZ stores the z-depths of all the surfaces into a multi-layered Z-buffer (Fig. 1). At the same time, a frame buffer is set up to store the corresponding facet numbers. The completed MPZ contains the 3D coordinates of the target in a view-specific coordinate system.

The MPZ ray tracer propagates a ray pixel by pixel along the ray direction (Fig. 2). Within every pixel tube, the z-depths for both the entry and exit points are first calculated. These two z-depths are then compared with all of the Z-buffer values within the pixel in order to check if there are any z-values between them.

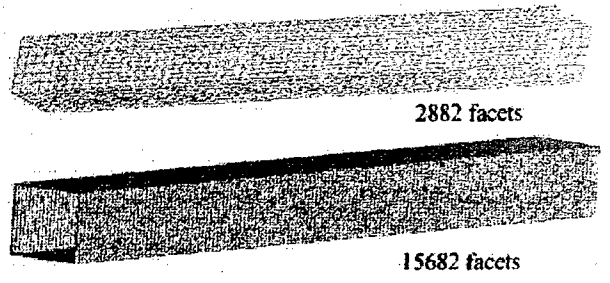

Figure 3 Faceted rectangular cavity structures. [Color figure can be viewed in the online issue, which is available at www.interscience.wiley.com.]

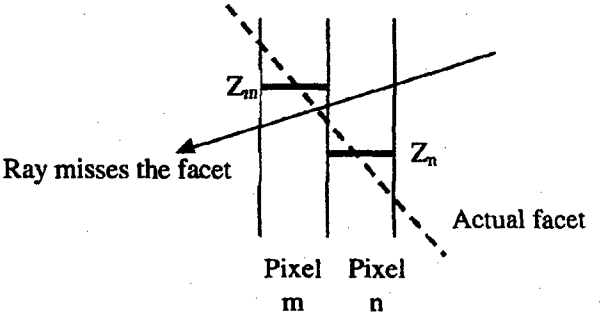

Figure 5 Missed ray at a large z-value gap between two adjacent pixels

If not, then the ray is propagated to the next pixel tube. If there are, then an intersection is reported. The closest Z-buffer value to that of the entry point is selected and the corresponding facet number is looked up in the frame buffer. An intersection routine is then called to calculate the hit point and the reflected ray direction. This procedure is repeated from pixel to pixel until the ray eventually exits the bounding box.

3. EVALUATION OF THE MPZ AGAINST THE BSP

In order to evaluate the performance of the MPZ ray tracer, we construct multiple facet models for the same straight rectangular-cavity structure of size 2 × 2 × 20 m (open at one end and closed at the other). The number of facets varies from 322 to 72,002 (Fig. 3 shows two such models). We run the BSP and MPZ algorithms on all of the facet models in order to compare and evaluate their computational performance. Three hundred rays are launched along the $\varphi = 135°$ and $\theta = 30°$ directions. It should be noted that we only include the ray-tracing time of the two algorithms in the comparison and the times for the BSP tree building and the MPZ scan conversion are not included. Figure 4 shows the result of the average ray-tracing time per ray versus the number of facets for both ray tracers. Since the cavity facets are not distributed uniformly in space, the resultant BSP tree is highly unbalanced. Consequently, the ray-tracing time of the BSP algorithm increases nearly linearly with the number of facets. On the contrary, the performance of the MPZ algorithm is almost independent of the number of facets. Even though the crossover point between the two algorithms does not occur until there is a very large number of facets (>70,000), the MPZ algorithm was implemented without any optimization, while the BSP algorithm is a standard published routine [5].

The MPZ performance should theoretically be independent of the number of facets, but the curve from the test result in Figure 4 shows small undulations. Closer examination reveals that a small portion of the rays are not traced correctly. The missed intersections are predominantly caused by the z-value gaps shown in Figure 5. These gaps between neighboring pixels occur after the scan conversion of a facet, and become larger for a facet that is nearly parallel to the Z-buffer direction. As a result, a ray can miss the facet, especially when the ray direction is nearly perpendicular to the z-direction. This problem will be further taken up in the next section. Another minor cause of the mistraced rays is due to the pixel quantization at the facet edges. Incorrect intersections can occur due to the serrated-edge approximation by pixels, as opposed to the original linear edge of a facet. However, this problem is a minor one, as such error decreases with a finer pixel size.

Next, we investigate the effect of the number of MPZ layers on the ray-tracing time. We use the same rectangular cavity to evaluate the computation time. Since only two Z-buffer layers are enough to describe the rectangular cavity, we use dummy z-values to pad the extra MPZ layers. This scheme guarantees that all the conditions are kept the same, except for the number of MPZ layers. Figure 6 shows the relationship between the average MPZ ray-tracing time per ray and the number of MPZ layers for the rectangular cavity. The result indicates that the ray-tracing time only increases slightly with the number of layers. This result is not

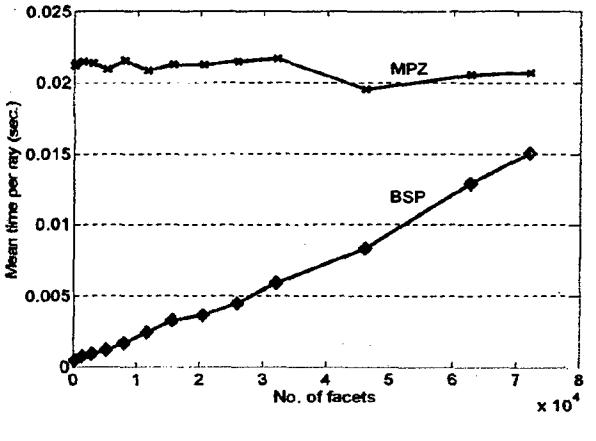

Figure 4 Performance comparison of the BSP and MPZ algorithms for the faceted rectangular cavities

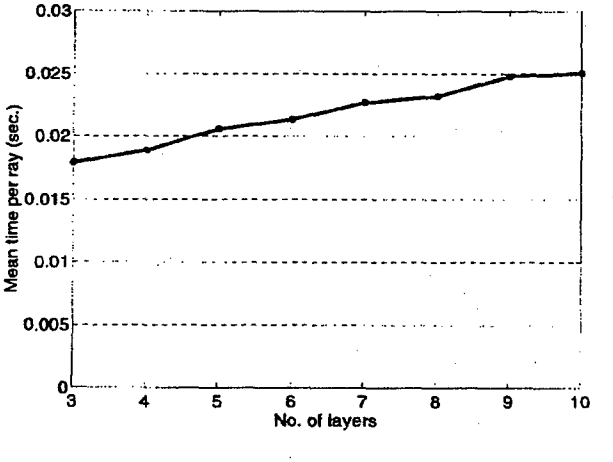

Figure 6 Relationship between the averaged time per ray and the number of MPZ layers

TABLE 1 Time-Performance Comparison Between the BSP and MPZ Algorithms for Complex Targets

	Targets								
	1	2	3	4	5	6	7	8	9
No. of facets	126	800	958	3992	5974	7994	10090	23988	56556
BSP average time per ray (ms)	0.13	0.12	2.50	16.84	13.02	5.16	4.61	5.64	56.48
MPZ average time per ray (ms)	5.35	3.46	8.98	10.04	11.00	18.45	6.14	12.91	43.66

surprising, since the computational overhead to check for a ray intersection against the stored Z-buffer values within a pixel is very small.

Table 1 shows the performance comparison between the MPZ and BSP algorithms for nine complex targets where the number of facets varies from 126 to 56,556. Because the complexity of the targets is different, the average number of ray bounces varies from target to target and no apparent performance trend can be found. However, the results do show a smaller performance gap between the MPZ and BSP algorithms as the number of facets increases.

4. MULTI-ASPECT MPZ (MAMPZ)

While the performance of the MPZ ray-tracing algorithm does not depend on the number of facets, it does depend directly on the number of pixels a ray traverses. Therefore, if we can reduce the number of pixels a ray traverses between bounces by decreasing the angle between the ray and the Z-buffer directions, the MPZ time performance should be further improved. Here, we investigate a multi-aspect MPZ (MAMPZ) approach. In the MAMPZ, multiple multilayered Z-buffers are first generated from the scan-conversion process along many aspect angles. The maximum number of multilayered Z-buffers is limited only by the available memory resource. The more aspect angles that are stored, the fewer pixels a ray needs to traverse in one bounce, and the better the time performance. During the ray trace, the multilayered Z-buffer structure that has the closest aspect to the ray direction is selected to carry out the ray tracing. A ray is then tracked by moving pixel by pixel along the ray direction inside this MPZ structure to check for possible intersections.

The computation time performance of the MAMPZ ray tracer is evaluated against that of the single-aspect MPZ and the BSP tree algorithm on the rectangular cavities. Generally, the traced rays for an object can be along any direction. If multiple MPZs are set up with an angular interval Δ along both the θ and ϕ directions, it will guarantee that every ray can find its closest MPZ with a maximum cross angle of $\Delta/2$. We call this angular interval $\Delta/2$ the MPZ aspect resolution. A fine aspect resolution means a large number of MPZs, which require a large amount of memory to store. Nonetheless, this concept can be tested easily for the rectangular cavity, since the ray directions can be limited to only two distinct directions by choosing the incident angle to be along $\phi = 0$ (θ is chosen to be 45°). Thus, by setting up the MPZs at a distance $\Delta/2$ from these two ray directions, we can evaluate the performance of the algorithm with different MPZ aspect resolutions. Figure 7 shows the computational complexity of the MAMPZ algorithm as a function of number of facets for two different MPZ aspect resolutions. The comparison indicates a seven-fold improvement in performance against that of the single-aspect MPZ, even for a 20° aspect resolution. Another 14-fold improvement can be achieved for a 1° aspect resolution. Consequently, the new MAMPZ algorithm can outperform the BSP algorithm for targets with as small as a few thousand facets if the aspect resolution is fine enough. Figure 8 shows the time performance of the MAMPZ algorithm for different aspect resolutions. The result displays a monotonic (and slightly nonlinear) decrease of ray tracing time versus the MAMPZ aspect resolution.

One important benefit of the MAMPZ is a decrease in the number of mistraced rays. The results in Figure 7 show the disappearance of undulations in the timing curves. As mentioned in the previous section, the mistracing usually occurs when the ray direction is nearly perpendicular to the z-direction. In MAMPZ, since each ray is traced by choosing the closest MPZ, the ray direction is always close to the z-direction. For the straight cavities, the percentage of mistraced rays decreases from above 1% for the single-aspect MPZ to below 0.2% for the 20° MAMPZ. This is an important advantage of the multi-aspect algorithm.

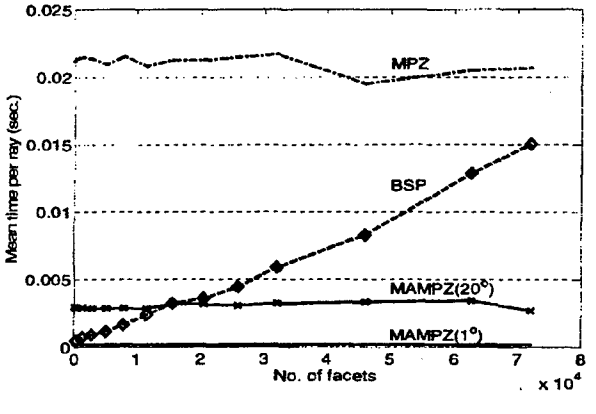

Figure 7 Performance of the MAMPZ for two different aspect resolutions

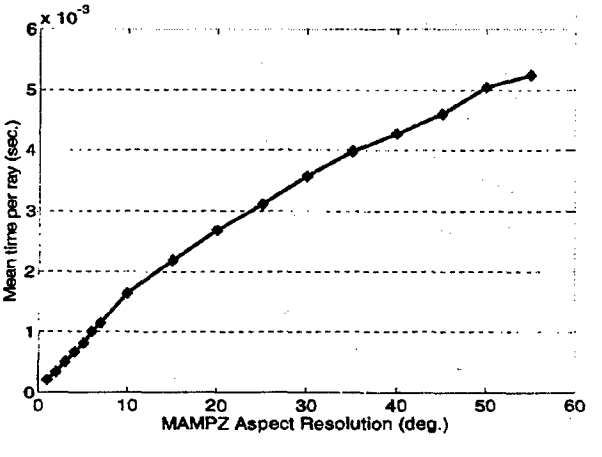

Figure 8 Time performance for different aspect resolutions of the MAMPZ

5. CONCLUSION

A ray tracer based on the multiplaten Z-buffer algorithm has been implemented and its performance has been evaluated against the standard BSP tree algorithm. Our results show that the computational complexity of the MPZ algorithm is independent of the number of facets and is only weakly dependent on the number of Z-buffer layers. The algorithm has been further extended by a multi-aspect MPZ approach. The results show that the extended algorithm can dramatically improve the ray-tracing speed in comparison to the single-aspect MPZ by cutting down the number of pixels each ray has to traverse. The MAMPZ also reduces the chance of mistraced rays, which are intrinsic to the Z-buffer quantization process. One price for the improvement in speed is the large memory requirement for storing the MPZs. For a single-aspect, 24-bit Z-buffer with three layers, the typical memory size is 8.6 MB for a 1000 × 960 pixel resolution. If an aspect resolution of 20° is used to set up uniformly distributed MPZs over all directions (note that only a hemispherical coverage is needed to cover all angles), the required memory is 175 MB. For a resolution of 1°, the number becomes 70 GB. Provided that such memory resources are available, the MAMPZ algorithm can achieve a 2nd order of magnitude acceleration in ray-tracing time. This makes the algorithm quite attractive in certain modeling and simulation applications where speed is critical.

ACKNOWLEDGMENTS

The authors would like to thank Dr. Charles Liang of Lockheed for bringing the MPZ algorithm to their attention, and Dr. J. L. Hu for helpful information. This work is supported by the Office of Naval Research under contract no. N00014-03-1-021.

REFERENCES

1. H. Ling, R. Chou, and S.W. Lee, Shooting and bouncing rays: Calculating the RCS of an arbitrarily shaped cavity, IEEE Trans Antennas Propagat 37 (1989), 194–205.
2. D.J. Andersh, M. Hazlett, S.W. Lee, D.D. Reeves, D.P. Sullivan, and Y. Chu, XPATCH: A high-frequency electromagnetic-scattering prediction code and environment for complex three-dimensional objects, IEEE Antennas Propagat Mag 36 (1994), 65–69.
3. J.L. Hu, Y. Ma, S.M. Lin, and W.B. Wang, Multiplaten Z-buffer algorithm and its application to multiple scattering, Electron Lett 33 (1997), 825–826.
4. J.L. Hu, C.H. Chan, and S.M. Lin, Computation of RCS of jet engine with complex terminations based on multiplaten Z-buffer algorithm, Microwave Opt Technol Lett 23 (1999), 281–284.
5. K. Sung and P. Shirley, Ray tracing with the BSP tree, Graphics GEMS IV, D. Kirk (Ed.), Academic Press, 1992, pp. 271–274.
6. J.M. Rius, M. Ferrando, and L. Jofre, GRECO: Graphical electromagnetic computing for RCS prediction in real time, IEEE Antennas Propagat Mag 35 (1993), 7–17.

MULTIWAVELENGTH RING LASERS EMPLOYING SEMICONDUCTOR OPTICAL AMPLIFIERS AS GAIN MEDIA

Junqiang Sun
Department of Optoelectronic Engineering
Huazhong University of Science and Technology
Wuhan, 430074, P.R. China

Received 24 April 2004

ABSTRACT: *Stable simultaneous multiwavelength lasing is demonstrated with a novel fiber-ring laser incorporating a semiconductor optical amplifier. Band-pass comb filtering is constructed in the ring cavity with the combination of a wideband Fabry–Perot comb filter and a bandpass filter. Ten lasing lines with a fixed wavelength spacing of 1.6 nm are implemented and the multiwavelength lasing ranges can be flexibly chosen.* © 2004 Wiley Periodicals, Inc. Microwave Opt Technol Lett 43: 301–303, 2004; Published online in Wiley InterScience (www.interscience.wiley.com). DOI 10.1002/mop.20451

Key words: *dense wavelength-division multiplexing; multiwavelength lasers; semiconductor optical amplifiers*

1. INTRODUCTION

Multiwavelength lasers are expected to be powerful multichannel sources used in wavelength division multiplexing (WDM) optical networks. Conventionally, these wavelengths are generated by employing either multiple discrete lasers or monolithically integrated multiwavelength laser arrays [1, 2]. However, their output power and lasing wavelength are susceptible to the variations of environmental temperatures and injection currents. Hence, a precise control system is required to inhibit wavelength shifts and power fluctuations, and thus WDM transmitters will become much more complicated and expensive. It is sometimes physically simpler to achieve multiwavelength oscillation with a fixed channel separation using a single gain medium. Naturally, erbium-doped fiber (EDF) is considered as a usual gain medium in multiwavelength lasers due to its high gain with broad gain bandwidth and compatibility with fiber-communication systems [3, 4]. However, the large homogeneous linewidth of EDF at room temperature poses a major barrier to obtaining stable simultaneous multiwavelength lasing. Consequently, multiwavelength oscillation with erbium-doped fiber lasers (EDFLs) was previously demonstrated by cooling EDF down to liquid-nitrogen temperature in order to reduce the homogeneous linewidth of EDF and thus greatly suppress the strong mode competition [5]. However, this method is inconvenient and may impact the device durability, leading to complexity in component configuration. Compared with EDF, the homogeneous broadening linewidth of semiconductor optical amplifiers (SOAs) was deduced to be about 0.6 nm around the wavelength of 1550 nm at room temperature, which makes multiwavelength oscillation with WDM ITU-grid spacing possible [6]. Accordingly, SOA-based lasers have been taken into consideration as a potential alternative to multiwavelength generation [7, 8]. Additionally, SOA-based lasers can operate at ultra-broad wavelength region from the S-band to L-band by designing the compositions of gain materials [9]. We have reported an SOA-based multiwavelength laser in which two cascaded sample fiber gratings were employed as equivalent reflectors [10]. In this paper, a novel approach is presented and stable 10-wavelength lasing with an equal channel separation is observed. Furthermore, adopting filters

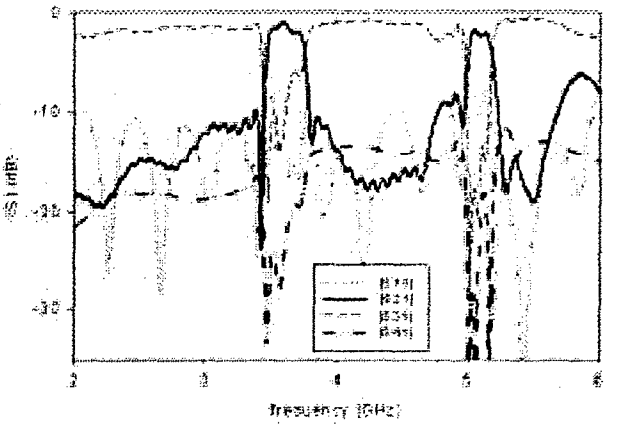

Figure 10 Simulated S-parameters for a backward power coupler operating at two frequencies

and good performance was demonstrated in fabricated devices implemented by means of the dual transmission line concept [14, 15], we have been pioneers in using the resonant-type approach in the design of these devices, and reasonable performance has been obtained. We have also explored the possibility of designing multifrequency couplers by using CSRRs. This paper has demonstrated that the resonant-type approach to left-handed lines is useful and promising, and it can be an alternative to the well-established dual-transmission-line approach in narrow- or moderate-bandwidth applications.

ACKNOWLEDGMENTS

This work has been supported by MCyT under project contracts TIC2002-04528-C02-01, TEC2004-04249, PROFIT 070000-2003-933, and PROFIT 330200-2004-113. The authors would also like to thank Conatel s.l. and Omicron Circuits s.l. for their contributions to the development of this work.

REFERENCES

1. V.G. Veselago, The electrodynamics of substances with simultaneously negative values of ϵ and μ, Sov Phys Usp 10 (1968), 509.
2. J.B. Pendry, A.J. Holden, D.J. Robbins, and W.J. Stewart, Magnetism from conductors and enhanced nonlinear phenomena, IEEE Trans Microwave Theory Tech 47 (1999), 2075–2084.
3. D.R. Smith, W.J. Padilla, D.C. Vier, S.C. Nemat-Nasser, and S. Schultz, Composite medium with simultaneously negative permeability and permittivity, Phys Rev Lett 84 (2000), 4184–4187.
4. C. Caloz, C-C. Chang, and T. Itoh, Full-wave verification of the fundamental properties of left-handed materials in waveguide configurations, J Appl Phys 90 (2001), 5483–5486.
5. A. Grbic and G.V. Eleftheriades, Experimental verification of backward wave radiation from a negative refractive index metamaterial, J Appl Phys 92 (2002), 5930–5935.
6. F. Martín, F. Falcone, J. Bonache, R. Marqués, and M. Sorolla, Miniaturized coplanar waveguide stop-band filters based on multiple tuned split-ring resonators, IEEE Microwave Wireless Compon Lett 13 (2003), 511–513.
7. F. Martín, F. Falcone, J. Bonache, R. Marqués, and M. Sorolla, A new split-ring resonator based left-handed coplanar waveguide, Appl Phys Lett 83 (2003), 4652–4654.
8. F. Falcone, F. Martín, J. Bonache, R. Marqués, T. Lopetegi, and M. Sorolla, Left-handed coplanar-waveguide band-pass filters based on bi-layer split-ring resonators, IEEE Microwave Wireless Compon Lett 14 (2004), 10–12.
9. F. Falcone, T. Lopetegi, J.D. Baena, R. Marqués, F. Martín, and M. Sorolla, Effective negative-ϵ'' stopband microstrip lines based on complementary split-ring resonators, IEEE Microwave Wireless Compon Lett 14 (2004), 280–282.
10. F. Falcone, T. Lopetegi, M.A.G. Laso, J.D. Baena, J. Bonache, M. Beruete, R. Marqués, F. Martín, and M. Sorolla, Babinet principle applied to the design of metasurfaces and metamaterials, Phys Rev Lett 93 (2004), 197401-1-4, 5.
11. R. Marqués, F. Mesa, J. Martel, and F. Medina, Comparative analysis of edge- and broadside-coupled split-ring resonators for metamaterial design: Theory and experiments, IEEE Trans Antennas Propagat 51 (2003), 2572–2581.
12. L. Liu, C. Caloz, C.-C. Chang, and T. Itoh, Forward-coupling phenomena between artificial left-handed (LH) transmission lines, J App Phys 92 (2002), 5560–5565.
13. P.K. Ikäläinen and G.L. Mathei, Wideband, forward-coupling microstrip hybrids with high directivity, IEEE Trans Microwave Theory Tech 35 (1987).
14. R. Islam and G.V. Eleftheriades, A planar metamaterial co-directional coupler that couples power backwards, IEEE MTT-S Dig, Philadelphia, PA (2003), 321–324.
15. C. Caloz and T. Itoh, A novel mixed conventional microstrip and composite right/left handed backward wave directional coupler with broadband and tight coupling characteristics, IEEE Microwave Wireless Compon Lett 14 (2004), 31–33.

AN EXPERIMENTAL INVESTIGATION OF BURIED-OBJECT IMAGING IN A HOMOGENEOUS MEDIUM USING SYNTHETIC-APERTURE RADAR CONCEPTS

Caner Ozdemir[1] and Hao Ling[2]
[1] Department of Electrical-Electronics Engineering
Mersin University
Çiftlikköy, Mersin, 33343, Turkey
[2] Department of Electrical and Computer Engineering
The University of Texas at Austin
Austin, TX 78712-1084

Received 4 December 2005

ABSTRACT: *An experimental investigation is conducted to image buried objects. A Fourier-based imaging algorithm based on synthetic-aperture radar (SAR) concepts is applied to the scattered data from buried dielectric targets in a homogeneous medium. An experimental setup is constructed to apply the algorithm. Three-dimensional images of water bottles and plastic targets buried in sand are presented.* © 2006 Wiley Periodicals, Inc. Microwave Opt Technol Lett 48: 1209–1214, 2006; Published online in Wiley InterScience (www.interscience.wiley.com). DOI 10.1002/mop.21578

Key words: *ground-penetrating radar; buried object detection; radar imaging; synthetic aperture radar*

1. INTRODUCTION

Detecting objects buried beneath the Earth's surface or situated interior to a visually opaque medium has been a topic of interest to many researchers across different disciplines. A number of ground-penetrating radar (GPR) algorithms have been adopted for various applications from mine detection to geophysics [1–4]. Recent developments in synthetic-aperture radar (SAR) imagery provided better resolved images for GPR problems [4–10]. Carin [4] proposed a matched-filter type scheme for detecting mine fields by constructing ultra-wideband SAR images. Halman [5] provided a SAR-based imaging technique that uses time-domain waveforms

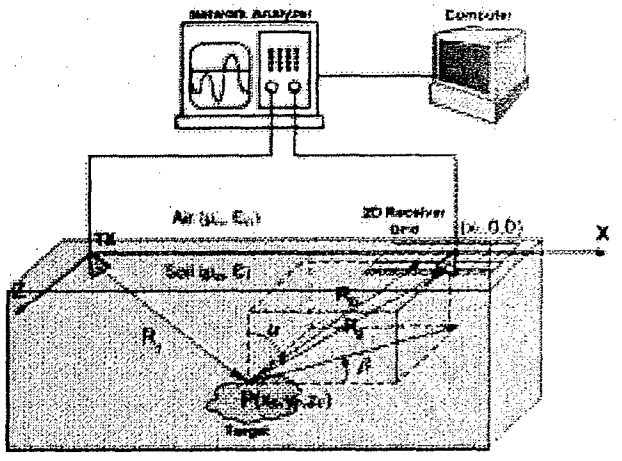

Figure 1 Geometry of the problem and the experimental setup. [Color figure can be viewed in the online issue, which is available at www.interscience.wiley.com]

to detect unexploded ordinances (UXOs). Similarly, Sullivan [6] and Vitebskiy [7] applied short-duration time signals to obtain ultra-wideband SAR images of UXOs. Marklein [8] and Witten [9] reported Fourier-based scalar iterative inversion schemes based on diffraction tomography (DT) algorithm. Although all these works demonstrated that good depth resolution could be realized in GPR images by using large frequency bandwidth, good cross-range resolution is usually harder to achieve. Moreover, most GPR methods do not offer direct imaging; that is, they are based on numerical iteration techniques that put significant burden on computational requirements in terms of speed and memory. Hansen [10] provided a fast DT algorithm that utilizes the fast Fourier transform (FFT) to expedite the imaging GPR. Recently, we reported a fast and effective SAR-based subsurface imaging technique that can provide good resolutions in both the range and cross-range domains [11]. Our algorithm differs from Witten's [9] and Hansen's [10] Fourier-based imaging algorithms, as we are able to relate the raw scattered field data to the distance-angle domain by utilizing the 3D FFT. A nonlinear transformation succeeds the FFT routine to transform the image from the distance-angle domain to the image domain. The algorithm is based on several simplifying approximations: (i) the air–soil interface can be ignored provided that the soil permittivity is low, (ii) the soil is homogeneous and low loss, and (iii) the transmitter and the receiver antennas are at the far field of the buried object. With these assumptions, we demonstrate that we can form a 3D image of the scattering from buried objects by inverse-Fourier transforming the multifrequency, multispatial scattered-field data and applying a domain-transformation formula. Some preliminary results for conducting targets were reported previously in [11]. In this work, we extend our previous experiments to more challenging dielectric targets and present the associated 3D SAR-based GPR images. This paper is organized as follows. In section 2 a description of the imaging algorithm is given. In section 3 the algorithm is applied to the measured data collected from a laboratory setup. Several dielectric objects are buried in sand and the collected data are imaged using the presented algorithm. In section 4, the work is summarized, and issues regarding the effectiveness and limitations of the imaging algorithm are discussed.

2. IMAGING ALGORITHM

Our imaging algorithm uses multifrequency, multispatial scattering data from a subsurface environment and inverts the data based on a simple point-scatterer model. This algorithm is an extension of our previously developed antenna coupling SAR imaging technique [12]. As shown in Figure 1, we assume that the transmitting and the receiving antennas are placed just under the ground, facing downward. While the transmitter is placed at a fixed location, the receiver position is varied on a 2D spatial grid (See Fig. 1). For each spatial grid location, the scattered field data are collected for various frequencies. Therefore, a multifrequency, multispatial 3D scattered-field data set is formed. If we assume the scattering occurs from a single point scatterer on the target (located in a homogeneous background) at a point $P(x_o, y_o, z_o)$, the scattered electric field at the receiver site can be written as

$$E_s = A_i \cdot e^{-jkR_1} \cdot e^{-jkR_{2i}}. \tag{1}$$

For an electromagnetic wave that leaves the transmitter, hits the point P and reaches the receiver, R_1 corresponds to the path length from the transmitter to point P, and R_{2i} corresponds to the path length from point P to any point (x_i', z_i') on the spatial grid at the receiver site. A_i is the complex amplitude of the scattered field and k is the wave number in the soil. Provided that the soil permittivity is low, the electromagnetic-wave interaction with the air–soil boundary is neglected. At this point, we will make two further assumptions that are commonly used in SAR imaging. We first assume that the frequency bandwidth is small compared to the

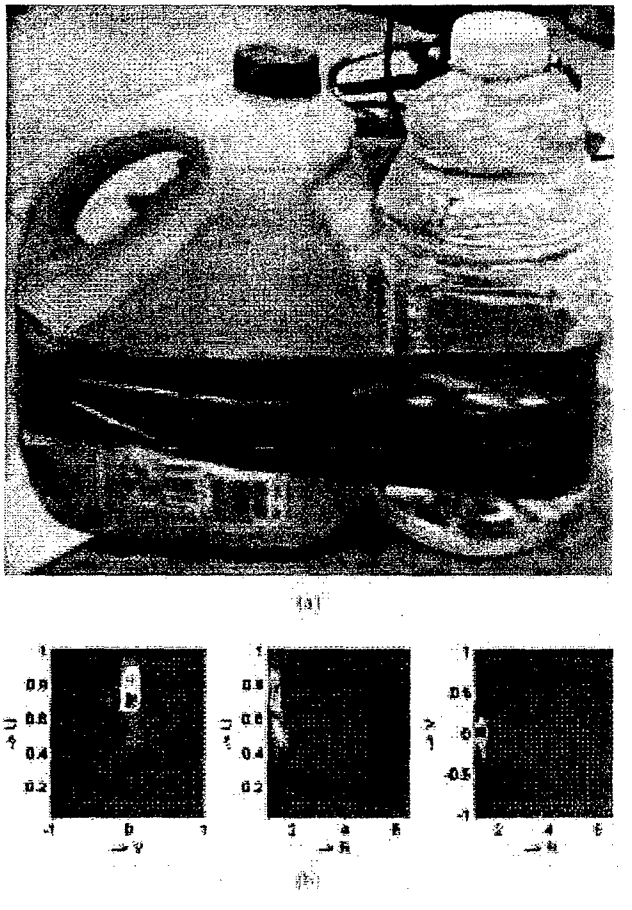

Figure 2 (a) Buried water target: two bottles filled with water and taped together; (b) 2D projected subsurface images for the buried bottle of water in the (R, U, V) domain. [Color figure can be viewed in the online issue, which is available at www.interscience.wiley.com]

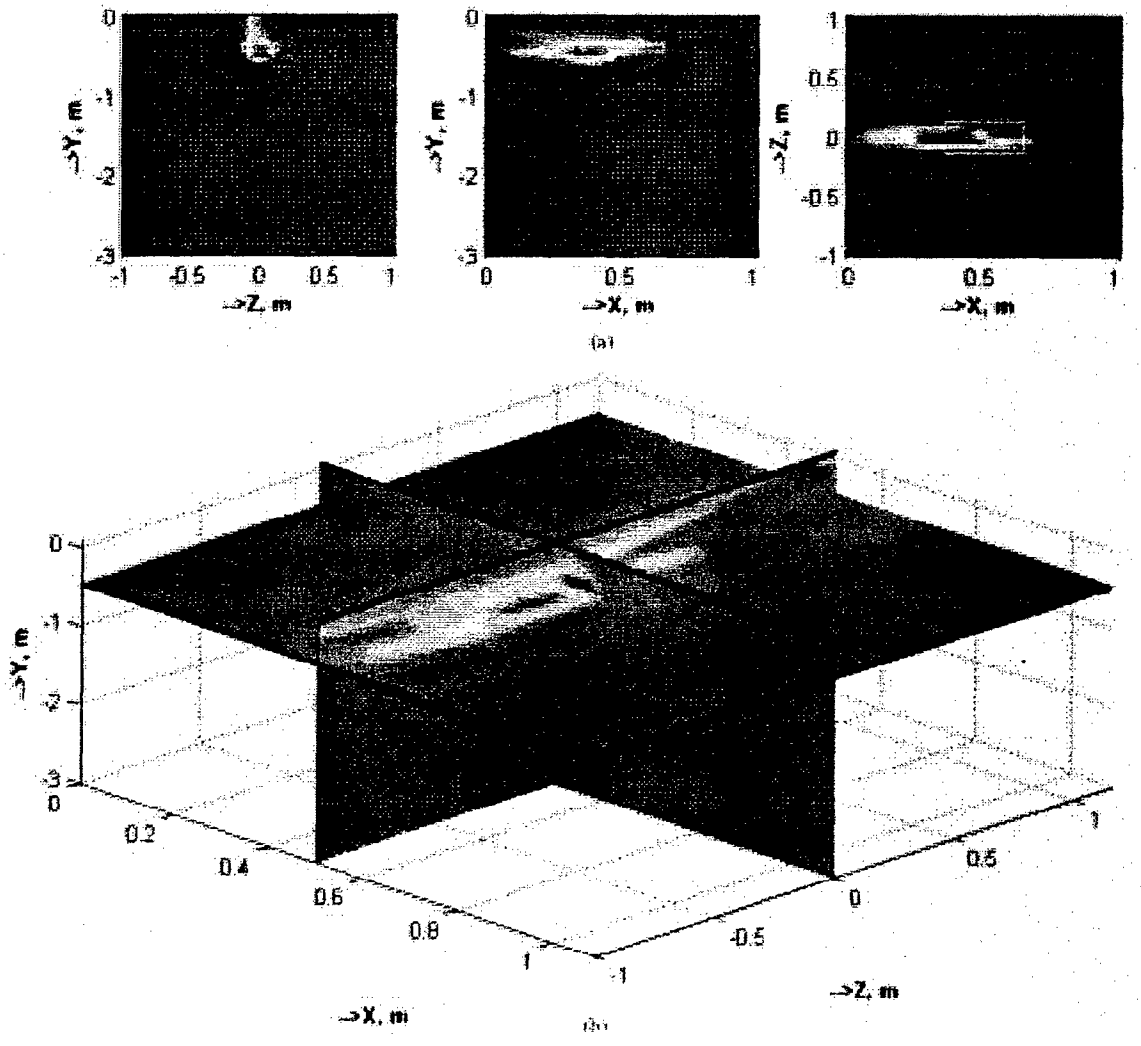

Figure 3 (a) 2D projected subsurface images for the buried bottle of water in the (x, y, z) domain; (b) sliced version of the 3D GPR image. [Color figure can be viewed in the online issue, which is available at www.interscience.wiley.com]

center frequency of operation. Second, we assume that the size of the spatial grid is small compared the path length from the target to the receiver's midpoint (which is labeled as R_2 in Fig. 1). That is, the object is located at the far-field of the receiver. Under these assumptions, the second phase term in (1) can be approximated as

$$kR_{2i} \cong kR_2 + k_c(x' \cdot \sin\alpha + z' \cdot \sin\alpha \sin\beta). \quad (2)$$

Here, k_c represents the wave number in the soil at the center frequency f_c and $x' = x - x_o$ and $z' = z$ are the coordinate variables of the receiver grid. In the second term of (2), k is replaced with k_c based on the small-bandwidth approximation. Therefore, the scattered-electric-field formula in (1) can be reorganized to give

$$E_S(k, x', z') = A_i \cdot e^{-jk(R_1+R_2)} \cdot e^{-jk_c \sin\alpha \cdot x'} \cdot e^{-jk_c \sin\alpha \sin\beta \cdot z'}. \quad (3)$$

In the above equation, we notice that there exist Fourier-transform relationships between k and $(R_1 + R_2)$, x' and $(k_c \cdot \sin\alpha)$, and z' and $(k_c \cdot \sin\alpha \cdot \sin\beta)$. *For simplicity, we let* $R = (R_1 + R_2)$, $U = (k_c \cdot \sin\alpha \cdot \sin\beta)$. By taking the 3D inverse Fourier transform (IFT) of (3), we can obtain the GPR image of point P as follows:

$$GPRI(R, U, V) = IFT_3\{E_S(k, x', z')\}$$

$$= A \cdot IFT\{e^{-jk(R_1+R_2)}\} \cdot IFT\{e^{-jk_c \sin\alpha \cdot x'}\} \cdot IFT\{e^{-jk_c \sin\alpha \sin\beta \cdot z'}\}$$

$$= A \cdot \delta(R - (R_1 + R_2)) \cdot \delta(U - k_c \sin\alpha) \cdot \delta(V - k_c \sin\alpha \sin\beta)$$

$$= A \cdot \delta(R - R_o) \cdot \delta(U - U_o) \cdot \delta(V - V_o), \quad (4)$$

where (R_o, U_o, V_o) is the distance-angle point that corresponds to the image point $P(x_o, y_o, z_o)$. Therefore, by taking the 3D IFT of the multifrequency, multispatial scattered field, it is possible to pinpoint the total travel distance and the angle information that correspond to the location of the target point P. In practice, the spot size of the point-spread response is limited by the finite frequency bandwidth and spatial dimensions of the collection area. Note that the image in the spatial (x, y, z) domain has not been generated. Therefore, once the image in the (R, U, V) domain is formed, we transform the image to the (x, y, z) domain by using the following transformation formulas (see the Appendix for derivation of this transformation):

$$x = \frac{(R^2 + x_o^2)\sin\alpha \cdot \cos\beta - 2R \cdot x_o}{2(x_o \sin\alpha \cdot \cos\beta - R)}, \quad y = \frac{(x_o - x)}{\tan\alpha \cdot \cos\beta},$$

$$z = (x_o - x)\tan\beta. \quad (5)$$

As it is obvious from these equations, this transformation is not linear. Therefore, the point-spread response is expected to be irregular in shape after the transformation into the (x, y, z) domain.

To summarize, the proposed SAR-based imaging algorithm entails the following steps: (i) collect 3D multi-frequency, multi-spatial scattered field data, $E_s(k, x', z')$; (ii) take the 3D IFT of this data to form the image in the (R, U, V) domain, $GPRI(R, U, V)$; (iii) form the image in the (x, y, z) domain by applying the transformation formulas in (5) to arrive at $GPRI(x, y, z)$. This Fourier imaging algorithm is derived based on the small-bandwidth, small-aperture approximation. Also, the algorithm requires that the dielectric constant of the soil to be known a priori. Furthermore, the algorithm assumes that the soil is low loss to ensure sufficient penetration depth for the detection of the subsurface object.

3. EXPERIMENTAL RESULTS

To test the proposed algorithm for different buried objects, the experimental setup shown in Figure 1 was constructed. A large wooden pit was filled with play sand. The object to be imaged was buried in the sand. As the transmitter and the receiver, two identical, coax-fed rectangular waveguide antennas whose aperture dimensions are 3.81 and 1.91 cm were used. The data were collected via an HP8753C network analyzer and then recorded on a computer. The real part of the dielectric constant of the sand is measured to be around 2.26 between 5 and 6 GHz [11] based on the measured phase-delay difference in sand and in air. Therefore, the dielectric constant of ground medium is in fact low as we assumed in our imaging algorithm. To test the effectiveness of our imaging method, two different dielectric objects were buried in the sand. We have previously reported on the simulated and measurement results for metallic targets in [11]. The algorithm produced successful images for these strong scattering targets. Here, we focus on the more challenging dielectric targets, including a bottled water target and a plastic target. Next, we present and discuss the results obtained from these dielectric objects.

3.1. Bottled Water

An object made of two bottles filled with water and taped together was used for this experiment [see Fig. 2(a)]. The size of the composite target was 27 × 30 × 12 cm. The target was placed at 38-cm below the sand surface. The transmitter (assumed to be located at the origin) and the receiver antennas were placed on top of the sand surface and pointed downward such that they were tilted at about 45° from the vertical axis (see Fig. 1). The center of the receiving grid was 1-m away from the transmitter antenna in the positive-x direction on the surface of the sand. S_{21} data were collected on a 10 × 10 2D spatial grid whose size is 52 cm (in the x' direction) and 14.69 cm (in the z' direction). The frequency was varied from 5.0609 to 5.9039 GHz for 25 evenly sampled points. Both the transmitter and the receiver were vertically polarized. Three-dimensional (25 × 10 × 10) frequency-spatial data were collected and stored on a computer. By applying our Fourier-based algorithm, we first obtained the image in the distance-angle domain, that is, in the (R, U, V) domain. Although the obtained image was 3D three 2D projected images onto the (R, U), (R, V), and (U, V) planes are shown in Figure 2(b) for display purposes.

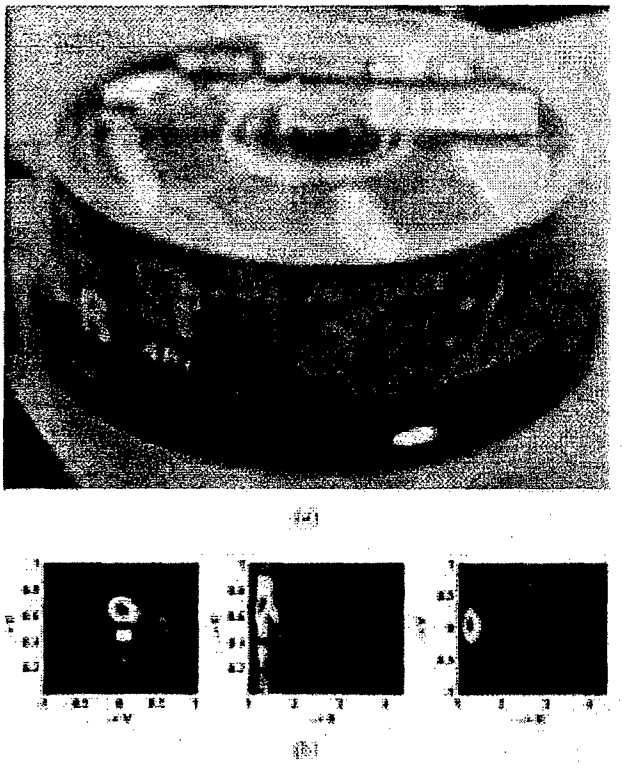

Figure 4 (a) Buried plastic target: a stack of 25 CDs; (b) 2D projected subsurface images for the buried plastic target in the (R, U, V) domain. [Color figure can be viewed in the online issue, which is available at www.interscience.wiley.com]

The dynamic range of the figures is selected as 12 dB. These image figures apparently display the key distinct spots corresponding to the dominant specular scattering from the water target. In fact, these particular spots correctly map the image location in (R, U, V) when the total travel distance and the associated angle information are calculated. To get the image in world coordinates, that is, in the (x, y, z) domain, we applied the coordinate transformation operation in (5). Then, a 3D image of the subsurface region was obtained. Figure 3(a) shows the 2D projected images in the (x, y, z) domain after applying the coordinate transformation. The dynamic range of the images is set at 12 dB. The outline of the buried bottled water is displayed in white for reference. In Figure 3(b), the resulting 3D GPR image is plotted using 2D slices in three orthogonal planes. The resultant images show that the location of the scattering mechanism on the buried object is well estimated by the proposed technique. Since the target actually consists of two bottles, the resultant image has significant spatial extent rather than being localized to a small spot.

3.2. Plastic Target

As expected, the bottled water is easily detected because its dielectric constant is very high (~81) relative to the background dry sand. On the other hand, low-dielectric-constant targets such as plastic mines are expected to be much more challenging to detect. In the experiment, a stack of plastic compact-disks (CDs) was buried 45-cm below the surface. The pack of 25 CDs, whose photograph is shown in Figure 4(a), constitutes a rigid plastic cylinder with a base diameter of 13 cm and a height of about 7 cm. Although the dielectric constant of the plastic CDs is not known

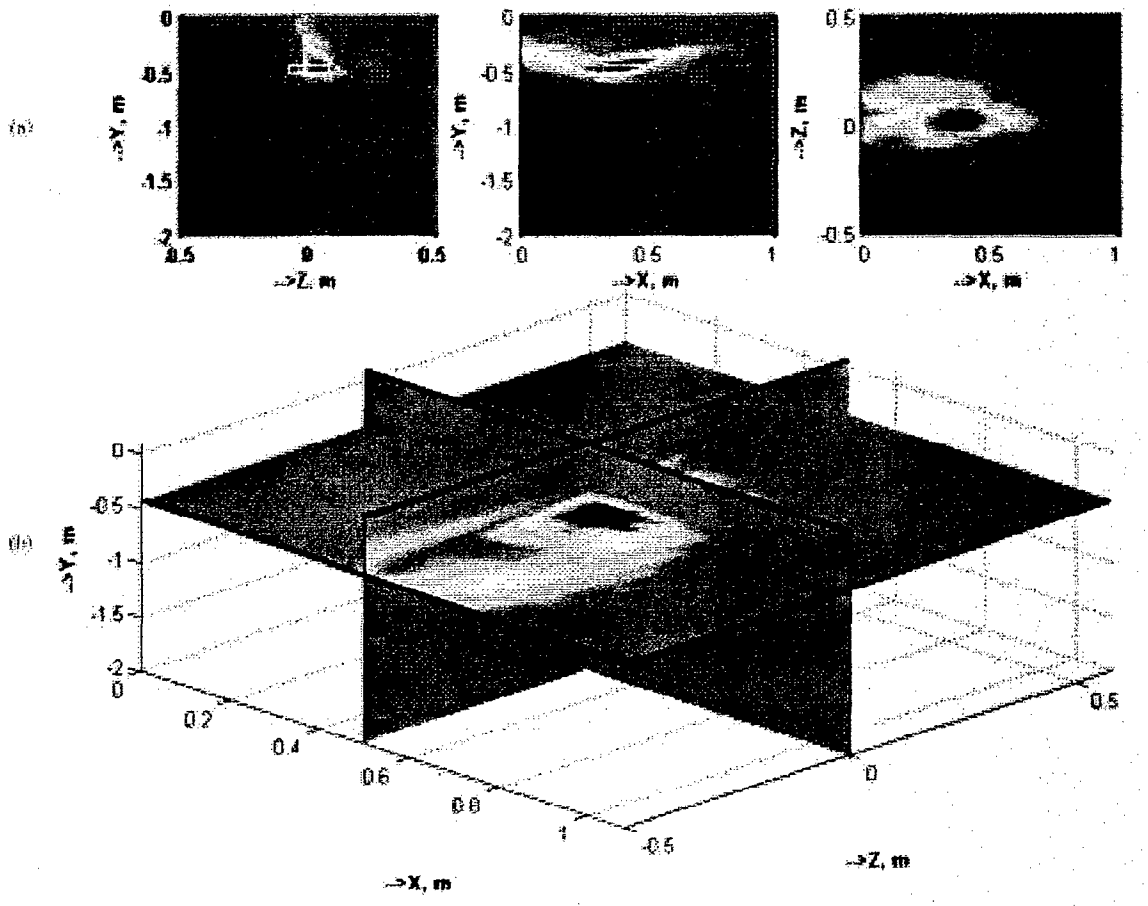

Figure 5 (a) 2D projected subsurface images for the buried plastic-CD target in the (x, y, z) domain; (b) sliced version of the 3D GPR image. [Color figure can be viewed in the online issue, which is available at www.interscience.wiley.com]

exactly, it is estimated to be between 2.9 to 4.4 from available polycarbonate data.

To measure the S_{21} parameter, the receiving grid was again placed 1-m away from the transmitter antenna. The size of the 10×10 spatial grid is 30.23 cm in the x direction and 14.69 cm in the z direction. At each grid point, the frequency was varied between 4.9335 and 6.00 GHz for 20 evenly sampled measured points. The antennas were vertically polarized for this experiment as well. By applying our proposed imaging algorithm, we first produced the image in the distance-angle domain, as plotted in Figure 4(b). Then, we obtained the 3D subsurface image of the scattering beneath the surface shown in Figure 5(a), after transforming the GPR image to the real image domain. The dynamic range of the figures is again set at 12 dB. The outline of the target is displayed in white. In Figure 5(b), a sliced version of the 3D GPR image is plotted. We observe that the present technique can successfully image this particular plastic target whose permittivity is not very different from the background permittivity. However, since the return from this dielectric target is much weaker than metallic and water targets, the SNR is lower, as compared to the previous results. Therefore, we obtain a lower contrast image compared to the previous image. In fact, the direct wave along the surface from the transmitter to the receiver falls within the dynamic range of the image. This shows up as a spot around $x = z = 0$ in the image.

CONCLUSION AND DISCUSSIONS

In this work, we have presented 3D GPR images for buried dielectric objects in dry sand. The algorithm in this work is based on the synthetic-aperture radar (SAR) concept. A measurement setup was built to examine the performance of the algorithm for dielectric objects. For this purpose, two different dielectrics, one with a high permittivity and another with low permittivity, were used in the experiments. Good 3D GPR images were obtained for both targets. Furthermore, it was shown that the image resolution in the cross-range dimensions could be made as good as that in the range dimension by properly controlling the collection aperture. Both high-contrast and low-contrast objects were adequately imaged by applying our imaging algorithm. This can be attributed to the fact that our coherent imaging algorithm uses many spatial points (100 in this work) to provide sufficient signal-to-noise ratio. Therefore, even when the dielectric constant of the target was close to that of the background medium and the return was significantly weaker than high-contrast targets, the target could still be observed in the resulting image, albeit at a lower SNR.

Although the imaging algorithm presented here is simple and fast, it is based on a number of simplifying assumptions, which may not be met in more general soil conditions or target geometries. First, the effect of air-soil boundary is neglected. In general, the air-soil boundary should be accounted for by using the proper Green's function [13]. Second, the present imaging algorithm was

derived based on the far-field, small-bandwidth, and small-aperture approximations. When these conditions are not completely met, further image distortion is unavoidable. For example, in our bottled-water experiment, we did notice that the image spot was slightly shifted from the midpoint of the target. Such an assumption may be circumvented by applying an interpolation technique [14]. Furthermore, in order to take advantage of the FFT for computational speed, the coordinate transformation given in (5) became necessary during image formation. As a result, a well-focused image spot in the original distance-angle domain becomes distorted after it is transformed into the spatial-image domain. A method to overcome this type of image degradation has been discussed in [12] and will be further investigated.

APPENDIX: TRANSFORMATION FROM DISTANCE-ANGLE DOMAIN TO IMAGE DOMAIN

Based on the geometry in Figure 1 where the transmitter is located at (0, 0, 0) and the receiver is placed at $(x_c, 0, 0)$, we start with the following to derive the transformation from (R, U, V) domain to (x, y, z) domain:

$$R = R_1 + R_2 = [x^2 + y^2 + z^2]^{1/2} + [(x_c - x)^2 + y^2 + z^2]^{1/2}, \tag{6a}$$

$$U = \sin\alpha = \frac{[(x_c - x)^2 + z^2]^{1/2}}{[(x_c - x)^2 + y^2 + z^2]^{1/2}}, \tag{6b}$$

$$V = \sin\alpha \cdot \sin\beta = \frac{[(x_c - x)^2 + z^2]^{1/2}}{[(x_c - x)^2 + y^2 + z^2]^{1/2}} \cdot \frac{z}{[(x_c - x)^2 + z^2]^{1/2}}$$

$$= \frac{z}{[(x_c - x)^2 + y^2 + z^2]^{1/2}}. \tag{6c}$$

One can reorganize (6a) to obtain the following:

$$[(x_c - x)^2 + y^2 + z^2 - x_c^2 + 2x_c x]^{1/2} = R - [(x_c - x)^2 + y^2 + z^2]^{1/2}. \tag{7}$$

Taking the square of both sides and deleting the identical terms on the both sides, we obtain

$$-x_c^2 + 2x_c x = R^2 - 2R \cdot [(x_c - x)^2 + y^2 + z^2]^{1/2}. \tag{8}$$

Then, substitute (6c) into (8) to obtain

$$2x_c x = R^2 + x_c^2 - \frac{2R \cdot z}{\sin\alpha \cdot \sin\beta}. \tag{9}$$

It is obvious from the geometry in Figure 1 that $z = (x_c - x) \cdot \tan\beta$. Inserting this into (9) and solving for x, we obtain

$$x = \frac{(R^2 + x_c^2)\sin\alpha \cdot \cos\beta - 2R \cdot x_c}{2(x_c \sin\alpha \cdot \cos\beta - R)}. \tag{10a}$$

Having resolved x, the other coordinate unknowns can easily be obtained from simple trigonometric relationships in Fig. 1 as

$$y = \frac{(x_c - x)}{\tan\alpha \cdot \cos\beta}, \tag{10b}$$

$$z = (x_c - x) \cdot \tan\beta. \tag{10c}$$

ACKNOWLEDGMENTS

This work is supported by the Scientific and Research Council of Turkey (TUBITAK) under project no. EEEAG-104E085, and in part by the Office of Naval Research under contract no. N00014-03-1-0021. The authors would also like to thank to Mr. Sungkyun Kim of the University of Texas for his help during the experiments.

REFERENCES

1. D.J. Daniels, Surface-penetrating radar, IEE Press, London, 1996.
2. T.P. Montoya and G.S. Smith, Land mine detection using a ground-penetrating radar based on resistively loaded vee dipoles, IEEE Trans Antennas Propagat 47 (1999), 1795–1806.
3. S. Nag and L. Peters, Jr., Radar images of penetrable targets generated from ramp profile functions, IEEE Trans Antennas Propagat 49 (2001), 32–40.
4. L. Carin, N. Geng, M. McClure, J. Sichina, and L. Nguyen, Ultra-wide-band synthetic-aperture radar for mine-field detection, IEEE Trans Antennas Propagat 41 (1999), 18–33.
5. J.I. Hafman, K.A. Shubert, and G.T. Ruck, SAR processing of ground-penetrating radar data for buried UXO detection: Results from a surface-based system, IEEE Trans Antennas Propagat 46 (1998), 1023–1027.
6. A. Sullivan, R. Damarla, N. Geng, Y. Dong, and L. Carin, Ultra wide-band synthetic aperture radar for detection of unexploded ordnance: modeling and measurements, IEEE Trans Antennas Propagat 48 (2000), 1306–1315.
7. S. Vitebskiy, L. Carin, M. Ressler, and F. Le, Ultrawide-band, short-pulse ground-penetrating radar: simulation and measurement, IEEE Trans Geosci Remote Sensing 35 (1997), 762–772.
8. R. Marklein, K. Balasubramanian, A. Qing, and K.J. Langenberg, Linear and nonlinear iterative scalar inversion of multi-frequency multi-bistatic experimental electromagnetic scattering data, Inverse Problems 17 (2001), 1597–1610.
9. A.J. Witten, J.E. Molyneux, and J.E. Nyquist, Ground penetrating radar tomography: algorithms and case studies, IEEE Trans Geosci Remote Sensing 32 (1994), 461–467.
10. T.B. Hansen and P.M. Johansen, Inversion scheme for ground penetrating radar that takes into account the planar air-soil interface, IEEE Trans Geosci Remote Sensing 38 (2000), 496–506.
11. C. Ozdemir, S. Lim, and H. Ling, A synthetic aperture algorithm for ground-penetrating radar imaging, Microwave Opt Technol Lett 42 (2004), 412–414.
12. C. Ozdemir and H. Ling, ACSAR: Antenna coupling synthetic aperture radar (ACSAR) imaging algorithm, J Electromag Waves Applic 13 (1999), 285–306.
13. W.C. Chew, Waves and fields in inhomogeneous media, IEEE Press, New York, 1999.
14. R. Pierri, A. Liseno, and F. Soldovieri, Shape reconstruction from PO multifrequency scattered fields via the singular value decomposition approach, IEEE Trans Antennas Propagat 49 (2001), 1333–1343.

Frontal imaging of human using three-element Doppler and direction-of-arrival radar

A. Lin and H. Ling

A two-dimensional Doppler and direction-of-arrival (DDOA) radar concept is proposed for the frontal imaging of humans. The system consists of a three-element receiver array configured to provide simultaneous DOA measurements in the azimuth and elevation planes. An experimental system has been built and tested. Two-dimensional frontal images of a human in free space as well as in a through-wall scenario are generated.

Introduction: Through-wall sensing of humans using radar is a topic of current interest for security, surveillance and search-and-rescue operations. Various aspects of human sensing have been investigated recently, including micro Doppler of humans [1–3] and position tracking and imaging using ultra-wideband systems [4, 5]. Ultra-wideband imagers utilise wideband pulses to gather range information and a one-dimensional aperture to resolve in azimuth. Consequently, the resulting imagery is a top-view of the target. While this type of imaging setup is useful for targets such as airplanes and ground vehicles, for human targets the frontal image may provide more information than the top-view. To acquire the frontal image, a two-dimensional collection aperture is required, leading to a significant increase in complexity.

In this Letter, we present a two-dimensional frontal imager by using only a three-element receiving array and a transmitter. The concept entails resolving the micro Doppler frequencies of the returned signals from a moving human, and then measuring the phase difference at each Doppler frequency component to determine the direction-of-arrival (DOA) of the various body parts. If each body part gives rise to a different Doppler frequency, then the resulting bearing map should correspond closely to a two-dimensional frontal view of the human. An experimental system operating at 2.4 GHz has been designed and constructed to test the concept. The system consists of a three-element receiving array configured to provide simultaneous DOA measurements in both the azimuth and elevation planes. Measurement results on a human subject are presented.

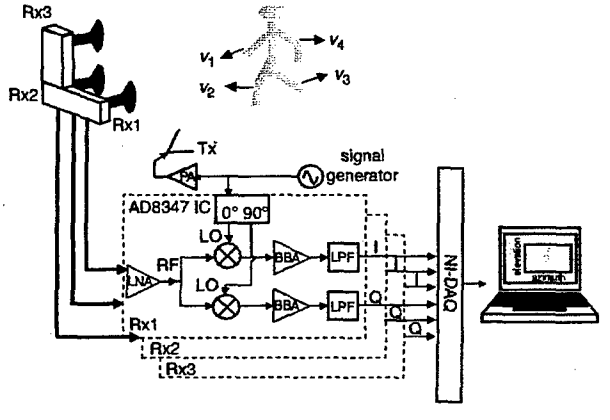

Fig. 1 *Radar system block diagram and conceptual operation*
Moving body parts (arms, legs) of a human produce different Doppler returns and are imaged by the radar

Radar concept: Fig. 1 shows the conceptual operation and the radar system block diagram. Different moving body parts of a human give rise to micro Doppler shifts with respect to the radar. Therefore, by first Doppler processing the data, we can extract the DOA information of the different Doppler frequency bins by measuring the phase difference among the receiver elements. Previously, we have reported on a one-dimensional bearing tracking system for multiple humans in the azimuth plane using a two-element Doppler and DOA radar [6]. The azimuth DOA of the received signals can be obtained from the measured phase difference between the two array outputs, $\Delta\phi = \phi_2 - \phi_1$, using the expression $\theta_{AZ} = \sin^{-1}(\lambda_c \Delta\phi / 2\pi d)$, where d is the spacing between the two antennas. In this work, an additional receiving antenna (Rx3) is placed directly above Rx2. Since Rx2 and Rx3 are placed vertically apart, they form a new array pair to acquire the DOA in the elevation plane, θ_{EL}. By correlating the azimuth and elevation bearing information at each Doppler bin f_{Di}, a data matrix $[A(f_{Di}), \theta_{AZ}(f_{Di}), \theta_{EL}(f_{Di})]$ can be constructed, where $A(f_{Di})$ is the radar return strength at the Doppler bin f_{Di}. Provided that each body part gives rise to a different Doppler frequency, the resulting $[A, \theta_{AZ}, \theta_{EL}]$ corresponds to an approximate two-dimensional frontal image of the human.

Radar design: The radar consists of a continuous-wave transmitter operating at a frequency of 2.4 GHz and three receiver elements. Three off-the-shelf quadrature receiver boards from Analog Devices (AD8347 IC) are used. The receiving antennas consist of three microstrip patches fabricated on 1.6 mm FR-4 substrate. The antennas are separated by $\lambda_c/2$, where $\lambda_c = 6.25$ cm, to provide the maximum resolution within the range −90° to 90° while avoiding any DOA ambiguity. After downconversion, the received signals are digitised by an NI-DAQ 6024E system. Since human movements produce time-varying Doppler shifts, the digitised signals are processed using a short-time Fourier transform (STFT) for Doppler separation before the DOA calculations are carried out. An integration time of 0.5 s and a Kaiser window with $\beta = 10$ are used in the STFT.

Results: We first use three loudspeakers as stable calibration targets to validate the system. The approximate (azimuth, elevation) co-ordinates of the three loudspeakers are (−15°, 5°), (−5°, 25°) and (5°, 5°) with respect to the radar receivers. The loudspeakers are driven by audio tones of 20, 30 and 66 Hz, respectively. Fig. 2*a* shows the measured azimuth DOA against time. The azimuth DOA of the three loudspeakers are found to be at the expected positions of −15°, −5° and 5°. Fig. 2*b* shows the elevation DOA against time, which correspond to the expected elevations of 5° and 25°. After correlating the azimuth and elevation measurements at each of their Doppler bins, a two-dimensional location mapping of the three loudspeakers can be constructed accordingly (Fig. 2*c*), which agrees well with the actual placement of the loudspeakers (Fig. 2*d*).

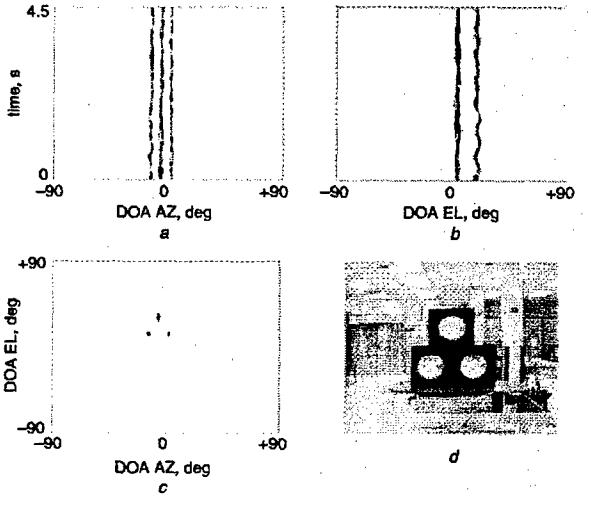

Fig. 2 *Measured data from three loudspeakers driven at three different audio tones*
a Azimuth DOA against time
b Elevation DOA against time
c Resulting frontal image
d Photo of actual loudspeaker placement

Next we use the same setup on a human subject. The subject stands at 2 m from the radar boresight. The height of the subject is approximately 1.8 m. During the measurement period the subject remains at the 2 m distance while moving each body part sequentially. After correlating the azimuth and elevation DOA measurements based on their Doppler information, a two-dimensional or frontal view of the human is

constructed (Fig. 3*a*). The measured frontal view shows the position of each limb, making an outline of the subject. The dynamic range of the image is 40 dB. The measurement is then repeated *in situ* with a 5-inch-thick gypsum/wooden wall in an interior room. The subject stands at approximately 1 m behind the wall while the radar measures the return against time. Fig. 3*b* shows the measured through-wall view of the human. Compared with the free-space image shown in Fig. 3*a*, the through-wall image appears larger since the subject stands closer to the radar. The image also appears to be less focused owing to the significant attenuation from the wall. However, the outline of the human is still visible. The dynamic range of the image is 20 dB and the transmitted power used is −10 dBm.

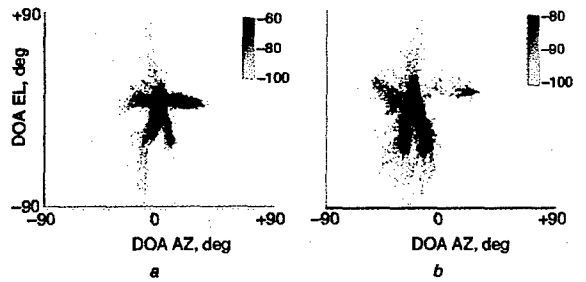

Fig. 3 *Measured frontal view of human in free space and of human through indoor wall*

a Measured frontal view of human in free space
b Measured frontal view of human through indoor wall

Conclusions: A very low complexity radar concept for generating the two-dimensional frontal image of a human is presented. The concept exploits the Doppler separation among the moving body parts, and derives their corresponding two-dimensional DOA using only a three-element receiver array. Measurements were performed using a low-cost, three-element receiver array operating at 2.4 GHz. By correlating the azimuth and elevation DOA measurements based on the Doppler information, the two-dimensional locations of the moving body parts were derived to construct a frontal view of a human in free space. The through-wall measurement result, showed some agreement with the free-space result, albeit at a much lower signal-to-noise ratio. It is worth pointing out that, while the proposed radar has very low complexity, it is based on the assumption that different body parts give rise to different Doppler frequencies. When this condition is not met in practice, the resulting bearing information is not accurate. Therefore, the present radar concept can be termed an 'imaging of opportunity' that captures glimpses of the human subject. This is similar to other types of target-motion induced sensing schemes such as inverse synthetic aperture radar.

Acknowledgments: This work is supported by the Office of Naval Research, the Texas Higher Education Coordinating Board under the Texas Advanced Technology Program and the National Science Foundation Major Research Instrumentation Program.

5 February 2006
Electronics Letters online no: 20060355
doi: 10.1049/el:20060355

A. Lin and H. Ling (*Department of Electrical and Computer Engineering, The University of Texas at Austin, Austin, TX 78712, USA*)

E-mail: adrian.lin@mail.utexas.edu

References

1 Geisheimer, J.L., Greneker, E.F., and Marshall, W.S.: 'High-resolution Doppler model of the human gait', *SPIE Proc., Radar Sensor Technology and Data Visualization*, 2002, **4744**, pp. 8–18
2 Chen, V.C., and Ling, H.: 'Time-frequency transforms for radar imaging and signal analysis' (Artech House, Norwood, MA, 2002), Chap. 8
3 Dorp, P., and Van Groen, F.C.A.: 'Human walking estimation with radar', *IEE Proc., Radar Sonar Navig.*, 2003, **150**, pp. 356–365
4 Hunt, A.R.: 'A wideband imaging radar for through-the-wall surveillance', *SPIE Proc., Sensors, and Command, Control, Communications, and Intelligence (C3I) Technologies*, 2004, **5403**, pp. 590–596
5 Tatoian, J.Z., Franceshetti, G., Lackner, H., and Gibbs, G.G.: 'Through-the-wall impulse SAR experiments'. IEEE Antennas Propagation Society Int. Symp. Dig., July 2005, paper S099p04u
6 Lin, A., and Ling, H.: 'Human tracking using a two-element antenna array', *SPIE Proc., Radar Sensor Technology and Data Visualization*, 2005, **5788**, pp. 57–64

Journal Paper [11]
To appear in *IEEE Trans. Aerospace Electronics Syst.*, July 2007

A Doppler and Direction-of-Arrival (DDOA) Radar for Multiple-Mover Sensing Based on a Two-Element Array

Adrian Lin and Hao Ling

Department of Electrical and Computer Engineering
The University of Texas at Austin
Austin, TX 78712

Abstract

A low-cost, two-element receiving array concept is investigated for detecting multiple moving targets in indoor surveillance applications. Conventional direction of arrival (DOA) detection requires the use of an antenna array with multiple elements. Here we investigate the use of only two elements in the receiver array. The concept entails resolving the Doppler frequencies of the returned signals from the moving targets, and then measuring the phase difference at each Doppler frequency component to calculate the DOA of the targets. Simulations are performed to demonstrate the concept and to asses the DOA errors for multiple movers. An experimental system is designed and constructed to test the concept. The system consists of a two-element receiver array operating at 2.4 GHz. Measurement results of human subjects in indoor environments are presented, including through-wall scenarios.

Keywords: Doppler, direction of arrival, radar, human tracking, through-wall

1 Introduction

The need for detecting moving targets (such as humans) and their locations is becoming one of the key necessities in security and surveillance systems, especially for law enforcement, counter-terrorism and urban warfare. Information such as the number of combatants and their locations can aid in decision making. Therefore, the capability of detecting multiple targets is an important feature in such systems. Recent work on radar detection of humans has focused mainly on the Doppler characteristics from a single human [1-5], or the ultra-wideband imaging of an entire scene [6-9].

Multiple target detection using a Doppler radar system has been explored in [10]. The system uses a superheterodyne receiver architecture operating at a 10.53 GHz carrier frequency to detect the velocity and acceleration of a rocket-driven flare. The Doppler returns are downconverted, digitized and processed using the short-time Fourier transform (STFT) [11, 12]. Multiple targets can then be detected as long as they move at different velocities, and their accelerations can be calculated by observing the rate of Doppler changes with respect to time as the result of the STFT process. The system, however, does not provide the bearing information of the targets.

In order to acquire the bearing information or the direction of arrival (DOA) of multiple targets, the standard approach is to use multiple receiving elements and to apply a direction finding algorithm such as MUSIC or ESPRIT [13, 14]. Such methods require the number of elements to be at least one greater than the maximum number of targets. That is, they require at least N + 1 elements to detect N targets. However, increasing the number of elements leads to an increase in the physical size, cost and complexity of the overall system.

In this paper, we explore the use of a low-cost, two-element receiving array for detecting multiple moving targets. The DOA of a mover is obtained from the phase difference of the reflected waves arriving at the two receiving antennas. However, a two-element receiving array is not able to resolve the DOA from multiple targets due to multiple wavefronts arriving simultaneously at the two receiving antennas. We exploit the fact that the different moving targets typically give rise to different Doppler shifts with respect to the radar. Therefore, by processing the data via Doppler discrimination, we can extract the DOA information by measuring the phase difference at each Doppler frequency component.

Numerical simulations are first conducted to test the concept. Detection of two movers is simulated to analyze factors influencing the DOA accuracy such as the Doppler separation between movers. A Monte Carlo simulation is then performed to predict the DOA error resulting from the reduced Doppler separation due to multiple movers. The confidence level of correctly detecting the DOA versus the number of movers is generated accordingly.

An experimental radar system is designed and constructed to test the concept. The system consists of a two-element antenna array, dual-quadrature integrated receivers (Analog Devices AD8347 ICs) and a transmitter operating at a frequency of 2.4 GHz. Since this IC is targeted for the consumer wireless market, it is extremely low cost. Microstrip antennas are used, resulting in a small form factor. The receiver uses a direct conversion architecture [15], eliminating the need of the second mixing process and filtering as in the superheterodyne architecture. The received signals are downconverted, digitized and processed for Doppler and DOA calculations. Measurement results of the

DOA from multiple targets are presented. The limitations of the proposed system resulting from DOA ambiguity of multiple moving targets are studied. The performance of the system under through-wall scenarios is also reported.

2 Basic Theory

To obtain the DOA information, consider a two-element receiver array as shown in Fig. 1(a). Assuming the far-field case, the incoming wave scattered off the target arrives at the two antennas with a path length difference x of:

$$x = d \sin\theta \tag{1}$$

where d is the spacing between the two antennas and θ is the DOA of the target. The measured phase difference $\Delta\psi$ of the two array outputs can be expressed in terms x by:

$$\Delta\psi = \frac{2\pi}{\lambda_c} x \tag{2}$$

where λ_c is the wavelength of the carrier frequency. Therefore, the DOA of the target can be obtained by:

$$\theta = \sin^{-1}\left(\frac{\Delta\psi}{2\pi d/\lambda_c}\right) \tag{3}$$

However, this scheme works when only one target is present. When multiple targets are present, the incoming signal at the two antennas is the summation of the scattered waves from all the targets. The individual phase information of each target is no longer available and therefore their corresponding DOA are not resolvable.

To obtain the DOA of multiple targets, we take advantage of the Doppler discrimination that is possible for moving targets. Referring to Fig. 1(b), consider the

signals arriving at the two receivers, $s_1(t)$ and $s_2(t)$. For the sake of simplicity, we assume that the scattered waves arriving at the receivers have the same strength. After the demodulation, the signals can be expressed as:

$$s_1(t) = e^{j\psi_1(t)} + e^{j\psi_2(t)} \tag{4}$$

$$s_2(t) = e^{j(\psi_1(t)+\Delta\psi_1)} + e^{j(\psi_2(t)+\Delta\psi_2)} \tag{5}$$

The phase term $\psi_n(t)$ of target n can be expressed as:

$$\psi_n(t) = -2\pi\left(\frac{2R_{0n}}{\lambda_c} - \frac{2v_n t}{\lambda_c}\right) \tag{6}$$

where R_{0n} and v_n are respectively the initial distance and the radial velocity of target n with respect to the radar. Similar to equation (2), the term $\Delta\psi_n$ is the phase delay due to the position of the antenna elements and the direction of the incident wavefront for target n.

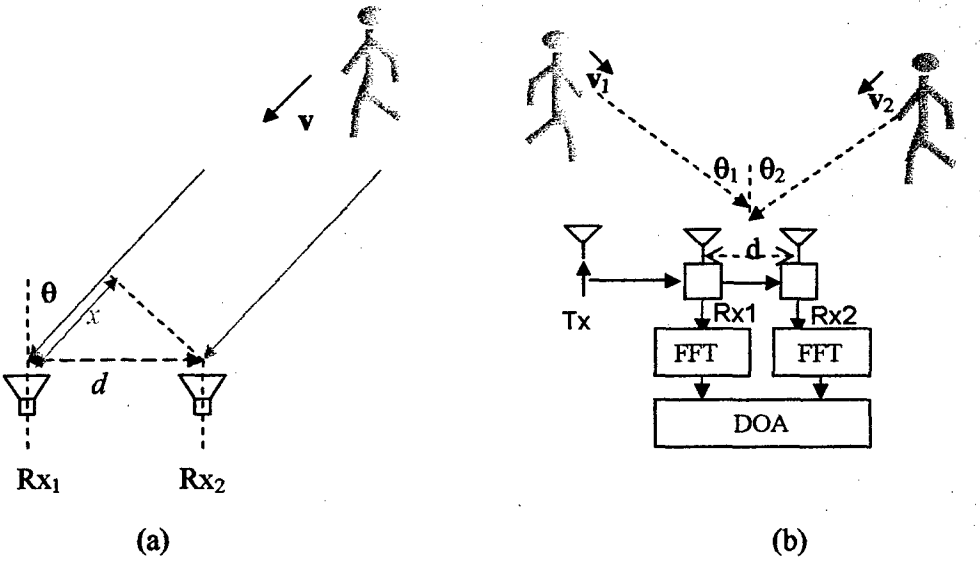

Figure 1. DOA detection using a two-element array: (a) Single target and (b) Multiple targets.

Next, we process each signal by the Fourier transform. By assuming infinite integration time and ignoring the constant term, the signals become:

$$S_1(f_D) = \delta(f_D - f_{D_1}) + \delta(f_D - f_{D_2}) \tag{7}$$

$$S_2(f_D) = \delta(f_D - f_{D_1})e^{\Delta\psi_1} + \delta(f_D - f_{D_2})e^{\Delta\psi_2} \tag{8}$$

where $f_{Dn} = 2v_n/\lambda_c$ is the Doppler frequency of target n. The phase difference $\Delta\psi_n$ at Doppler bin f_{Dn} for target n can be calculated as:

$$\Delta\psi_n(f_{Dn}) = \angle S_1(f_{Dn}) - \angle S_s(f_{Dn}) \tag{9}$$

If the targets generate different Doppler frequencies due to the difference in their radial velocities with respect to the radar, then the DOA of target n with respect to the receiver array boresight can be determined by:

$$\theta_n = \sin^{-1}\left(\frac{\angle S_1(f_{D_n}) - \angle S_2(f_{D_n})}{2\pi d/\lambda_c}\right) \tag{10}$$

which is similar to equation (3). It can be seen from equation (10) that this concept applies as long as the Doppler frequencies from different targets are sufficiently distinct.

3 Simulations

Two simulations are performed to test the concept. The first simulation is used to evaluate the DOA calculation result as the Doppler spacing between the two movers is reduced. The second simulation is used to assess the DOA error as the result of reduced Doppler spacing for more than two movers.

Fig. 2(a) shows the simulation result of the Doppler frequency versus DOA from two moving targets. The Doppler of the first target is 8 Hz with a DOA of -20° while the second target has 80 Hz Doppler and +20° DOA. An FFT integration time of 0.25 second and Kaiser windowing with $\beta = 1$ are used in the Doppler processing. Under this

Doppler spacing (8:80), the algorithm produces the correct DOA information for both targets. The Doppler of the first target is then increased to 76 Hz while its DOA is kept at -20°. With the reduced Doppler spacing (76:80), the DOA of the two targets become hard to identify and are erroneous (as shown in Fig. 2(b)). This is expected since the minimum resolvable Doppler separation is 4 Hz due to the 0.25 second integration time.

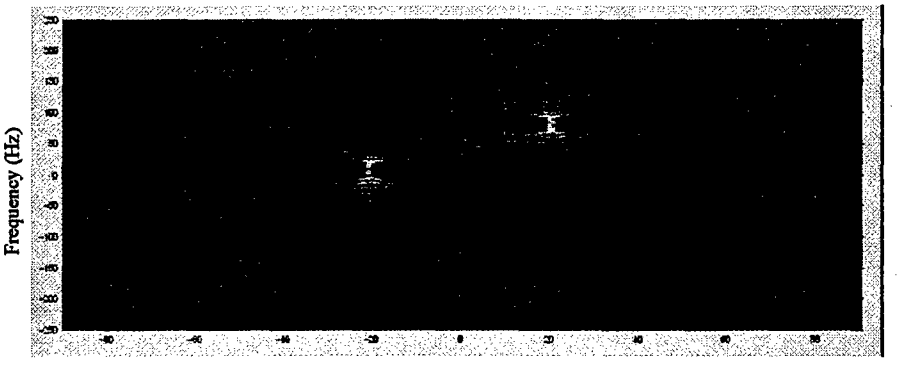

(a)

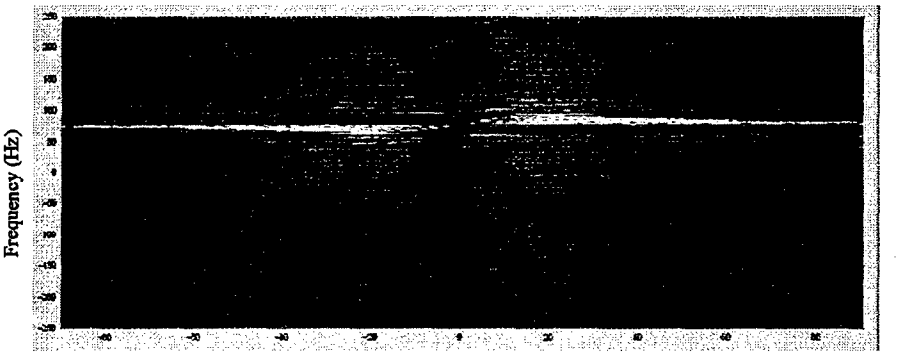

(b)

Figure 2. Simulations for two targets: (a) Doppler spacing 8:80 and (b) Doppler spacing 76:80

To predict the DOA error behavior as the result of reduced Doppler spacing for two or more movers, we run a more exhaustive Monte-Carlo simulation with more realistic

input parameters. The simulations input parameters include a spatial boundary of 10 m by 10 m, moving targets with speeds with uniform distributions from 0 m/s to 6 m/s, and a direction that is uniformly distributed from 0 to 2π. A carrier frequency of 2.4GHz is assumed. Two or more moving targets are placed inside the boundary with the selected velocities. These parameters are used to mimic people in a typical indoor environment. Amplitude decay as a function of $1/r^4$, where r is the distance of the target from the radar, is also accounted for in the simulation. The decay calculation is included to evaluate the effect of the received signal strengths of the two targets on the DOA calculation. Fig. 3(a) illustrates the simulation setup. The Monte Carlo simulations use the monostatic configuration where both the receiver and transmitter are co-located at the (0,0) coordinate. One hundred thousand realizations are generated. The DOA errors with respect to the Doppler separation of multiple moving targets are calculated. However, only the worst DOA error of all targets is recorded in each realization. The recorded DOA errors are then plotted at the end of all realizations.

Figs. 3(b)-(d) show the simulation results for multiple moving targets, for two, five and seven movers. The worst case DOA error is plotted versus the Doppler separation between the targets. For each Monte Carlo sample, the target with the worst DOA error is identified first. The minimum Doppler separation between that target and the others is obtained next. The DOA error of that target is then plotted versus the minimum Doppler separation. The different color shades indicate the relative signal strengths between the targets, with the redder colors representing more similar strengths and black representing a difference in strengths of more than 50 dB. As seen by the trend in Fig. 3(b), the DOA error generally gets larger when there is smaller Doppler separation between the two

targets, and vice versa. However, there are also cases that contain large DOA errors even though the Doppler separations are large. From the darker color results, we know that they correspond to cases where there is a significant difference in the signal strengths of the two targets (more than 50 dB). This corresponds to the case when one target is located much closer to the radar (thus a much larger reflected signal) than the other. This phenomenon is referred to as the close-far effect, where the side-lobe energy from the stronger, close-in target contaminates the phase of the much weaker signal from the far-away target in its frequency bin.

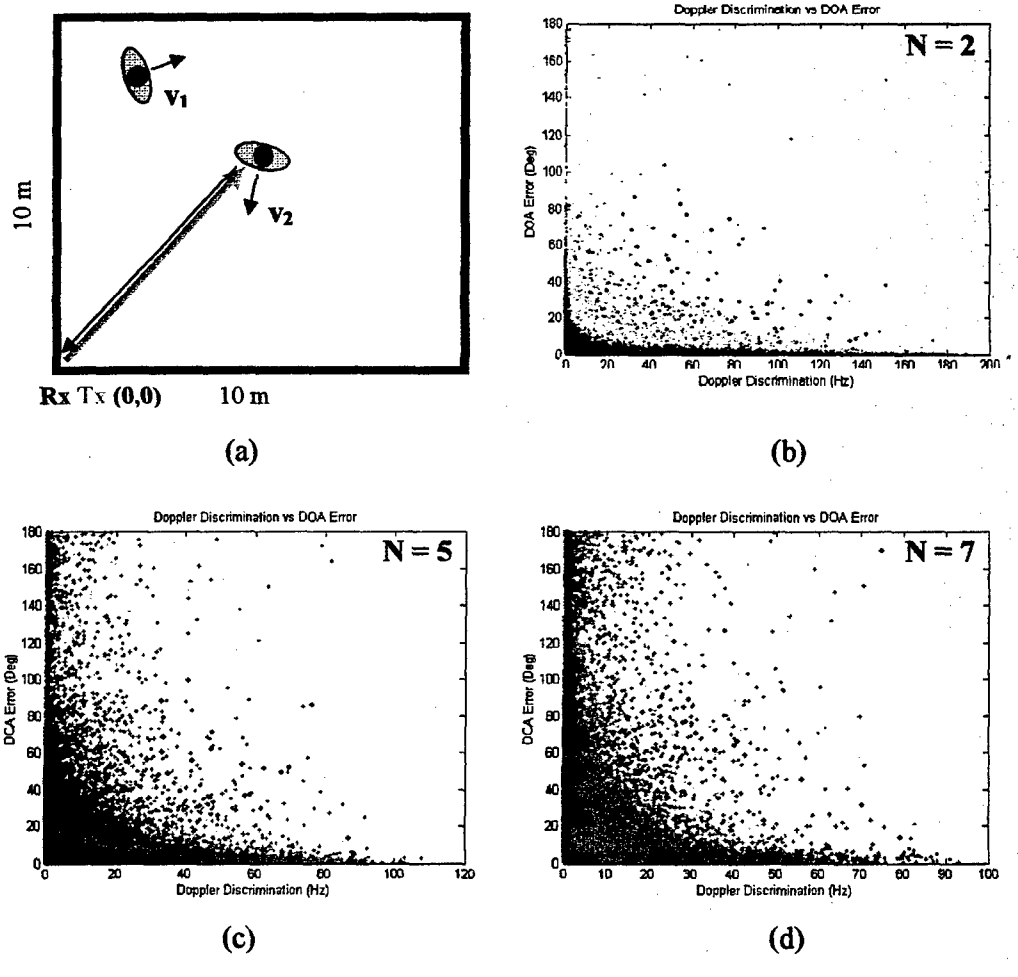

Figure 3. Monte Carlo simulations for N movers: (a) Setup and (b-d) Worst DOA errors vs. Doppler separation for N = 2,5 and 7, respectively.

As N increases, the DOA error increases, as observed in Figs. 3(c) and (d). At the end of the simulations, we count the number of successful DOA detections for a given number of movers. If the difference between the calculated and the expected DOA is less than 5° then the sample is considered a success. A profile of the percentages of successful DOA detections can be generated accordingly. As shown in Fig. 4, the percentage of successful cases decreases as the number of movers is increased. This is expected since a larger number of movers result in more occurrences of close Doppler spacing (similar velocities). From the simulation, it can be concluded that the DOA accuracy of the two-element system is affected by the number of movers. Nevertheless, a success rate of 70% can be maintained for four targets or fewer.

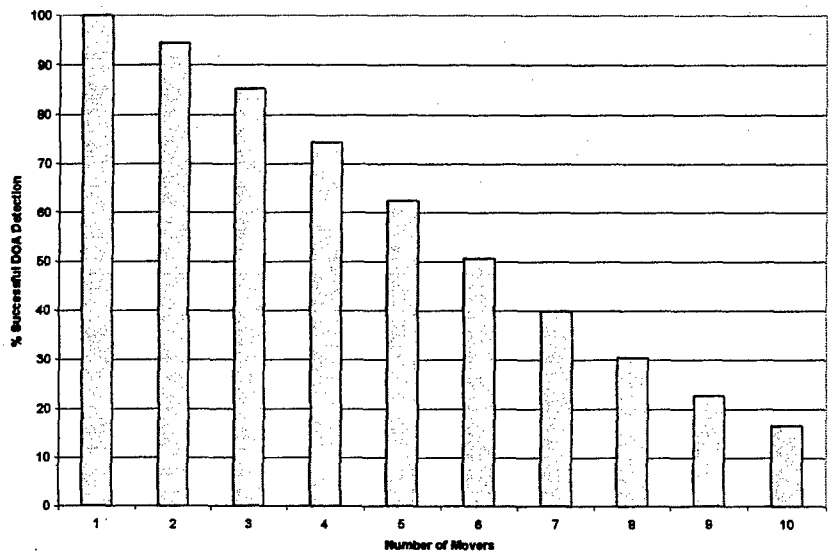

Figure 4. Successful DOA detection profile with 5° failure threshold.

The above simulation uses a point-scatterer model to study the system behavior as the number of movers is increased. In the actual case of human tracking, however, the Doppler spacing is further reduced by the overlapping micro-Doppler returns from the

body parts of each mover. Therefore, a more realistic model should be used to account for the micro-Doppler effects. In [16], we incorporated the micro-Doppler effects for human limbs in a similar simulation and found that the successful DOA detection rate is around 70% for *three* movers. This is more consistent with our observations on the actual measurement results.

It is also worthwhile to compare the performance of our two-element system to that of a multi-element array here. Our analysis has shown that the performance of the two-element system depends on the Doppler separation among multiple targets. The performance is worst when the targets have the same Doppler return, in which case the phase information from each target is not resolvable, leading to erroneous bearing determination. In a conventional multiple-element system, spatial beamforming can be utilized to obtain the locations of multiple targets. However, the bearing accuracy depends on the beamwidth of the array. Higher accuracy requires the use of a larger aperture (for narrower beamwidth) and correspondingly more array elements. Hence the implementation complexity and cost of such a system will be higher than that of the two-element system.

4 System Design and Implementation

An experimental radar system is designed and constructed to test the concept. Our radar receiver consists of a two-element direction-finding array, each with full quadrature detectors, to determine both the Doppler shift and the DOA of the target. The transmitter uses a continuous wave (CW) operating at 2.4 GHz carrier frequency. Two microstrip antennas are used as receiving antennas. The antennas are fabricated on a 1.6 mm thick FR-4 substrate with a dielectric constant of 4.3. Each patch is of dimensions 3 cm by 3

cm and follows the conventional half-wavelength microstrip antenna design [17]. The antennas are configured to receive the vertical polarization, since the human body is predominantly vertical (height is greater than width). The spacing between the feed points is 5 cm (slightly less than $\lambda_o/2$) to avoid DOA ambiguity while providing good sensitivity in the scanning range from -90° to 90°.

Two low-cost, off-the-shelf integrated boards manufactured by Analog Devices (AD8347) are used as the quadrature (or I/Q) receivers. Each receiver has the low-noise amplifier (LNA), I/Q mixers, gain control, and baseband amplifications all integrated on one chip. The chip allows a direct conversion from RF to baseband, eliminating the need for special analog filtering as in the superheterodyne conversion. Fig. 5 shows the radar system block diagram and the actual hardware implementation. Appendix A describes the range estimate of the system based on the radar equation. Appendix B discusses the procedure used to correct for the I/Q imbalance in the system.

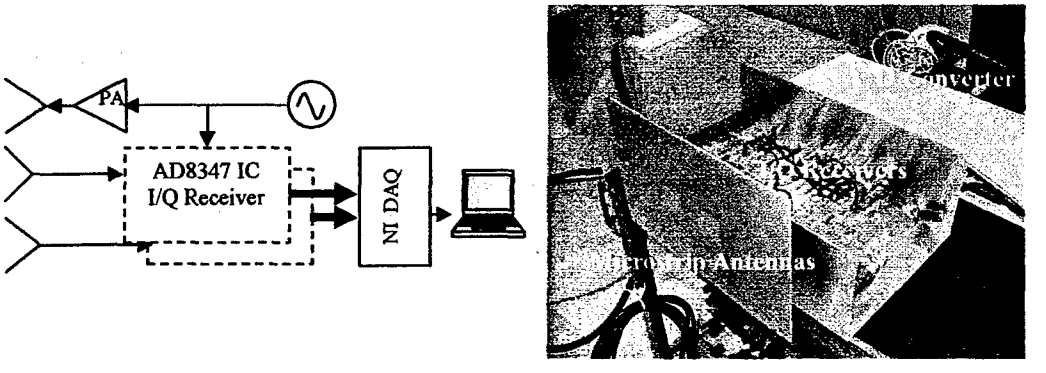

(a) (b)

Figure 5. Radar hardware: (a) System block diagram and (b) Hardware implementation

After being received and downconverted, the reflected signals from the moving targets are digitized by a 12-bit analog to digital converter (ADC) from National Instruments. The signals are sampled at a 500 Hz sampling rate, which is sufficient to sample humans movement data at 2.4 GHz. The sampled data are then logged into a computer and further processed using Matlab software. The signal processing is performed on the time domain data using the FFT to obtain the Doppler spectrum for each channel. By comparing the phase difference between the two Doppler spectra at each Doppler bin, we can then generate the DOA information one Doppler frequency at a time using Eq. (10).

5 Measurements

A series of measurements are conducted using the radar hardware to validate the simulations. The first measurement series is performed using loudspeakers driven by audio tones. The loudspeakers are chosen as calibration targets since they produce very stable and repeatable results. The next measurement series is carried out with human subjects.

5.1 Loudspeakers Measurements

To demonstrate multiple target detection, two loudspeakers are used. The vibrating membrane of each loudspeaker is covered by aluminum tape to enhance its return. The back-and-forth vibration of the membrane results in a radar return that is frequency modulated. The two loudspeakers are placed at -25°and -15° to the radar boresight and driven by a 55 Hz and a 35 Hz audio tone, respectively. Both loudspeakers are located at

about 4.5 m away from the radar and separated by 0.6 m from each other (Fig. 6(a)). Their expected Doppler returns are +/- 55 Hz and +/- 35 Hz with the DOA of -25° and -15°, respectively. The two-sided nature of the Doppler is due to the frequency modulation. The measured data are plotted in Fig. 6(b) and clearly show the expected returns.

To investigate the effect of Doppler separation on the DOA accuracy, the 55 Hz audio tone is lowered in 1 Hz decrement approaching the 35 Hz tone. Since the length of the FFT integration time used in this measurement is 1 s, the corresponding minimum resolvable Doppler separation is 1 Hz. Therefore, the DOA calculation is expected to be accurate up to about 1 Hz. The measured data is plotted in Fig. 6(c) and clearly shows that the DOA accuracy is still maintained for a 1 Hz Doppler separation. Both audio tones are then set to 35 Hz. Fig. 6(d) shows the measured data with the incorrect DOA as the result of zero Doppler separation.

(a)

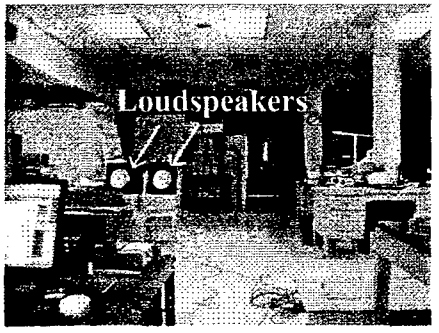

(b)

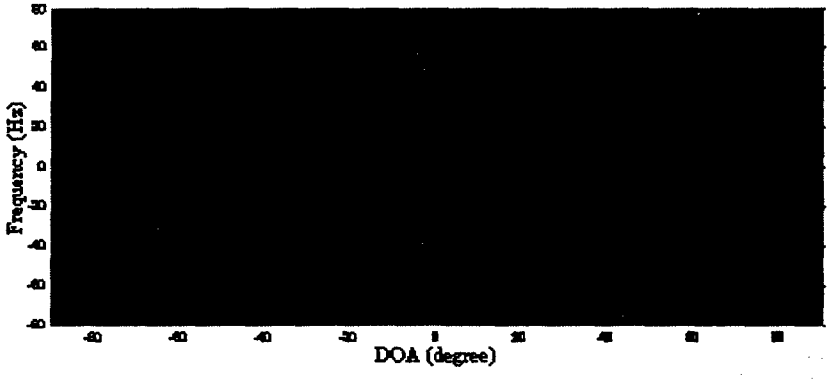

(c)

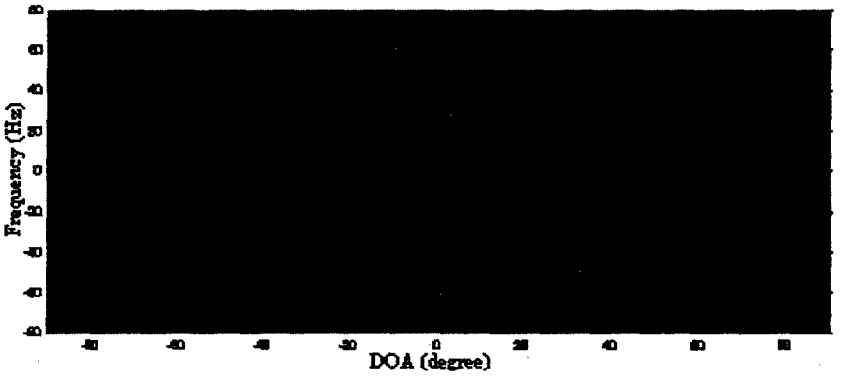

(d)

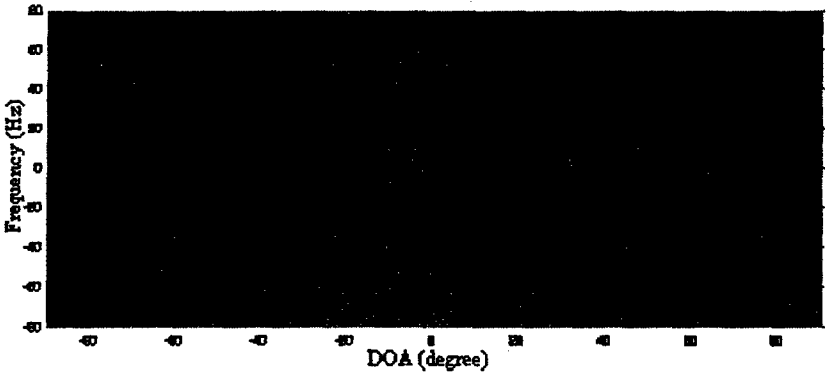

Figure 6. Two loudspeakers measurement: (a) Setup, (b) Doppler spacing (55:35), (c) Doppler spacing (36:35) and (d) Doppler spacing (35:35)

The next measurement involves three loudspeakers driven at different audio tones: 55, 75, and 35 Hz. The purpose is to demonstrate detection of more than two movers with using only a two-element array. They are placed at approximately -50°, -20° and +55° to the radar boresight at about 6.5, 10 and 2 m away from the radar (Fig 7(a)). Their expected Doppler returns are +/- 55 Hz, +/- 75 Hz and +/- 35 Hz with the DOA of -50°, -20° and +55°, respectively. The measured data are plotted in Fig. 7(b) and clearly show the expected returns. Also note from Fig. 7(a) that the environment is full of stationary clutter. However, they do not contaminate the DOA results due to the Doppler processing.

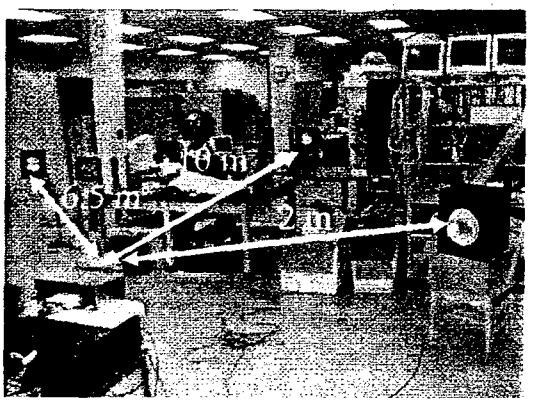

(a)

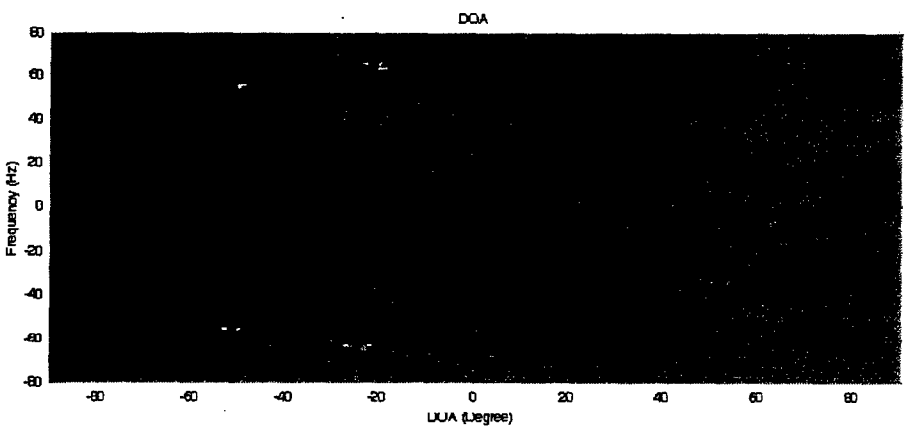

(b)

Figure 7. Three loudspeakers measurement: (a) Setup and (b) Measured Doppler and DOA.

It can be summarized from the loudspeaker measurements that the DOA accuracy can be maintained as long as there is sufficient Doppler separation. One of the factors influencing the Doppler separation is the integration time. Longer integration results in better Doppler resolution. However, long integration time might introduce other issues, especially for fast moving targets. This is similar to photography when shooting fast moving objects with a low shutter speed. In particular, Doppler returns from humans contain complex higher-order motions of body parts such as arms, legs, etc. The higher-order information is contained in the so-called micro Doppler returns [1-5]. The next set of measurements is taken on moving humans to analyze such phenomena affecting the DOA accuracy.

5.2 Human Measurements

Since radar returns from humans contain time-varying micro Doppler features, the measured data should be processed using the short-time Fourier Transform (STFT). The STFT is well-suited for analyzing a non-stationary signal. For a signal *s(t)*, its STFT is defined as:

$$STFT_s(t,f) = \int_{-\infty}^{+\infty} s(\tau)h(t-\tau)e^{-j2\pi f\tau}d\tau \qquad (11)$$

where *h(t)* is the sliding analysis window. Windowing the signal leads to a tradeoff in time resolution versus frequency resolution. Good time resolution requires a short duration sliding window, while good frequency resolution requires a long duration window. For the human measurements, we empirically determined that a good sliding

window duration to be around 1 second. The result of the STFT is then presented as a spectrogram, which is the squared modulus of its STFT.

Figure 8 shows the spectrogram of a human walking toward and away from the radar. As shown in the spectrogram, the micro Doppler modulation results in higher overall Doppler frequencies than the main body returns. For a 2.4 GHz carrier frequency the main body return of a human walking at 1.5 m/s produces a 24 Hz Doppler shift; however, the body parts produce much higher Doppler shifts up to one hundred Hertz.

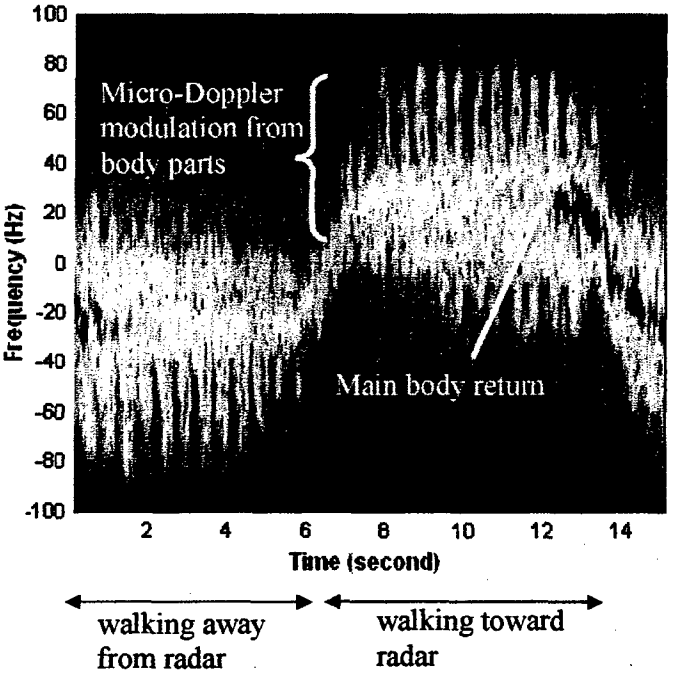

Figure 8. Spectrogram of a walking human.

If there are multiple humans walking simultaneously then there is a possibility that their micro Doppler returns will overlap with each other. The overlapping micro Doppler returns degrade the Doppler discrimination, which could lead to an increase in the DOA error.

Figure 9(a) shows the measurement setup for a walking human. The walking path starts at about 20° to the left of the radar. The subject walks in a straight path away from and then returns toward the radar. The turning point is approximately 10 m away from the radar. During the walk, the radar continuously measures and outputs the DOA of the subject (Fig. 9(b)). The different colors indicate the strengths of the returned signal, from red (strongest) to blue (weakest). As expected, as the subject walks farther away from the radar the return signals gets weaker as indicated by the color. The plot also shows that the signal fades out at approximately t = 4.5 second, when the subject stops and turns around toward the radar. When the subject stops the corresponding Doppler return falls into the zero Doppler bin and is filtered out by the software. Hence the signal appears to fade out the most during this time interval. The round-trip walking trajectory appears to be curved since it is plotted at the perspective or angular view of the radar.

The next measurement scenario involves a human walking from the right to the left of the radar as shown in Fig. 10(a). The starting position is approximately 40° to the right of the radar. As in the previous human measurement, the radar continuously collects and plots the DOA while the subject walks across the radar (Fig. 10(b)). As expected, the walking trajectory spans approximately ± 40° of the radar boresight. The DOA trace also shows detailed movements of the body parts as indicated by the arrows corresponding to the right and left feet of the subject. Through the time sequence, it is possible to identify that the subject's left foot reaches -20° at t = 2.5 s first. In the subsequent stride, the right foot reaches -40° at t = 4 s. Since the left foot is also closer toward the radar, its return is stronger than the right foot, as indicated by the arrow pointing to the redder color area on the plot.

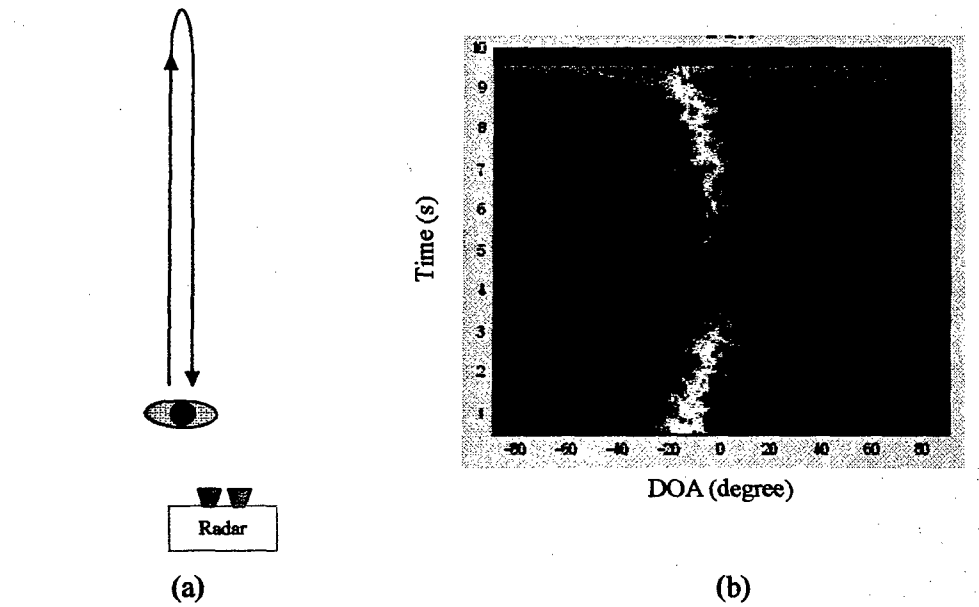

Figure 9. Measurement of a human walking away and towards the radar: (a) Setup and (b) DOA vs. time

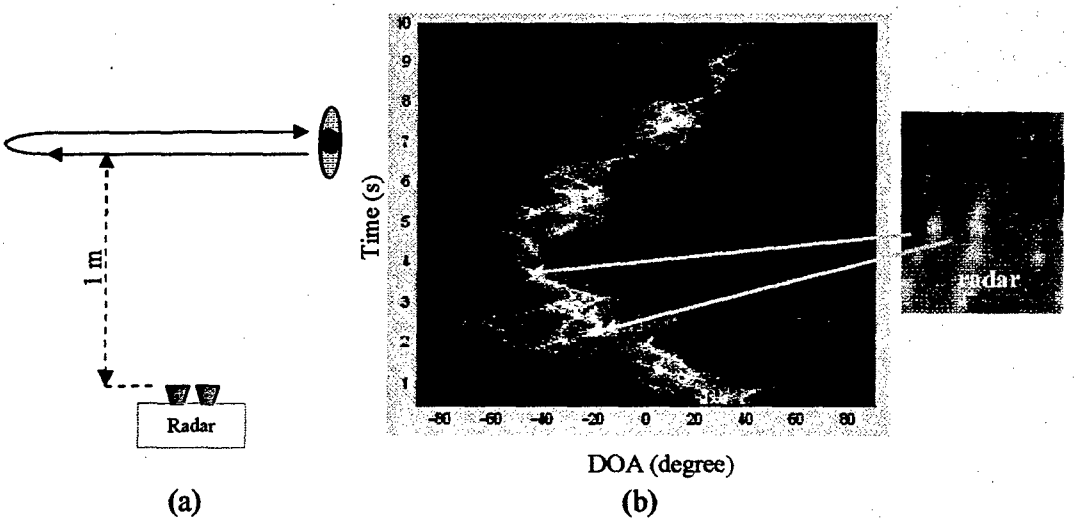

Figure 10. Measurement of a human walking across the radar: (a) Setup and (b) DOA vs. time

To demonstrate DOA detection of multiple targets, the next set of measurements involves multiple human subjects. Fig. 11(a) shows the setup for two humans walking at

the same speed but in opposite directions. As expected, the measured DOA vs. time plot (Fig. 11(b)) shows two traces corresponding to the angular positions of the two subjects as they walk during the data acquisition.

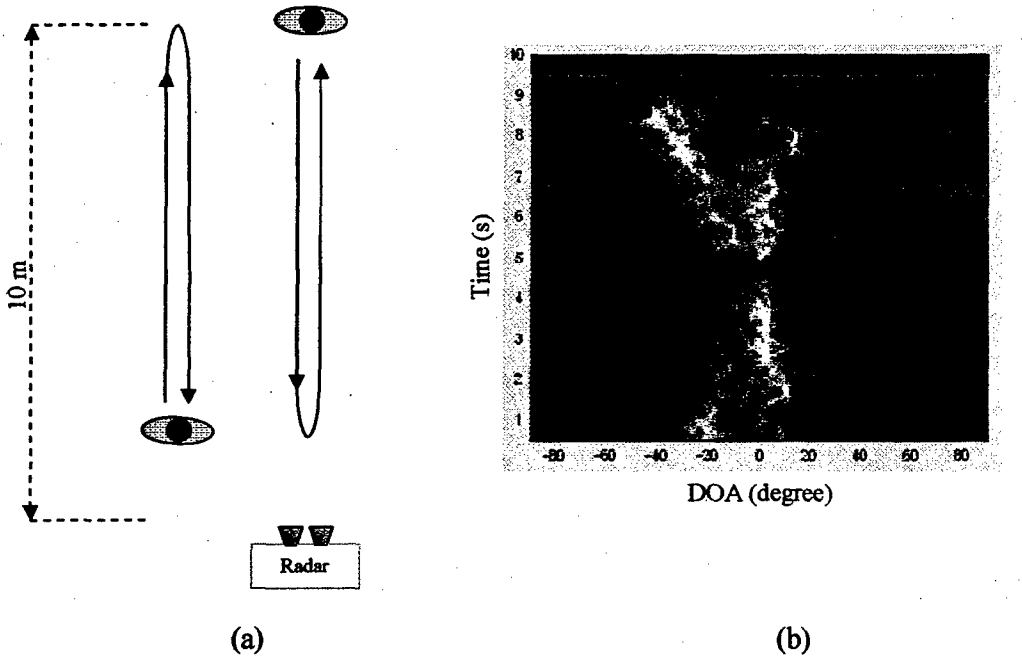

Figure 11. Measurement of two humans walking in opposite direction: (a) Setup and (b) DOA vs. time

In the next scenario, the two humans walk in the same direction, first away and then toward the radar (Fig. 12(a)). Since they move at about the same speed, their Doppler returns overlap significantly thus resulting in DOA error. As shown in Fig. 12(b), the overlapping instances appear as lines bridging across the two correct traces, as indicated by the arrow. This DOA behavior due to overlapping Doppler returns is similar to the earlier simulation result of Fig. 2(b). The system basically produces incorrect DOA under this condition. This is an intrinsic limitation of this radar, which we have addressed earlier in the simulation.

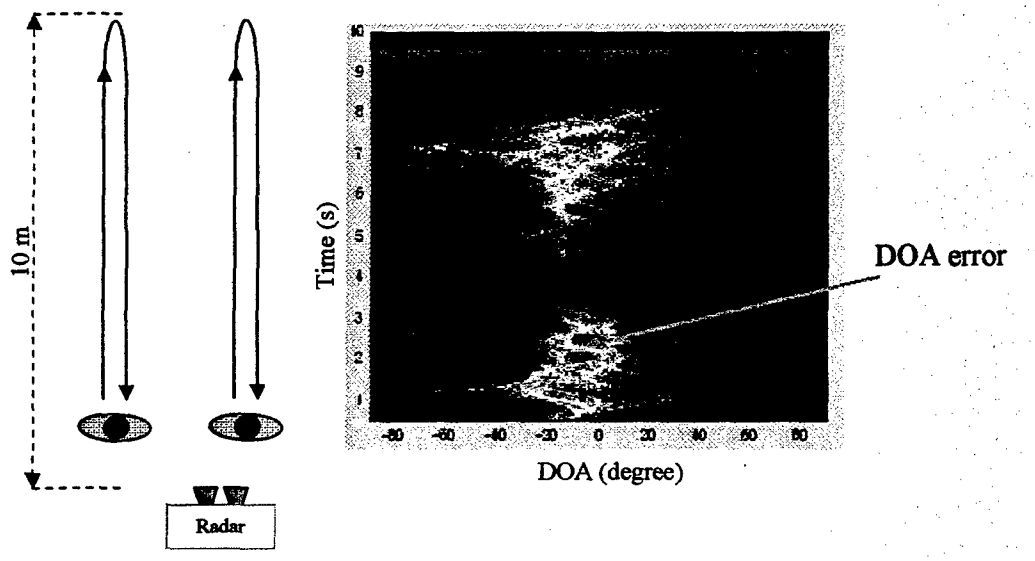

Figure 12. Measurement of two humans walking at the same speed: (a) Setup and (b) DOA vs. time

The last measurement set involves three human subjects. Two of the subjects walk at the same speed but in opposite directions while the third one walks sideways with respect to the radar boresight (Fig. 13(a)). The measured DOA vs. time plot (Fig. 13(b)) shows three traces corresponding to the angular positions of the three subjects as they walk during the data acquisition. Again, there are some instances where line features bridging across the three correct traces appear in the figure due to the overlapping Doppler returns. Such appearance is rather similar to the cross term effects in the Wigner-Ville distribution [11]. However, the radar is still capable of capturing three distinct targets over a large portion of the time intervals.

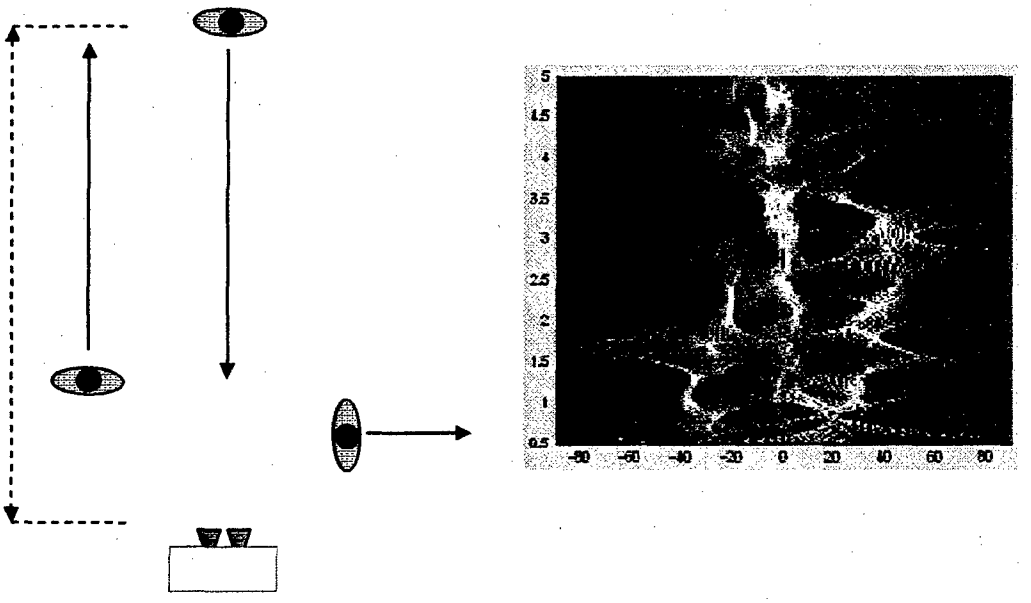

Figure 13. Measurement of three humans: (a) Setup and (b) DOA vs. time

6 Through-wall Measurements

Next, we evaluate the system performance in through-wall scenarios. Since a Doppler shift can only be induced by a moving target, Doppler sensing provides very good stationary clutter suppression. In through-wall scenarios, the returns from the wall itself fall into the DC bin and are filtered out while the Doppler frequency components are passed through, although attenuated. From [18], significant wall penetration is expected at 2.4 GHz compared to the higher frequencies.

Figure 14(a) shows the through-wall measurement setup where the radar is placed against a 15-inch exterior brick wall. Figure 14(b) shows the DOA vs. time of a human walking away and towards the radar on the opposite side with approximately a 10 m

maximum walking distance from the wall. In this scenario, the human walks in a straight path along the radar boresight. As expected, the corresponding trajectory is approximately straight at 0° DOA as shown in the measured data. We have also tested the through-wall performance using two loudspeakers placed at different locations off boresight (reported earlier in [19]). We found that the wall did not produce any noticeable effect on the DOA accuracy.

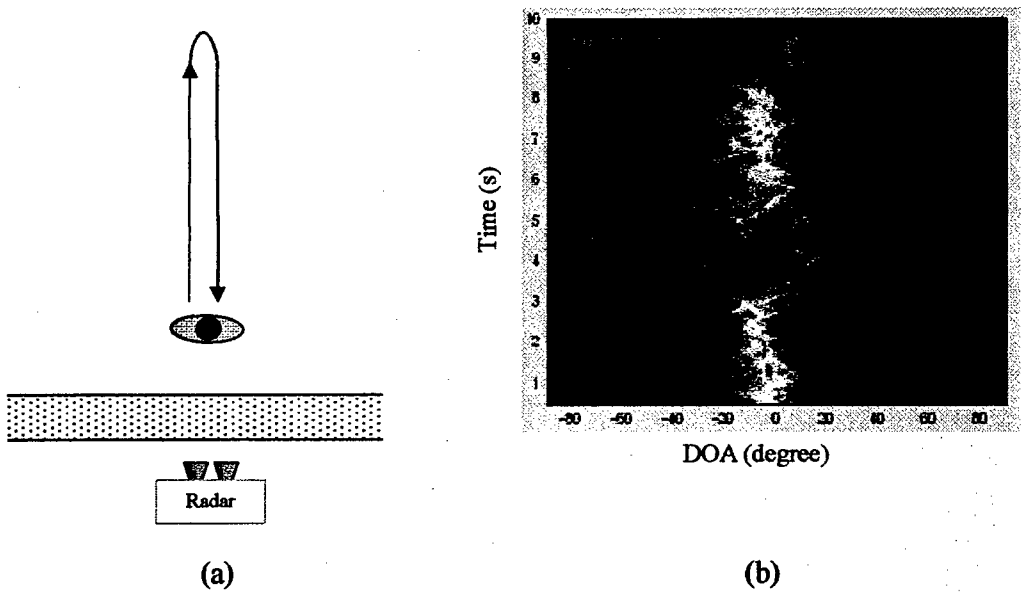

Figure 14. Through-wall measurement of a walking human: (a) Setup and (b) DOA vs. time

Measurements are also performed to evaluate the wall attenuation on the radar returns for different types of walls. A loudspeaker is used again as a test target, positioned at 4 m away from the radar boresight.

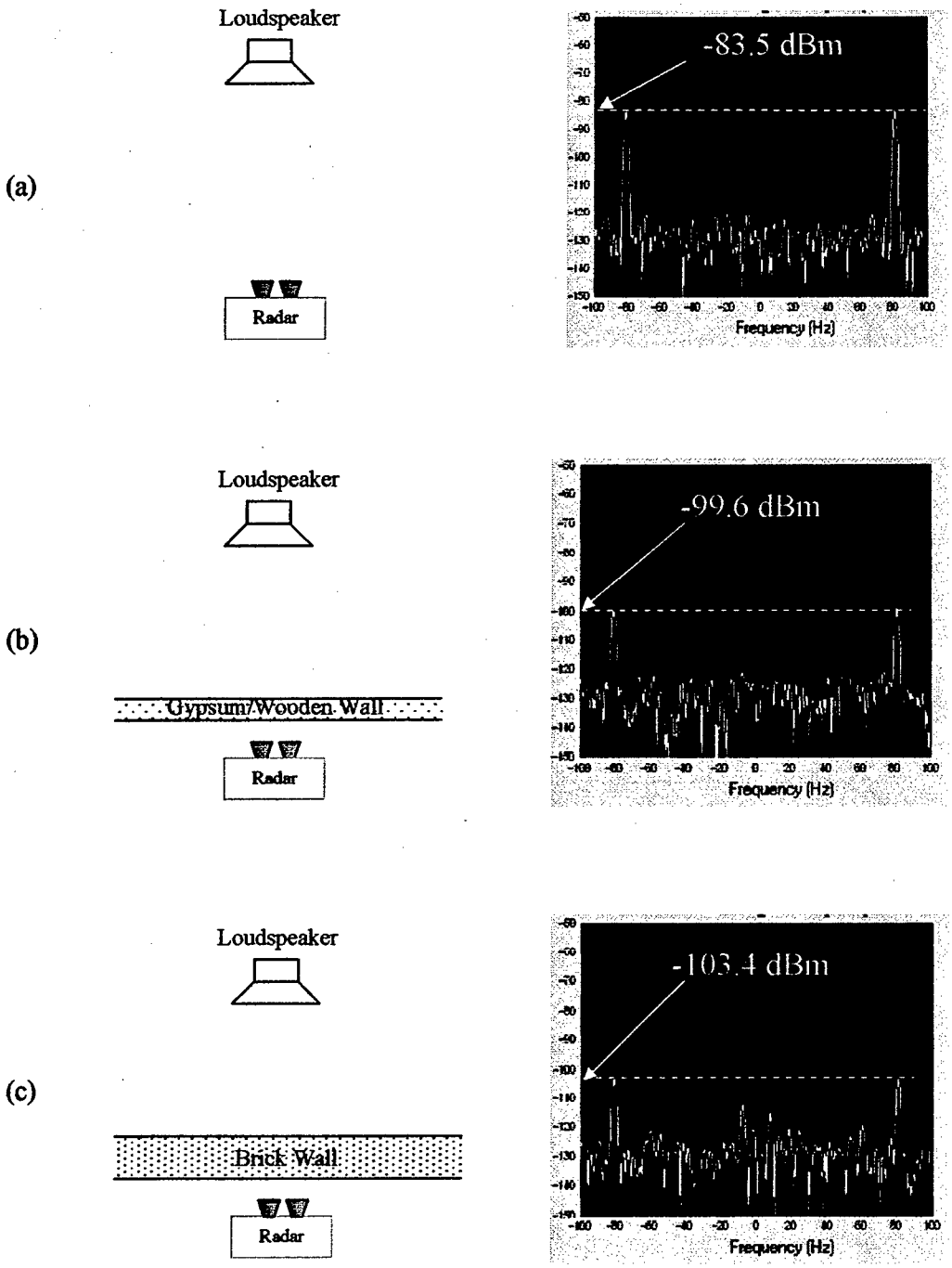

Figure 15. Wall attenuation measurements: (a) Free space, (b) 5" Gypsum/wooden wall and (c) 15" Brick wall

Three measurements are carried out: in free space (no wall), in-situ with a gypsum/wooden wall in an interior room, and in-situ with an exterior brick wall. As shown in Fig. 15, the processed radar returns are -83.5 dBm, -99.6 dBm and -103.4 dBm for the free space, the 5" gypsum/wooden wall and the 15" brick wall, respectively. Therefore, it can be concluded that the attenuations of the gypsum/wooden wall and brick wall are respectively 16 dB and 20 dB.

7 Conclusions

Simulation and measurement results of a Doppler and DOA radar for detecting multiple moving targets have been studied. The measurements were performed using a low-cost, two-element receiver array operating at 2.4 GHz. Based on the measurement results, it has been shown that simultaneous DOA detection of multiple movers using a two-element array is feasible. Our study also showed that the system could be used in indoor and through-wall scenarios due to the use of Doppler processing to suppress stationary clutters. Future work includes additional studies of through-wall scenarios. Extension of the concept to gather two-dimensional bearing and three-dimensional location information has also been investigated and reported in [21-24].

Acknowledgements

This work is supported by the Office of Naval Research, the Texas Higher Education Coordinating Board under the Texas Advanced Technology Program and the National Science Foundation Major Research Instrumentation Program. The authors thank S. Sundar Ram, Y. Yang and M. Starosta for their help in the data collection.

References

[1] J. L. Geisheimer, E. F. Greneker and W. S. Marshall, "High-resolution Doppler model of the human gait," *SPIE Proc., Radar Sensor Technology and Data Visualization*, vol. 4744, pp. 8-18, July 2002.

[2] V. C. Chen, "Analysis of radar micro-Doppler with time-frequency transform", *Proc. of the 10th IEEE Workshop on Statistical Signal and Array Processing*, pp. 463-366, Pocono Manor, PA, Aug. 2000.

[3] J. Li and H. Ling, "ISAR feature extraction from non-rigid body targets using adaptive chirplet signal representation," *IEE Proc. – Radar, Sonar and Navigation*, vol. 150, pp. 284-291, Aug. 2003.

[4] P. van Dorp and F. C. A. Groen, "Human walking estimation with radar," *IEE Proc. – Radar, Sonar and Navigation*, vol. 150, pp. 356-365, Oct. 2003.

[5] G. Greneker, "Very low cost stand-off suicide bomber detection system using human gait analysis to screen potential bomb carrying individuals," *SPIE Proc., Radar Sensor Technology and Data Visualization*, vol. 5788, p. 46-56, May 2005.

[6] A. M. Attiya, A. Bayram, A. Safaai-Jazi and S. M. Riad, "UWB applications for through-wall detection," *IEEE Antennas Propagat. Soc. Int. Symp. Digest*, vol. 3, pp. 1868-1875, Apr. 2000.

[7] S. Nag, H. Fluhler and M. Barnes, "Preliminary interferometric images of moving targets obtained using a time-modulated ultra-wideband through-wall penetration radar," *Proc. 2001 IEEE Radar Conf.*, pp. 64-69, May 2001.

[8] J. Z. Tatoian, G. Franceshetti, H. Lackner and G. G. Gibbs, "Through-the-wall impulse SAR experiments," *IEEE Antennas Propagat. Soc. Int. Symp. Digest,* paper no. S099p04u, July 2005.

[9] Y. Yang and A. E. Fathy, "See-through-wall imaging using ultra wideband short-pulse radar system," *IEEE Antennas Propagat. Soc. Int. Symp. Digest,* vol. 3B, pp. 334-337, July 2005.

[10] C. P. Bodenstein, W. C. Venter, G. J. Kahl, "A Doppler radar for multiple targets," *IEEE Trans. Instrumentation Measurement*, vol. 43, pp. 706-710, Oct.1994.

[11] S. Qian and D. Chen, *Introduction to Joint Time-Frequency Analysis – Methods and Applications*, Prentice Hall, Englewood Cliffs, NJ, 1996.

[12] V. Chen and H. Ling, *Time-Frequency Transforms for Radar Imaging and Signal Analysis*, Artech House, Norwood, MA, 2002.

[13] R. Schmidt, "Multiple emitter location and signal parameter estimation," *IEEE Trans. Antennas Propagation*, vol. 34, pp. 276-280, Mar. 1986.

[14] R. Roy, A. Paulraj and T. Kailath "ESPRIT – A subspace rotation approach to estimation of parameters of cissoids in noise," *IEEE Trans. Acoust., Speech, Signal Processing*, vol. ASSP-34, pp. 1340-1342, Oct.1986.

[15] B. Razavi, *RF Microelectronics*, Prentice-Hall, NJ, 1998.

[16] A. Lin, "A Low-complexity radar for human tracking," Ph.D. Dissertation, The University of Texas at Austin, May 2006.

[17] C. A. Balanis, *Antenna Theory*, John Wiley & Sons, 2nd Edition, 1997.

[18] T. B. Gibson and D. C. Jenn, "Prediction and measurement of wall insertion loss", *IEEE Trans. Antennas Propagation*, vol. 47, pp. 55-57, Jan. 1999.

[19] A. Lin and H. Ling, "Through-wall measurements of a Doppler and direction-of-arrival (DDOA) radar for tracking indoor movers," *IEEE Antennas Propagat. Soc. Int. Symp. Digest*, vol. 3B, pp. 322-325, July 2005.

[20] H. G. Park, C. Park, H. Oh and M. G. Kyeong, "RF gain/phase and I/Q imbalance error correction technique for multi-channel array antenna systems," *Proc. IEEE Vehicular Tech. Conf.*, vol. 1, pp. 175-179, May 2001.

[21] A. Lin and H. Ling, "Frontal imaging of human using a three-element Doppler and Direction-of-Arrival (DDOA) radar," *Electronics Letters*, vol. 42, pp. 660-661, May 2006.

[22] A. Lin and H. Ling, "Two-dimensional human tracking using a three-element Doppler and Direction-of-Arrival (DOA) radar," *Proc. 2006 IEEE Radar Conf.*, pp. 248-251, April 2006.

[23] A. Lin and H. Ling, "Location tracking of indoor movers using a two-frequency Doppler and Direction-of-Arrival (DDOA) radar," *IEEE Antennas Propagat. Soc. Int. Symp. Digest*, paper no. 1125, July 2006.

[24] A. Lin and H. Ling, "Three-dimensional tracking of humans using a very low-complexity radar," submitted for publication in *Electronics Letters*, May 2006.

Appendix A. Radar Range Estimate

The radar equation is used to estimate the maximum operating range of our radar:

$$R_{\max} = \left(\frac{P_T G_T G_R \lambda_c^2 \sigma}{(4\pi)^3 S_{NF} (S/N_{\min})} \right)^{1/4} \tag{12}$$

where

P_T = transmitter output power = -10.3 dBm
G_T = transmitter antenna (horn) gain = 7 dBi
G_R = receiver antenna (microstrip) gain = 1 dBi
λ_c = carrier frequency wavelength = 0.125 m
σ = human body radar cross-section = 0 dBsm
S_{NF} = system noise floor = -130 dBm
S/N_{min} = minimum signal-to-noise ratio = 10 dB

Using Eq. (12) with the parameters above, we estimate the maximum operating range of our radar for human detection in free-space to be 46.4 m. This free-space range estimate agrees fairly well with our outdoor measurements on human subjects. For the wall attenuations of 16 dB (gypsum/wooden wall) and 20 dB (brick wall), the estimated maximum operating ranges become 18.5 m and 14.7 m, respectively.

Appendix B. Correction for I/Q Imbalance

Since our radar uses the homodyne architecture, it is inherently sensitive to the hardware gain and phase errors of the in-phase and quadrature (I/Q) downconversion mixers [15]. The I/Q gain and phase errors introduce signals at the image frequencies of the actual downconverted signal, and may interfere with other target returns at those

frequencies. A correction algorithm is therefore needed to correct the I/Q gain and phase errors.

During the calibration, a known sinusoidal tone at a frequency of f_{dcal} above the carrier frequency f_c is injected at the RF input terminal. The signal level of the calibration tone is set to maximize the system dynamic range while avoiding input saturation. This level is typically 10 dB below the 1 dB input compression point of the system. After the calibration tone is downconverted, the actual I/Q gain and phase errors are measured at the frequency f_{dcal}.

The following equations are then used to represent the actual measured downconverted I and Q signals:

$$I = A(1+\varepsilon)\cos(\omega_{d_{cal}} t) \tag{13}$$

$$Q = A\sin(\omega_{d_{cal}} t + \psi) \tag{14}$$

where A is the signal amplitude, ε and ψ are the I/Q gain and phase errors respectively. The errors can then be corrected by the following equation [20]:

$$\begin{bmatrix} I_{corr} \\ Q_{corr} \end{bmatrix} = \begin{bmatrix} E & 0 \\ P & 1 \end{bmatrix} \begin{bmatrix} I \\ Q \end{bmatrix} \tag{15}$$

$$E = \frac{\cos\psi}{1+\varepsilon} \tag{16}$$

$$P = \frac{-\sin\psi}{1+\varepsilon} \tag{17}$$

The corrected I and Q signals then become:

$$I_{corr} = EI = A\cos(\omega_{d_{cal}} t)\cos\psi \tag{18}$$

$$Q_{corr} = PI + Q = A\sin(\omega_{d_{cal}} t)\cos\psi \tag{19}$$

As shown in Eqs. (18) and (19), the corrected I and Q signals are of equal amplitude and 90° of each other. Note that this algorithm works as long as the errors do not vary as a function of frequency. Since our radar has a very narrow bandwidth (250 Hz) and the errors are relatively stable throughout the bandwidth, the algorithm can therefore be employed. We typically use f_{dcal} of 40 Hz for the calibration.

Journal Paper [12]
Accepted for publication in *Electronics Lett.*

Three-Dimensional Tracking of Humans Using a Very Low-Complexity Radar

A. Lin and H. Ling

A low-complexity radar for human tracking in three-dimensional space is reported. The system consists of a three-element receiving array and two continuous wave (CW) frequencies configured to provide azimuth bearing, elevation bearing and range measurements. Doppler processing is used for clutter removal as well as to separate multiple moving targets. A radar prototype is constructed and tested. Three-dimensional tracking of multiple humans is performed in both unobstructed and through-wall scenarios.

Introduction: Human detection and tracking is a topic of interest in security and surveillance applications. A popular approach for through-the-wall imaging is to use ultra-wideband (UWB) [1-4], which offers high down-range resolution. To obtain cross-range location information, UWB radars use either a physical or synthetic aperture. High angular resolution is needed for the cross-range localization of targets at long distances, leading to the requirement of a large aperture. Furthermore, for human detection and tracking in an indoor setting, clutter suppression becomes challenging and requires complex signal filtering algorithms.

In this paper, we present a low-complexity radar architecture capable of tracking multiple humans in three dimensions. The concept entails using Doppler pre-processing to suppress stationary clutter as well as to distinguish multiple movers based on their different Doppler frequencies. A three-element receiver is then used to determine two-dimensional bearing information for each target. The phase difference measurement from the horizontal two-element array is used to obtain the azimuth direction of arrival (DOA), while that from the vertical two-element array is used for the elevation DOA. In addition, the phase difference measured at two CW frequencies is used for target ranging. Therefore, the entire receiver system comprises only three antenna elements and four receiver modules. A radar prototype is designed and constructed to test the concept. Measurement results on human subjects are presented.

Radar Concept and Design: Fig. 1(a) shows the radar system block diagram. Earlier, we reported on the one- and two-dimensional DOA tracking of multiple movers using a single CW frequency [5, 6]. Here our system operates at two CW frequencies fc_1 (2.4 GHz) and fc_2 (2.39 GHz). The two CW frequencies are combined, amplified and transmitted simultaneously. The scattered wave off a target is received by three antennas connected to the radar receivers. The local oscillator (LO) frequency of receivers Rx_1, Rx_2, and Rx_3 is set to fc_1, and that of Rx_4 is set to fc_2. The down-converted signal for each

receiver is low-pass filtered and digitized, and the time-varying Doppler spectrum of the targets is obtained by applying the short-time Fourier transform (STFT). To determine the DOA and the range, we compare the phase differences between the receiver outputs at each Doppler frequency component. The elevation and azimuth DOA are found, respectively, by the formulas $\theta_{EL} = \sin^{-1}(\lambda_{c1}\Delta\phi_{32}(f_D)/2\pi d)$ and $\theta_{AZ} = \sin^{-1}(\lambda_{c1}\Delta\phi_{21}(f_D)/2\pi d\cos\theta_{EL})$, where λ_{c1} is the wavelength of fc_1, $\Delta\phi_{mn}(f_D)$ is the phase difference between the two array outputs m and n at the Doppler frequency f_D, and d is the spacing between the two horizontal or vertical antennas. The received signal at Rx_3 is also routed into Rx_4, but mixed with LO2 at fc_2. The phase difference, $\Delta\phi_{43}$, is then measured to calculate the target range, R, using the following expression: $R = c\Delta\phi_{43}(f_D)/4\pi\Delta f$, where $\Delta f = fc_1 - fc_2$ and c is the speed of light. Since the phase difference $\Delta\phi_{43}$ is modulo 2π, it follows that the maximum unambiguous range is 15 m. By correlating the range and DOA information at each Doppler bin f_D, a data matrix $[A(f_D), \theta_{AZ}(f_D), \theta_{EL}(f_D), R(f_D)]$ can be constructed, where $A(f_D)$ is the radar return strength at the Doppler bin f_D. This resulting map shows the three-dimensional locations and strengths of the targets, provided that the targets have different Doppler frequencies. Fig. 1(b) shows the photo of the radar receivers. The three antennas are microstrip patches with 5 cm spacing between each horizontal and vertical pair. Four off-the-shelf integrated quadrature receivers are

used. A window size of 0.5 s is used in the STFT.

Results: The radar is first tested using loudspeakers driven by audio amplifiers at different monotones. Fig. 2(a) shows the measurement setup and the loudspeakers locations. The first loudspeaker is located at the approximate (θ_{AZ}, θ_{EL}, R) coordinate of (-40°, -5°, 3 m) and driven by a 35 Hz audio tone. The second loudspeaker is positioned at approximately (20°, 15°, 6 m) and driven by a 55 Hz audio tone. Figs. 2(b)-2(d) show, respectively, the measured azimuth DOA, the elevation DOA and the range plotted vs. Doppler frequency. Excellent agreement with the expected locations of the targets in bearing and range is observed. Further, it is seen that the Doppler discrimination allows us to determine the three-dimensional locations of two (or more) targets.

Three-dimensional tracking of two human subjects is shown next. Two human subjects walk back-and-forth along straight paths at approximately the same speed but in opposite directions (Fig. 3(a)). During the walk, the radar continuously measures and outputs the azimuth bearing, the elevation bearing and the range of the subjects (Figs. 3(b-d)). During the first four seconds of the measurement, Fig. 3(b) shows two distinct azimuth-bearing trajectories: the first one progressing from approximately -20° toward -60°, and the second one from 20° to 15°. The elevation tracks of the two human subjects are

shown in Fig. 3(c); however, the tracks are not distinguishable since the subjects walk on the same elevation plane (at ground level). Fig. 3(d) shows the measured range tracks, which crisscross as the subjects walk back-and-forth. By using the spherical-to-Cartesian transformation, the corresponding front view and top view maps are constructed and shown in Figs. 3(e) and (f), respectively. The top view in Fig. 3(f) shows good agreement with the actual walking paths in Fig. 3(a).

A through-wall measurement is also conducted with the radar situated indoors next to an exterior wall while a human subject on the opposite side of the wall walks in a straight path away from and toward the radar. The starting position is approximately 4 m from the radar up to a maximum distance of 35 m (Fig. 4(a)). The wall construction is a 15"-thick double-brick with supporting internal wooden frames and insulation materials. Fig. 4(b) shows the range measurement of the subject during the walk. Since the maximum unambiguous range is 15 m, the measured range repeats whenever the subject walks past an integer multiple of 15 m of distance from the radar. During the first 17 seconds, the subject travels twice the 15 m distance plus the remaining 5 m, as evidenced by the three distinct range tracks during the time interval 0 to 5 seconds, 5 to 14 seconds, and 14 to 17 seconds. Thus, the radar is capable of measuring a

human subject at least up to 35 m away through this wall. The transmitter output power used is +11 dBm.

Conclusion: A low-complexity radar concept for tracking multiple humans in three-dimensional space (azimuth, elevation and range) has been presented. Measurements using a prototype consisting of three antenna elements and four integrated receivers operating at 2.4 and 2.39 GHz have been performed to validate the concept. The three-dimensional tracking of moving humans is realized by correlating the range, azimuth and elevation DOA measurements based on their Doppler information. The in-situ measurement result through a 15"-thick exterior brick wall showed tracking up to a distance of 35 m.

References

1 ATTIYA, A. M., BAYRAM, A., SAFAAI-JAZI, A. and RIAD, S.M, "UWB applications for through-wall detection," *IEEE Antennas Propagat. Soc. Int. Symp. Digest*, vol. 3, pp. 1868-1875, Apr. 2000.

2 HUNT, A. R., "A wideband imaging radar for through-the-wall surveillance," *SPIE Proc., Sensors, and Command, Control, Communications, and Intelligence (C3I) Technologies*, vol. 5403, pp. 590-596, Sep. 2004

3 TATOIAN, J. Z., FRANCESHETTI, G., LACKNER, H. and GIBBS, G. G., "Through-the-wall impulse SAR experiments," *IEEE Antennas Propagat. Soc. Int. Symp. Digest,* paper no. S099p04u , July 2005

4 YANG, Y. and FATHY, A. E., "See-through-wall imaging using ultra wideband short-pulse radar system," *IEEE Antennas Propagat. Soc. Int. Symp. Digest,* vol. 3B, pp. 334-337, July 2005.

5. LIN, A. and LING, H., "Human tracking using a two-element antenna array," SPIE Defense and Security Symposium, Radar Sensor Technology IX, vol. 5788, pp. 57-64, Orlando, FL, Apr. 2005.

6. LIN, A. and LING, H., "Two-dimensional human tracking using a three-element Doppler and direction-of-arrival (DDOA) radar," *Proc. IEEE Radar Conference*, paper no. 7152, Apr. 2006.

Acknowledgments: This work is supported by the Office of Naval Research, the Texas Higher Education Coordinating Board under the Texas Advanced Technology Program and the National Science Foundation Major Research Instrumentation Program.

Authors' affiliations:
A. Lin and H. Ling (Department of Electrical and Computer Engineering, The University of Texas at Austin, Austin, TX 78712, U.S.A.). E-mail: adrian.lin@mail.utexas.edu, ling@ece.utexas.edu

Figure captions:

Fig. 1. (a) Radar system block diagram. (b) Radar receiver prototype photo.

Fig. 2. Measured data from two loudspeakers driven at two different audio tones. (a) Photo of the actual loudspeaker placement. (b) Doppler versus azimuth DOA. (c) Doppler versus elevation DOA versus time. (c) Doppler versus range.

Fig. 3. Measurement results of two human subjects in an unobstructed indoor environment. (a) Walking patterns up to 10 m distance. (b) Azimuth DOA versus time. (c) Elevation DOA versus time. (d) Range versus time. (e). Cross-range versus elevation (front-view). (f) Cross-range versus down-range (top-view).

Fig 4. In-situ range measurement of a walking human through a 15"-thick exterior brick wall. (a) Setup. (b) Measured range track of up to 35 m.

Fig. 1

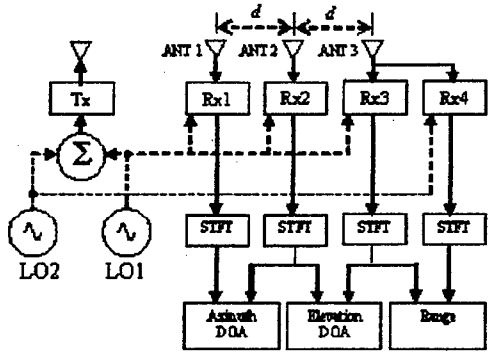
d
d
ANT 1
ANT 2
ANT 3
Tx
Rx1
Rx2
Rx3
Rx4
Σ
LO2
LO1
STFT
STFT
STFT
STFT
Azimuth DOA
Elevation DOA
Range

(a)

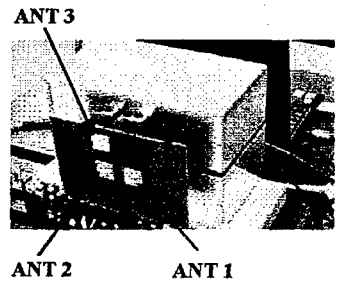
ANT 3
ANT 2
ANT 1

(b)

Fig. 2

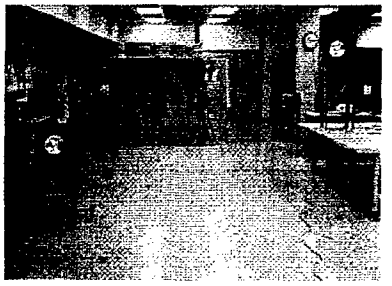

(a)

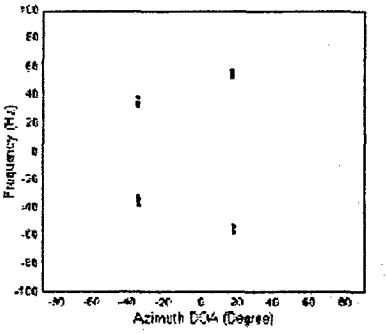
Frequency (Hz)
Azimuth DOA (Degree)

(b)

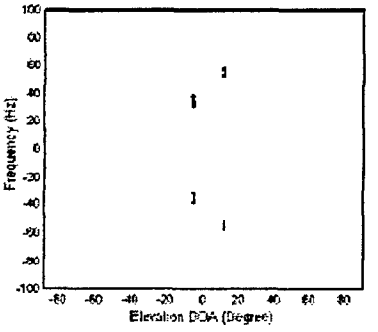
Frequency (Hz)
Elevation DOA (Degree)

(c)

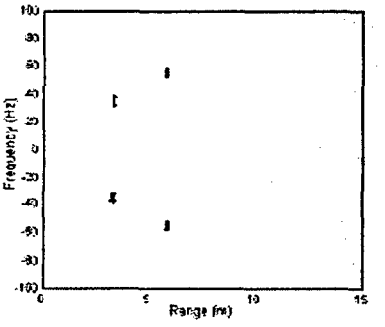
Frequency (Hz)
Range (m)

(d)

Fig. 3

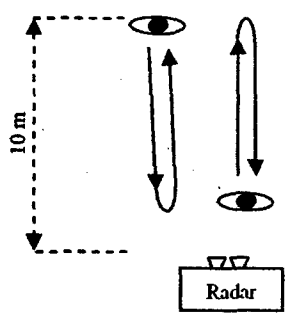
10 m
Radar

(a)

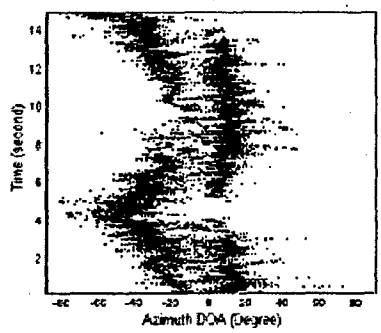
Time (second)
Azimuth DOA (Degree)

(b)

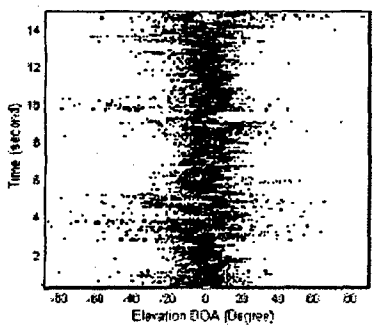
Time (second)
Elevation DOA (Degree)

(c)

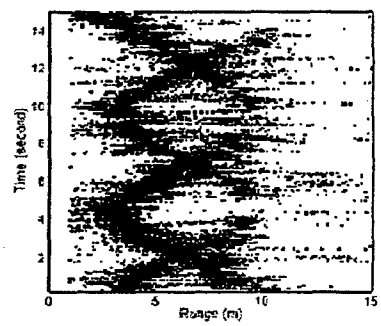
Time (second)
Range (m)

(d)

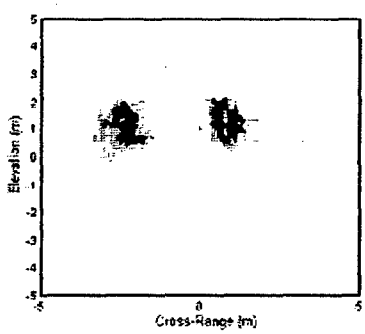
Elevation (m)
Cross-Range (m)

(e)

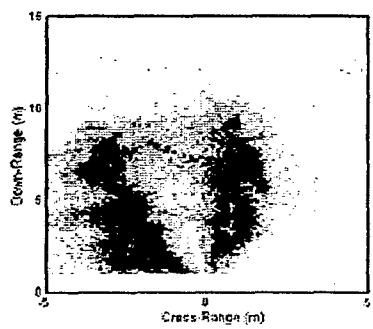
Down-Range (m)
Cross-Range (m)

(f)

Fig. 4

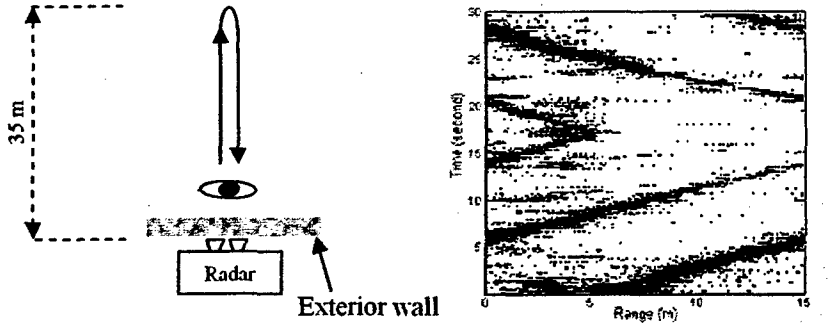

(a) (b)

AN ALGORITHM FOR GROUND PENETRATION IMAGING USING SYNTHETIC APERTURE RADAR CONCEPT

C. Ozdemir
Dept. of Electrical-Electronics Engineering, Mersin University,
Çiftlikköy, 33343 Mersin, TURKEY.
S. Lim, H. Ling
Dept. of Electrical and Computer Engineering, The Univ. of Texas at Austin,
Austin, TX 78712-1084 USA.

Abstract: A new algorithm for ground penetrating radar (GPR) imaging based on the synthetic aperture radar concept is presented. It is shown that 3D GPR images of underground can be formed by 3D inverse-Fourier transforming the multi-frequency, multi-spatial scattered field data. The proposed algorithm is tested with measurement data. The resulting GPR images demonstrate the effectiveness of the proposed algorithm.

INTRODUCTION

Subsurface imaging to detect and identify buried objects has long been a topic of interest for researchers from a wide variety of disciplines [1-4]. Many different imaging techniques have been proposed to identify metallic objects underground. It is relatively harder to detect non-metallic, low-contrast objects since their reflections are weaker. Another challenging aspect in most ground penetrating radar (GPR) imaging is the resolution issue. Although GPR images typically have good depth resolution by utilizing the frequency diversity, it is usually very hard to achieve a good resolution in the cross-range dimensions. To achieve high-resolution GPR images, different approaches have been proposed including transformation techniques for B-scan GPR data [2], the back propagation and iterative conjugate gradient inversion [3, 4]. These techniques; however, do not offer direct GPR imaging and requires significant use of computer resources. Therefore, there is a need for a fast GPR imaging algorithm that has the ability to produce high-resolution images for both metallic and non-metallic buried objects.

In this work, we set out to develop a new GPR imaging algorithm based on the synthetic aperture radar (SAR) concept. We have previously developed 3D imaging algorithms to visualize antenna-platform interactions by processing the multi-frequency, multi-spatial scattered fields [5, 6]. Here, we extend our previous work and develop a SAR-based GPR imaging algorithm to achieve good resolution along both the depth and the cross-range dimensions.

GPR IMAGING ALGORITHM

Our GPR imaging method uses synthetic aperture radar concept. We use both the frequency and spatial diversity to form images for buried objects and/or soil inhomogeneities by processing the 3D multi-frequency, multi-spatial scattered fields. We assume that the frequency bandwidth is small compared to the center frequency of operation, and that the spatial aperture for the scattered field collection is also small compared to the path length R_{2i} from the buried object to the receiver site (see Fig. 1). Under these assumptions, the scattered field can be approximated as follows:

$$E_s(k, x', z') = A_i \cdot e^{-jk(R_{1i}+R_{2i})} \cdot e^{-jk_c \cdot x' \sin\alpha_i} \cdot e^{-jk_c \cdot z' \sin\alpha_i \sin\beta_i} \qquad (1)$$

where A_i is the strength of the scattered electric field, $k = 2\pi\sqrt{\varepsilon_r}/\lambda$ is the wave number in the soil and ε_r is the dielectric constant of the soil. While k changes with the frequency, k_c is assumed to be constant and represents the wave number at the center frequency. From (1), it is obvious that there are Fourier relationships between the pairs k-and-R, x'-and-($\sin\alpha$), and z'-and-($\sin\alpha \cdot \sin\beta$). Therefore, if we take the 3D inverse Fourier transform of the scattered field with respect to k, x', and z', it is possible to pinpoint the total travel distance and the angles that are related to the scatterer location. The resultant image will be in the $R=R_1+R_2$, $U=\sin\alpha$ and $V=\sin\alpha \cdot \sin\beta$ domains as given below:

$$E_s(R, U, V) = A_i \cdot \delta(R - (R_{1i} + R_{2i})) \cdot \delta(U - \sin\alpha_i) \cdot \delta(V - \sin\alpha_i \sin\beta_i) \qquad (2)$$

After generating the GPR image in the (R, U, V) domain, we can easily transform it to the desired (x, y, z) domain by using the simple trigonometric relationships between (R, α, β) and (x, y, z) [6]. Although, this

transformation is unique and correctly maps the scattering points on the buried object, it causes some defocusing effect in the resultant image because of its non-linear nature.

EXPERIMENTAL RESULTS

The above proposed algorithm was tested with an experimental set-up. For this purpose, a wooden pit was constructed and filled with play-sand. An HP-85047A network analyzer was used to measure the S_{21} between the transmitter and the scattered field at the receiver (see Fig.1). Two identical C-band open-ended waveguide antennas were used at the transmitter and the receiver. The transmitting antenna was assumed to be placed at the origin, and the receiving grid was placed at about 1m away in the positive x-direction. The dielectric constant of the sand was measured to be approximately constant at 2.26 between 5GHz and 6GHz. This calculation of the dielectric constant was obtained by comparing the phase velocities of the wave in the air and inside the sand. As a dielectric scatterer, a stack of 25 compact discs (CD) was used. The dimensions of the plastic CD stack were 7.5cm in height and 12.5cm in diameter. The dielectric constant of the stack, which was buried at 46cm below the sand surface, was not known. The scatterer was placed at 50cm away from the origin at the x-direction. The receiving grid contains 10x10=100 receiving points. The size of the grid was 31.04cm in the x-direction and 14.83cm in the z-direction. For all 100 receiving points, the transmitter frequency was varied from 4.9226 GHz to 5.9352 GHz over 25 evenly sampled points. The measured data were collected onto a PC. After collecting the 3D multi-frequency, multi spatial measurement data, the proposed algorithm was applied to form the image. The Fast Fourier transform (FFT) was used to efficiently carry out the image generation. Fig. 2(a) shows the resulting GPR images projected onto the 2D *U-V*, *R-U* and *R-V* planes. Fig. 2(b) depicts the GPR images projected onto the 2D *Z-Y*, *X-Y* and *X-Z* planes. Also shown in red in these plots are the projected profiles and locations of the actual object. It is easy to see that our method well estimates the location of the scatterer. Although the resolutions in both the range and cross-range domains are fairly good, they are degraded somewhat by the non-linear transformation from the (R, α, β) to the (x, y, z) domain. Ways to remove this distortion are currently being investigated. Fig. 3 shows a 3D-GPR image obtained by contour plotting the image strength.

CONCLUSIONS

We presented a fast imaging algorithm for ground penetrating radar based on the SAR approach. We have shown that a 3D GPR image can be constructed by taking the 3D inverse FFT of the multi-frequency, multi-spatial scattered fields. To test our algorithm, an experimental set-up was constructed and measured data from a dielectric object were collected. Obtained results demonstrate well-localized GPR images with good resolutions.

Acknowledgements: This work is supported by *the Scientific and Research Council of Turkey* (TUBITAK) under NATO-B2 research scholarship programme and in part by the Office of Naval Research under contract No. N00014-03-1-0021.

REFERENCES

[1] Daniels, D.J., *"Surface-Penetrating Radar,"* London: IEE Press, 1996.

[2] Capineri, L., Grande, P., Temple, J. A. G., "Advanced Image-Processing Technique for Real-Time Interpretation of Ground-Penetrating Radar Images," *Int. J. of Imaging Systems Tech.*, **vol.1**, 1998, no. 9, pp. 51-59.

[3] Morrow, I.L., and Van Genderen, P, "A 2-D Polarimetric Backpropagation Algorithm for Ground-Penetrating Radar Applications," *Microwave Opt. Tech. Lett.*, **vol.28**, no.1, 2001, pp. 1-4

[4] Van Dongen, K.W.A., Van Den Berg, P.M. and Fokkema, J.T., "A Directional Borehole Radar For Three-Dimensional Imaging, Proc. GPR 2002, *Ninth Intern. Conf. on GPR*, **vol. I**, 2002, Santa Barbara, USA, pp. 25-30.

[5] Ozdemir, C., Bhalla, R., and Ling, H., "A Radiation Center Representation of Antenna Radiation Patterns on a Complex Platform," *IEEE Trans. Antennas Propagat.*, **vol.48**, no.6, 2000, pp. 992-1000.

[6] Ozdemir, C. and Ling, H., "ACSAR - Antenna Coupling Synthetic Aperture Radar (ACSAR) Imaging Algorithm," J. Electromag. Waves App., **vol.13**, no.3, 1999, pp. 285-306.

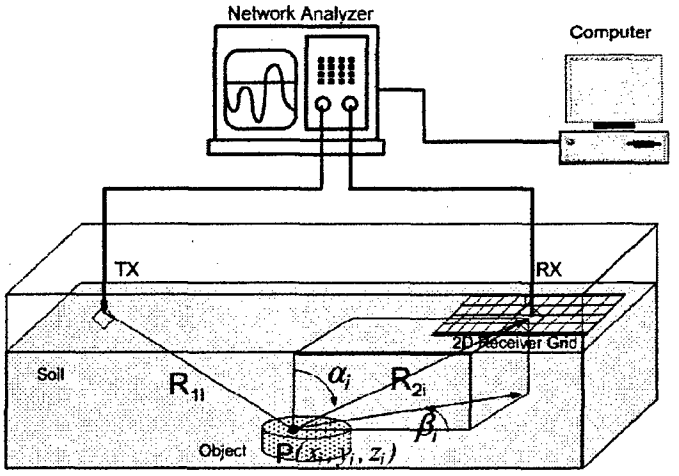

Figure 1. Geometry for GPR imaging, including the experimental set-up.

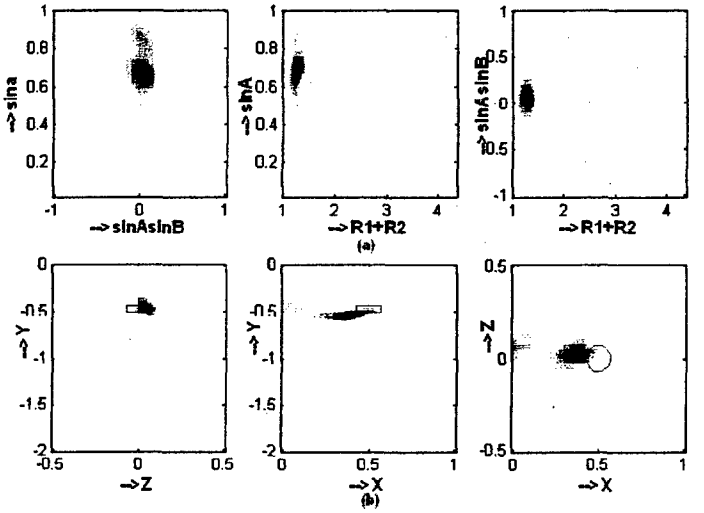

Figure 2. 2D projected GPR images in (a) the (R, U, V) domain , and (b) the (x, y, z) domain.

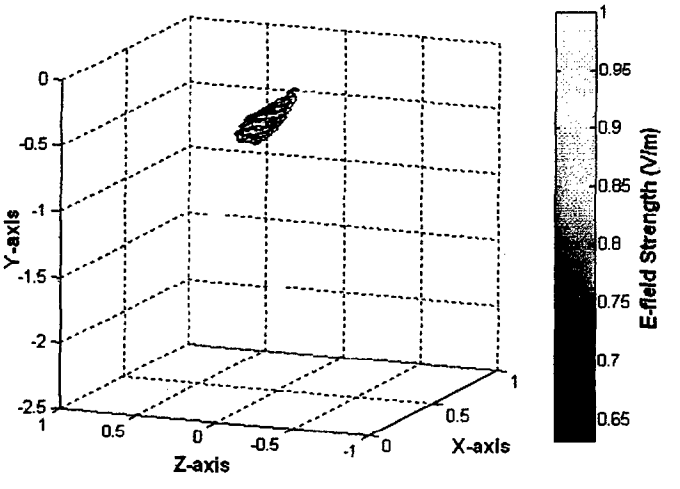

Figure 3. The 3D GPR image formed from the measurement data.

IFSAR Modeling of Terrains and Targets Using a Ray-Based Electromagnetic Technique

Rajan Bhalla and Hao Ling[+]

SAIC
20 Burlington Mall Road, Suite 130
Burlington, MA 01803, USA

[+]Department of Electrical and Computer Engineering
The University of Texas at Austin
Austin, TX 78712 U.S.A

ABSTRACT

This paper describes a methodology of modeling interferometric synthetic aperture radar (IFSAR) images using ray-based high frequency electromagnetic (EM) techniques. Various ray-based EM techniques have been developed in the past for 2D SAR simulations [1],[2]. This work will extend on those approaches for modeling IFSAR images.

Keywords

SAR, IFSAR, Radar Imaging, Electromagnetic Scattering

1. INTRODUCTION

Interferometric synthetic aperture radar (IFSAR) is a technique that allows an automated way to carry out 3D mapping of terrains and targets [3]. IFSAR gives the height estimate for a scene and hence leads to a 3D image of a region. IFSAR is carried by first generating a SAR image pair from two antennas that are spatially or temporally separated as shown in Fig. 1. The phase difference between the SAR image pair is proportional to the topography. After registering the SAR images, the difference in phase in each pixel is extracted to generate an interferogram. Since the phase can only be measured within 2π radians, phase unwrapping is carried out to extract the absolute phase for each pixel that will be proportional the local height. While IFSAR algorithm is typically applied to measurement data, it is useful to develop an IFSAR simulator for research and advanced development of the IFSAR technology. The IFSAR simulator can be used to choose system parameters, study new phenomenologies, experiment with processing procedures and plan new missions. In this paper we will present an IFSAR simulation methodology to simulate the interferogram based on a ray-based electromagnetic (EM) simulation [4].

2. APPROACH

A number of ray-based EM techniques have been developed for computing the scattering from large complex targets [5],[6]. In these techniques, EM computation is carried out by shooting rays at the target or scene as shown in Fig. 2. The EM fields for each ray are tracked and computed based on the principle of physical and/or geometrical optics. The total field scattered from the target is then computed by summing up the EM contribution of each ray. These methods can be extended for SAR computation and a closed form expression for the contribution of the ray can be derived as [1],

$$SAR(r, xr) = \sum_{i\ rays} \alpha_i e^{-j2k\rho_i} h(r - r_i, xr - xr_i) \qquad (1)$$

where r_i, xr_i, α_i are the range, cross-range and amplitude of the ray, respectively. $h(\cdot)$ is the ray impulse response function. The additional phase function $e^{-j2k\rho_i}$ is the phase delay of the ray. For IFSAR simulation, we use the sensor scenario shown in Fig. 1 to first simulate two SAR images, SAR_1 and SAR_2 from the two antennas. The interferogram can then be expressed as,

$$\text{Interferogram} = \text{Phase}(SAR_1 \times SAR_2^*) \qquad (2)$$

The interferogram phase at any arbitrary SAR cell is proportional to the difference of the range distance ρ_1, ρ_2 to the two sensors as,

$$\text{Interferogram}(r,xr) \propto (\rho_2 - \rho_1) \propto h \qquad (3)$$

It can be mathematically shown that the interferogram phase is proportional to the height h in Fig. 2 [3]. IFSAR can be collected in various modes including the single antenna transmit mode, the ping-pong mode or the repeat pass mode. In the single antenna transmit interferometric mode, one antenna is used for transmit, and data are received on two antennas separated by the physical baseline. In the ping-pong interferometric mode, the antenna used for transmit alternates between the two receive

antennas, but data are still received on both antennas. In the repeat pass mode a single antenna is used for both transmit and receive, and multiple passes are used to form a temporal baseline. These modes can be simulated by the appropriate choice of simulating either bistatic or monostatic SAR images in (1) [7].

One of the post processing steps that needs to be done on an IFSAR to generate the 3D represntation of the target is phase unwrapping. Phase unwrapping is necessitated by the 2π cyclical ambiguity in the raw interferometric phase and consists of removing that ambiguity by conversion from relative to absolute phase differences. There are two main classes of algorithms to perform phase unwrapping. The first class of algorithms is based on the integration-with-branch-cuts approach originally developed by Goldstein et al [8]. A second class of algorithms is based on a least squares fitting of the unwrapped solution to the gradients of the wrapped phase. The performance of phase unwrapping algorithms is affected by a number of factors and parameters in these algorithms have to be tuned to arrive at good height estimates. The various problem areas for phase unwrapping include regions where the signal-to-noise ratio is too small, side lobes from bright scattering centers spilling over into neighboring cells, multi-bounce interactions and multiple scattering centers in the same pixel. Correlation between the SAR images can be used to guide the phase unwrapping process.

3. RESULTS

We present some preliminary results from our ray-based IFSAR simulator. The results include terrain map reconstruction of urban environments as well as ground targets. Fig. 3(a). shows the CAD model of an urban scene in Austin, Texas. Figs. 3(b) and 3(c) show the corresponding SAR and IFSAR for the scene. The SAR was simulated at X-band with 1-foot resolution. A ping-pong mode for the IFSAR simulation was used for computing the interferogram. Phase unwrapping was carried out using Goldstein's algorithm. Fig. 3(d) shows the 3D CAD reconstruction from the scene and shows a fairly good comparison of the prominent building features to the original CAD model. Since the two SAR images were generated at a single look angle, the IFSAR fails to provide a height estimate in areas that were shadowed in the SAR images. One way to correct for this is by fusing multiple IFSAR views of the scene to build a unified 3D representation of the scene. The fusion is accomplished by summing up all the IFSAR images after registering them to a common coordinate system. The SAR pixel amplitude can be used to make summing decision in overlapping areas of the image from different views. In the second set of results shown in Fig. 4, we consider a ground vehicle. Figs. 4(a) and 4(b) show a series of SAR and IFSAR for the target at different azimuth views. The high resolution SAR was simulated at X-band. Fig. 4(c) shows the corresponding 3D CAD reconstruction fused from the multi-view IFSAR imagery.

4. CONCLUSIONS

In this paper we presented a methodology of modeling IFSAR images using a ray-based high frequency electromagnetic technique. The IFSAR simulation technique is an extension of our 2D SAR simulation work. We presented some IFSAR examples for terrains and targets. This IFSAR simulation capability is very useful to gain a better understanding of the scattering phenomenology and can contribute to sensor development for 3D target identification and engagement.

5. REFERENCES

[1] R. Bhalla and H. Ling, "Image-domain ray-tube integration formula for the shooting and bouncing ray technique," *Radio Science*, vol. 30, pp. 1435-1446, September-October 1995.

[2] R. Bhalla and H. Ling, "A fast algorithm for signature prediction and image formation using the shooting and bouncing ray technique," *IEEE Trans. Antennas Propagat.*, vol. AP-43, pp. 727-731, July 1995.

[3] P. Rosen, S. Hensley, I. Joughin, F. Li, S. Madsen, E. Rodriguez, R. Goldstein, "Synthetic aperture radar interferometry," *Proc. IEEE* vol. 88, no. 3, pp. 333-382, March 2000.

[4] R. Bhalla, H. Ling and B. Houshmand, "IFSAR simulation using the shooting and bouncing ray technique," URSI National Radio Science Meeting, p. 152, Orlando, FL, July 1999.

[5] H. Ling, R. Chou and S. W. Lee ,"Shooting and bouncing rays: calculating the RCS of an arbitrarily shaped cavity," *IEEE Trans. Antennas Propagat.*, vol. AP-37, pp. 194–205, February 1989.

[6] P.H. Pathak, R.J. Burkholder, R. Chou and G. Crabtree, "A generalized ray expansion method for analyzing the EM scattering by open-ended waveguide cavities," IEEE AP-S International Symposium Digest, pp. 840–843, Santa Clara CA, June 1989.

[7] R. Bhalla, H. Ling, S. W. Lee and J. Hughes, "Bistatic scattering center extraction using the shooting and bouncing ray technique," SPIE AeroSense '99, Algorithms for Synthetic Aperture Radar Imagery, vol. 3721, pp. 612-619, Orlando, FL, April 1999.

[8] R. M. Goldstein, H. A. Zebker and C. L. Werner, "Satellite radar interferometry: two-dimensional phase unwrapping," *Radio Science*, vol. 23 no. 4, pp. 713-720, 1988

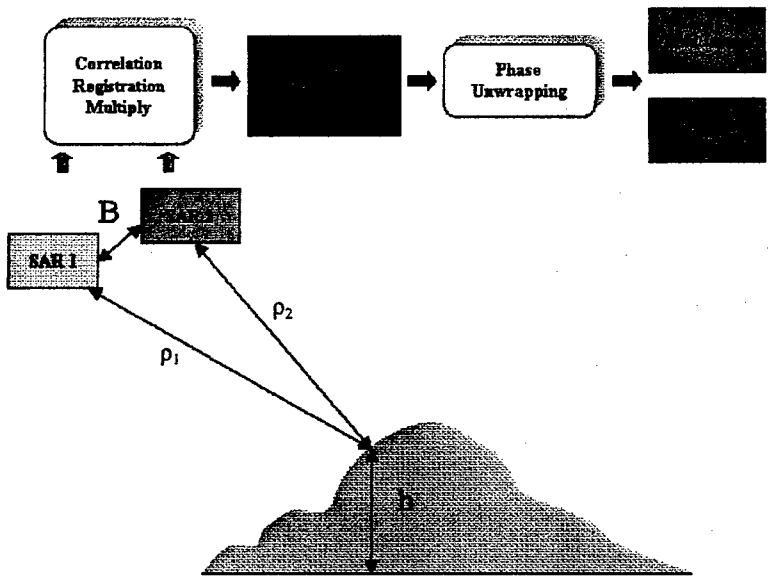

Fig. 1. Concept of IFSAR processing

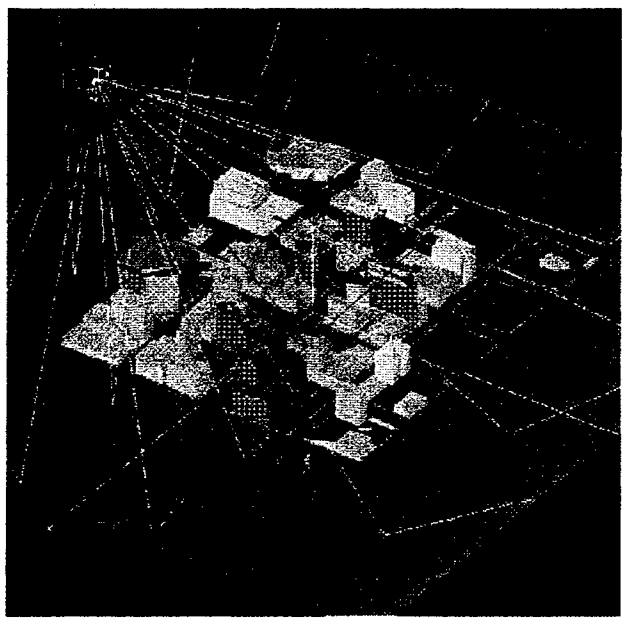

Fig. 2. Example ray shoot on a target. A ray-based EM code shoots rays to determine lit and shadow regions. EM fields are computed based on either geometrical optics or physical optics.

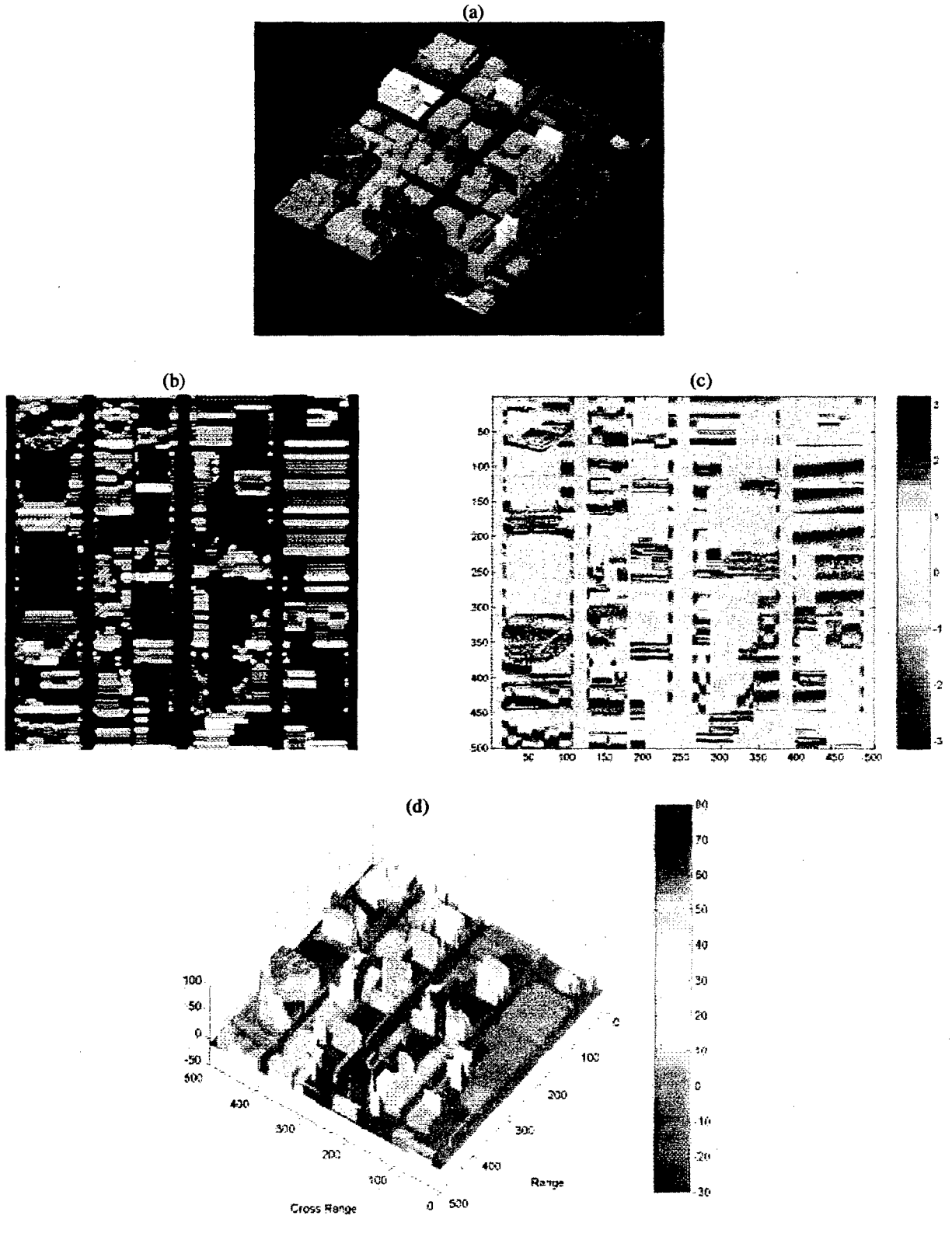

Fig. 3. SAR/IFSAR simulation and 3D model reconstruction. The SAR/IFSAR pair is simulated using the ray-based EM code. (a) 3D CAD model for Austin, Texas. (b) Simulated 2D SAR image from the Austin CAD model. (c) Simulated IFSAR interferogram. (d) 3D model reconstructed from the IFSAR using Goldstein's algorithm.

(a)

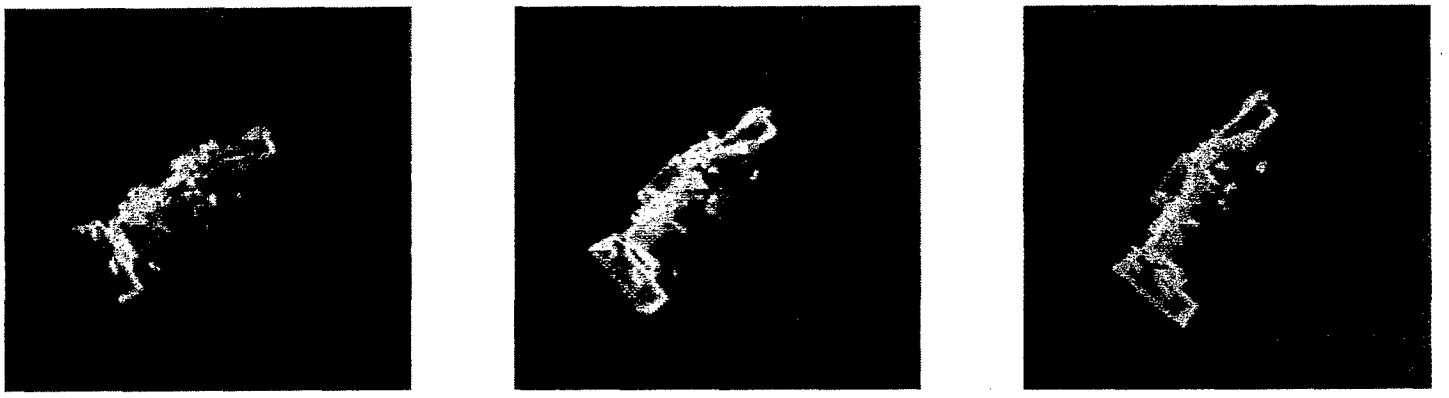

(b)

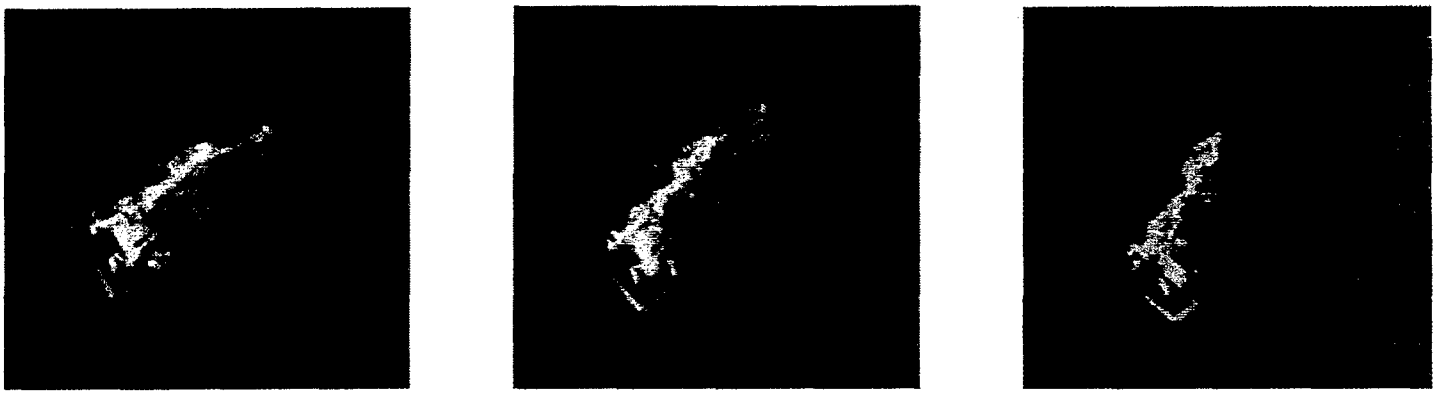

(c)

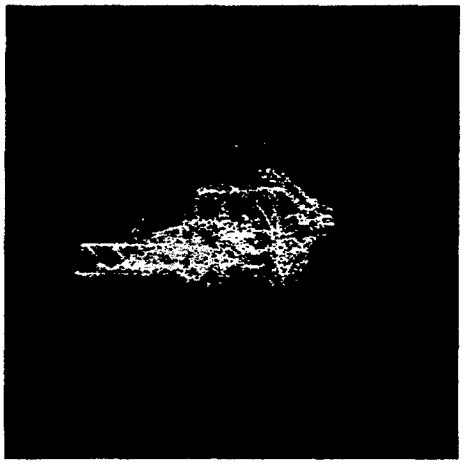

Fig. 4. SAR/IFSAR simulation and 3D model reconstruction for a ground vehicle simulated using the ray-based EM code. (a) Simulated 2D SAR images for the ground target at 3 different views. (b) Simulated IFSAR interferograms at the corresponding views. (c) 3D model reconstructed from the IFSAR.

Multi-Baseline IFSAR Study Using an SBR Based Simulator

Rajan Bhalla*[a] and Hao Ling[b]

[a]SAIC, 20 Burlington Mall Road, Suite 130, Burlington, MA 01803, USA
[b]Department of Electrical Engineering , The University of Texas at Austin, Austin, TX 78712

ABSTRACT

This paper describes the results of a multi-baseline IFSAR study using a shooting and bouncing ray (SBR) based IFSAR simulator. The SBR technique has been used in the past for 2-D SAR and IFSAR simulations. This paper extends on those approaches for modeling multi-baseline IFSAR images. IFSAR gives the height estimate for a target and hence leads to a 3-D image of the target. The 3-D reconstruction is dependent on the choice of IFSAR sensor parameters. We present a tradeoff study the sensor resolution versus the number of baselines using the SBR based simulator.

Keywords: SAR, IFSAR, Radar Imaging, Electromagnetic Scattering

INTRODUCTION

Interferometric synthetic aperture radar (IFSAR) is a well-established technique for carrying out 3-D target and terrain mapping. IFSAR is conventionally carried out by first generating a SAR image pair from two antennas that are spatially separated. The phase difference between the SAR image pair is proportional to the height on the target. Conventional single-baseline IFSAR scenario does not provide any resolution in the height dimension and hence cannot resolve scatterers that fall within the same (range)-(cross range) bin in the SAR image. To overcome this limitation, multi-baseline IFSAR scenarios have been proposed [1,2,3,4,5]. Although a multi-baseline IFSAR setup can potentially overcome the resolution limitation in the height dimension, there are practical challenges to build a long multi-baseline IFSAR system. It this work, we will extend the IFSAR simulator based on the shooting and bouncing ray (SBR) technique [6] to handle multi-baseline simulations. We will then present a tradeoff study related to the choice of the multi-baseline sensor parameters. 3-D target reconstruction results from the multi-baseline simulator will be presented. We will introduce an error metric to characterize the error in height reconstruction to evaluate the choice of various IFSAR sensor parameters. This study will demonstrate the utility of the simulation for choosing system parameters, experimenting with processing procedures and possible mission planning.

APPROACH

IFSAR gives the height estimate for a scene and hence leads to a 3-D image of a region. IFSAR is carried by first generating a SAR image pair from two antennas that are spatially or temporally separated as shown in Fig. 1. The phase difference between the SAR image pair is proportional to the height of the topography. After registering the SAR images, the difference in phase in each pixel is extracted to generate an interferogram. Since the phase can only be measured within 2π radians, phase unwrapping is carried out to extract the absolute phase for each pixel that will be proportional the local height. While IFSAR algorithm is typically applied to measurement data, it is useful to develop an IFSAR simulator for research and advanced development of the IFSAR technology.

The IFSAR simulation methodology to simulate the interferogram is based on the shooting and bouncing ray technique [6]. In this approach, the EM computation is carried out by shooting rays at the target or scene as shown in Fig. 2. The EM fields for each ray are tracked and computed based on the principle of physical and/or geometrical optics. The total field scattered from the target is then computed by summing up the EM contribution of each ray. This method can be extended for SAR computation and a closed form expression for the contribution of the ray can be derived as [7, 8]:

$$SAR(r, xr) = \sum_{i\,rays} \alpha_i e^{-j2k_c\rho_i} h(r - r_i, xr - xr_i) \quad (1)$$

where r_i, xr_i, α_i are the range, cross-range and amplitude of the ray, respectively. $h(\cdot)$ is the ray impulse response function. The additional phase function $e^{-j2k_c\rho_1}$ is the phase delay of the ray, where k_c is the wave number at the central frequency. For IFSAR simulation, we use the sensor scenario shown in Fig. 1 to first simulate two SAR images, SAR_1 and SAR_2 from the two antennas. The interferogram can then be expressed as,

$$\text{Interferogram} = \text{Phase}(SAR_1 \times SAR_2^*) \quad (2)$$

The interferogram phase at any arbitrary SAR cell is proportional to the difference of the range distance ρ_1, ρ_2 to the two sensors as,

$$\text{Interferogram}(r,xr) \propto (\rho_2 - \rho_1) \propto h \quad (3)$$

It can also be shown mathematically that the interferogram phase is proportional to the height h in Fig. 1 [1, 9, 10]. One of the post processing steps that needs to be done on an 2 sensor IFSAR to generate the 3-D representation of the target is phase unwrapping. Phase unwrapping is necessitated by the 2π cyclical ambiguity in the raw interferometric phase and consists of removing that ambiguity by conversion from relative to absolute phase differences. There are numerous algorithms available to perform the phase unwrapping [11].

The above analysis and processing for a 2 sensor IFSAR system can be extended to a multi-sensor IFSAR system, also called a multi-baseline IFSAR system. There are various ways to setup a multi-baseline IFSAR system with N array elements. Each antenna element is used to generate a SAR image. Considering the SAR image of the first antenna element as the reference, each pair of antenna elements can be used to generate an interferogram. The interferogram between the SAR image for the 1st and m^{th} antenna element is then,

$$\text{Interferogram}_m = \text{Phase}(SAR_1 \times SAR_m^*) \quad (4)$$

Provided that the subtended angle of the baseline is not too large, the N interferograms can be efficiently simulated using one single ray trace and thus do not significantly increase the computation time for the simulation. The post processing required on the N SAR images and interferograms to generate a 3-D image depend on the configuration of the N array elements in the multi-baseline IFSAR system. The antennas in the system can be either uniformly or non-uniformly sampled. With 2 sensors generating an interferogram and using phase unwrapping can be straightforward but with N sensors it can be very complex to phase unwrap N interferograms concurrently. There have been algorithms developed to phase unwrap N interferograms for certain specific multi-baseline system architectures but they lack in generality. One such commonly used system is a 3-sensor system with a large and small baseline [12]. The small baseline inteferogram is used to assist in phase unwrapping the large baseline interferogram in areas with high fringe rates. For ease of post processing, the simplest way to set up the multi-baseline system would be as a uniformly sampled linear array as shown in Fig. 3. In the uniformly sampled array configuration, we operate directly on the N SAR images to resolve the individual scatterers in the SAR cell and we can use beamforming or direction-of-arrival (DOA) algorithms to resolve the individual scatterers [13]. Using the N SAR images, the signal model for a SAR cell at (r,xr) can be represented as,

$$E = [E_1 \quad E_2 \quad \ldots] \quad (5)$$

where E_m is the value of the m'th SAR at (r,xr). The scattering strength in each individual SAR cell can be interpreted as a summation of scattering centers at various heights θ_p as shown in Fig. 3. The signal model for a SAR cell can be modeled as,

$$\hat{E} = \sum_{p=1}^{d} a_p e^{-jkB \sin\theta_p} \quad (6)$$

where B is the inter-element distance and a_p is the strength of the p'th scattering center. There are various beamforming techniques to estimate a_p and θ_p from E [3,12,13]. Both parametric (MUSIC, Min-Norm, ESPRIT, modified Prony) and non-parametric (Capon) spectral estimation techniques have been applied for mutli-baseline IFSAR with good success [3]. In this paper we used a Prony based estimator for modeling [15,16,17]. The set of scattering centers $\{r, xr, a_p, \theta_p\}$

computed for all the SAR cells represents a 3-D image of the target. We can also compute an error metric based on the sum of the parameterization error for each SAR cell. The error metric can be written as:

$$\text{MSE} = \sum_{\text{SAR cells}} \left| E_m - \hat{E}_m \right| \tag{7}$$

where E_m, $\hat{E}_m$, is the received and parameterized multi-baseline signal for the N element array in the m'th SAR cell. This MSE error is an average error across the whole image and is a good indicator of the spatial error in the location of each individual scattering centers. We will next present results from some system design studies for a multi-baseline system.

RESULTS

Results of a tradeoff study from our ray-based multi-baseline IFSAR simulator are presented. The simulator is implemented in the SBR-based radar simulation code Xpatch. We use a backhoe target for our study. The backhoe target is used in the AFRL data dome challenge set and its data have been publicly released. Figs. 4(a),(b),(c) show the backhoe target and its simulated 2-D and 3-D SAR images. The overlay of the 3-D SAR image and 3-D CAD model is performed using the E3Doer® visualization package distributed by SAIC. Fig. 4(d) shows an IFSAR interferogram generated for the backhoe. The IFSAR is generated using 2-inch resolution at a center frequency of 10 GHz. The look angle on the target is AZ=10° and EL=30°. Multiple IFSAR images at various azimuth angles can be fused to form a composite 3D model of the target. The fusion is accomplished by combining all the 3-D images after registering them to a common coordinate system. The SAR pixel amplitude is used to make summing decisions in overlapping areas of the image from different views. The final composite 3D model reconstructed from the 2 sensor IFSAR system with a baseline of 1 meter is shown in Fig. 4(e). Besides visualizing the 3-D images we can also compute the MSE error metric as described in (7).

Using the same methodology, we can extend the 2-sensor IFSAR simulation for multiple sensors. Fig. 5 shows the MSE computed for different number of sensor elements plotted versus a function of azimuth look. The MSE is computed for 2, 3, 4 and 5 sensor elements in a multi-baseline IFSAR scenario for various SAR resolutions. For the 2-inch resolution case shown in Fig. 5(a), we observe that the MSE error decreases to less than 2% by using 3 sensors instead of 2 sensors. Additional sensors did not improve the results drastically. For the 4-inch resolution case shown in Fig. 5(b), we observe that 4 sensors are now required to achieve approximately the same level of MSE. The same trend continues in Fig. 5(c), which shows the 6-inch resolution case. These trends can be explained as follows. Decreasing the SAR resolution results in more scatterers to be included in a SAR cell and causes the MSE error to increase, especially when the number of sensors is small. By using more sensors, these scatterers residing in the same SAR image cell can be resolved, thus leading to an improved MSE. This explanation is next verified by simulation. We extract a set of high-resolution 3-D scattering centers for the backhoe target using Xpatch [18,19]. These 3-D scattering centers are then binned at various spatial resolutions. Fig. 6 shows the average number of scattering centers in each 3-D SAR cell plotted versus azimuth. For the 2-inch resolution case, there are typically between 2 to 3 scattering centers in each cell. This agrees with the results in Fig. 5(a), which show the need for ~4 sensors to achieve a low MSE. The average number of scattering centers increases to 7 for the 4-inch resolution case and 12 for the 6-inch resolution case. However, we note that the MSE results in Fig. 5 do not show the need to increase the number of sensors to beyond 5. To see why this is the case, we examine the strength of the dominant scatterer in each 3-D SAR cell. We compute the percentage signal strength contributed by the dominant scatterer in each of the SAR cell. The dominant scatterer signal percentage is computed as $\max(|a_p|^2)/\sum|a_p|^2$. Fig. 7 shows this percentage averaged over all of the SAR cells. As we can see from Fig. 7, even though the average number of scatterers at 6-inch resolution is 12, the dominant scatterer accounts for about 70% of the signal strength. Hence by using only a few (<= 5) sensors, we can limit the MSE to a low level, as was seen earlier. It is not necessary to use as many as 24 sensors to resolve the scattereres.

CONCLUSION

In this paper we presented a methodology for modeling multi-baseline IFSAR images using the SBR technique. We presented a multi-baseline IFSAR study for the backhoe target. The study was carried out by computing the MSE error for various resolutions and different number of sensors. For IFSAR with 2-inch resolution, the number of sensors needed was around 4 to achieve a 2% MSE, whereas for 6-inch resolution, about 5 sensors were needed to achieve the same level of MSE. There are other sensors parameters (stand-off distance, frequency, processing algorithm, baseline, signal-noise ratio, etc.) that can impact the MSE. A more detailed study to evaluate the impact of these sensor parameters on a wider class of targets can be readily carried out using the same software. This IFSAR simulation capability can be very useful to gain a better understanding of the scattering phenomenology and can contribute to sensor development for 3-D target identification and engagement.

Acknowledgements

The authors would like to thank Gerard Titi at DARPA and Edmund Zelnio, Dr. Vince Velten, Mike Minardi, Dr. Ron Dilsavor, Kiran Naidu and Tom Majumder at Air Force Research Lab for valuable guidance and useful discussions.

REFERENCES

1. P. Rosen, S. Hensley, I. Joughin, F. Li, S. Madsen, E. Rodriguez, R. Goldstein, "Synthetic aperture radar interferometry," *Proc. IEEE* vol. 88, no. 3, pp. 333-382, March 2000.
2. R. M. Goldstein, H. A. Zebker and C. L. Werner, "Satellite radar interferometry: two-dimensional phase unwrapping," *Radio Science*, vol. 23 no. 4, pp. 713-720, 1988.
3. F. Gini, F. Lombardini and M. Montanari, "Layover Solution in Multibasline SAR Interferometry," *IEEE Trans. Aerospace and Electronics Systems*, vol. 38, pp. 1344-1356, Oct. 2002.
4. J. Homer, I. D. Longstaff and G. Callaghan, "High resolution 3-D SAR via multi-baseline interferometry," in *Proc. IEEE Int. Geosci. Remote Sensing Symp.*, Lincoln, NB, pp. 796-798, 1996.
5. S. Xiao and D. C. Munson, "Spotlight-mode SAR imaging of a three-dimensional scene using spectral estimation techniques," in *Proc. IEEE Int. Geosci. Remote Sensing Symp.*, Seattle, pp. 642-644, 1998.
6. H. Ling, R. Chou and S. W. Lee, "Shooting and bouncing rays: calculating the RCS of an arbitrarily shaped cavity," *IEEE Trans. Antennas Propagat.*, vol. AP-37, pp. 194–205, February 1989.
7. R. Bhalla and H. Ling, "Image-domain ray-tube integration formula for the shooting and bouncing ray technique," *Radio Science*, vol. 30, pp. 1435-1446, September-October 1995.
8. R. Bhalla and H. Ling, "A fast algorithm for signature prediction and image formation using the shooting and bouncing ray technique," *IEEE Trans. Antennas Propagat.*, vol. AP-43, pp. 727-731, July 1995.
9. R. Bhalla and H. Ling, "IFSAR Modeling of Terrain and Target using a Ray-based Electromagnetic Technique," *Proceeding of the IASTED International Conference*, ARP 2004, pp. 186-190, July 2004.
10. R. Bhalla, H. Ling and B. Houshmand, "IFSAR simulation using the shooting and bouncing ray technique," *URSI National Radio Science Meeting Digest*, p. 152, Orlando, FL, July 1999.
11. R. M. Goldstein, H. A. Zebker and C. L. Werner, "Satellite radar interferometry: two-dimensional phase unwrapping," *Radio Science*, vol. 23 no. 4, pp. 713-720, 1988.
12. E. Sansosti, R. Lanari, G. Fornaro, G. Francesceschetti, M. Tesauro, G. Puglisi and M. Coltelli, "Digital elevation model generation using ascending and descending ERS-1/ERS-2 tandem data," *International Journal of Remote Sensing*, Vol. 20, no. 8, pp. 1527-1547, May 1999.
13. Harry L. Van Trees, *Detection, Estimation and Modulation theory : Optimum Array Processing*, John Wiley and Sons, 2002.
14. J. Li, P. Stoica and Z. Wang, "On Robust Capon Beamforming and Diagonal Loading," *IEEE Trans. Signal Processing*, vol. 51, pp. 1702-1715, July 2003.
15. R. Carriere and R. L. Moses, "High Resolution Radar Target Modeling Using a Modified Prony Estimator," *IEEE Trans. Antennas Propagat.*, Vol. AP-40, Jan. 1992, pp. 13-18.

16. N. Kannan and D. Kundu, "On modified EVLP and ML methods for estimating superimposed exponential signals.," *Signal Processing*, no. 39, 223-233, 1994.
17. M. R. Osborne and G. K. Smyth, "A modified Prony algorithm for fitting sums of exponential functions.," *SIAM Journal of Scientific Computing*, no. 16, pp. 119-138, 1995.
18. R. Bhalla and H. Ling, "3D scattering center extraction of complex targets using the shooting and bouncing ray technique," *IEEE Trans. Antennas Propagat.*, vol. 44, pp. 1445-1453, Nov. 1996.
19. R. Bhalla, J. Moore and H. Ling, "A global scattering center representation of complex targets using the shooting and bouncing ray technique," *IEEE Trans. Antennas Propagat.*, vol. AP-45, pp. 1850-1856, December 1997.

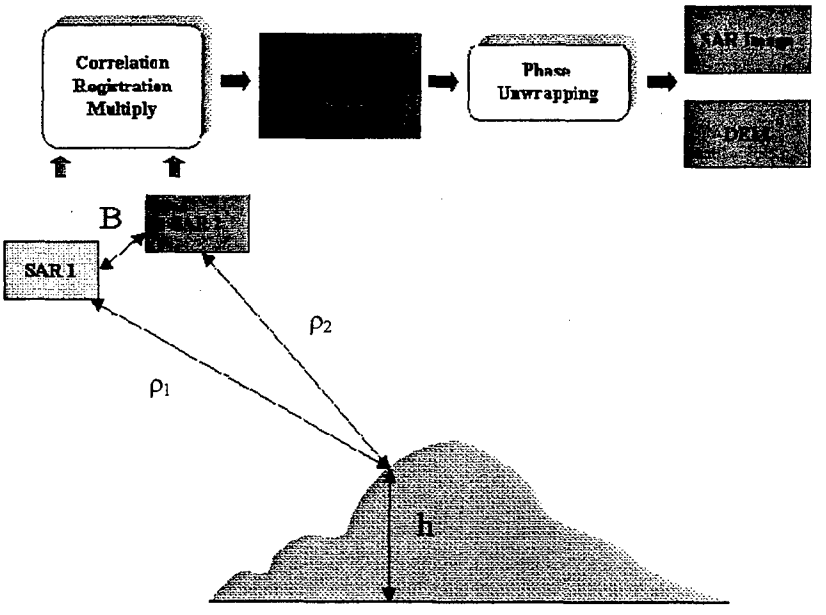

Fig. 1. Concept of IFSAR processing.

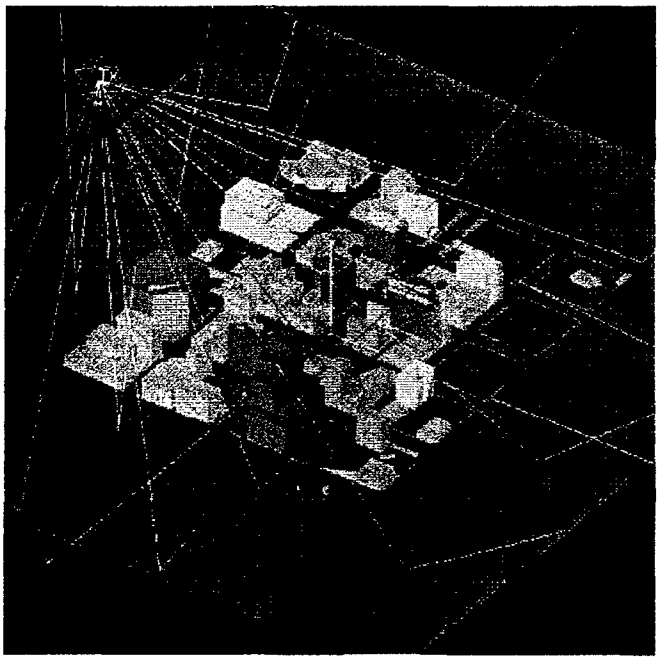

Fig. 2. Example ray shoot on a target. A ray-based EM code shoots rays to determine lit and shadow regions. EM fields are computed based on either geometrical optics or physical optics.

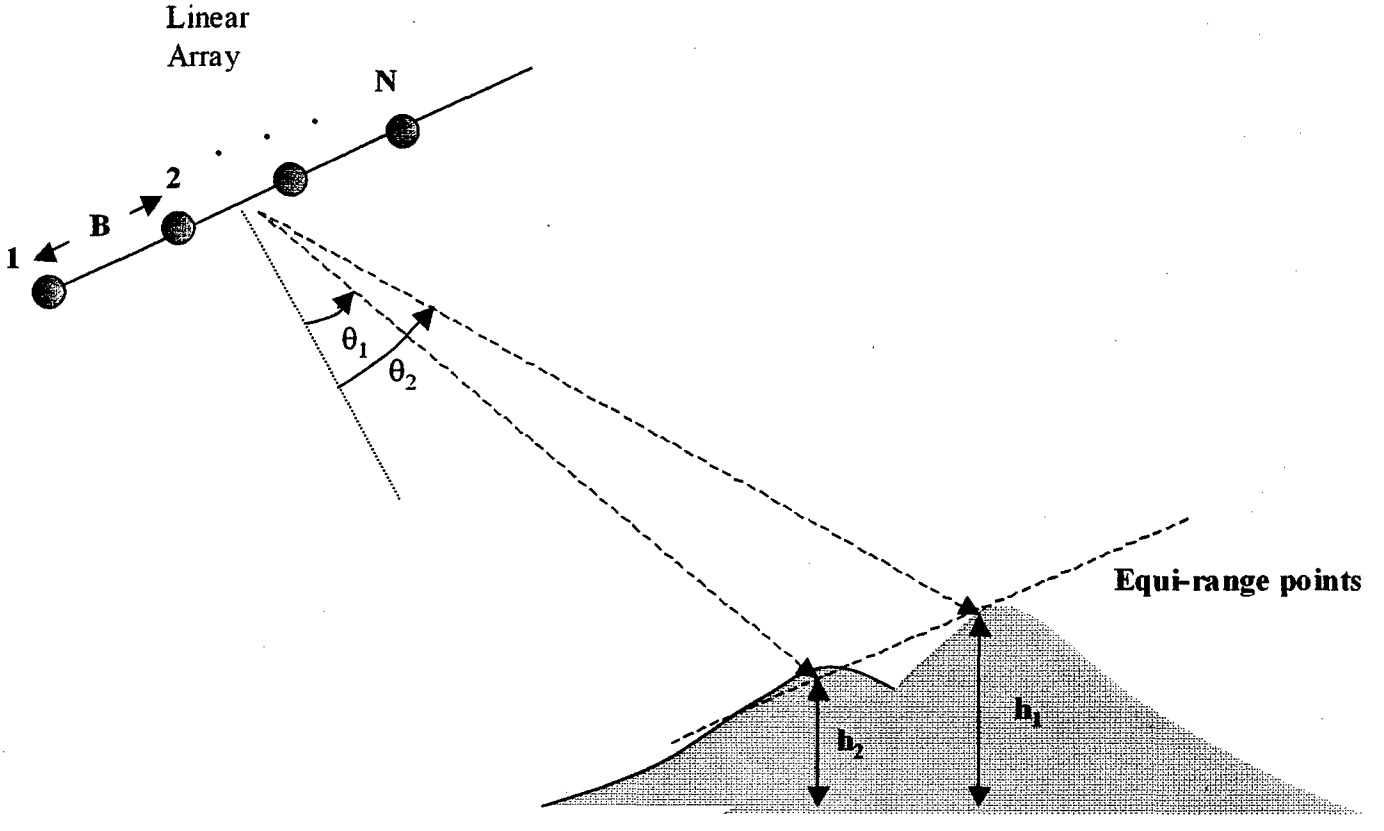

Fig. 3. Multi-baseline IFSAR scenario. The N-element linear array with inter-element distance B can be used to resolve multiple scatterers in a SAR cell.

(a)

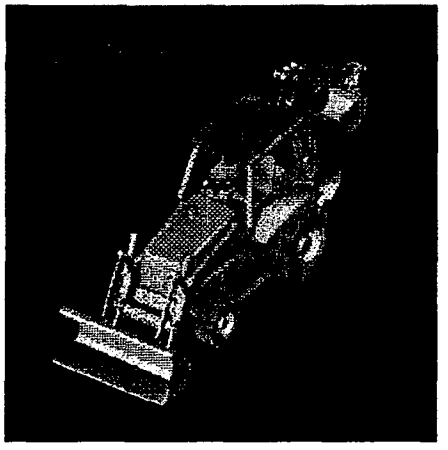

(b)

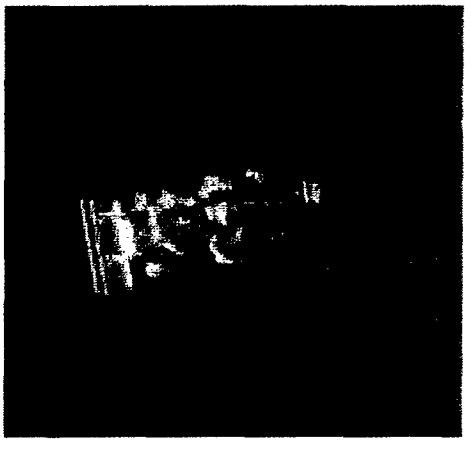

(c)

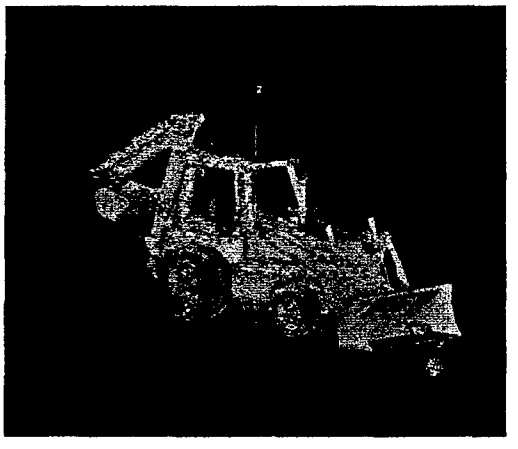

(d)

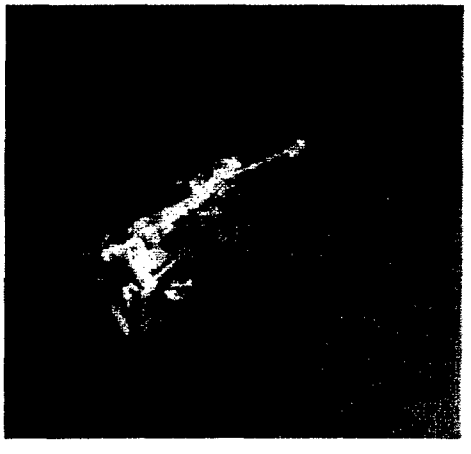

(e)

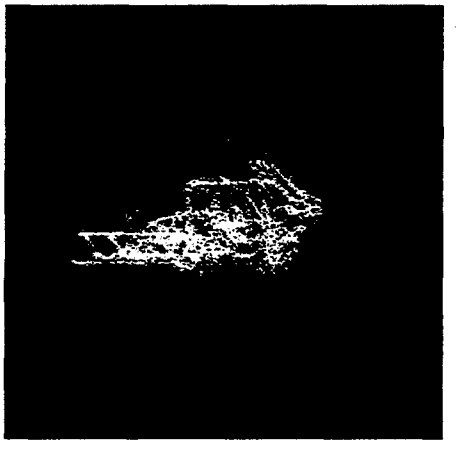

Fig. 4. SAR/IFSAR simulation and 3D model reconstruction for a backhoe simulated using SBR. (a) Simulated 2D SAR images for the backhoe target (b) 3-D SAR image for the backhoe (c) Simulated IFSAR interferogram (c) 3D model reconstructed from the IFSAR.

(a)

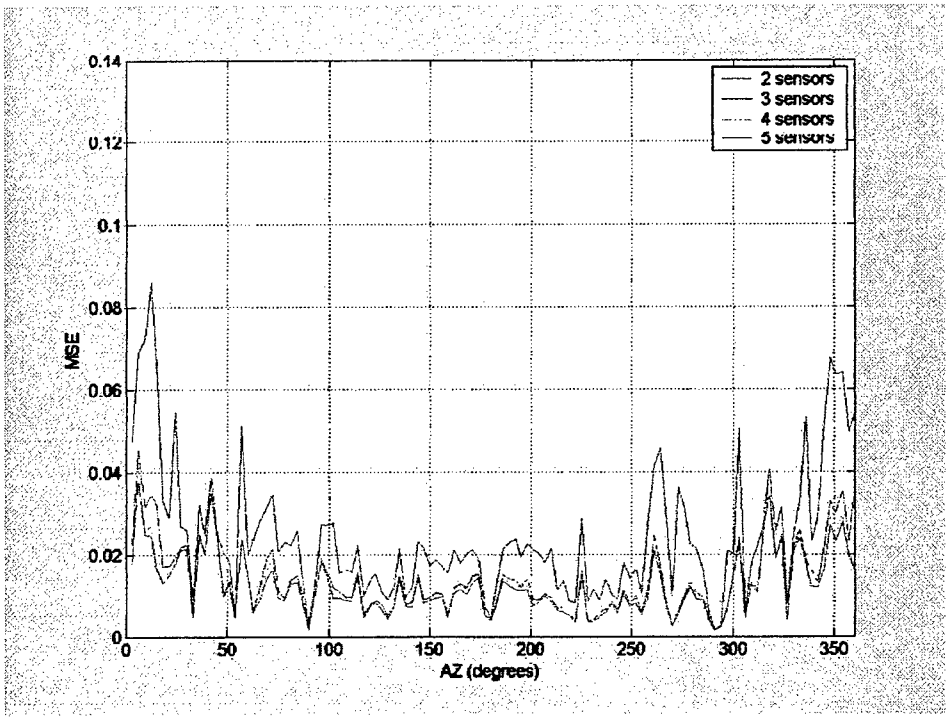
2 sensors
3 sensors
4 sensors
5 sensors
MSE
AZ (degrees)
0
0.02
0.04
0.06
0.08
0.1
0.12
0.14
0
50
100
150
200
250
300
350

(b)

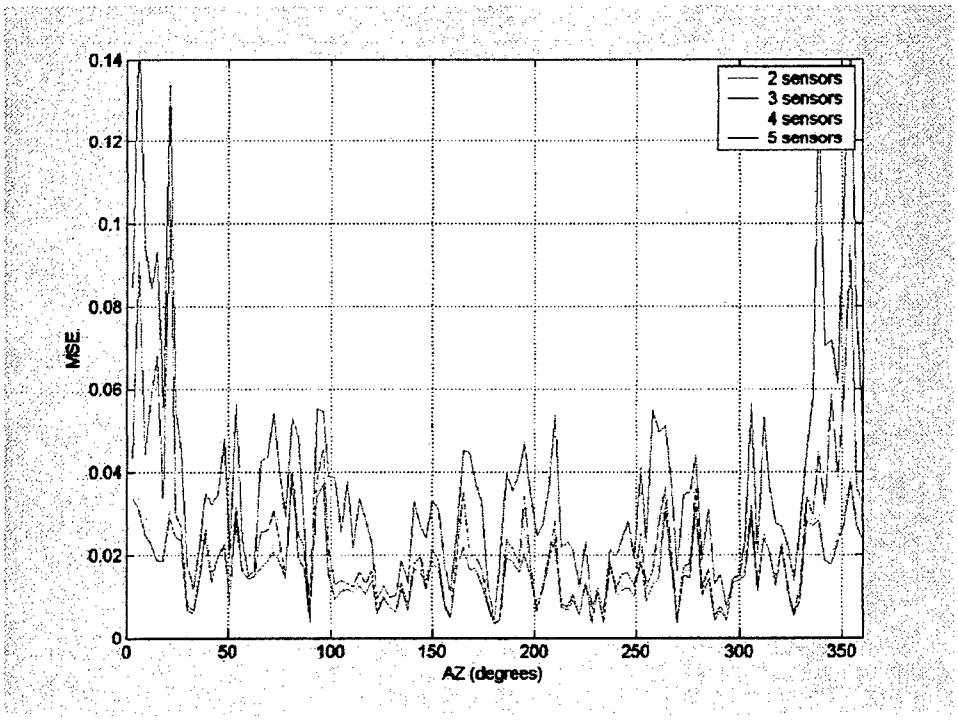
2 sensors
3 sensors
4 sensors
5 sensors
MSE
AZ (degrees)
0
0.02
0.04
0.06
0.08
0.1
0.12
0.14
0
50
100
150
200
250
300
350

(c)

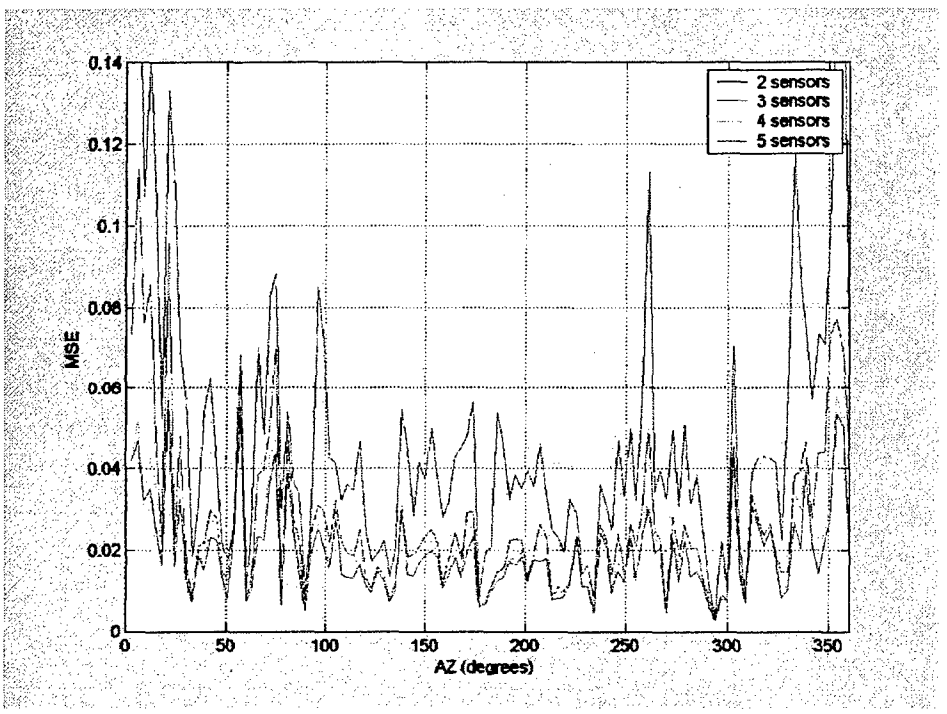

Fig. 5. The MSE error for different number of sensor elements. The MSE was computed for 2,3,4,5 sensors elements in a multi-baseline IFSAR scenario for various SAR resolutions. (a) SAR resolution = 2 inch (b) SAR resolution = 4 inch (c) SAR resolution = 6 inch. Decreasing SAR resolution bandwidth causes more scatterers to fall in a SAR cell and causes MSE errors to increase for fixed number of sensors.

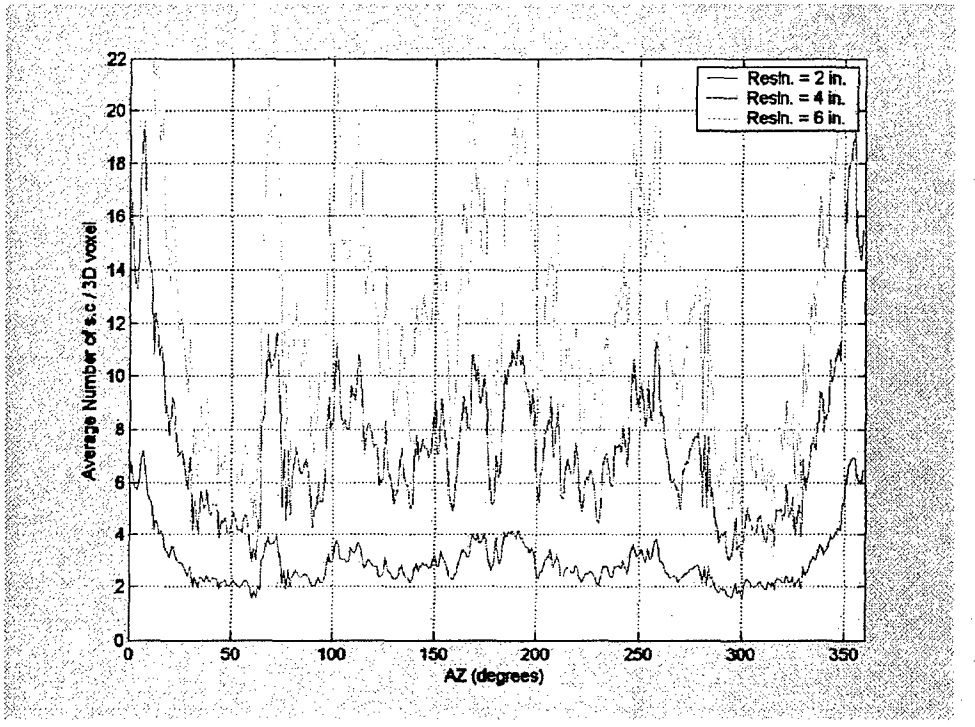

Fig. 6. The average number of 3-D scattering centers in a SAR cell for different SAR resolutions. For SAR with 2 inch resolution the average number of scatters is 3, and the number increases to 7, 12 for 4 inch and 6-inch SAR resolution respectively.

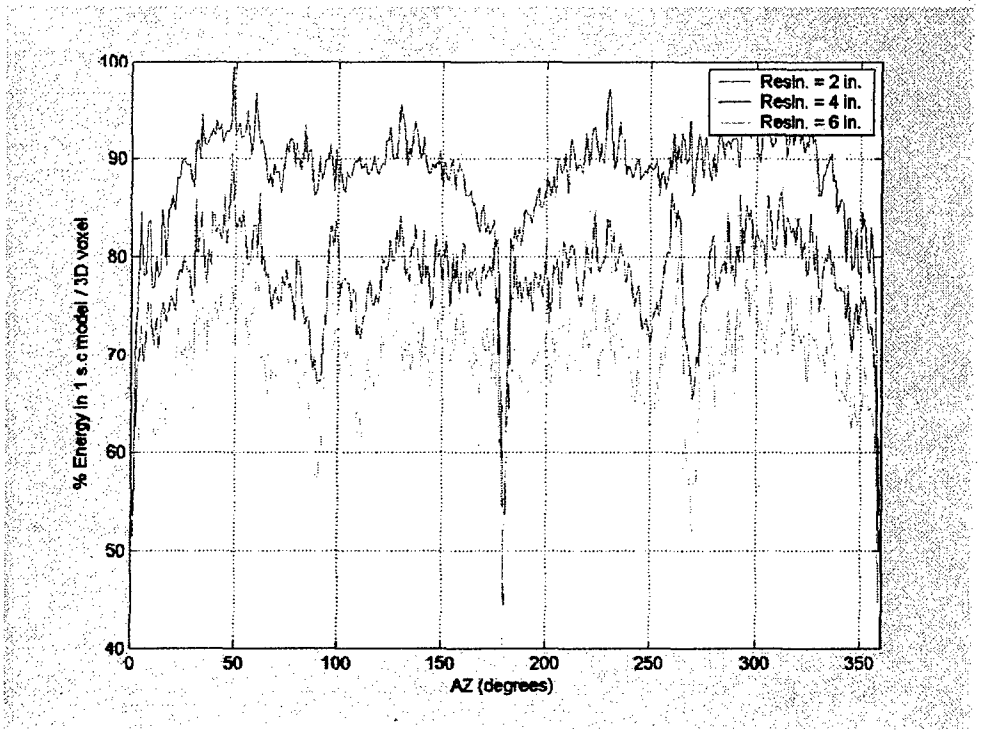

Fig. 7. The dominant scatterer energy in the SAR cell. A two-element IFSAR system resolves the height of the dominant scatterer in the SAR cell therefore as the contribution of the dominant scatterer decreases the error in height for the two-element system would correspondingly increase.

3-D SAR Image Formation from Sparse Aperture Data Using 3-D Target Grids

Rajan Bhalla*[a], Junfei Li[b] and Hao Ling[c]

[a]SAIC, 20 Burlington Mall Road, Suite 130, Burlington, MA 01803, USA
[b]Dept. of Electrical Engineering, The University of Texas - Pan American, Edinburg, TX 78541
[c]Department of Electrical Engineering , The University of Texas at Austin, Austin, TX 78712

ABSTRACT

The performance of ATR systems can potentially be improved by using three-dimensional (3-D) SAR images instead of the traditional two-dimensional SAR images or one-dimensional range profiles. 3-D SAR image formation of targets from radar backscattered data collected on wide angle, sparse apertures has been identified by AFRL as fundamental to building an object detection and recognition capability. A set of data has been released as a challenge problem. This paper describes a technique based on the concept of 3-D target grids aimed at the formation of 3-D SAR images of targets from sparse aperture data. The 3-D target grids capture the 3-D spatial and angular scattering properties of the target and serve as matched filters for SAR formation. The results of 3-D SAR formation using the backhoe public release data are presented.

Keywords: SAR, Sparse Apertures, Radar Imaging, Electromagnetic Scattering

1. INTRODUCTION

Constructing a synthetic aperture radar (SAR) image of a target requires data collection in both the frequency and angular dimensions. If the data is uniformly sampled and the sampling rate is dense enough to meet Nyquist sampling, a 2-D or 3-D SAR image can be obtained by using a two-dimensional or three-dimensional FFT algorithm [1]. However, in real-world data collection, this ideal situation can rarely be fulfilled in the angular aperture, especially in a 2-D angular aperture for 3-D image formation. Fig. 1 shows some possible examples of 2-D data collection apertures.

3-D SAR formation from seriously under-sampled data is in general an ill-posed inverse problem. A number of works have attempted to address this problem from the image processing perspective [2,3]. These approaches use parametric and non-parametric interpolation techniques to fill the gaps in the data. In this paper, we use an alternative approach. The ill-posed nature of this problem can be compensated to some extent using a priori information about the scattering characteristics of the target. One way to pose this problem is to ask the question – "Given a library of known targets, what is the best 3-D SAR image that can be obtained from the sparse data ?" This problem is easier to solve than the original problem with an unknown target. Our solution to this problem involves starting with a library of targets, capturing the scattering physics of the targets by the use of a set of "3-D target grids," and then forming the 3-D SAR images on these grids. These 3-D target grids can be interpreted to be model-based matched filters and hence behave as optimal linear detectors for SAR formation.

Our previous work on reconstructing 3-D SAR image from sparse apertures involved using an adaptive feature extraction (AFE) algorithm based on a general 3-D scattering center model [4,5,6]. AFE is an iterative back projection algorithm. The iteration loop is added specifically to overcome the high-sidelobe problem of the standard back projection. After range alignment, we assume that the range position is resolved via range compression. Our approach in this paper entails extending this approach and using a filter bank of 3-D target models to form 3-D SAR images. The 3-D target models are pre-computed to form 3-D target grids that capture the 3-D scattering behavior of the target and hence serve as a matched filter for the 3-D SAR reconstruction process. Using the library of targets for reconstruction can overcome some of the drawback of sparse apertures and significantly speed up the reconstruction of 3-D SAR images. A number of techniques have been proposed previously to enhance SAR images using filter banks, these

methods require either estimating or exhaustively searching through a bank of matched filters [17-23]. The approach proposed in this paper uses a matched filter bank predicted from the target and hence is optimal for that target. The SAR formation procedure is computationally efficient since it does not require exhaustive searching through a bank of matched filters.

This paper is organized as follows. In Section 2 we present our approach for forming 3-D SAR images from sparse apertures. In Section 3 we present results of the 3-D SAR image formation for sparse collection apertures on the AFRL public-release backhoe data [7,8].

2. APPROACH

In radar cross section studies, it is well known that the electromagnetic scattering from an electrically large target can be approximately modeled as if it is emanating from a discrete set of points on the target called scattering centers (see Fig. 2). The 3D scattering center model, while only an approximation, provides a useful sparse abstraction of the actual complex target in many radar applications. The 3-D scattering center model for a target with N_s scattering centers can be described as,

$$E(\bar{k}) = \sum_{i=1}^{N_s} \sigma_i e^{-j2\bar{k}\cdot\bar{r}_i} \tag{1}$$

where σ_i and r_i are the complex amplitude and location of the 3-D scattering centers respectively, $\bar{k}$ is the wave vector and $E(\bar{k})$ is the scattered field. This model can also be represented in the image domain and the 3-D SAR image of a target can be reconstructed from the scattering center model as,

$$\text{Image3D}(x,y,z) = \sum_{i=1}^{N_s} \sigma_i h(x-x_i, y-y_i, z-z_i) \tag{2}$$

where Image3D is the 3-D SAR image of the target and h(.) is the point spread response for the radar. An automated algorithm to extract the 3-D point scatterer model of a target from its geometrical computer-aided design (CAD) model based on the shooting and bouncing ray (SBR) method was developed in [9,10]. In this approach, we first generate the 3-D SAR image of the target based on a one-look SAR algorithm [11]. In step two, we use the image-processing algorithm CLEAN [12] to extract the 3-D position and strength of the scattering centers from the 3-D SAR image. This extraction algorithm has been tested extensively on canonical target sets as well as fairly complex models of air and ground targets and formed the basis of 2-D SAR simulation in DARPA's MSTAR program. For very complex targets, the scattering center model extracted at a particular aspect angle is not expected to be valid over all angular extent. This is due to shadowing and other complex multiple scattering phenomena. To fully characterize a target at all aspects, 3-D scattering center extraction will need to be carried out at various angles on a fairly dense grid in both elevation (θ) and azimuth (ϕ). Once the scattering center models are extracted at all the angles on the grid, we can obtain an global scattering center model by establishing correspondence between the scattering centers extracted at various aspect angles and mapping the angular visibility of the scattering centers. The 3-D point scatter models fused at various angles form a unified 3-D target grid for the target that represents the 3-D spatial and angular scattering properties of the target. The set of 3-D locations r_i localizing the scattering on the targets with its associated angular behavior $\sigma_i(\theta,\phi)$ forms a 3-D target grid, $\{r_i, \sigma_i\}$ and can be interpreted as a library of phenomenology-based basis functions for modeling the scattering from the target. Fig. 3 shows a set of 3-D CAD models and Fig. 4 shows the corresponding target grids for these targets. There are approximately 10000 3-D point scatterers in the examples shown in Fig. 4.

Our approach to form 3-D SAR images from sparse data is to form the images on the pre-determined 3-D target grids. Fig. 5 shows the flow diagram for this approach. Given a library of targets we extract the 3-D target grids using the process highlighted above. The 3-D SAR image can be obtained by projection of the radar data $E(\bar{k})$ on the 3-D target grid $\{r_i, \sigma_i\}_m$ for the m'th target as,

$$\{\hat{\sigma}_i\}_m = < E(\bar{k}), E'_m(\bar{k}) > \tag{3}$$

where $\{\hat{\sigma}_i\}_m$ is the normalized projection for the m'th target and $\{E_m^i(\bar{k})\}_i$ is the set of the target-specific phenomenology-based basis function for the m'th target defined as,

$$E_m^i(\bar{k}) = \sigma_i e^{-j2\bar{k}\cdot\bar{r}_i} \tag{4}$$

Since the 3-D target grid is non-uniformly sampled in the 3-D space, this projection can be performed more efficiently in the time domain. An objective function based on the image energy can be computed as,

$$Eg_n^m = \sum_{i=1}^{N_s} |\hat{\sigma}_i \sigma_i|^2 \tag{5}$$

where Eg_n^m is the energy in the m'th target. The best estimate of the 3-D SAR image is the one that maximizes the energy in the projection over the library of available 3-D target grids. Alternatively other objective or cost functions based on a combination of energy and entropy can also be used for selecting the 3-D target grid with the best projection. The 3-D SAR image can then be obtained from the projection parameters $\{\hat{\sigma}_i\}_m$ of the 3-D target grid with the maximum energy as,

$$Image3D(x,y,z) = \sum_{i=1}^{N_s} \hat{\sigma}_i \sigma_i \, h(x-x_i, y-y_i, z-z_i) \tag{6}$$

where $r_i = (x_i, y_i, z_i)$ Depending on the sparseness of the data we perform adaptive feature extraction to the approach highlighted earlier. Adaptive feature extraction (AFE) is a model-based signal processing method that is similar to CLEAN and the matching pursuit algorithm [13]. AFE can compensate for the high sidelobes in the image. The basic idea is to extract the strongest point scatterer first. Then the response from this point scatterer is subtracted from the total signal. The process is then iterated for the remaining point scatterers.

3-D target grid can be interpreted to be the matched filter for the 3-D target since the radar data projected onto the grid is matched to the spatial and angular scattering behavior of the target. The 3-D target grid does filter out some of the high side lobes due to the sparseness of the data and the AFE algorithm can be used to improve its performance. The 3-D SAR image obtained is a "best estimate" obtained under the assumption that the target being measured is actually present in the library. An energy criterion can be used to rule out projections without significant energy. For the case in which part of the targets may be occluded the 3-D target grids should be sub-divided into smaller grids and the 3-D SAR image be formed in parts. We will next present some results to evaluate the 3-D SAR image reconstruction using this approach highlighted above.

3. RESULTS

We will use the backhoe sample data released in SPIE, 04. Fig. 6. shows the backhoe target and a sample 2-D and 3-D SAR image from the data set. The 2-D image was generated using an 18° aperture. The 3-D image was generated using a full 2-D aperture of 18°. The resolution of the images is 2 inches at a center frequency of 10 GHz. Fig. 6(c) shows the overlay of the 3-D SAR image with the 3-D CAD of the target. This visualization was performed using the E3Doer® package distributed by SAIC. The library chosen for this study consists of three targets: (1) a car, (2), the backhoe, and (3) a tank shown in Fig. 3. The corresponding 3-D target grids were generated for these targets and are shown in Fig. 4. There are approximately 10000 point scatterers in the 3-D target grids. Given a library of targets the corresponding 3-D projection on the 3-D target grids can be obtained. An airborne sensor flying along a racetrack path around the target as shown in Fig. 7 is chosen to generate the 3-D SAR image. The 360° aperture around the target is then broken up into 36 sub-apertures. In each of the 10° sub-aperture the path involves the sensor flying diagonally along the elevation and azimuth dimensions. The sensor collects data for only part of its aperture. In this example only 6° of the 10° aperture is used. The backhoe radar data from the dome corresponding to the flight path is then selected and projected on to the library of filter banks containing the 3-D target grids. A 3-D SAR image for each 36 sector is computed for each target grid to yield 36 3-D SAR images. These 36 3-D SAR images are then fused to yield a composite 3-D SAR image for the complete target. The composite 3-D SAR images for the 3 target grids in the library are shown in Fig. 8. Also a brute-force 3-D SAR image utilizing a full 2-D 18° aperture corresponding to the

racetrack pattern is computed from the data. As can be seen from Fig. 8, the backhoe reconstructed on the 3-D target grid matches the brute-force image very well. The energies in the 3-D SAR images for the tank and the car are both less that 1% and hence a simple relative energy threshold criterion can be used to rule out these images as being the correct target. Though only 3 target are chosen in this particular example a bigger library does not significantly increase the computation time since the 3-D target grids can be binned and the bins common among the 3D target grids do not need to be recomputed.

4. CONCLUSION

In this paper we presented an innovative technique to form 3-D SAR images from sparse apertures. The 3-D SAR formation process consisted of projecting the radar data onto a library of target-specific phenomenology-based basis functions called 3-D target grids. The best estimate of the 3-D SAR image was chosen based on an energy objective function. The 3-D target grids captured the angular and spatial scattering behavior of the target and served as matched filter. Preliminary results from this technique appeared to be encouraging. If more than one sensor is available on the air platform then 3-D images can also be alternatively formed using an IFSAR approach [14,15,16].

Acknowledgements

The authors would like to thank Gerard Titi at DARPA and Edmund Zelnio, Dr. Vince Velten, Mike Minardi, Dr. Ron Dilsavor, Kiran Naidu and Tom Majumder at Air Force Research Lab for valuable guidance and useful discussions.

REFERENCES

1. W. G. Carrara, R. S. Goodman and R. M. Majewski, *Spotlight Synthetic Aperture Radar - Signal Processing and Algorithms*, Artech House, Boston, MA, 1995.
2. P. Stoica, E.G. Larsson, and J. Li, "Adaptive filterbank approach to restoration and spectral analysis of gapped data," *The Astronomical Journal*, Vol. 120, pp. 2163-2173, October 2000.
3. M. D. Sacchi, T. J. Ulrych and C. J. Walker, "Interpolation and extrapolation using a high-resolution discrete Fourier transform", *IEEE Trans. Signal Processing*, 46, pp. 31-38, 1998.
4. Y. Wang and H. Ling, "Adaptive ISAR image construction from unevenly undersampled data," *IEEE Trans. Antennas Propagat.*, vol. AP-48, pp. 329-331, February 2000.
5. J. Li, H, Ling and V. C. Chen, "An algorithm to detect the presence of 3D target motion from ISAR data," *Multidimensional Systems and Signal Processing*, Special Issue on Radar Signal Processing and Its Applications, vol. 14, no. 1, pp. 223-240, January 2003.
6. J. Li and H. Ling, "3D ISAR image reconstruction of a target with pose data using adaptive feature extraction," *Journal of Electromagnetic Waves and Applications*, vol. 15, no. 11, pp. 1571-1587, November 2001.
7. G. Titi, E. Zelnio, K. Naidu, R. Dilsavor, M. Minardi, N. Subotic, R. Moses, L. Potter, L. Lin, R. Bhalla, and J. Nehrbass, "Visual SAR Using All Degrees of Freedom", *MSS Tri-Service Radar Symposium*, Albuquerque, NM, June 21-25, 2004.
8. Visual-D Challenge Problem and Backhoe Sample Data, AFRL/SNAS, May 2004.
9. R. Bhalla and H. Ling, "3D scattering center extraction of complex targets using the shooting and bouncing ray technique," *IEEE Trans. Antennas Propagat.*, vol. 44, pp. 1445-1453, Nov. 1996.
10. R. Bhalla, J. Moore and H. Ling, "A global scattering center representation of complex targets using the shooting and bouncing ray technique," *IEEE Trans. Antennas Propagat.*, vol. AP-45, pp. 1850-1856, December 1997.
11. R. Bhalla and H. Ling, "A fast algorithm for signature prediction and image formation using the shooting and bouncing ray technique," *IEEE Trans. Antennas Propagat.*, vol. AP-43, pp. 727-731, July 1995.
12. J. Tsao and B. D. Steinberg, "Reduction of sidelobe and speckle artifacts in microwave imaging: the CLEAN technique," *IEEE Trans. Antennas and Propagat.*, vol. 36, no.4, pp. 543-556, Apr. 1988.
13. S. G. Mallat and Z. Zhang, "Matching pursuits with time-frequency dictionaries," *IEEE Trans. Signal Processing*, vol. 41, no. 12, pp. 3397-3415, Dec. 1993.
14. R. Bhalla, H. Ling and B. Houshmand, "IFSAR simulation using the shooting and bouncing ray technique," URSI National Radio Science Meeting, p. 152, Orlando, FL, July 1999.

15. R. Bhalla and H. Ling, "IFSAR Modeling of Terrain and Target using a Ray-based Electromagnetic Technique," *Proceeding of the IASTED International Conference*, ARP 2004, pp. 186-190, July 2004.
16. R. Bhalla and H. Ling, "Multi-Baseline IFSAR Study using a SBR based Simulator," to appear in *SPIE Defence and Security Symposium '05, Algorithms for Synthetic Aperture Radar Imagery*, Orlando, FL, March 2005.
17. S. DeGraaf, "SAR imaging via modern 2-D spectral estimation methods," *IEEE Transactions on Image Processing* 7, pp. 729–761, May 1998.
18. D. Rossi and A. Willsky, "Reconstruction from projections based on detection and estimation of objects–Parts I and II: Performance analysis and robustness analysis," *IEEE Transactions on Acoustics, Speech, and Signal Processing* 32, pp. 886–906, August 1984.
19. M. R. Allen and L. E. Ho, "Wide-angle wideband SAR matched filter image formation for enhanced detection performace," *SPIE Symposium, Algorithms for Synthetic Aperture Radar Imagery*, 2230, pp. 302–314, Orlando, FL, April 1994.
20. L. C. Trintinalia, R. Bhalla, and H. Ling, "Scattering center parameterization of wide-angle backscattered data using adaptive Gaussian representation," *IEEE Transactions on Antennas and Propagation*, 45, pp. 1664–1668, November 1997.
21. R. L. Moses, L. Potter, and M. Çetin, "Wide Angle SAR Imaging," *SPIE Defense and Security Symposium, Algorithms for Synthetic Aperture Radar Imagery XI*, E. G. Zelnio and F. D. Garber, Eds., Orlando, Florida.
22. R. D. Chaney, A. S. Willsky, and L. M. Novak, "Coherent aspect-dependent SAR image formation," *SPIE Symposium, Algorithms for Synthetic Aperture Radar Imagery*, 2230, pp. 256–274, Orlando, FL, April 1994.
23. E. G. Larsonn, G. Liu, P. Stoica, and J. Li, "High-resolution SAR imaging with angular diversity," *IEEE Transactions on Aerospace and Electronic Systems*, 37, pp. 1359–1372, October 2001.

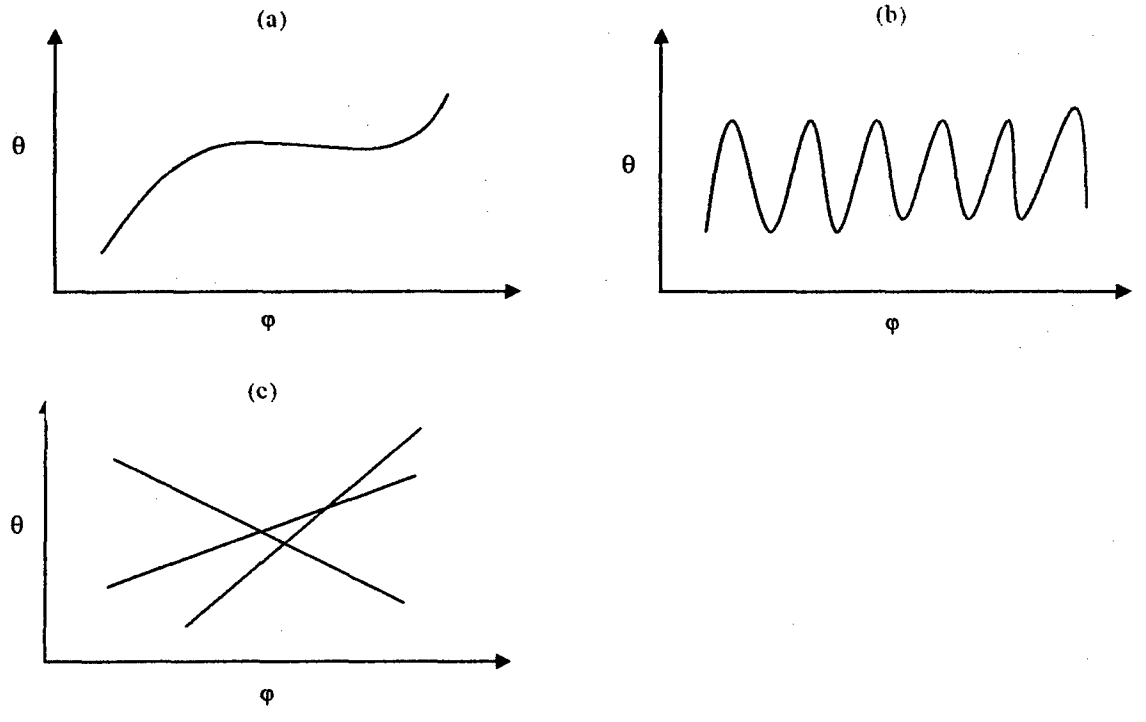

Fig. 1. Possible sparse angular apertures encountered in SAR data collection.

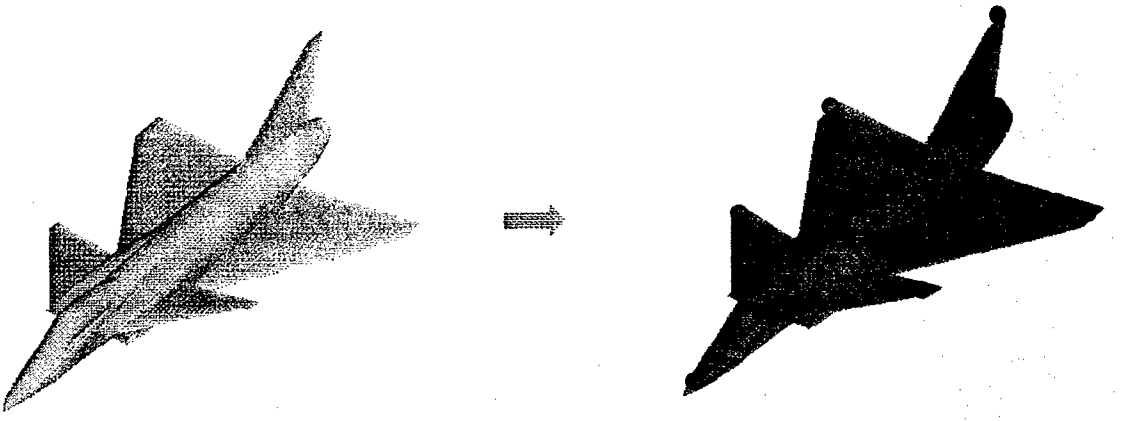

Fig. 2. A 3-D scattering representation of the target. The scattering from the target can be modeled as if emanating from a discrete set of sparse 3-D points.

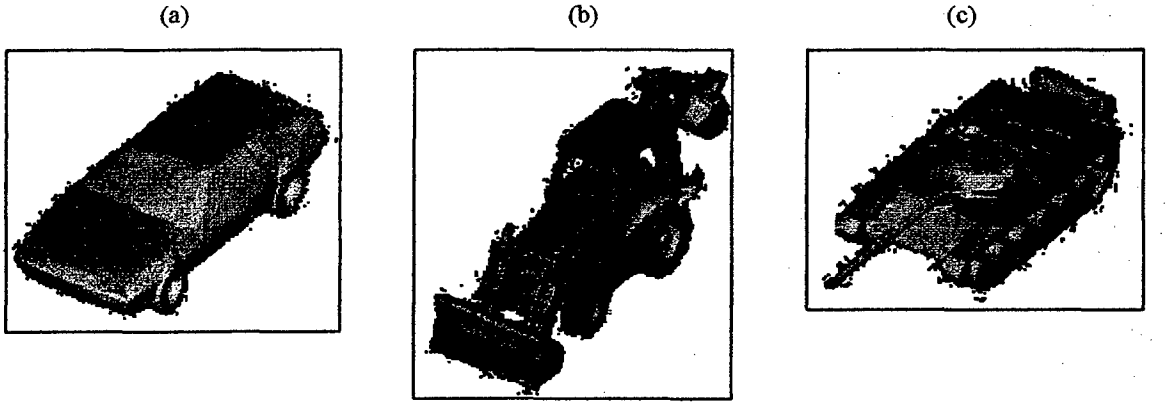

Fig. 3. The CAD model of targets used in the library. (a) car, (b) backhoe, (c) tank.

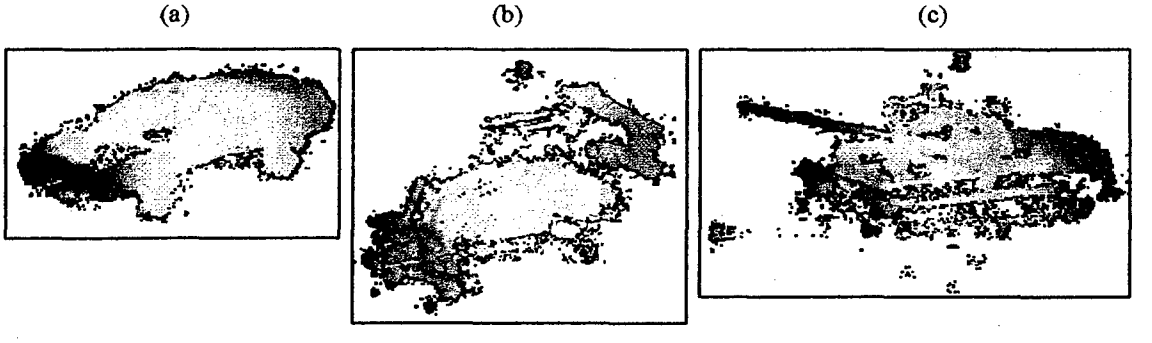

Fig. 4. The 3-D target grid for the library of targets. (a) car, (b) backhoe, (c) tank. The 3-D target grids are color-coded based on the x-axis for ease of 3-D visualizations. The average number of 3D points in the 3-D target grids is about 10000.

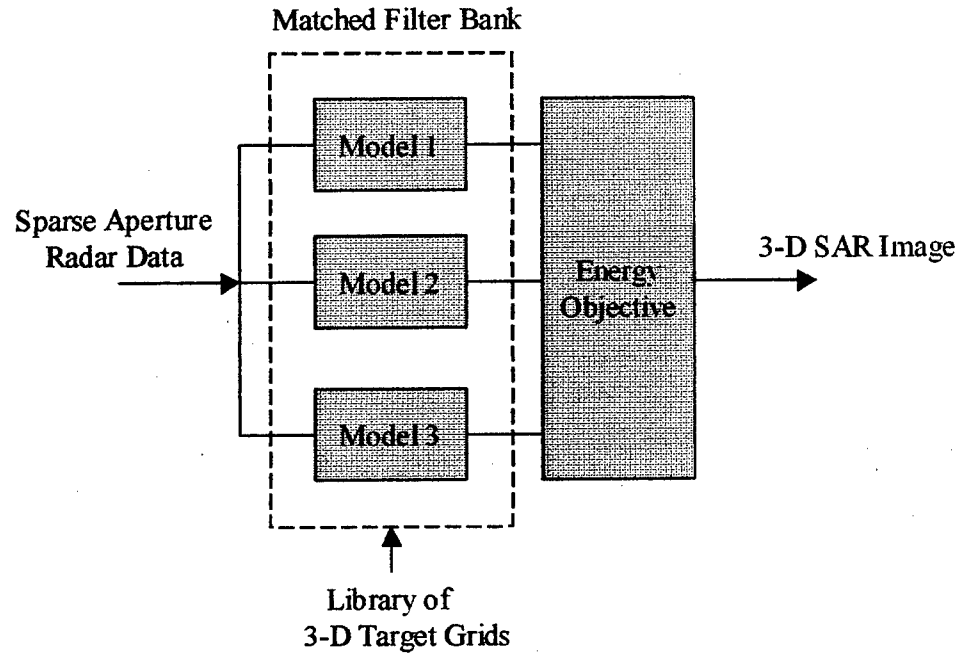

Fig. 5. Flow diagram of the 3-D SAR formation algorithm. A library of 3-D target grids is used for 3-D SAR formation. The sparse data are projected on the matched filter bank of 3-D target grids. The "best estimate" of the 3-D SAR image from the library is selected based on a cost function.

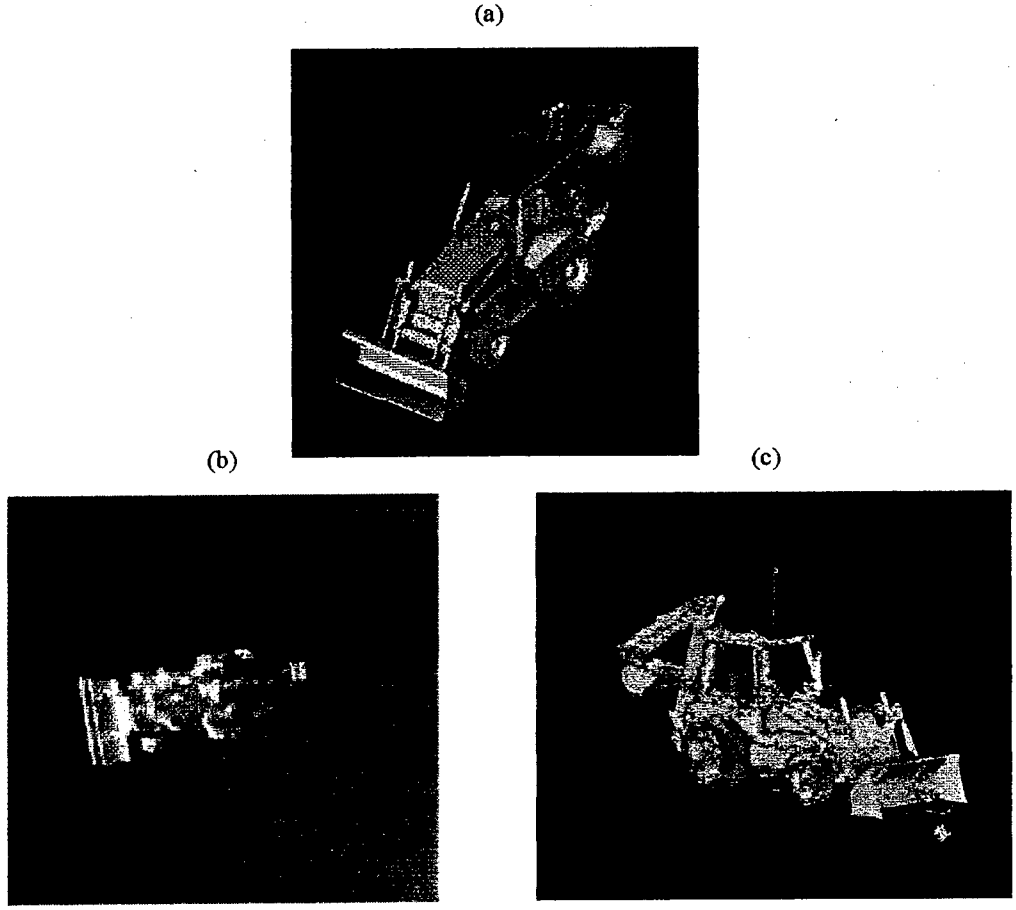

Fig. 6. The backhoe public release data. (a) Backhoe CAD model. (b) 2-D SAR image of the backhoe target. (c) 3-D SAR image of the backhoe target. The 2-D SAR image was generated using an 18° aperture. The 3-D SAR image was generated using an 18° 2-D aperture centered at (AZ,EL)=(10°,30°) at a center frequency of 10 GHz and resolution of 2 inches.

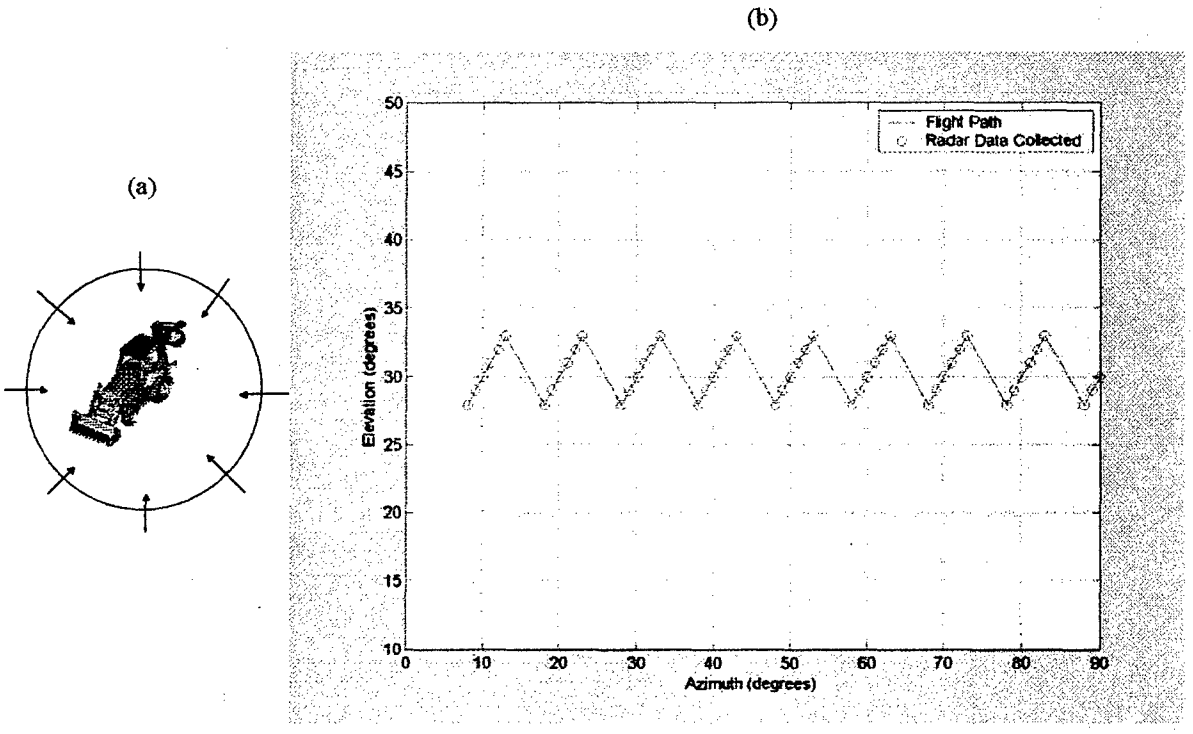

Fig. 7. The flight path used to collect sparse radar data from the data dome for 3-D SAR formation. (a) The sensor flys in a racetrack pattern around the target. (b) 6° degree data segments in each 10° data sector are used. Only one quadrant (0°-90°) is shown in the figure. The data used in image formation are shown with red circles.

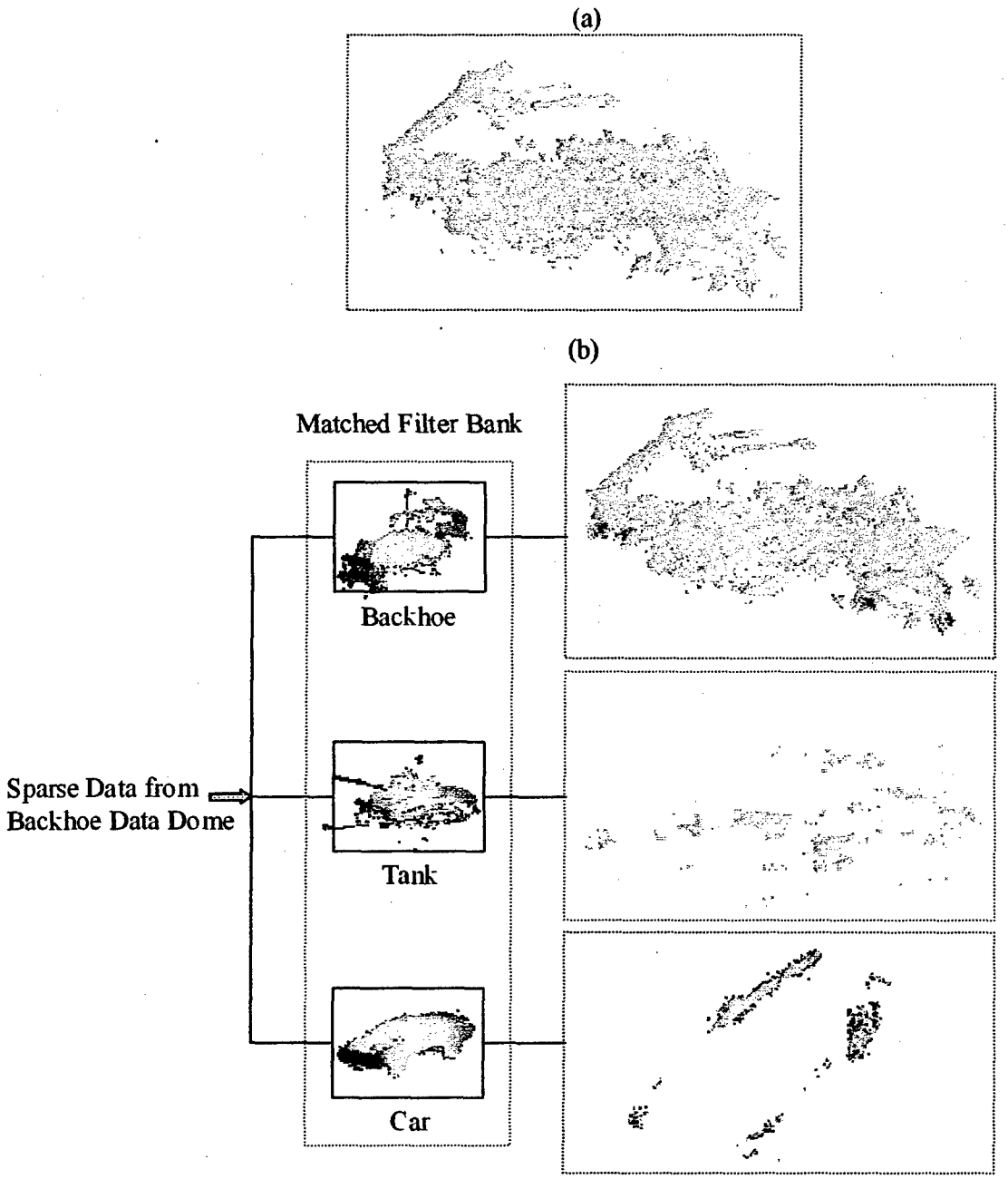

Fig. 8. The 3-D SAR image formed on the library of 3-D target grids. (a) 3-D SAR image using the full 18° 2-D aperture from the data dome. (b) 3-D SAR image for the library of 3-D target grids using a sparse aperture. The 3-D SAR images are plotted with 40 dB of dynamic range. Red in the SAR image is high and the magnitude scales as RGB (Red-Green-Blue).

Human Tracking Using a Two-Element Antenna Array

Adrian Lin and Hao Ling
Department of Electrical and Computer Engineering
The University of Texas at Austin
Austin, TX 78712

ABSTRACT

We investigate the use of a low-cost, two-element receiving array for tracking human movements in indoor surveillance applications. Conventional direction of arrival (DOA) detection requires the use of an antenna array with multiple elements. Here we investigate the use of only two elements in the receiver array. The concept entails simultaneously resolving the Doppler frequencies of the returned signals from the moving targets and the DOA of the targets. Simulation is performed to demonstrate the concept. Both the monostatic and the bistatic scenario where the transmitter and the receiving array are placed at different locations are investigated. DOA errors and tolerances are analyzed for each scenario. An experimental system is constructed to test the concept. The system consists of a two-element receiver array operating at 2.4 GHz. Measurement results of various collection scenarios are presented.

Keywords: Doppler, direction of arrival, radar, human tracking

1. INTRODUCTION

We explore the use of a low-cost, two-element receiving array for tracking human movements. The direction of arrival (DOA) of a moving human is obtained from the phase difference of the reflected waves arriving at the two receiver antennas. However, a two-element receiving array is unable to resolve individual DOA from multiple moving humans due to multiple phase differences arriving simultaneously at the two receiving antennas. Conventional methods are to increase the number of receiving elements and to apply direction finding algorithms such as MUSIC [1-3]. We investigate a way to overcome this issue while maintaining the use of a two-element receiving array for human tracking.

The basic concept of our approach is to detect both the Doppler frequency and the DOA information of the movers. Under a monostatic scenario, Doppler discrimination allows the detection of multiple movers, depending on the unique combination of speed and direction of each mover. An extra degree of discrimination freedom can be achieved in a bistatic scenario since the incident and reflected wave vectors of each mover are different, depending on the transmitter and receiver placement.

Extensive Monte Carlo simulation is performed to demonstrate the concept. Both the monostatic scenario and the bistatic scenario where the transmitter and the receiving array are placed at different locations are investigated. DOA errors resulting from the imperfect Doppler discrimination are analyzed for each scenario.

An experimental system is constructed to test the concept. The system consists of a two-element antenna array, dual-quadrature integrated receivers (Analog Devices AD8347 ICs) and a transmitter operating at a frequency of 2.4 GHz. Microstrip antennas are used, resulting in a small form factor. The received signals are downconverted, digitized and processed using the FFT for Doppler and DOA calculations.

Measurement results of the DOA from multiple targets are presented. The limitations of the proposed system resulting from DOA ambiguity of multiple moving targets are studied.

2. METHODOLOGY

Our radar receiver consists of a two-element direction-finding array, each with full quadrature detectors, to determine both the Doppler shift and the direction of arrival of the target. The transmitter uses a continuous wave (CW) operating at 2.4 GHz carrier frequency. The position of the transmitter and receiver can be arranged in a monostatic or a bistatic configuration.

In the monostatic configuration, the radar transmitter and receiver are co-located with Doppler shift given by $f_D = 2v/\lambda_c$. In the bistatic configuration, the radar transmitter and receiver are not located at the same position and the Doppler shift is given by $f_D = (\mathbf{u_r}-\mathbf{u_i})\bullet\mathbf{v}/\lambda_c$. The bistatic radar Doppler frequency is related to the component of target velocity v along the difference of the reflected and incident unit vectors, $(\mathbf{u_r}-\mathbf{u_i})$, and λ_c is the wavelength of the transmitted carrier. Since the Doppler shift is only induced for a moving target, Doppler sensing provides very good clutter suppression in a highly cluttered environment such as indoors.

The DOA of the received signal can be obtained by the measured phase difference of the two array outputs, $\Delta\phi = \phi_2 - \phi_1$, as follows: $\theta = sin^{-1}(\lambda_c\Delta\phi/2\pi d)$ where d is the spacing between the two antennas (Fig. 1). To provide the maximum resolution while avoiding DOA ambiguity within the scanning range of θ from -90° to 90°, the distance between the two antennas is set to $\lambda_c/2$.

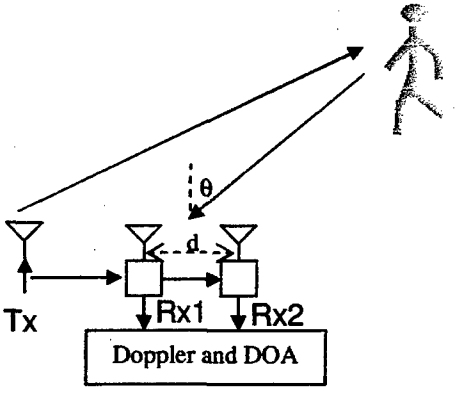

Figure 1. Basic radar operation.

For proof-of-concept, we have constructed a low-cost system that consists of a transmitter and a two-element direction-finding array. For the transmitter, an RF signal generator capable of outputting CW frequency at 2.4 GHz is utilized. For the receiver, an off-the-shelf IC receiver manufactured by Analog Devices (AD8347) is used. This integrated receiver has all the required features including low-noise amplifier (LNA), I/Q mixers, gain control, and baseband amplification. Low-pass filtering with a cut-off frequency of 250 Hz is used for anti-aliasing before the A/D converter. The National Instruments NI-DAC 6024E is used for digitizing the receiver output. Fig. 2 shows the system block diagram and the actual radar implementation.

The signals reflected from the moving targets are received, downconverted, digitized and processed using the FFT for Doppler discrimination. By measuring the phase difference at each Doppler frequency component, we can obtain the DOA information of multiple targets. This scheme works as long as their Doppler frequencies are sufficiently distinct. We discuss in the following section several cases where erroneous DOA information might occur as the result of poor Doppler discrimination.

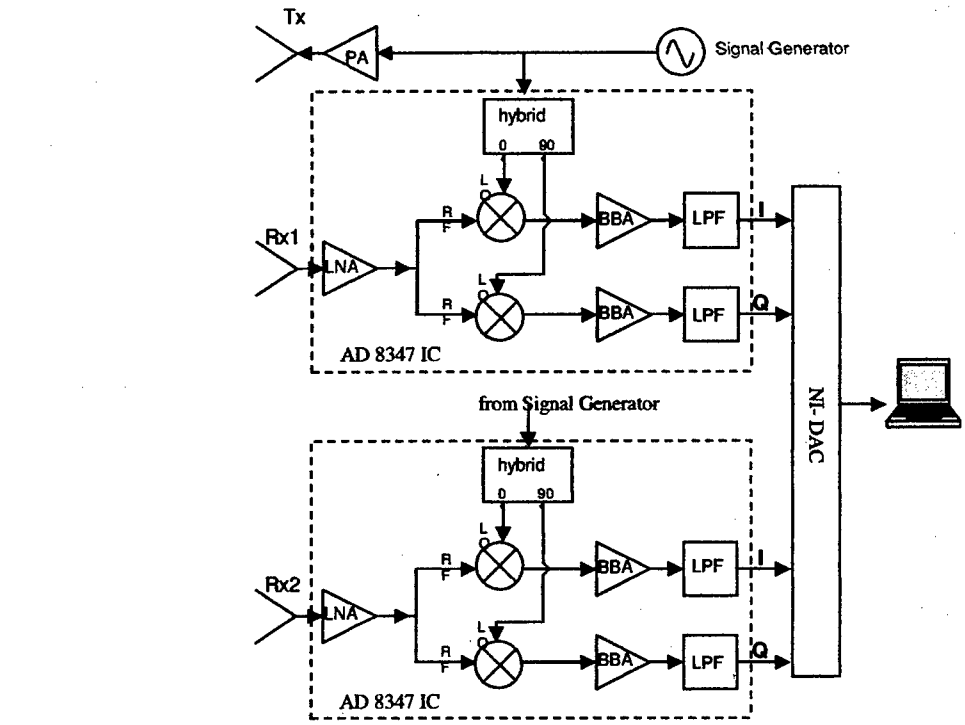

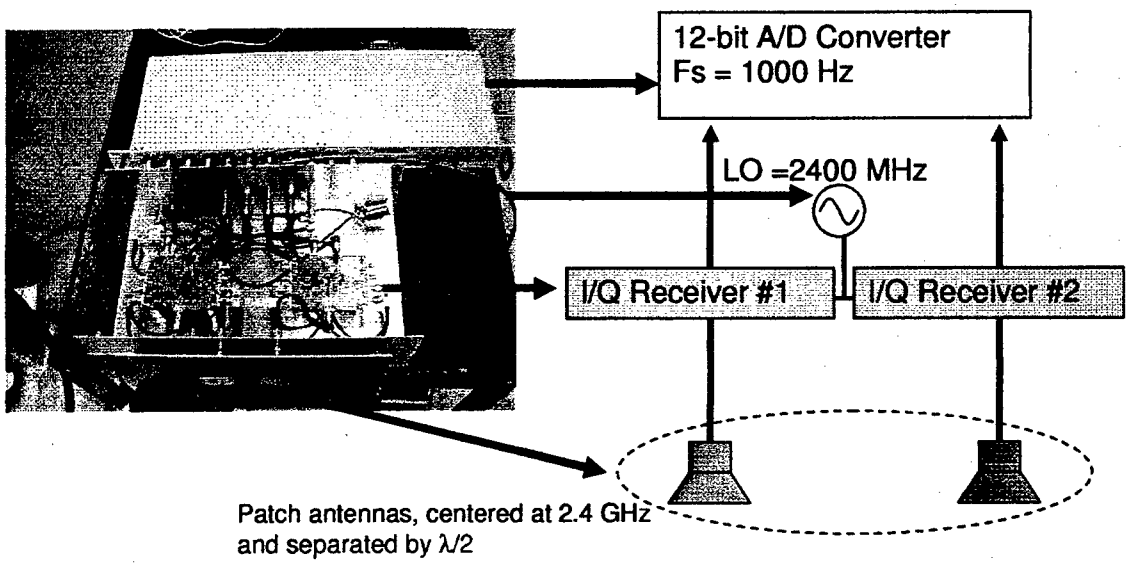

Figure 2. Radar system block diagram and actual hardware implementation.

3. SIMULATION DATA

Fig. 3 shows the simulation result of the Doppler and DOA from two moving targets. The Doppler of the first target is 8 Hz with a DOA of -20° while the second target has 80 Hz Doppler and +20° DOA. Both Doppler returns have the same received power level. Under this Doppler spacing (8:80), the detection algorithm produces the correct DOA information for both targets. The Doppler of the first target is then increased to 76 Hz while its DOA is kept at -20°. With the reduced Doppler spacing (76:80), the DOA of the two targets become hard to identify and are erroneous (as shown in Fig. 4). To predict the DOA error behavior as the result of reduced Doppler discrimination, we run a more exhaustive Monte-Carlo simulation with more realistic input parameters.

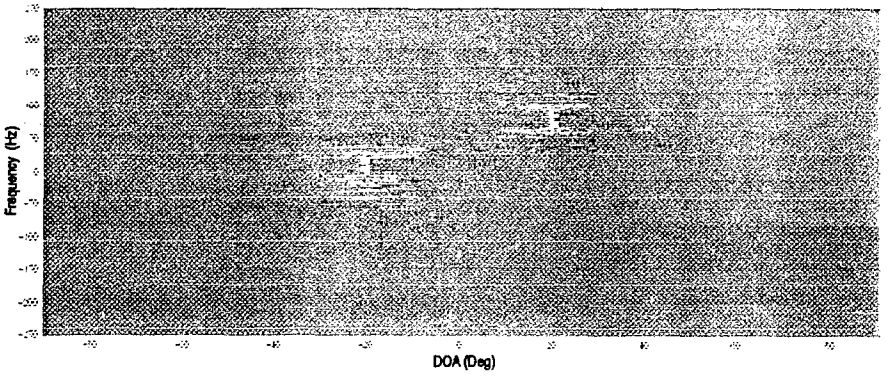

Figure 3. Doppler and DOA simulation result of two moving targets (Doppler spacing 8:80).

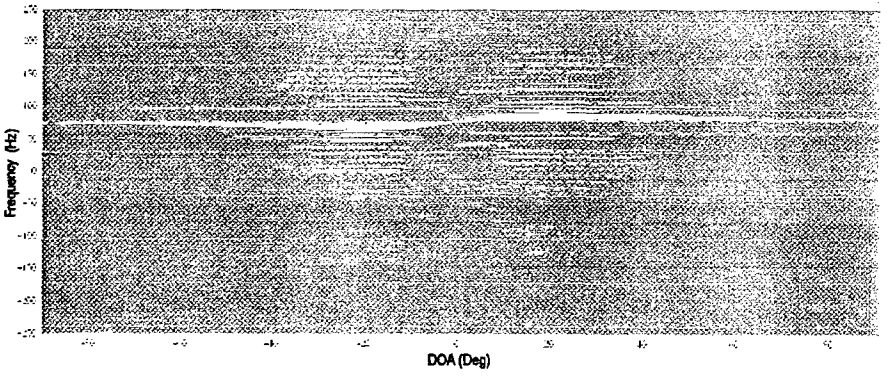

Figure 4. Doppler and DOA simulation result of two moving targets (Doppler spacing 76:80).

The simulations input parameters include a spatial boundary of 10 m by 10 m, moving speed with a uniform distribution from 0 m/s to 6 m/s, and a velocity direction that is uniformly distributed from 0 to 2π. Two moving targets are placed inside the boundary with the given speed and velocity range. These parameters are used to mimic a typical office environment of 10 m by 10 m with two moving humans. Amplitude decay as a function of distance is also calculated and accounted for in the simulation to evaluate the effect of the received signal strengths of the two targets. Fig. 5 illustrates the simulation setup. The receiver and transmitter coordinates are shown for the monostatic and bistatic configurations.

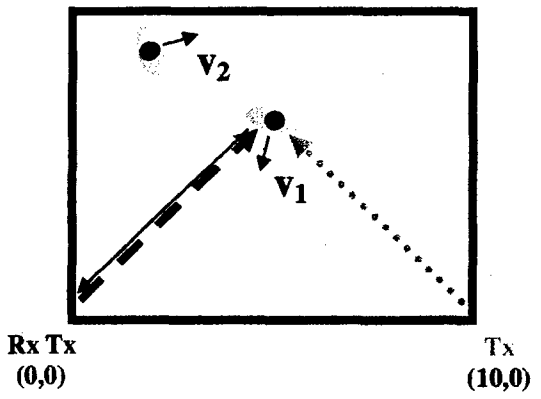

Figure 5. Simulation setup for two moving targets in a spatial boundary of 10 m by 10 m.

The first simulation case uses the monostatic configuration where both the receiver and transmitter are co-located at the (0,0) coordinate. One hundred thousand realizations are generated. The DOA errors with respect to the Doppler discrimination of the two moving targets are calculated and plotted. Fig. 6(a) shows the simulation result using the Kaiser window with the smallest main-lobe setting (but the highest side-lobes). The different color/grey shades indicate the relative signal strengths between the two targets, with the lighter shades representing more similar strengths. As expected, the DOA error is the largest when the Doppler separation between the targets is the smallest, and vice versa.

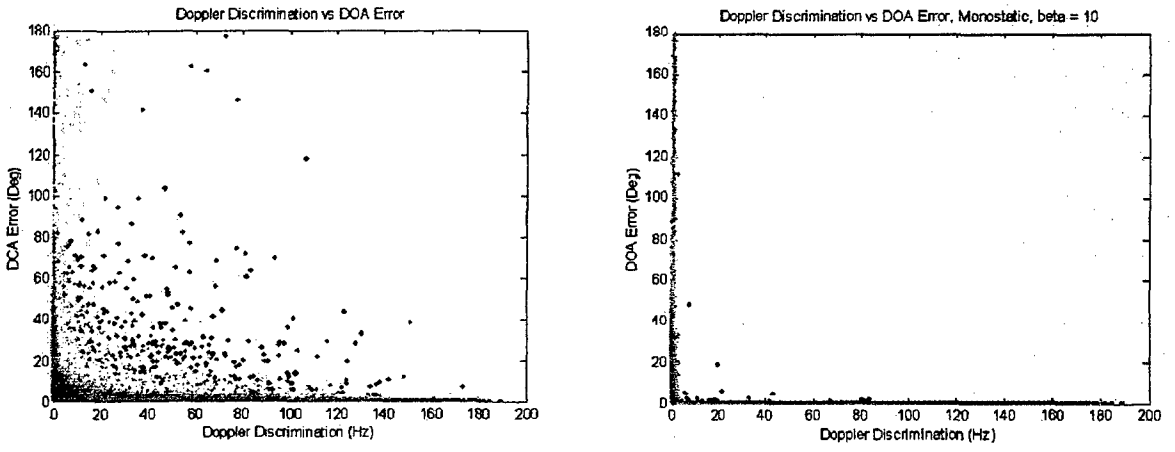

(a) (b)

Figure 6. Monostatic simulation results using a Kaiser window with: (a) Highest side-lobes and (b) Reduced side-lobes.

However, there are also cases that contain large DOA errors even though the Doppler separations are large. From the darkness of the points, we also know that they correspond to cases where there is a significant difference in signal strengths (larger than 50 dB). This is caused by one target located much closer to the radar (thus much larger signal strength) than the other. This phenomenon is referred to as the close-far effect, where the side-lobe energy from the stronger, close-in target contaminates the much weaker, far-away target in its frequency bins. One way to mitigate the close-far effect is to decrease the side-lobe energy by setting the Kaiser window parameter accordingly. Fig. 6(b) shows the simulation result with the lower side-lobe window. This time there are much fewer occurrences of the DOA error due to the close-far effect.

We repeat the simulations above for the bistatic configuration where the radar receiver is located at (0,0) and the transmitter is at (10,0). Fig. 7(a) shows the simulation result with the highest side-lobe window setting. The DOA error trend is very similar to the monostatic case, but there are fewer occurrences of the close-far effect. With a lower side-lobe window setting, the close-far effect is hardly noticeable, as shown in Fig. 7(b). We verify the simulation cases above by measurements and discuss the results in the following section.

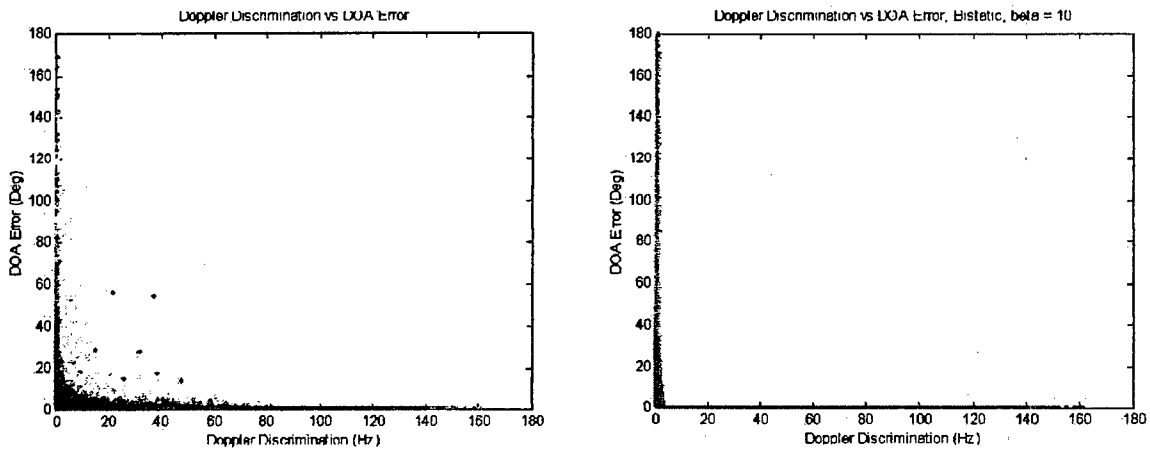

(a) (b)

Figure 7. Bistatic simulation results using a Kaiser window with: (a) Highest side-lobes and (b) Reduced side-lobes.

4. MEASUREMENT RESULTS

To demonstrate the multiple target detection, we use two loudspeakers as stable test targets. The vibrating membrane of each loudspeaker is covered by aluminum tape to enhance its return. The audio tone causes the loudspeaker membrane to vibrate back and forth and the radar return is an FM signal. The two loudspeakers are placed at -25°and +15° to the radar boresight and driven by a 55 Hz and a 35 Hz audio tone, respectively. Both loudspeakers are located at about 15 feet away from the radar (Fig. 8(a)). Their expected Doppler returns are +/- 55 Hz and +/- 35 Hz with the DOA of -25° and +15°, respectively. The measured data are plotted in Fig. 8(b) and clearly show the expected returns.

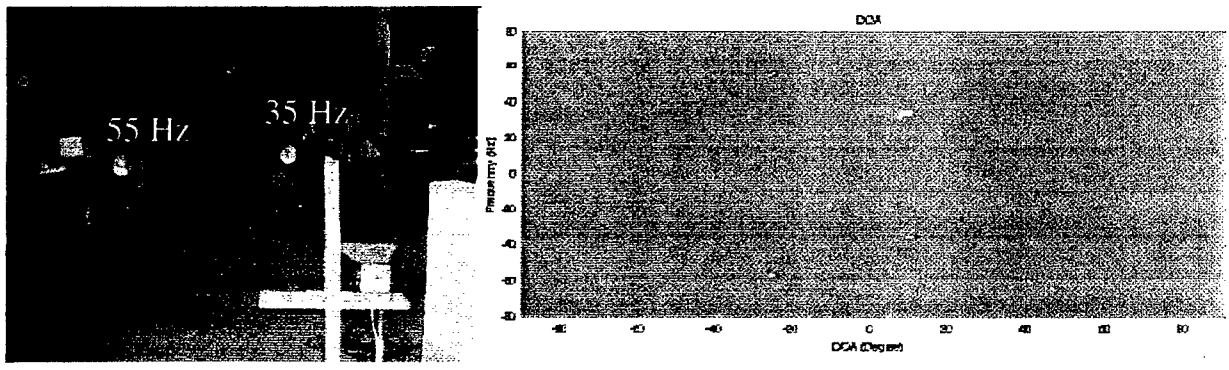

(a) (b)

Figure 8. Measurement results of two loudspeakers: (a) Setup and (b) Measured Doppler and DOA.

Moving human detection is next demonstrated. Two people move in the room with the person on the left (-15°) moving away and the person on the right (+20°) moving toward the radar. The measured Doppler and DOA returns are shown in Fig. 9. The wider Doppler spread is caused by the higher-order movements (arm/leg swings). These higher-order movements result in microDoppler returns [4, 5]. The measurement is taken with 0.5 second refresh time resulting in a wider DOA angle spread depicting the accumulated Dopplers during the 0.5 second duration. This is analogous to when a fast moving object is photographed with slow shutter speed.

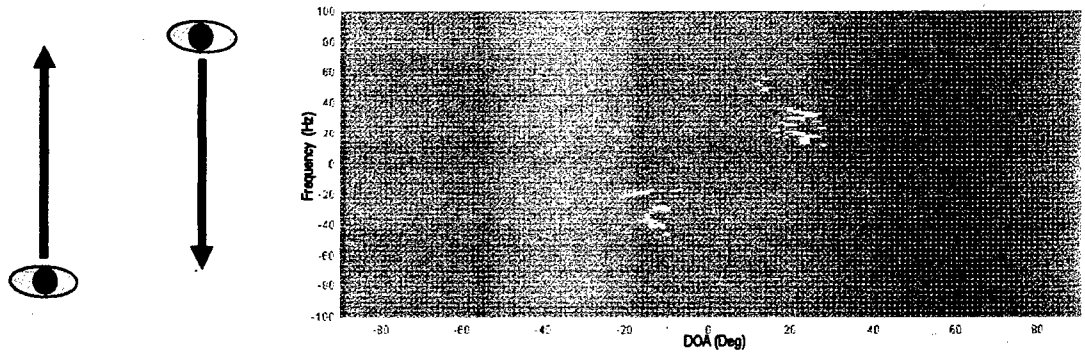

Figure 9. Doppler and DOA measurement results of two people walking in opposite directions.

The next set of measurement results shows the close-far phenomenon. First the monostatic configuration is used in an outdoor setting (Fig. 10(a)). The two loudspeakers are placed at -20°and -10° to the radar boresight and driven by 75 Hz and 55 Hz audio tones, respectively. The loudspeaker at -20° is located at 3 feet from the radar while the other one (at -10°) is at 42 feet away. As predicted by the simulation, the monostatic case clearly shows the close-far effect where the incorrect DOA is measured for the far-away target as shown in Fig. 10(b). The closer loudspeaker dominates the Doppler return of the far-away one, causing both DOA to be -20° (instead of -20°and -10°). In the bistatic configuration (Fig. 11(a)), the transmitter is placed at equidistance from the two loudspeakers. As shown in Fig. 11(b), this time the correct DOA are measured for both targets (-20°and -10°).

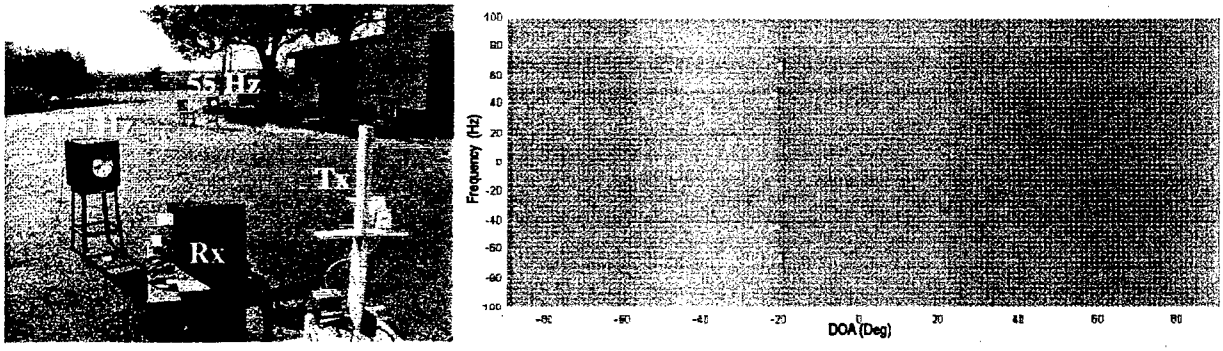

(a) (b)

Figure 10. Close-far monostatic measurement of two loudspeakers: (a) Setup and (b) Measured Doppler and DOA.

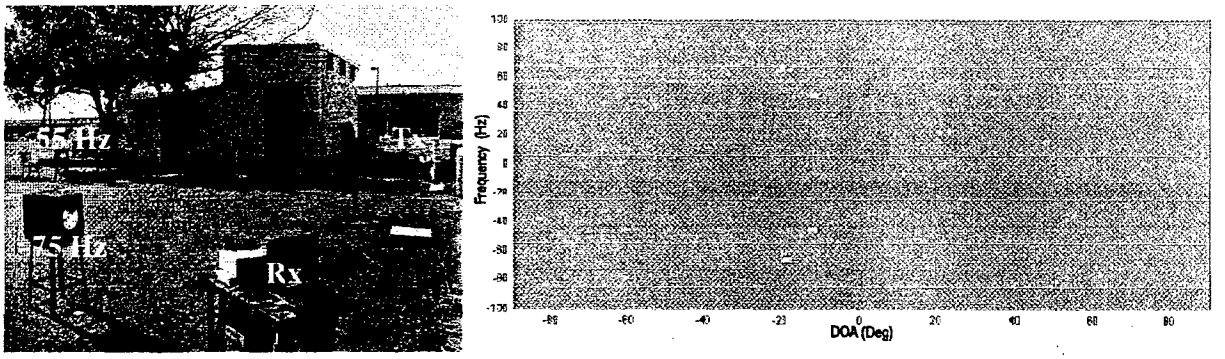

(a) (b)

Figure 11. Close-far bistatic measurement of two loudspeakers: (a) Setup and (b) Measured Doppler and DOA.

5. CONCLUSIONS

Doppler and DOA simulation and measurement results of multiple moving targets have been presented. The measurements were performed using a low-cost, two-element receiver array operating at 2.4 GHz. Based on our measurement results, it is shown that simultaneous DOA detection of multiple movers using a two-element array is feasible. Our study also shows that the DOA accuracy is influenced by the Doppler separation and the close-far effect. Both our simulation and measurement results show that the bistatic radar configuration can be used to mitigate the close-far effect thus improving the DOA accuracy.

ACKNOWLEDGMENT

This work is supported by the Office of Naval Research and the Texas Higher Education Coordinating Board under the Texas Advanced Technology Program.

REFERENCES

[1] H. Mewes, J.L. ter Haseborg, F. Wolf, "A multichannel direction finding system", *Proc. IEEE Antennas Propagat. Soc. Int. Symp.*, pp 682-685, June 28-July 2 1993.

[2] T. Svantesson, M. Wennstrom, "High-Resolution direction finding using a switched parasitic antenna", *Proc. 11th IEEE Sig. Processing Workshop on Statistical Sig. Processing*, pp 508-511, Aug 6-8, 2001.

[3] J.G. Worms, "RF direction finding with a reduced number of receivers by sequential sampling", *Proc. IEEE Int. Conf. on Phased Array Sys. and Tech.*, pp 165-168, May 21-25 2000.

[4] J. L. Geisheimer, E. F. Greneker and W. S. Marshall, "High-resolution Doppler model of the human gait," *SPIE Proc., Radar Sensor Technology and Data Visualization*, vol. 4744, pp. 8-18, July 2002.

[5] H. Ling, "MicroDoppler exploitation: data collection and analysis," Naval International Cooperative Opportunities in Science and Technology (NICOP) program on Time-Frequency ISAR and NCTI, London, England, June 2004.

Through-Wall Measurements of a Doppler and Direction-of-Arrival (DDOA) Radar for Tracking Indoor Movers

Adrian Lin* and Hao Ling
Department of Electrical and Computer Engineering
University of Texas at Austin
Austin, TX 78712, USA

Introduction

Increasing demands on security and surveillance systems in military and law enforcement applications have prompted studies on through-wall detection of moving targets such as humans [1,2]. Recent developments show implementations of through-wall radars employing ultra-wideband (UWB) [3] and pulsed-Doppler signals [4]. UWB-based radars use very short pulses thus can provide high spatial resolution for through-wall imaging. However, certain wall materials such as bricks have significant dispersion and loss effects, causing only the lower portion of the signal band to be useful. For concrete walls, UWB radar is not suitable for through-wall detection [5]. Pulsed-Doppler based through-wall radars use Doppler shifts for motion detection and pulse timing for target ranging information. Using a carrier frequency of 5.8 GHz, the radar in [4] can provide a range accuracy of approximately 30 cm with minimum target velocity of 4 cm/sec. However, the range of the system is limited to 4 m.

In this paper, we demonstrated the use of a low-cost, two-element receiving array for tracking human movements in indoor surveillance applications. The concept entails simultaneously resolving the Doppler frequencies and the directions of arrival (DOA) of the returned signals from moving targets. The carrier frequency is 2.4 GHz as it provides significant through-wall penetration [6-8]. Moving target detection up to 30 feet distance through a 15-inch brick wall is demonstrated. Through-wall data of multiple movers is also collected using our system.

DDOA Radar

The system consists of a two-element receiver array operating at 2.4 GHz. Two microstrip antennas spaced a half wavelength apart are used as receiving antennas. Two low-cost, off-the-shelf integrated boards manufactured by Analog Devices (AD8347) are used as the quadrature receivers. Each receiver has the low-noise amplifier (LNA), I/Q mixers, gain control, and baseband amplifications all integrated on one board. After the down-converted signals are digitized, the fast Fourier transform is applied for Doppler discrimination and the phase difference between the two channels is used to calculate the DOA. Figure 1 illustrates the basic radar concept.

Through-Wall Measurement Results

Figure 2 shows the spectrogram results of through-wall Doppler measurements of a person walking toward the radar. The left figure was taken from a 5 GHz system built earlier [9]. The right figure shows the result from the present 2.4 GHz radar under approximately the same setup. The radar is placed against a 15-inch exterior brick wall while a person walks toward the wall on

the opposite side. The data show that the person is visible only during the last 3 seconds of the walk for the 5 GHz system, whereas the person is visible over the entire 10-second duration for the 2.4 GHz system. As expected, the 2.4 GHz carrier offers a longer detection range due to better wall penetration than at higher frequencies.

To measure the maximum through-wall detection distance, we use a loudspeaker driven by a 55 Hz audio tone as a stable test target. The vibrating membrane of the loudspeaker is covered by aluminum tape to enhance its return. The tone causes the loudspeaker membrane to vibrate back and forth and the radar return is an FM signal with fundamentals at +/- 55 Hz. Figure 3 shows the measurement setup and the results. First the loudspeaker is placed at approximately 20° to the left of the radar boresight at 30 feet distance from the other side of the wall. The return from this distance has sufficient power such that the correct Doppler and DOA can be measured (+/- 55 Hz and -20° respectively as shown in Fig. 3(b)). The loudspeaker is then moved to a 40 feet distance. This time erroneous DOA is measured due to the weaker signal, although the Doppler return is still vaguely recognizable (Fig. 3(c)). Therefore, we approximate the maximum through-wall detection range of our radar to be about 30 feet at a transmit power level of 23 dBm.

Multiple targets detection is next demonstrated. Two loudspeakers are placed at 10°and 30° to the left of the radar boresight and driven by 75 Hz and 55 Hz audio tones, respectively. Both loudspeakers are located at about 12 feet away from the wall (Fig. 4(a)). Their expected Doppler returns are +/- 75 Hz and +/- 55 Hz with the DOA of -10° and -30°, respectively. The measured data are plotted in Fig. 4(b) and clearly show the expected returns. Moving human data will be presented.

Conclusion

Doppler and DOA through-wall measurement results have been presented. The measurements were performed using a low-cost, two-element receiver array operating at 2.4 GHz. Based on our measurement results, our system is capable of detecting an indoor mover from outside a 15-inch brick wall with a range of 30 feet. Through-wall Doppler and DOA detection of multiple movers in a highly cluttered indoor environment was also demonstrated using our system.

Acknowledgment

This work is supported by the Office of Naval Research and the Texas Higher Education Coordinating Board under the Texas Advanced Technology Program.

References

[1] L. M. Frazier, "Surveillance through walls and other opaque materials," *Proc. IEEE National Radar Conference Electronic Systems*, pp. 27-31, May 1996.

[2] L. M. Frazier, "Motion detection radar (MDR) for law enforcement," *IEEE Potentials*, vol. 16, Issue 5, pp. 3079-3082, June 20-25, 2004.

[3] A. M. Attiya, A. Bayram, A. Safaai-Jazi and S. M. Riad, "UWB applications for through-wall detection," *IEEE Antennas Propagat. Soc. Symp.*, vol. 3, pp. 1868-1875, April 2000.

[4] D. G. Falconer, R. W. Ficklin and K.G. Konolige, "Robot-mounted through-wall radar for detecting, locating, and identifying building occupants," *Proc. IEEE Int. Conf. Robotics Automations*, vol. 2, pp. 1868-1875, April 2000.

[5] S. M. Riad, A. Muqaibel and A. Bayram, "Ultra-wideband propagation measurements and channel modeling," *DARPA NETEX Program, Report on Through-the-Wall Propagation and Material Characterization*, Nov. 2002.
[6] S. Todd, M. El-Tanany, G. Kalivas and S. Mahmoud, "Indoor radio path loss comparison between the 1.7 GHz and 37 GHz bands," *IEEE Int. Conf. Universal Personal Comm.*, vol. 2, pp. 621-625, Oct. 1993.
[7] W. Mohr, "Radio propagation for local loop applications at 2 GHz," *IEEE Third Annual Int. Conf. Universal Personal Comm.*, pp. 119-123, 27 Sept. 1994.
[8] D.I. Axiotis and M.E. Theologou, "Building penetration loss at 2 GHz for mobile communications at high elevation angles by HAPS," *IEEE Int. Symp. Wireless Personal Multimedia Comm.*, vol. 1, pp. 282-285, Oct. 2002.
[9] H. Ling, "MicroDoppler exploitation: data collection and analysis," Naval International Cooperative Opportunities in Science and Technology (NICOP) program on Time-Frequency ISAR and NCTI, London, England, June 2004.

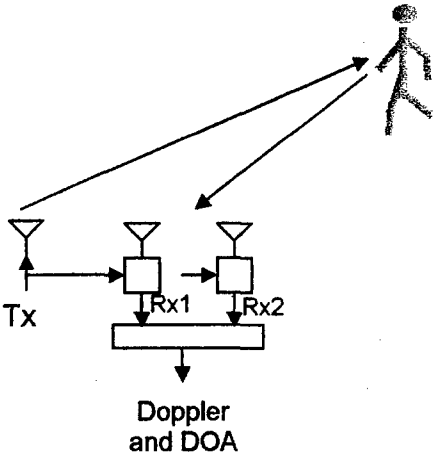

Figure 1. Basic radar operation.

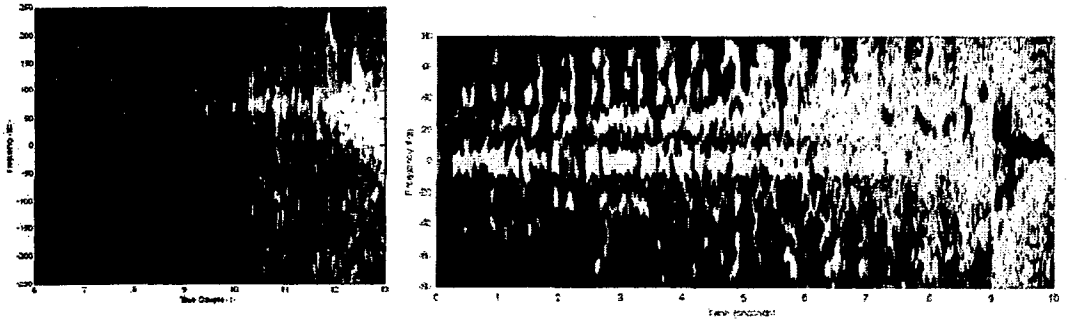

(a) (b)

Figure 2. Through-wall Doppler of a walking person: (a) 5 GHz and (b) 2.4 GHz.

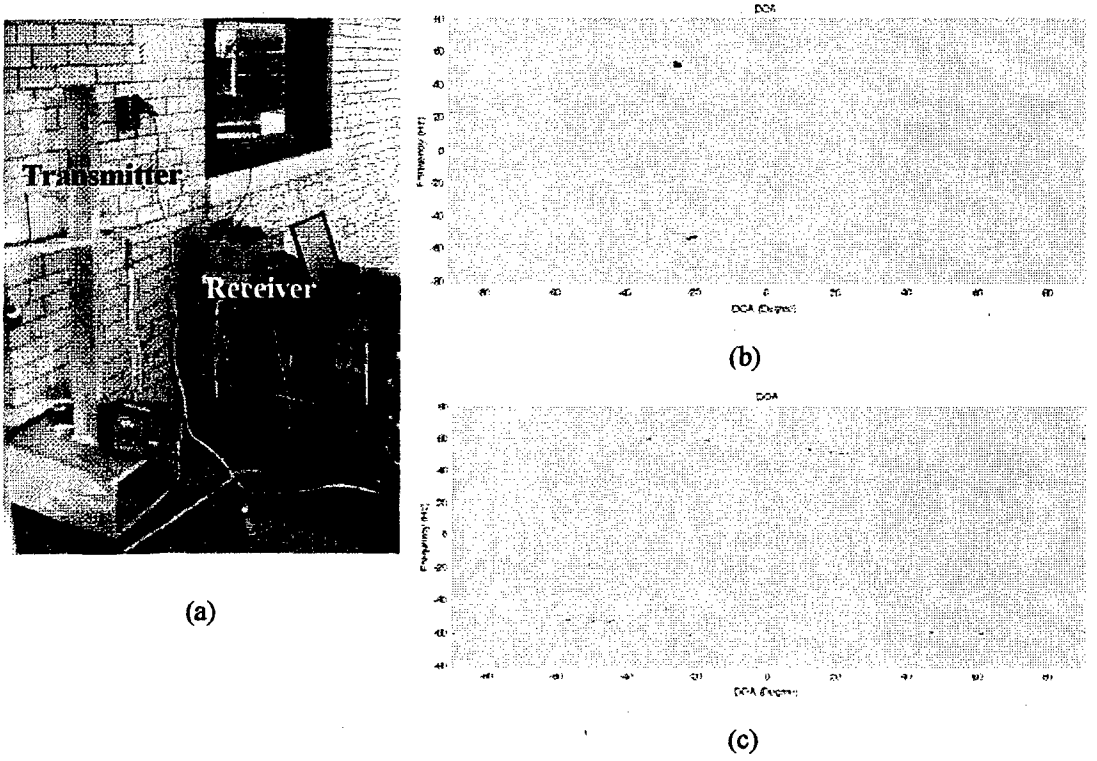

Figure 3. Through-wall Doppler of a single loudspeaker: (a) Radar system. (b) DDOA of the loudspeaker at 30' distance. (c) DDOA of the loudspeaker at 40' distance.

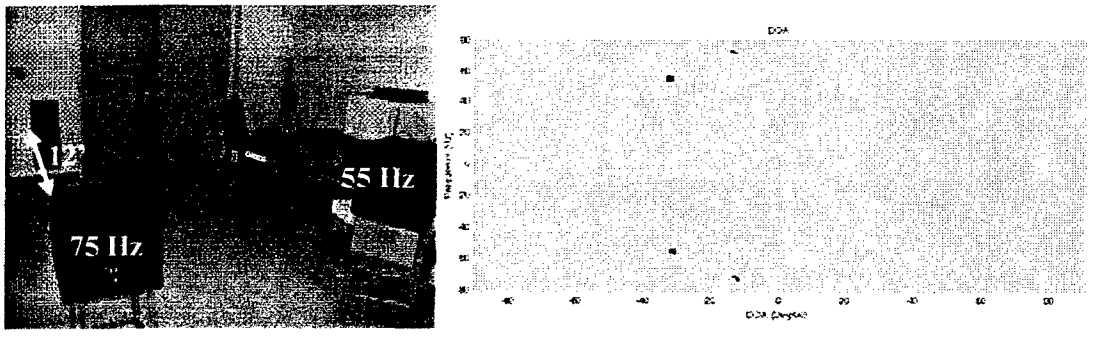

Figure 4. Through-wall Doppler of two loudspeakers: (a) Loudspeakers placement. (b) DDOA of the two loudspeakers.

Two-Dimensional Human Tracking Using a Three-Element Doppler and Direction-of-Arrival (DDOA) Radar

Adrian Lin and Hao Ling
Department of Electrical and Computer Engineering
University of Texas at Austin
Austin, TX 78712, USA
Email: adrian.lin@mail.utexas.edu

***Abstract*—We investigate the use of a low-cost, three-element receiving array for two-dimensional direction-of-arrival (DOA) sensing of multiple movers. The concept entails resolving the Doppler frequencies of the returned signals from the moving targets, and then measuring the phase difference at each Doppler frequency component to calculate the DOA of the targets. The three-element receiving array is configured to provide simultaneous DOA measurements in both the azimuth and elevation planes. An experimental system is constructed to test the concept and measurement results of multiple movers are presented.**

I. Introduction

Increasing demands on security and surveillance systems in military and law enforcement applications have prompted studies on human detection using radar. Information such as the number of humans and their locations in a high clutter environment is crucial for counter-terrorism, urban warfare and disaster search. Recent work on human detection includes both investigations on the Doppler characteristics from human movements [1-3] and the development of ultra-wideband imagers [4-6].

For Doppler detection, which is attractive for stationary clutter suppression, a directional receiving antenna can be used to provide the additional bearing information or the direction of arrival (DOA) of a moving target. Conventional DOA sensing of multiple targets requires the use of an antenna array with multiple elements, in combination with the use of direction finding algorithms. Such methods require the number of elements to be at least one greater than the number of targets. However, increasing the number of elements leads to an increase in the physical size, cost and complexity of the overall system.

In [7, 8], we reported on the DOA sensing of multiple moving targets from a two-element receiver array by utilizing Doppler discrimination. The phase difference of the reflected waves arriving at two receiver antennas are measured at each Doppler bin to allow for the DOA determination of multiple movers with sufficient Doppler separation. The two antennas are spatially separated in the horizontal dimension. Thus one-dimensional DOA sensing in the horizontal (azimuth) plane can be achieved.

In this paper, we extend the idea to the two-dimensional (azimuth and elevation) tracking of multiple movers by using a receiving array consisting of three elements. The receiver array is implemented using three commercial off-the-shelf integrated receivers. With two-dimensional information, it becomes possible to track multiple humans moving at different elevations of a structure such as in a multi-storied building.

II. Basic Theory

Different moving targets typically give rise to different Doppler shifts with respect to the radar. Therefore, by processing the data via Doppler discrimination, we can extract their DOA information by measuring the phase difference at each Doppler frequency component. More explicitly, if we assume the time signals received at the two antenna elements to be $f_1(t)$ and $f_2(t)$, then after the Doppler processing the signals become $F_1(f_D)$ and $F_2(f_D)$, respectively. If the targets of interest generate different Doppler frequencies f_{Di} due the difference in their velocities with respect to the radar transceiver, then the DOA of target i with respect to the array boresight is given by:

$$\theta_i = \sin^{-1}\left[\frac{\angle F_1(f_{Di}) - \angle F_2(f_{Di})}{(2\pi d / \lambda_c)}\right] \qquad (1)$$

where d is the spacing between the elements and λ_c is the RF wavelength. Referring to Fig. 1(a), if the two receiving

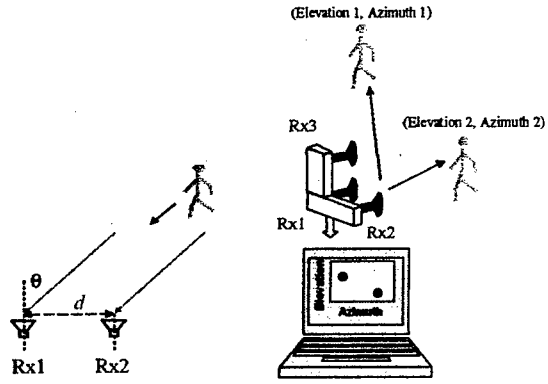

Fig 1. DOA sensing in: (a) One-dimensional (azimuth) and (b) Two-dimensional (azimuth, elevation)

elements (Rx1 and Rx2) are placed horizontally apart, they provide DOA (θ_{AZ}) information in the horizontal (azimuth) plane.

To obtain the bearing information in the elevation direction, an additional receiving antenna (Rx3) is placed directly above Rx1 as shown in Fig. 1(b). The additional receiver Rx3 and the existing receiver Rx1 form a new pair of elements to provide the DOA in the elevation plane, θ_{EL}. The Doppler and DOA processing in Eq. (1) is then repeated for the Rx1 and Rx3 signals. Finally, by correlating the DOA results based on their associated Doppler, it is possible to construct the data matrix $[A(f_{Di}), \theta_{AZ}(f_{Di}), \theta_{EL}(f_{Di})]$, where $A(f_{Di})$ is the signal strength at the Doppler component f_{Di}. Hence, the two-dimensional bearing sensing of multiple movers can be achieved, provided that the movers have different Doppler frequencies.

III. Radar Design

An experimental system is designed and constructed to test the concept. The system consists of a three-element antenna array, three dual-quadrature integrated receivers (Analog Devices AD8347 ICs) and a transmitter operating at a frequency of 2.4 GHz. Since the IC is targeted for the consumer wireless market, it is very low cost (less than $100 per evaluation board assembly). Three microstrip patch antennas on a 1.6 mm thick FR-4 substrate are used. To provide the maximum resolution while avoiding DOA ambiguity within the scanning range from -90° to 90°, the distances between the two antennas in both the azimuth and elevation planes are set to $\lambda_c/2$. The received signals are downconverted, digitized by the NI-DAQ 6024E and processed using the FFT for Doppler discrimination before the DOA calculations are carried out. Fig. 2 shows the system block diagram and a photo of the radar hardware.

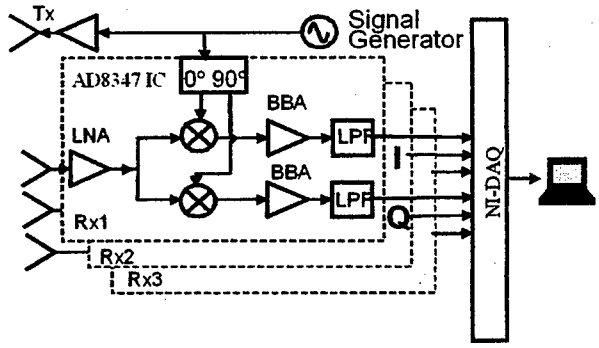

(a)

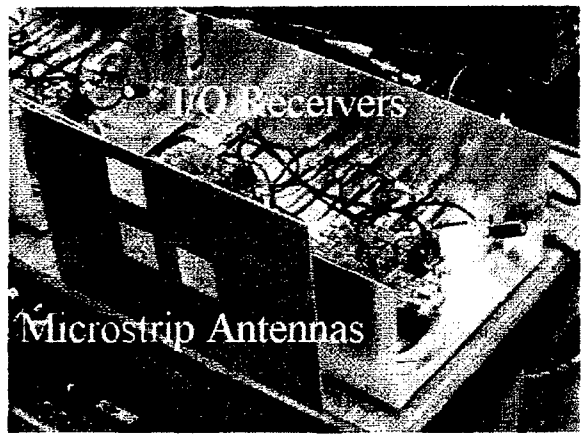

(b)

Fig 2. Radar (a) system block diagram and (b) actual hardware implementation.

IV. Measurement Results

1) Loudspeakers. We use three loudspeakers driven by 20 Hz, 30 Hz and 66 Hz audio tones as stable test targets. The vibrating membrane of each loudspeaker is covered by aluminum tape to enhance its return. The tones cause the loudspeaker membrane to vibrate back and forth and the radar returns are FM signals with fundamentals at +/-20 Hz, +/-30 Hz and +/-66 Hz. The three loudspeakers are placed at the approximate (azimuth, elevation) coordinates of (-28°, -10°), (-30°, 10°) and (-15°, 18°) respectively. The measurement setup and results are shown in Fig 3. As expected, Fig. 3(b) shows that the Doppler and azimuth DOA of the three loudspeakers are (+/-20 Hz, -28°), (+/-30 Hz, -30°) and (+/-66 Hz, 18°). Fig. 3(c) shows the Doppler and elevation DOA of (+/-20 Hz, -10°), (+/-30 Hz, 10°) and (+/-66 Hz, 18°), which correspond to the expected elevations. By correlating the two measurements based on the Doppler information, a two-dimensional DOA plot can be constructed accordingly. Fig. 3(d) shows the resulting azimuth and elevation coordinates of the three loudspeakers.

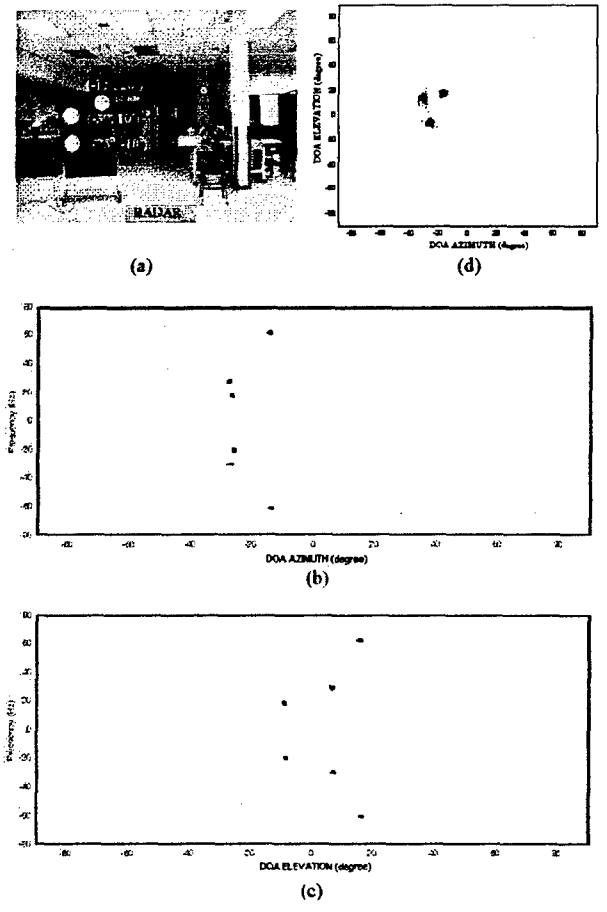

Fig 3. Loudspeakers measurement: (a) Setup, (b) Doppler and azimuth DOA. (c) Doppler and elevation DOA and (d) Two-dimensional DOA (azimuth, elevation)

A comparison of Figs. 3(a) and 3(d) shows a close correspondence of the DOA results to the frontal perspective of the radar.

2) Bouncing Ball. To show two-dimensional trajectory tracking we use a bouncing basketball as a moving target. The ball is also covered by aluminum tape to enhance its return. The ball is launched from the left side of the radar toward the radar boresight and bounces on the floor three times during its trajectory. Fig. 4 shows the measurement setup and results. The short-time Fourier transform [9, 10] is used to process the measured data to extract the Doppler components of the moving target with respect to time. The corresponding DOA versus time plots are used to show the motion trajectory of the ball in the azimuth and elevation planes, as shown in Figs. 4(b) and (c). After correlating the DOA information from both planes according to the Doppler, a two-dimensional DOA trajectory is generated (Fig. 4(d)). It shows the entire time that the ball is in motion.

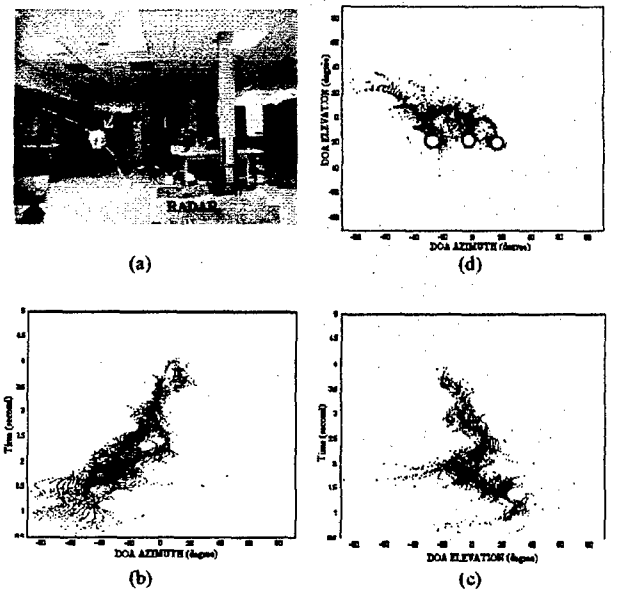

Fig 4. Bouncing basketball: (a) Setup, (b) Azimuth DOA vs. time, (c) Elevation DOA vs. time and (d) Two-dimensional DOA trajectory.

The gray shading indicates the signal strength. The measured trajectory result agrees with the actual trajectory: the first bounce is at approximately (-30°, -20°), followed by subsequent bounces at (-10°, -20°) and (15°, -20°) as indicated by the three white dots.

3) Human Walking. The next measurement involves human subjects. Two human subjects in front of a building walk in the patterns shown in Fig. 5(a). The subject on the left begins at point A (at approximately (-60°, -20°) with respect to the radar) and climbs a staircase to the top at point B (-20°, 40°). The subject then turns around and descends to the ground level back to point A. The subject on the right starts at point C (at approximately (20°, -20°) at the ground level) and walks to the right until reaching point D at (85°, -20°). The subject then turns around and walks back to point C. The radar is placed approximately 10 m away from the building. Since a directional horn is used as the radar transmitter, the measurable angular range in the azimuth plane is limited to approximately +/-70°. Figs. 5(b), (c) and (d) show the measured azimuth, elevation and two-dimensional DOA trajectories, respectively. As we can see from Fig. 5(d), the measured walking trajectories span from point A to point B for the person on the left, and from point C to point D for the person on the right.

V. Conclusion

Two-dimensional DOA sensing of multiple movers using a Doppler and DOA (DDOA) radar has been presented. Measurements were performed using a low-cost, three-element receiver array operating at 2.4 GHz. By correlating the azimuth and elevation DOA measurements based on the

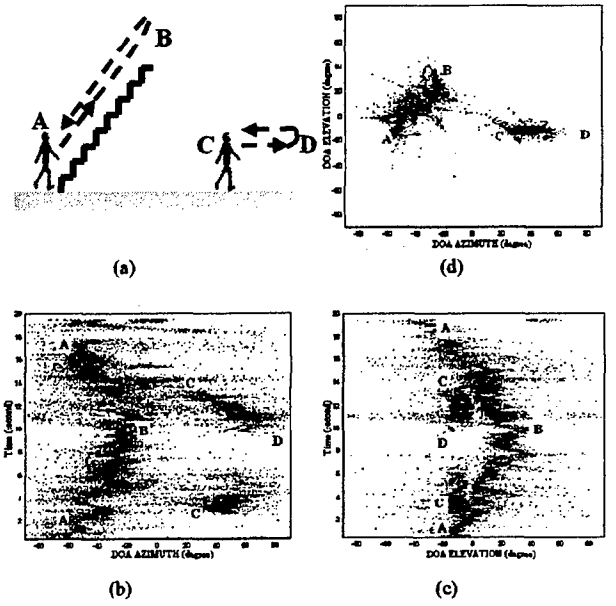

Fig 5. Two humans tracking: (a) Setup, (b) Azimuth DOA vs. time, (c) Elevation DOA vs. time and (d) Two-dimensional DOA trajectory.

Doppler information, the two-dimensional locations of multiple moving targets can be derived accordingly. Preliminary measurement results show good agreement with the actual setup. Improvement in the signal processing and more extensive data collection will be carried out next in our research.

VI. ACKNOWLEDGMENT

This work is supported by DARPA, the Office of Naval Research, Texas Higher Education Coordinating Board under the Texas Advanced Technology Program and the National Science Foundation Major Research Instrumentation Program.

VII. REFERENCES

[1] J. L. Geisheimer, E. F. Greneker and W. S. Marshall, "High-resolution Doppler model of the human gait," *SPIE Proc., Radar Sensor Technology and Data Visualization*, vol. 4744, pp. 8-18, July 2002.

[2] V. C. Chen, "Analysis of radar micro-Doppler with time-frequency transform", *Proc. of the 10th IEEE Workshop on Statistical Signal and Array Processing*, pp. 463-366, Pocono Manor, PA, Aug. 2000.

[3] P. van Dorp and F. C. A. Groen, "Human walking estimation with radar," *IEE Proc. – Radar, Sonar and Navigation*, vol. 150, pp. 356-365, Oct. 2003.

[4] S. Nag, H. Fluhler and M. Barnes, "Preliminary interferometric images of moving targets obtained using a time-modulated ultra-wideband through-wall penetration radar," *Proc. 2001 IEEE Radar Conf.*, pp. 64-69, May 2001.

[5] A. R. Hunt, "Image formation through walls using a distributed radar sensor network," *SPIE Proc., Sensors, and Command, Control, Communications, and Intelligence (C3I) Technologies*, vol. 5778, pp. 169-174, May 2005.

[6] J. Z. Tatoian, G. Franceshetti, H. Lackner and G. G. Gibbs, "Through-the-wall impulse SAR experiments," *IEEE Antennas Propagat. Soc. Int. Symp. Digest*, July 2005.

[7] A. Lin and H. Ling, "Human tracking using a two-element antenna array," *SPIE Proc., Radar Sensor Technology and Data Visualization*, vol. 5788, p. 57-64, May 2005.

[8] A. Lin and H. Ling, "Through-wall measurements of a Doppler and direction-of-arrival (DDOA) radar for tracking indoor movers," *IEEE Antennas Propagat. Soc. Int. Symp. Digest*, July 2005.

[9] S. Qian and D. Chen, *Introduction to Joint Time-Frequency Analysis – Methods and Applications*, Prentice Hall, Englewood Cliffs, NJ, 1996.

[10] V. Chen and H. Ling, *Time-Frequency Transforms for Radar Imaging and Signal Analysis*, Artech House, Norwood, MA, 2002.

Location Tracking of Indoor Movers Using a Two-Frequency Doppler and Direction-of-Arrival (DDOA) Radar

Adrian Lin* and Hao Ling
Department of Electrical and Computer Engineering
University of Texas at Austin
Austin, TX 78712, USA

Introduction

Two-dimensional location tracking of humans is useful for physical security applications. Previously, we reported on a two-element Doppler and Direction-of-Arrival (DDOA) radar for a bearing tracking of multiple humans [1, 2]. In this paper, we add the ranging capability to the radar to achieve two-dimensional location tracking. In contrast to conventional pulsed-based or frequency-modulated continuous wave (FMCW) radar, multiple frequency continuous wave (MFCW) radar is a simple and low-cost way to acquire range information [3, 4]. To keep the radar architecture as simple as possible, we use only two frequencies. However, a two-frequency system can only acquire the range for a single-target configuration. To overcome this limitation, we take advantage of the Doppler separation among the moving targets as a prefilter before measuring the phase difference to arrive at the range information of the moving targets. This two-tone approach in conjunction with the two-element DDOA radar can then provide the two-dimensional locations of humans. Multiple human location tracking results are collected using our system.

Two-Frequency DDOA Radar

Figure 1(a) illustrates the basic radar architecture. The system operates at two CW frequencies fc_1 (2.4 GHz) and fc_2 (10 MHz below fc_1). The frequency separation is selected to achieve a maximum unambiguous range of 15 m. The two CW frequencies are combined and transmitted simultaneously. The scattered wave off a target is received by two microstrip antennas spaced a half wavelength apart. Three low-cost, off-the-shelf integrated boards manufactured by Analog Devices (AD8347) are used as the quadrature receivers. Each receiver has a low-noise amplifier (LNA), I/Q mixers, gain control, and baseband amplifiers all integrated on one board. The actual radar hardware is shown in Fig. 1(b). The local oscillator (LO) frequency of receivers Rx_1 and Rx_2 is set to fc_1, and that of Rx_3 is set to fc_2. The down-converted signals are digitized and the Doppler frequencies of the target are extracted after applying the sliding-window fast Fourier transform. The phase difference $\Delta\Phi_{21}$ at each Doppler bin from Rx_1 and Rx_2 is measured to obtain the bearing information θ using the following equation:

$$\theta = \sin^{-1}\left(\frac{\lambda_{c1}\Delta\Phi_{21}}{2\pi d}\right) \tag{1}$$

where d is the spacing between the receiving antennas and λc_1 is the wavelength of fc_1. The received signal at Rx_2 is also routed into Rx_3 and the phase difference $\Delta\Phi_{32}$ at each Doppler bin from Rx_2 and Rx_3 is measured to calculate the target range R using the following equation:

$$R = \frac{c\Delta\Phi_{32}}{4\pi\Delta f} \tag{2}$$

where $\Delta f = fc_1 - fc_2$ and c is the speed of light. By correlating the bearing and range information based on their associated Doppler, it is possible to assemble the data matrix $[A(f_{Di}), \theta(f_{Di}), R(f_{Di})]$, where $A(f_{Di})$ is the signal strength at the Doppler bin f_{Di}. The two-dimensional range and bearing information of multiple movers can then be obtained accordingly as long as the movers have different Doppler frequencies.

Measurement Results

We first use two loudspeakers as stable test targets. The vibrating membrane of each loudspeaker is covered by aluminum tape to enhance its return. Fig. 2(a) shows the measurement setup and the loudspeakers locations. The first loudspeaker is located at approximately 20° to the left of the radar boresight at 4 m distance, driven by a 40 Hz audio tone. The second loudspeaker is positioned at approximately 20° to the right of the radar at 5.5 m distance, driven by a 50 Hz audio tone. The measured data are plotted in Fig. 2(b), and show good agreement with the expected bearings of -20° and +20°. Fig. 2(c) shows the range measurements which agree with the expected ranges of 4 m and 5.5 m. By using the polar-to-Cartesian transformation $(R\sin\theta, R\cos\theta)$, a location map can be constructed and is shown in Fig. 2(d). The coordinates of the left and right loudspeakers are close to the expected locations at (-1.4 m, 3.8 m) and (1.8 m, 5.2 m).

Preliminary human location tracking measurements are described next. Two human subjects walk in a straight path at approximately the same speed but in opposite directions (Fig. 3(a)). During the walk, the radar continuously measures and outputs the bearing and range information of the subjects (Fig. 3(b, c)). During the first five seconds of the measurement, Fig. 3(b) shows two distinct bearing trajectories: the first one progressing from approximately -20° toward 0°, and the second one from 0° toward 20°. These measured bearing trajectories are expected since they are plotted based on the perspective of the radar. As the subject to the left walks in a straight path away from the radar, the measured bearing angle advances toward the radar boresight. The opposite happens for the subject on the right: the measured bearing angle advances away from the radar boresight as the subject walks closer to the radar.

Fig. 3(c) shows the measured range tracks. In the first five seconds of the measurement, there are two distinct range tracks: the first one starts at about 1 m and ends at 10 m while the second one progresses from approximately 10 m to 1 m. The first range track is associated with the subject to the left of the radar, who walks away from the radar during this time. The second range track belongs to the subject to the right, who walks closer toward the radar during the time interval. At approximately t = 5 sec, both subjects turn around and walk back to their original starting positions. This is clearly shown in Figs. 3(b) and 3(c) as changes in the bearing and range tracks at t = 5 sec. The corresponding two-dimensional location map is constructed and shown in Fig. 3(d).

Conclusion

Two-dimensional bearing and range tracking of multiple indoor movers using a two-frequency Doppler and DOA radar have been presented. Measurements were performed using a low-cost, two-element receiver array operating at two CW tones. The

attractiveness of the system is that it has very low complexity. However, its performance is dependent on the Doppler separation between the targets.

Acknowledgment

This work is supported by the Office of Naval Research, the Texas Higher Education Coordinating Board under the Texas Advanced Technology Program and the National Science Foundation Major Research Instrumentation Program.

References

[1] A. Lin and H. Ling, "Human tracking using a two-element antenna array," *SPIE Proc., Radar Sensor Technology and Data Visualization*, vol. 5788, p. 57-64, May 2005.

[2] A. Lin and H. Ling, "Through-wall measurements of a Doppler and direction-of-arrival (DDOA) radar for tracking indoor movers," *IEEE Antennas Propagat. Soc. Int. Symp. Digest,* paper no. S099p03a, July 2005.

[3] M. A. Solano, J. S. Ipina, J. M. Zamanillo and C. Perez-Vega, "X-band Gunn diode oscillator for a multiple-frequency continuous-wave radar for educational purposes," *IEEE Trans. on Education*, vol. 45, No. 4, pp. 316-322, Nov. 2002.

[4] M. G. Anderson, "Multiple frequency continuous wave radar design for micro-Doppler extraction," Master Thesis, The University of Texas at Austin, May 2005.

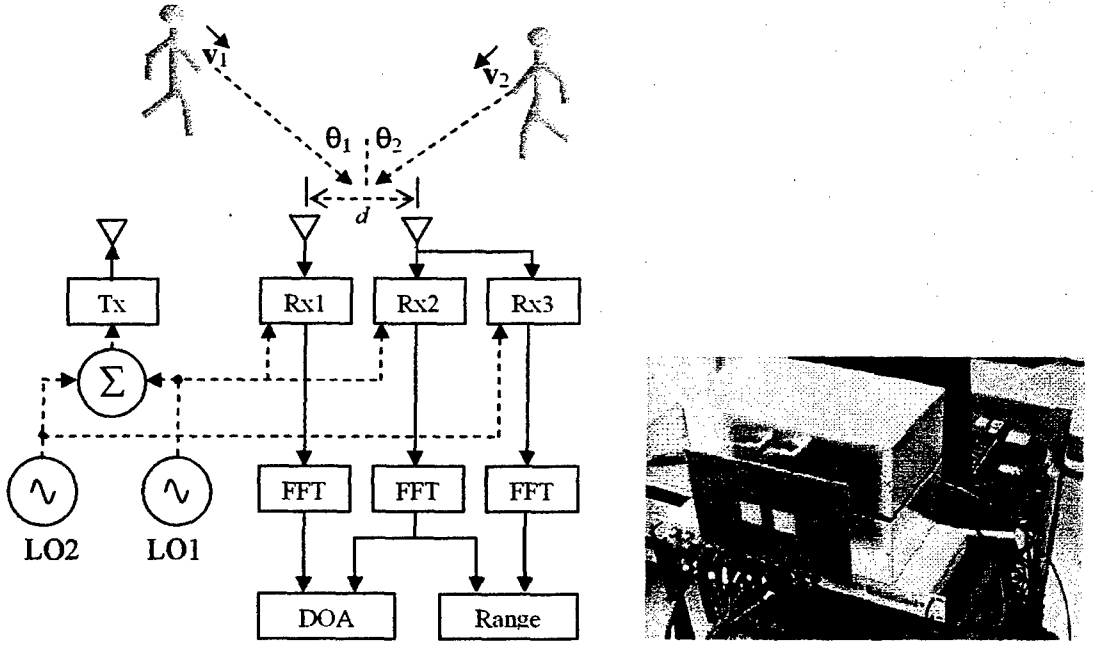

Figure 1. (a) Basic radar operation and (b) actual radar hardware.

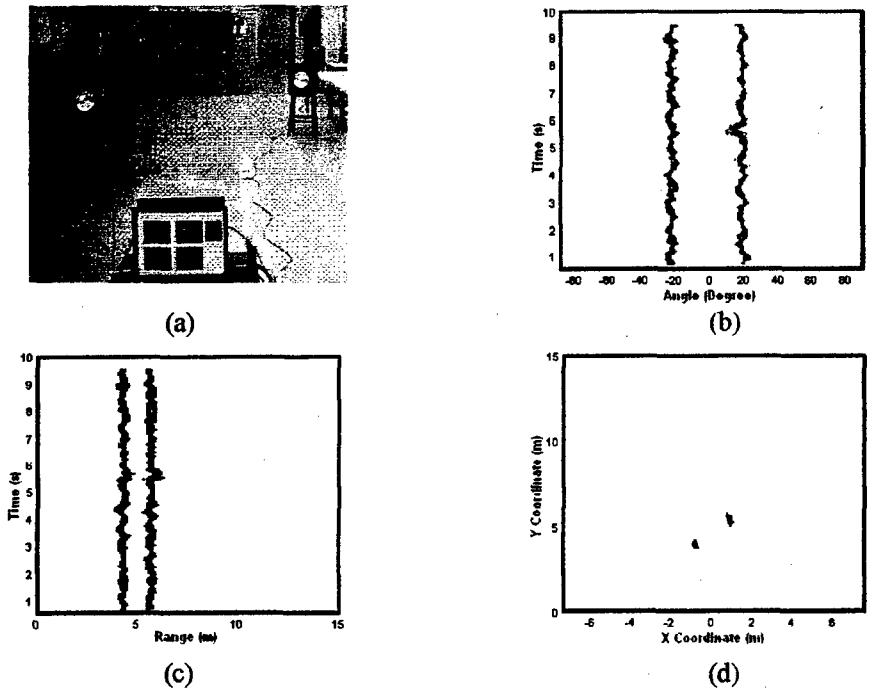

Figure 2. Loudspeakers measurements: (a) setup, (b) bearing track, (c) range track, (d) 2-D location map.

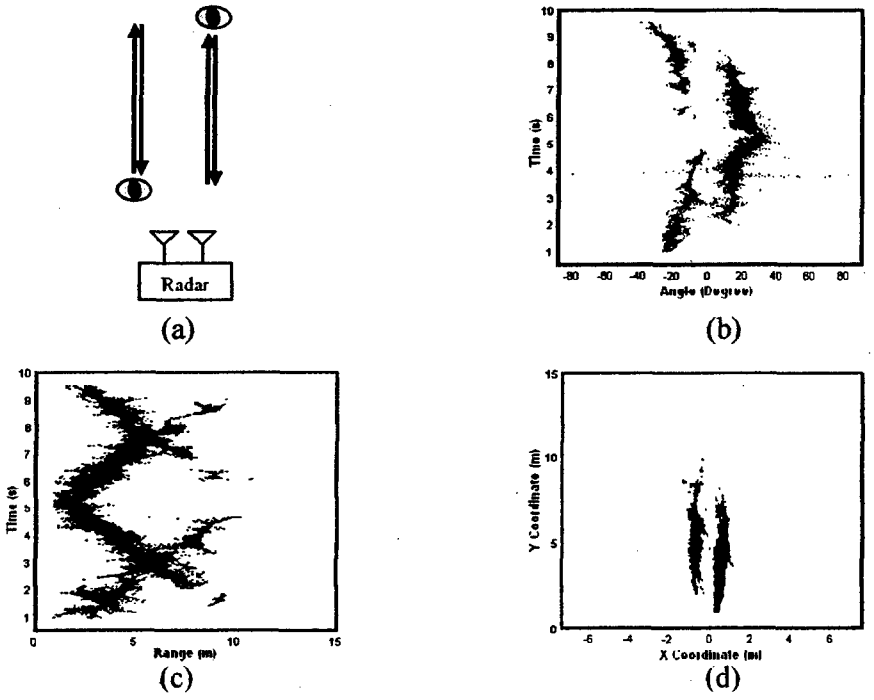

Figure 3. Humans walking measurements: (a) setup, (b) bearing track, (c) range track, (d) 2-D location map.